

**Mechanismen hochfrequenter
synaptischer Übertragung**

Von der Medizinischen Fakultät
der Universität Leipzig
genehmigte

HABILITATIONSSCHRIFT

zur Erlangung des akademischen Grades
Doctor habilitatus
(Dr. habil.)

vorgelegt von

Dr. med. Dipl. phys. Stefan Jens Hallermann
geboren am 24.7.1975 in Würzburg

Tag der Verleihung 27. September 2011

Bibliographische Beschreibung

Hallermann, Stefan: *Mechanismen hochfrequenter synaptischer Übertragung*

Universität Leipzig, kumulative Habilitationsschrift

129 Seiten, inklusive 8 Originalarbeiten, 5 Abbildungen und Literaturstellen

Die schnelle und präzise Informationsverarbeitung unseres Nervensystems basiert auf hochfrequenter synaptischer Übertragung zwischen Nervenzellen. Hierbei löst der Einstrom von Calcium-Ionen (Ca^{2+}) die Fusion Transmittergefüllter Vesikel an spezialisierten präsynaptischen Nervenendigungen aus. Obwohl viele der hieran beteiligten Proteine bekannt sind, ist deren zeitliches und räumliches Zusammenspiel und deren Regulation durch Ca^{2+} bisher ungenügend verstanden.

Mit präsynaptischen Ableitungen von hippokampalen Moosfasersynapsen wurde ein großer Vorrat an fusionsbereiten Vesikeln gefunden, die schnell fusionieren können. Um die molekularen Mechanismen zu verstehen, die an der Fusion einer hohen Anzahl synaptischer Vesikel innerhalb weniger Millisekunden beteiligt sind, wurden die genetischen Möglichkeiten der Fruchtfliege *Drosophila melanogaster* genutzt. Es zeigte sich, dass das Protein Bruchpilot in *Drosophila* am Aufbau der Cytomatrixstruktur beteiligt ist, dass die Anreicherung von Bruchpilot an der Freisetzungsstelle und die Größe des postsynaptischen Glutamatrezeptorfeldes lokal äußerst spezifisch aufeinander abgestimmt werden, und dass Bruchpilot maßgeblich an der Vesikelnachladung beteiligt ist. Die Funktion der Vesikelnachladung konnte auf intramolekularem Niveau einem bestimmten Teil des Bruchpilot Moleküls (dem C-Terminus) zugeordnet werden.

Um diese an Invertebraten gewonnen Befunde auf Synapsen des zentralen Nervensystems von Wirbeltieren zu übertragen, wurden cerebelläre Moosfasersynapsen untersucht, an denen hochfrequente synaptische Übertragung und schnelle Vesikelnachladung beschrieben wurden. Obwohl das *Drosophila*-Protein Bruchpilot kein direktes Sequenzhomolog bei Vertebraten hat, erschien das Invertebraten-spezifische Cytomatrixprotein Bassoon ein interessanter Kandidat zu sein, der bei der hochfrequenten synaptischen Übertragung eine ähnliche Funktion ausführen könnte. In der Tat zeigte die mechanistische Untersuchung von Bassoonmutanten, dass Bassoon die Nachladerate an Synapsen des zentralen Nervensystems beschleunigt.

Die Ergebnisse der vorliegenden Arbeit sind von Bedeutung für unser Verständnis schneller Informationsverarbeitung in unserem Nervensystem und sollten neue Aspekte für unser Verständnis der Pathophysiologie neurologischer Erkrankungen eröffnen.

Inhaltsverzeichnis

1	Einführung in die Thematik	5
1.1	Hochfrequente synaptische Übertragung	5
1.2	Die Cytomatrix an der Freisetzungsstelle	9
2	Zielsetzung	13
3	Originalarbeiten	15
3.1	Hallermann <i>et al.</i> , 2003, Proc Natl Acad Sci U S A 100: 8975-8980	15
3.2	Kole*, Hallermann* und Stuart, 2006, J Neurosci, 26:1677-1687	22
3.3	Schmid*, Hallermann* <i>et al.</i> , 2008, Nat Neurosci, 11:659-666	34
3.4	Fouquet <i>et al.</i> , 2009, J Cell Biol, 186:129-145	43
3.5	Geis <i>et al.</i> , 2010, Brain 133:3166-3180	61
3.6	Hallermann <i>et al.</i> , 2010a, HFSP J, 4:75-84	77
3.7	Hallermann <i>et al.</i> , 2010b, J Neurosci, 30: 14340-14345	91
3.8	Hallermann <i>et al.</i> , 2010c, Neuron im Druck	98
4	Diskussion und Ausblick	113
4.1	Die Bedeutung der Cytomatrix für die hochfrequente Übertragung	113
4.2	Ca ²⁺ -Abhängigkeit der Vesikelfusion und -nachladung	115
4.3	Ableitungen von cerebellären Moosfaserendigungen	117
5	Literaturverzeichnis	121
6	Erklärung	126
7	Lebenslauf	127

1 Einführung in die Thematik

1.1 Hochfrequente synaptische Übertragung

Evolutionärer Selektionsdruck hat zu der Entwicklung präziser und schneller Informationsverarbeitung unseres zentralen Nervensystems geführt. Bei der Ausübung von Sportarten wie etwa Tischtennis können daher mit erstaunlicher Präzision und Geschwindigkeit visuelle, propriozeptive und vestibuläre Signale verarbeitet und motorische Bewegungen gesteuert werden (Iacoboni, 2001; Todorov, 2004). Vermutlich wird die Größe eines bestimmten Signals in unserem Nervensystem als Frequenz von Aktionspotentialen codiert (Abb. 1A; London *et al.*, 2010), wobei auch der Zeitpunkt der Aktionspotentiale bis in den Sub-Millisekunden-Bereich für die Informationsverarbeitung genutzt wird (Kumar *et al.*, 2010). Für eine schnelle Informationsverarbeitung mit einem hohen dynamischen Bereich erscheinen daher hohe Aktionspotentialfrequenzen erforderlich. Entsprechend wurden im Kleinhirn Frequenzen von bis zu einem kHz *in vivo* gemessen (Jörntell und Ekerot, 2006). Während die Generierung und Weiterleitung hochfrequenter Aktionspotentialfolgen vergleichsweise gut verstanden sind (Lien und Jonas, 2003), sind die Mechanismen hochfrequenter synaptischer Übertragung weitgehend ungeklärt.

Unser Verständnis der hochfrequenten synaptischen Übertragung, an der eine Vielzahl an Proteinen und Lipiden beteiligt ist (Südhof, 2004), basiert größtenteils auf detaillierten Analysen einiger weniger Arten von Synapsen. Hierzu zählen die neuromuskuläre Endplatte (Katz, 1969), die Tintenfisch-Riesensynapse (Llinás, 1999), die Bipolarzellsynapse in der Retina (von Gersdorff und Matthews, 1994), die innere Haarzelle (Beutner *et al.*, 2001) und die Held'sche Calyx, eine Nervenendigung im auditorischen System des Hirnstamms (Forsythe, 1994). Diese Synapsen erlauben einen direkten Zugang zu den präsynaptischen Nervenendigungen mit elektrophysiologischen Techniken. Hierbei erleichtert sich die Analyse der Mechanismen der synaptischen Übertragung maßgeblich dadurch, dass die Membranspannung kontrolliert, die Membrankapazität gemessen und Wirksubstanzen eingewaschen werden können.

Inwieweit sich die an diesen Modellsynapsen gewonnenen Erkenntnisse übertragen lassen auf zentrale Synapsen, die hochfrequente Signale langanhaltend übertragen können, ist unklar. Da an Moosfasersynapsen des Hippocampus präsynaptische *patch-clamp* Ableitungen etabliert wurden (Geiger und Jonas, 2000), ergab sich die Möglichkeit, die Mechanismen der Transmitterfreisetzung mit Kapazitätsmessungen zu untersuchen. Hierbei kann die Vesikelfusion direkt anhand einer Kapazitätserhöhung gemessen werden (Lindau und Neher, 1988).

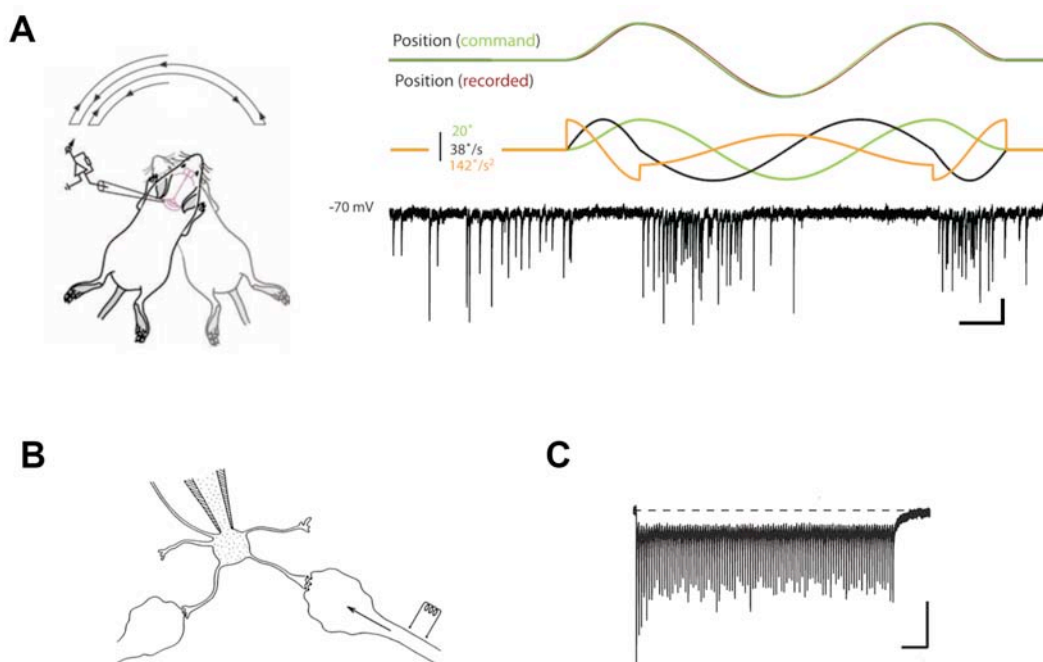


Abb. 1: Hochfrequente Signalübertragung

A Schematische Darstellung einer *whole-cell patch-clamp* Ableitung von einer Körnerzelle des Cerebellums einer horizontal rotierenden Maus *in-vivo*. Rechts oben: Das Positions-Kommandosignal (grün) und die gemessene Position (braun). Mitte: Entsprechende Position (grün), Geschwindigkeit (schwarz) und Beschleunigung (orange). Unten: Beispiel einer Stromspur mit postsynaptischen Strömen, deren Frequenz annähernd linear mit der Geschwindigkeit in eine Richtung korreliert (Skalierungsbalken 10 pA, 500 ms; Abb. modifiziert nach Arenz *et al.*, 2008).

B Schematische Darstellung der synaptischen Morphologie und der *whole-cell patch-clamp* Ableitung von einer cerebellären Körnerzelle. Die Stimulation der Moosfaser mit einer extrazellulären Reizelektrode ist angedeutet (Abb. modifiziert nach Silver *et al.*, 1996).

C Gemittelte postsynaptische Ströme, hervorgerufen durch 100 Stimulation einer Moosfaser mit 100 Hz (Skalierungsbalken 20 pA, 100 ms; Abb. modifiziert nach Saviane und Silver, 2006).

Kapazitätsmessungen in der *whole-cell* Konfiguration der *patch-clamp* Technik wurden ursprünglich für einfache Strukturen entwickelt (Lindau und Neher, 1988), und es war unklar, ob sie auf komplexe Strukturen wie z. B. hippocampale Moosfasersynapsen angewendet werden könnten. Weiterhin wurde davon ausgegangen, dass die durch Vesikelfusion an hippocampalen Moosfasersynapsen hervorgerufenen Kapazitätsänderungen nahe am Auflösungslimit der Methode liegen dürften. Mit optimierter Technik (hochfrequenter 5 kHz-Sinuswellenstimulation) konnte gezeigt werden, daß quantitative Kapazitätsmessungen mit hoher räumlicher Auflösung und Spezifität in hippocampalen Moosfasersynapsen möglich sind, und dass Moosfasersynapsen über einen sehr großen Vorrat an fusionsbereiten Vesikeln verfügen, der schnell fusionieren kann (Kapitel 3.1; Hallermann *et al.*, 2003; siehe auch Kushmerick und von Gersdorff, 2003).

Whole-cell patch-clamp Ableitungen können auch von entsprechenden postsynaptischen Strukturen durchgeführt werden. Hiermit konnte der Frage nachgegangen werden, ob die dort vorkommenden hyperpolarisationsaktivierten HCN-Kanäle eine kleine Einzelkanalleitfähigkeit haben und welche Erklärungen es hierfür gäbe (Kole *et al.*, 2006). Es zeigte sich eine geringe Einzelkanalleitfähigkeit, die zu einer signifikanten Reduktion des Rauschens der Membranspannung führt, welches durch das stochastische Verhalten der Kanäle bedingt ist. Aufgrund der geringen Kapazität der kleinen dendritischen Struktur scheint die hohe Offenwahrscheinlichkeit der HCN Kanäle unter Ruhebedingungen ein Störfaktor zu sein, der die Signalübertragung beeinflussen kann. Wären HCN-Kanäle zehnfach leitfähiger, würde nur ein Zehntel der Kanäle benötigt und die durchschnittliche Membranspannung in den Dendriten wäre unbeeinflusst. Allerdings würde das Rauschen der Membranspannung steigen und die Präzision der synaptischen Übertragung und damit der Informationsverarbeitung signifikant sinken (Kapitel 3.2; Kole *et al.*, 2006).

Mit optischen Methoden konnte außerdem untersucht werden, ob die hochfrequente synaptische Übertragung bei bestimmten neurologischen Erkrankungen gestört ist. Bei Mäusen konnte die intrathekale Applikation von

Immunglobulinen, welche von Patienten mit der paraneoplastischen neurologischen Erkrankung *stiff-person syndrome* aufgereinigt wurden, die Symptome der Patienten hervorrufen. Ursächlich hierbei sind Antikörper gegen das Protein Amphiphysin, das bei der Endocytose der Vesikel eine entscheidende Rolle spielt (Wigge und McMahon, 1998). Bei einer Analyse mit FM-Farbstoffen, mit denen der Vesikelzyklus untersucht werden kann (Betz und Bewick, 1992), zeigte sich, dass die hochfrequente Übertragung insbesondere in inhibitorischen Neuronen signifikant beeinträchtigt ist (Kapitel 3.5; Geis *et al.*, 2010).

Zur Untersuchung der molekularen Mechanismen der synaptischen Übertragung ist die Untersuchung der neuromuskulären Synapse von Larven der Fruchtfliege *Drosophila melanogaster* aus verschiedenen Gründen geeignet. Die vielfältigen genetischen Manipulationsmöglichkeiten von *Drosophila* lassen sich mit hochauflösenden elektrophysiologischen und optischen Methoden kombinieren. Die neuromuskuläre Synapse bei *Drosophila* kann außerdem wegen der strukturellen Ähnlichkeit und der Verwendung von Glutamat als Neurotransmitter als Modellsystem für erregende zentral Synapsen von Wirbeltieren angesehen werden (Kapitel 3.3, 3.4, 3.6 und 3.7; für eine detailliertere Einführung in die Thematik siehe Kapitel 1.2).

Zur weiteren Untersuchung der Mechanismen der hochfrequenter synaptischer Übertragung bei Wirbeltieren ist die Moosfasersynapse des Cerebellums ein idealer Kandidat. An dieser Synapse können hohe Frequenzen (> 100 kHz) zeitlich präzise und lang anhaltend übertragen werden, und eine Untersuchung dieser hohen Übertragungsraten ist auch ohne präsynaptische Ableitungen möglich (Abb. 1B und C; Saviane und Silver, 2006; Hallermann *et al.*, 2010c). Für die hohen Übertragungsraten scheint ein großer Vorrat an synaptischen Vesikeln, eine kleine Anzahl an Freisetzungstellen und eine hohe Nachladerate verantwortlich zu sein (Kapitel 3.8; Sargent *et al.*, 2005; Saviane und Silver, 2006; Hallermann *et al.*, 2010c).

1.2 Die Cytomatrix an der Freisetzungsstelle

In elektronenmikroskopischen Studien wurden an Freisetzungsstellen elektronendichte Strukturen, sogenannte Cytomatrixstrukturen, beobachtet, die in ihrer Größe und Form abhängig von Spezies und Synapsentyp variieren und an die synaptischen Vesikel gebunden sind (Abb. 2A). An der neuromuskulären Synapse von *Drosophila melanogaster* konnten entscheidende molekulare Komponenten der Cytomatrix aufgeklärt werden. Es zeigte sich, dass das Protein Bruchpilot in *Drosophila* am Aufbau der Cytomatrixstruktur beteiligt ist (Fouquet *et al.*, 2009; Kittel *et al.*, 2006; Wagh *et al.*, 2006). Mit Antikörpern gegen den N-terminalen- und C-terminalen Teil des Bruchpilotmoleküls konnte die räumliche Anordnung von Bruchpilot innerhalb der Freisetzungsstelle bestimmt werden (Abb. 2B; Kapitel 3.3; Fouquet *et al.*, 2009). An einigen sensorischen Synapsen, die ihre Transmitterfreisetzung durch graduelle Potentialschwankungen steuern, wurden prominente Cytomatrixstrukturen detektiert, die teilweise eine bandartige Struktur haben. Diese sog. *ribbon*-Synapsen (Abb. 2C) sind in der Lage, hohe Raten der Vesikelfusion und der Vesikelnachladung über lange Zeit aufrecht zu erhalten (Khimich *et al.*, 2005). Es wurde deshalb vermutet, dass *ribbon*-Strukturen wie ein Fließband den Vesikelnachschub zur Freisetzungsstelle unterstützen (Lenzi und von Gersdorff, 2001). Allerdings können auch einige konventionelle Synapsen, die ihre Transmitterfreisetzung über Aktionspotentialfolgen steuern, hohe Raten der Vesikelnachladung aufrechterhalten, obwohl sie keine prominenten Cytomatrixstrukturen enthalten (Saviane und Silver, 2006; Xu-Friedman und Regehr, 2003). In hochauflösenden cryoelektronen-tomographischen Aufnahmen zeigten sich filamentöse Strukturen, die Vesikel an der präsynaptischen Membran zu binden scheinen (Abb. 2D; siehe auch Siksou *et al.*, 2007). Welche Moleküle an diesen Strukturen beteiligt sind, und welche Funktionen die Cytomatrix ausübt ist bisher größtenteils ungeklärt.

Um die molekularen Mechanismen besser zu verstehen, die an der synaptischen Übertragung beteiligt sind, können die genetischen Möglichkeiten der Fruchtfliege *Drosophila melanogaster* genutzt werden (Fouquet *et al.*, 2009;

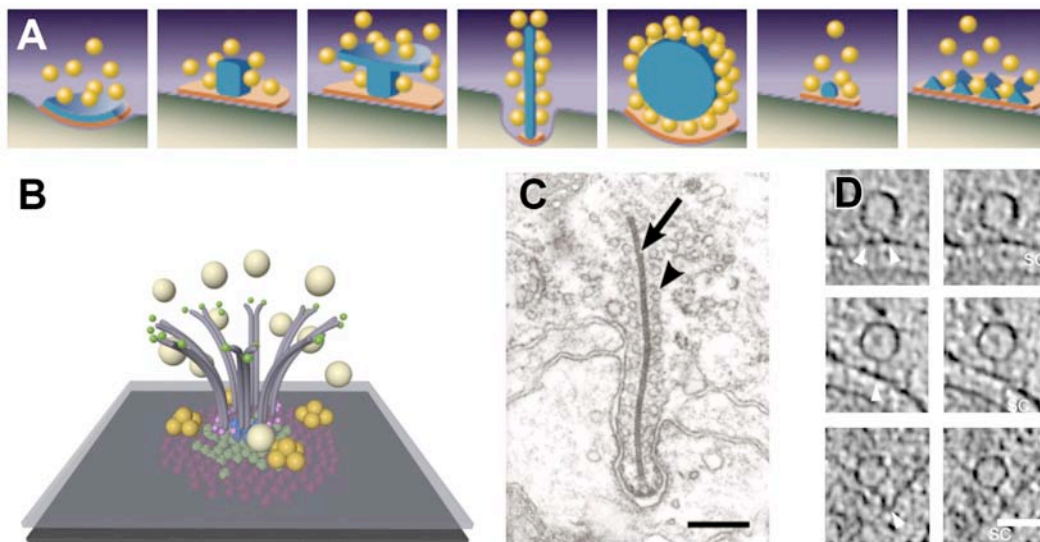


Abb. 2: Die Cytomatrix an der Freisetzungsstelle

A Schematische Darstellung und elektronenmikroskopische Aufnahmen von Freisetzungsstellen unterschiedlicher Synapsen verschiedener Spezies (modifiziert nach Zhai und Bellen, 2004). Von links nach rechts: Neuromuskuläre Synapse (NMJ) von *C. elegans*; NMJ des Flußkrebse; NMJ des *Drosophila melanogaster* - wegen der T-förmigen Struktur wird die Cytomatrix hier auch als *T-bar* bezeichnet; Elektroorgan des Rochens - wegen der Band-artigen Struktur, wird die Cytomatrix hier als *ribbon* bezeichnet; sacculäre Haarzelle des Frosches; NMJ der Eidechse; erregende Synapse im Hippocampus des Menschen.

B Detaillierte schematische Darstellung der Freisetzungsstelle an der NMJ der *Drosophila*. Das Bruchpilotmolekül ist am Aufbau des *T-bars* entscheidend beteiligt (siehe drittes Bild von links in A). C-Terminus und N-Terminus der Bruchpilotmoleküle sind in grün und magenta angedeutet. Neben den synaptischen Vesikeln (hell gelb) und den postsynaptischen Glutamatrezeptoren des Typs GluRIIA (grün) sowie GluRIIB (rot) sind noch Ca^{2+} -Kanäle (blau) und Liprin- α Moleküle (gelb) dargestellt (Abb. aus Fouquet *et al.*, 2009).

C Elektronenmikroskopische Aufnahme einer *ribbon*-Synapse des Elektroorgans des Rochens. Das elektronendichte *ribbon* (Pfeil) scheint synaptische Vesikel (Pfeil) zu binden (Abb. aus Lenzi und von Gersdorff, 2001).

D Hochauflösende Hochdruck-Cryo-Elektronen-Tomographische Aufnahmen von hippocampalen Synapsen machen filamentöse Strukturen (weiße Pfeilspitzen) sichtbar, die Vesikel mit der präsynaptischen Membran verbinden. Rechte Aufnahme: das links gezeigte Vesikel in einer 2.7 nm entfernten tomographischen Schnittebene (Abb. modifiziert nach Fernández-Busnadiego *et al.*, 2009).

Hallermann *et al.*, 2010a; Hallermann *et al.*, 2010b; Schmid *et al.*, 2008). Es zeigte sich, dass die Anreicherung von Bruchpilot an der Freisetzungsstelle und die Größe des postsynaptischen Glutamatrezeptorfeldes lokal äußerst spezifisch aufeinander abgestimmt sind (Kapitel 3.4; Schmid *et al.*, 2008). Die Analyse hochfrequenter synaptischer Übertragung in Bruchpilotmutanten deutete darauf hin, dass Bruchpilot zentral an der Vesikelnachladung beteiligt ist (Kapitel 3.6; Hallermann *et al.*, 2010a). Diese Funktion konnte im Folgenden bestätigt und die Funktionen auf intramolekularem Niveau einem bestimmten Teil des Bruchpilot-Moleküls (dem C-Terminus) zugeordnet werden (Kapitel 3.7; Hallermann *et al.*, 2010b). Hierbei konnten Bruchpilot-Allele genutzt werden, die in chemischen Mutagenese-Screens identifiziert wurden, und denen 50, 30 oder lediglich 1 % des C-terminalen Endes von Bruchpilot fehlten. In Allelen, in denen nur 1 % der C-terminalen Aminosäuren von Bruchpilot fehlten, erschien die Größe und Form der Cytomatrix normal. Die synaptischen Vesikel waren allerdings nicht an der Cytomatrix angereichert. In diesen Mutanten waren die basale synaptische Übertragung und die Verteilung der Ca^{2+} -Kanäle innerhalb der aktiven Zone normal, die hochfrequente synaptische Übertragung und die synaptische Erholung nach hochfrequenter Übertragung aber defizient. Hierdurch konnte die Bedeutung der an der Cytomatrixstruktur angereicherten synaptischen Vesikel für die hochfrequente synaptische Übertragung geklärt werden (Hallermann *et al.*, 2010b).

Um diese an Invertebraten gewonnen Befunde auf Synapsen des zentralen Nervensystems von Wirbeltieren zu übertragen, erschien die Untersuchung cerebellärer Mossfasersynapsen sinnvoll. Wegen der hohen Übertragungsraten an einzelnen Freisetzungsstellen (Saviane und Silver, 2006) sollten sich an diesen Synapsen molekulare Manipulationen gut funktionell untersuchen lassen (Kapitel 3.8; Hallermann *et al.*, 2010c). Obwohl das *Drosophila*-Protein Bruchpilot kein direktes Sequenzhomolog bei Vertebraten hat, erschien das Vertebraten-Protein Bassoon (tom Dieck *et al.*, 1998) ein interessanter Kandidat zu sein, der bei der hochfrequenten synaptischen Übertragung eine ähnliche Funktion ausführen könnte. Wie Bruchpilot ist Bassoon ein sehr großes Protein, das an der Freisetzungsstelle angereichert ist. Bassoon ist als evolutionärer „Neuling“ nur in Wirbeltieren vorhanden und dort ein wichtiger Baustein erregender und

hemmender Freisetzungstellen sowie von *ribbon*- und konventionellen Synapsen (Gundelfinger *et al.*, 2003; tom Dieck *et al.*, 1998). In Bassoon-Knockout-Mausmutanten fehlten in *ribbon*-Synapsen in der Retina und der inneren Haarzelle die elektronendichten Cytomatrixstrukturen, und die auditorische Informationsverarbeitung und die Vesikelnachladung waren gestört (Dick *et al.*, 2003; Frank *et al.*, 2010; Khimich *et al.*, 2005). Allerdings erschienen an konventionellen Synapsen die Nachladeraten in hippocampalen Zellkulturen von Bassoonmutanten normal (Altrock *et al.*, 2003). Auch in einer Doppelmutante von Bassoon und Piccolo, einem Homolog von Bassoon, erschien die Nachladerate in neuronalen Zellkulturen normal (Mukherjee *et al.*, 2010). Eine detaillierte Analyse an cerebellären Mossfasersynapsen mit hohen Stimulationsfrequenzen zeigte aber, dass hohe Übertragungsraten nur mit Hilfe des Proteins Bassoon erreicht werden können. Die basale synaptische Übertragung war normal in Bassoonmutanten, allerdings führte hochfrequente synaptische Übertragung zu stärkerer synaptischer Depression (Hallermann *et al.*, 2010c). Die weiteren mechanistischen Untersuchungen mit Fluktuationsanalyse, Analyse spontaner postsynaptischer Ströme und quantitativen Modellrechnungen der quantalen Parameter während und nach hochfrequenter Stimulation sprachen für eine unveränderte Anzahl an Freisetzungstellen und eine unveränderte Freisetzungswahrscheinlichkeit, aber für eine verlangsamte Rate der Vesikelnachladung in Bassoonmutanten (Hallermann *et al.*, 2010c).

2 Zielsetzung

Um fundamentale Aspekte der hochfrequenten synaptischen Übertragung zu untersuchen, wurden die drei folgenden glutamatergen Synapsen gewählt: die Moosfasersynapse im Hippocampus der Maus, die neuromuskuläre Synapse der Fruchtfliege *Drosophila melanogaster* und die Mossfasersynapse im Cerebellum der Maus.

Zur direkten Analyse der Transmitterfreisetzung wurden zuerst präsynaptische Kapazitätsmessungen an Moosfaserendigungen durchgeführt. Die Methode musste für diese morphologisch komplexen Synapsen etabliert werden, da bisher davon ausgegangen worden war, dass Kapazitätsmessungen nur an sphärischen Zellen mit einem einzelnen elektrischen Kompartiment quantitativ durchführbar seien. Anschließend wurden die Anzahl der fusionsbereiten Vesikel und deren Fusionsrate bestimmt (Kapitel 3.1). Im Hippocampus wurden außerdem Unterschiede zwischen erregender und hemmender Übertragung mit optischen Methoden untersucht (Kapitel 3.5)

Um die molekularen Mechanismen zu verstehen, die an der Fusion einer hohen Anzahl synaptischer Vesikel innerhalb weniger Millisekunden beteiligt sind, wurden die genetischen Möglichkeiten der *Drosophila* genutzt. Hierbei wurde zuerst die räumliche Anordnung eines zentralen Proteins innerhalb der Freisetzungsstelle (Bruchpilot) bestimmt (Kapitel 3.3). Des Weiteren wurde die genaue räumliche Abstimmung der Freisetzungsstelle mit den postsynaptischen Glutamatrezeptoren analysiert (Kapitel 3.4). Die Vesikelnachladung hochfrequenter synaptischer Übertragung wurde zuerst in Mutanten analysiert, denen Bruchpilot fehlt (Kapitel 3.6). Daraufhin konnten durch chemische Mutagenese-Screens Bruchpilot-Allele identifiziert werden, denen 50, 30 oder lediglich 1 Prozent des C-terminalen Endes von Bruchpilot fehlten. In diesen Mutanten wurde die Anreicherung der synaptischen Vesikel an der Freisetzungsstelle analysiert und die Funktion der angereicherten Vesikel für die hochfrequente synaptische Übertragung untersucht (Kapitel 3.7).

Um diese an Invertebraten gewonnen Befunde auf Synapsen des zentralen Nervensystems von Wirbeltieren zu übertragen, wurde die hochfrequente synaptische Übertragung an cerebellären Moosfasersynapsen untersucht. An diesen Synapsen wurden hohe Übertragungsraten an einzelnen Freisetzungstellen beschrieben, und es war daher zu erwarten, dass molekulare Manipulationen zur Beeinträchtigung der hochfrequenten Übertragung führen. Das Vertebraten-Protein Bassoon schien ein interessanter Kandidat zu sein, der eine ähnliche Funktion wie Bruchpilot bei der *Drosophila* auszuführen könnte. Wie Bruchpilot ist Bassoon ein sehr großes Protein, das an der Freisetzungstelle angereichert und für die Cytomatrixstruktur von großer Bedeutung ist. In Bassoonmutanten wurde daher die Mechanismen der hochfrequenten Übertragung an cerebellären Mossfasersynapsen analysiert (Kapitel 3.8).

3 Originalarbeiten

3.1 Hallermann *et al.*, 2003, Proc Natl Acad Sci U S A 100: 8975-8980

Seite 16-21

A large pool of releasable vesicles in a cortical glutamatergic synapse

Stefan Hallermann, Christian Pawlu, Peter Jonas*, and Manfred Heckmann

Physiologisches Institut, Universität Freiburg, D-79104 Freiburg, Germany

Communicated by Roger A. Nicoll, University of California, San Francisco, CA, May 12, 2003 (received for review March 25, 2003)

To probe exocytosis at a cortical glutamatergic synapse, we made capacitance measurements in whole-cell recorded hippocampal mossy fiber terminals. Evaluation of different methods by using a morphology-based equivalent electrical model revealed that quantitative capacitance measurements are possible in this presynaptic structure. Voltage pulses leading to presynaptic Ca^{2+} inflow evoked large capacitance signals that showed saturation with increasing pulse duration. The mean peak capacitance increase was 100 fF, corresponding to a pool of $\approx 1,400$ releasable vesicles. Thus hippocampal mossy fiber synapses have a vesicular "maxipool." Large pool size and rapid vesicle recycling may underlie the uniquely large extent of activity-dependent plasticity in this synapse.

Our current knowledge about fundamental aspects of synaptic transmission is largely based on the highly detailed analysis of a limited number of synapse types, such as the neuromuscular junction, the squid giant synapse, the retinal bipolar cell synapse, and the calyx of Held (1–10). These synapses offer direct access to presynaptic terminals, which has greatly facilitated the mechanistic analysis of transmitter release (e.g., ref. 5). However, glutamatergic synapses in higher brain circuits differ substantially from these "model synapses" in both morphological and functional aspects; for example, in the properties and extent of synaptic plasticity (11–13). Thus, to obtain a complete picture of cortical synaptic transmission and plasticity, direct examination of cortical synapses is unavoidable.

Electrical recording of postsynaptic currents is the standard assay to probe transmitter release. However, this approach has limitations, especially when applied to cortical synapses. The postsynaptic assay is difficult to calibrate, because neither the number of transmitter molecules in a synaptic vesicle nor the density of postsynaptic receptors are precisely known. The assay may be nonlinear, because of saturation or desensitization of postsynaptic receptors (14, 15). Furthermore, different modes of transmitter release (e.g., kiss-and-run versus full fusion; refs. 16 and 17) cannot be distinguished, and endocytosis cannot be measured directly. In synapses with "giant" presynaptic terminals, presynaptic capacitance measurements have been used to probe exo- and endocytosis quantitatively (9, 14, 18, 19). However, application of this technique to cortical presynaptic terminals is not trivial. The sensitivity of the technique needs to be optimized, because the expected capacitance changes are near the absolute limits of resolution. Furthermore, the interpretation of recorded signals must take into account the multicompartment electrical structure of the presynaptic terminals (20, 21).

To quantitatively measure exo- and endocytosis at a cortical glutamatergic synapse in real time, we performed presynaptic capacitance measurements in hippocampal mossy fiber terminals (22–26). After validation of capacitance measurement methods by using equivalent electrical models, we addressed the following fundamental questions: How large is the releasable pool of vesicles at mossy fiber terminals (27–30)? Is the release rate derived from capacitance measurements more consistent with univesicular or multivesicular release (31, 32)? How fast is endocytosis after depletion of the releasable vesicle pool (33)?

Methods

Recording from Mossy Fiber Terminals in Acute Hippocampal Slices.

Transverse 250- to 300- μm -thick slices were cut from the hippocampi of 20- to 26-day-old Wistar rats with a custom-built vibratome (34). The animals were killed by decapitation in accordance with national and institutional guidelines. For the dissection and storage of the slices a solution containing 64 mM NaCl, 25 mM NaHCO_3 , 10 mM glucose, 120 mM sucrose, 2.5 mM KCl, 1.25 mM NaH_2PO_4 , 0.5 mM CaCl_2 , and 7 mM MgCl_2 (95% O_2 /5% CO_2) was used. The slices were incubated for 30 min at 35°C and then held at room temperature for <3 h. During experiments, the slices were superfused with a physiological extracellular solution containing 125 mM NaCl, 25 mM NaHCO_3 , 25 mM glucose, 2.5 mM KCl, 1.25 mM NaH_2PO_4 , 2 mM CaCl_2 , and 1 mM MgCl_2 (95% O_2 /5% CO_2). Recordings were made from mossy fiber terminals in the *stratum lucidum* of the hippocampal cornu ammonis area 3 (CA3) region as described (22, 23). Patch pipettes were pulled from borosilicate glass tubing (2-mm outer diameter, 0.5-mm wall thickness) and filled with an intracellular solution containing 155 mM CsCl, 6.25 mM MgCl_2 , 0.26 mM EGTA, 0.04 mM CaCl_2 , 4 mM Na_2ATP , 0.3 mM NaGTP , and 10 mM HEPES; the pH was adjusted to 7.3 with CsOH. This composition theoretically gives ≈ 50 nM free Ca^{2+} , ≈ 0.2 mM free EGTA, and ≈ 2 mM free Mg^{2+} (35). The pipette open-tip resistance was 5–12 M Ω . All recordings were made in a bath solution containing 105 mM NaCl, 25 mM NaHCO_3 , 25 mM glucose, 2.5 mM KCl, 1.25 mM NaH_2PO_4 , 2 mM CaCl_2 , 1 mM MgCl_2 , 1 μM tetrodotoxin (TTX), 20 mM tetraethylammonium chloride (TEA), and 5 mM 4-aminopyridine (4AP); to avoid depolarization of the recorded terminals, this solution was applied directly after whole-cell voltage clamp was established. To minimize pipette capacitance, care was taken to maintain the bath solution at the lowest possible level. Recordings were made with an EPC-9/2 amplifier (HEKA Electronics, Lambrecht/Pfalz, Germany) in the voltage-clamp mode. The pipette capacitance was compensated in the cell-attached configuration ("C-fast"; time constants 1–3 μs). All measurements were made at $21 \pm 2^\circ\text{C}$, unless otherwise specified (34°C in Fig. 3F). Data are reported as mean \pm SEM, unless otherwise noted. Significance was assessed by using a two-sided Mann–Whitney test.

Development of Morphology-Based and Reduced Equivalent Models of Mossy Fiber Terminals.

Current transients were evoked by square pulses with alternating amplitudes of ± 20 mV from a holding potential of -100 mV. The internal two-pole Bessel filter for stimulus voltage was set to 2 μs , the three-pole Bessel filter for current was set to 100 kHz, and the sampling frequency was set to 200 kHz. Responses to positive and negative pulses

Abbreviations: ΔC_m , capacitance change; C_m , membrane capacitance; R_a , access resistance; R_m , membrane resistance.

See commentary on page 8618.

*To whom correspondence should be addressed at: Physiologisches Institut, Universität Freiburg, Hermann-Herder-Strasse 7, D-79104 Freiburg, Germany. E-mail: peter.jonas@physiologie.uni-freiburg.de.

were averaged separately and plotted against each other for corresponding time points; experiments with signs of nonlinearity (slope <0.99 or >1.01) were discarded (5 of 17 boutons). For subsequent analysis, average responses to positive pulses (for $0.02 \text{ ms} < t \leq 5 \text{ ms}$) were used. To obtain a morphology-based model, boutons were filled with 0.1% biocytin during recording (36). Slices were fixed with 2.5% paraformaldehyde, 1.25% glutaraldehyde, and 15% picric acid and were developed with avidin-biotinylated horseradish peroxidase complex (ABC, Vector Laboratories), using 0.05% 3,3'-diaminobenzidine as chromogen. One biocytin-filled bouton was selected for reconstruction with a light microscope ($\times 100$ oil immersion objective; NEUROLUCIDA 3 system, MicroBrightField, Colchester, VT). No correction was made for shrinkage. The diameter of the axon was $0.14\text{--}0.40 \mu\text{m}$, consistent with electron-microscopic data (34). After conversion into NEURON format, access resistance, shunt conductance, and specific parameters C_m , R_i , and R_m were determined by direct fitting of the current transients (37) with Fitpraxis of NEURON 5.1 (ref. 38; $1\text{-}\mu\text{s}$ time step). Current transients were also fitted by simple equivalent electrical models. A one-compartment model, a two-compartment model, a model with one compartment and an attached cylinder, and a three-compartment model were tested. For the two- and three-compartment models, the circuit was assembled in the Laplace domain, and the current as a function of time was obtained by inverse Laplace transformation. For the compartment-cylinder model, the current transient was calculated as reported (39). Direct fitting was performed with MATHEMATICA 4.1 (Wolfram Research, Champaign, IL), minimizing the sum of squares of differences between measured and simulated traces. To achieve uniqueness, the number of free parameters was reduced by homogeneity assumptions ($R_m C_m = \text{const.}$, which gives five free parameters for both the two-compartment model and the compartment-cylinder model and seven free parameters for the three-compartment model).

Evaluation of Different Methods for Capacitance Measurements by Using the Morphology-Based Model. The performance of square-pulse and sine-wave methods was evaluated by using the morphology-based model. Current transients or sine-wave responses were simulated in NEURON ($1\text{-}\mu\text{s}$ time step), applying square or sinusoidal voltage commands at the bouton. "Sample" frequencies were 200 and 50 kHz, respectively, for square and sinusoidal commands. Gaussian noise with realistic amplitude was generated by using the random number generator of MATHEMATICA. Noise was filtered at 100 kHz for the square-pulse responses and 10 kHz for the sine-wave responses (Gaussian filter), and points corresponding to the sample points of simulated traces were added. Square-pulse techniques (40) were tested as described above (for $0.02 \text{ ms} < t \leq 5 \text{ ms}$). Sine-wave techniques were tested as follows. Amplitude and phase of the resulting current were determined under steady-state conditions by fitting with a sinusoidal function or the sum of two sinusoidal functions. Amplitude and phase were converted into real and imaginary parts of the complex admittance. For the single sine-wave technique, real part, imaginary part, and dc were converted into C_m , R_a , and R_m by using equation 28 of Gillis (26). For the double sine-wave technique, real parts and imaginary parts for the two frequencies were converted into C_m , R_a , and R_m according to Rohlicek and Schmid (ref. 41; and see ref. 42). Changes were implemented as an increase in specific membrane capacitance or a decrease in specific resistance at a given position. To estimate the noise in C_m measurements due to thermal (Johnson) fluctuations in resistors, the power spectral density of the current noise was calculated as $S_I(f) = 4k_B T \text{Re}[Y]$, where k_B is the Boltzmann constant, T is the absolute temperature, and $\text{Re}[Y]$ is the real part of the admittance of the morphology-based model. The current variance at a given bandwidth was determined by

using equations 48 and 49 of Gillis (26) and converted into the C_m noise by using a linear approximation [equation 50 of Gillis (26)].

Capacitance Measurements in Mossy Fiber Terminals. Capacitance measurements in whole-cell recorded hippocampal mossy fiber terminals were performed by using the "sine + dc" mode (25) of the software lock-in extension of PULSE in the EPC-9/2 amplifier. The sine-wave frequency was set to 5 kHz and the peak amplitude was set to $\pm 50 \text{ mV}$; the holding potential was -100 mV . The internal two-pole Bessel filter for stimulus voltage was set to $20 \mu\text{s}$, the three-pole Bessel filter for current was set to 10 kHz, and the sampling frequency was set to 50 kHz. The reversal potential of the dc was assumed to be 0 mV. To evoke release, 0.2- to 100-ms pulses to 0 mV were applied every 5–15 s. Measurements of capacitance changes were performed in a time interval $<10 \text{ min}$ after the whole-cell configuration was established. Because the membrane time constant τ_m of the bouton was $\approx 10 \text{ ms}$, a time interval of $3 \tau_m$ (30 ms) after the pulse was considered invalid and blanked from the C_m recordings. ΔC_m was measured as the difference of C_m 50 ms before and 200–300 ms after the step, except in the experiments in which sine-wave and square-pulse techniques were compared (difference of C_m 2 s before and 2 s after the step). With these settings, the contribution of Na^+ channel gating charge movements is likely to be small (43, 44). First, the high sine-wave frequency will minimize gating charge effects (44). Second, the observed ΔC_m is unlikely to be generated directly by gating charge movements, which are much faster. It is also unlikely to arise from charge immobilization due to inactivation, because recovery of Na^+ channels from inactivation is complete within $\approx 20 \text{ ms}$ in mossy fiber terminals (P.J., unpublished work). Finally, if significant charge immobilization occurred, we would expect a decrease of C_m , rather than an increase, after the pulse. To examine exocytosis, data were recorded at a resolution of one sine-wave cycle per data point. ΔC_m versus pulse duration relations were fitted with the sum of two exponentials. Only experiments with a signal-to-noise ratio (defined as ΔC_m at 10 ms divided by standard deviation of data points around the fitted curve) >2 were used. Amplitude-weighted decay time constants, τ_w , were calculated as $(A_1 \tau_1 + A_2 \tau_2)/(A_1 + A_2)$, where A_1 and A_2 are amplitudes and τ_1 and τ_2 are time constants of the components. In 1 of 26 recordings, the stimulus evoked a *negative* ΔC_m significantly larger than the recording noise; this experiment was excluded from the analysis. To examine endocytosis, data were averaged (25 sine-wave cycles per data point) and reduced (0.1 Hz) before storage. To determine the endocytosis time constant, traces were corrected for drifts by linear regression to the baseline, and the decay was fitted with a single exponential plus an offset. In a subset of experiments (Fig. 3F), $4 \mu\text{M}$ tetanus toxin, 0.3 mM DTT, and 0.1% BSA were added to the pipette solution. These experiments were performed at 34°C to promote the action of the toxin (45, 46).

Results

Standard capacitance measurement techniques were originally developed for single compartments (24–26), and it is unclear whether they can be extended to complex structures such as mossy fiber terminals (47–49). To determine the number of compartments necessary to represent the electrical structure of the mossy fiber terminals, we compared different models, starting from a model based on realistic morphological properties. A whole-cell-recorded biocytin-filled bouton was selected for reconstruction (Fig. 1A), and the previously recorded current transients were analyzed by direct fitting (Fig. 1B; ref. 37). This analysis gave a realistic electrical model of the bouton, with a membrane time constant, τ_m , of 9.4 ms. Next, several reduced models were tested. In the reconstructed bouton, a three-

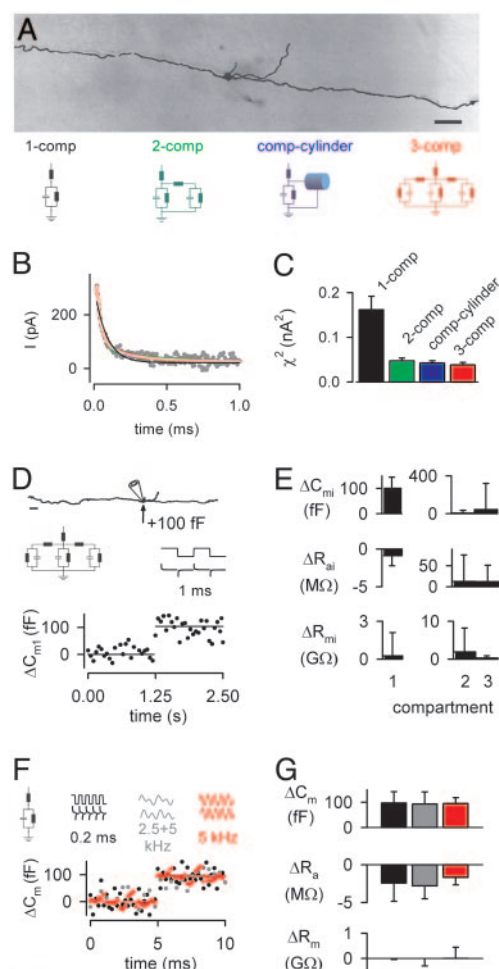


Fig. 1. Performance of capacitance measurement methods in a morphology-based electrical model of hippocampal mossy fiber terminals. (A) Photomicrograph of a bouton in *stratum lucidum* filled with biocytin during recording. The reconstructed morphology is shown superimposed (scale bar, 10 μm). (B) Average current transient (50 individual sweeps) in the same bouton in response to 5-ms pulses from -100 mV to -80 mV, superimposed with the predictions of the morphology-based model (white curve) and the simple compartmental models (see model schematics for color code) obtained by direct fitting (for 0.02 ms $< t \leq 5$ ms). Direct fitting yielded an access resistance of 30.7 M Ω , a shunt resistance of 11.6 G Ω , an apparent specific membrane capacitance of 2.3 $\mu\text{F}\cdot\text{cm}^{-2}$, a cytoplasmic resistivity of 124 $\Omega\cdot\text{cm}$, and a specific membrane resistance of $4,100$ $\Omega\cdot\text{cm}^2$. Although the high apparent specific membrane capacitance suggests an underestimation of the surface area in the light-microscopic reconstruction, the model is expected to realistically capture the electrical properties. (C) Sum of squares of differences (χ^2) between recorded and calculated current transients for simple compartmental models ($n = 12$). When the same recorded transients were fitted with the sum of three exponentials, mean time constants of $\tau_1 = 21 \pm 1$ μs , $\tau_2 = 113 \pm 8$ μs , and $\tau_3 = 985 \pm 70$ μs were obtained. (D) Illustration of the three-compartment square-pulse technique [SQ₃; pulse duration 1 ms; current noise $\sigma = 50$ pA/ $\sqrt{50}$ (to simulate averaging of 50 traces)]. (E) Accuracy of ΔC_m , ΔR_{ai} , and ΔR_{mi} ($i = 1 \dots 3$) estimates for SQ₃. (F) Illustration of the one-compartment square-pulse technique (SQ₁; black; pulse duration 0.2 ms), the double sine-wave technique (SW₂; gray; frequencies 2.5 and 5 kHz), and the single sine-wave technique (SW₁; red; frequency 5 kHz). (G) Accuracy of ΔC_m , ΔR_a , and ΔR_m estimates for SQ₁, SW₂, and SW₁. In all cases, a capacitance increase of 100 fF was simulated at the bouton in the morphology-based model. The peak-to-peak amplitude of the command voltage was ± 50 mV. Noise was $\sigma = 50$ pA and was filtered at 100 kHz for SQ₃ and SQ₁, and at 10 kHz for SW₂ and SW₁. In E and G, error bars represent standard deviations.

compartment model provided a markedly better fit than the one-compartment, two-compartment, or compartment-cylinder models; the three-compartment model was only slightly inferior

to the morphology-based model (Fig. 1B). Among the reduced models, the three-compartment model gave the best fit of the current transients in 12 of 12 boutons (Fig. 1C). On average, the capacitance of the first compartment, presumably corresponding to the presynaptic terminal, was $C_{m1} = 1.44 \pm 0.20$ pF, whereas the capacitances of the higher compartments were 0.92 ± 0.14 and 3.33 ± 0.57 pF. For the three-compartment model, the mean access resistances, R_{ai} ($i = 1 \dots 3$), were 20.8 ± 1.6 , 128 ± 18 , and 442 ± 55 M Ω , and the mean membrane resistances, R_{mi} , were 4.8 ± 0.7 , 8.5 ± 1.6 , and 2.7 ± 0.7 G Ω ($n = 12$). Thus C_{m1} is ≈ 10 times smaller than at the calyx of Held (32, 50).

The capacitance changes caused by exocytosis in mossy fiber terminals are expected to be near the absolute limits of resolution of established methods. Therefore, we systematically evaluated the performance of different techniques in the presence of recording noise, with a plausible presynaptic capacitance increase implemented at the bouton in the morphology-based model ($\Delta C_m = 100$ fF). We first considered using a three-compartment square-pulse technique (SQ₃) for real-time measurements of presynaptic capacitance changes. However, although the SQ₃ technique provided accurate estimates of the parameters of the first compartment, the temporal resolution was clearly insufficient, because averaging of several traces was necessary to obtain robust results (Fig. 1D and E). We therefore explored alternative approaches, such as a one-compartment square-pulse technique (SQ₁; ref. 40), a double sine-wave technique (SW₂, “Rohlicek”; ref. 41), and a single sine-wave technique (SW₁, “sine + dc”; ref. 25). Identical command voltage amplitudes were chosen to allow a rigorous comparison. For a given temporal resolution, the accuracy of ΔC_m measurements (measured ΔC_m /implemented ΔC_m) was similar for the three techniques, but the best amplitude resolution was obtained with the single sine-wave approach (Fig. 1F and G).

To be able to use the sine-wave method as a quantitative assay of exocytosis in mossy fiber terminals, we performed additional tests of accuracy and specificity (Fig. 2). The accuracy of the method in the morphology-based model was frequency dependent, rising with increasing sine-wave frequency (Fig. 2A). However, the predicted thermal noise of C_m measurements increased at higher frequencies, limiting the maximal sine-wave frequency that can be used experimentally to roughly 5 kHz (Fig. 2B). To examine the possibility of cross-talk of any parameters other than presynaptic capacitance onto the ΔC_m signal, we simulated plausible capacitance increases ($\Delta C_m = 100$ fF) and large conductance increases ($\Delta G_m = 0.5$ nS, corresponding to a maximal increase of $\approx 100\%$) at presynaptic and various axonal locations in the morphology-based model with 5 kHz sine-wave frequency (Fig. 2C and D). Capacitance increases in the presynaptic compartment were monitored accurately, although they were associated with ΔR_a signals in the opposite direction. The relation between measured ΔC_m and implemented ΔC_{m1} was linear, and the accuracy of the measurement was 91% (Fig. 2C Left). Changes in the access resistance ΔR_{ai} were monitored precisely, without effect on the other parameters (Fig. 2C Center). Conductance increases were also determined accurately, although they were associated with a small positive ΔC_m signal (Fig. 2C Right). For capacitance increases in more distant compartments, the ΔC_m signal decayed steeply as a function of distance from the presynaptic site (Fig. 2D Left; ≈ 3 μm per e-fold change), whereas for conductance increases in more distant compartments the ΔR_m signal declined gradually (Fig. 2D Right; 56 μm per e-fold change). Interestingly, the sign of ΔR_a after simulated exocytosis reversed at a distance of ≈ 2 μm (Fig. 2D Left). In conclusion, the high-frequency sine-wave technique showed a high spatial resolution and specificity, consistent with earlier conclusions (21). Cross-talk to the C_m trace was minimal, except for large conductance changes in the presynaptic terminal; however, such conductance changes would be readily de-

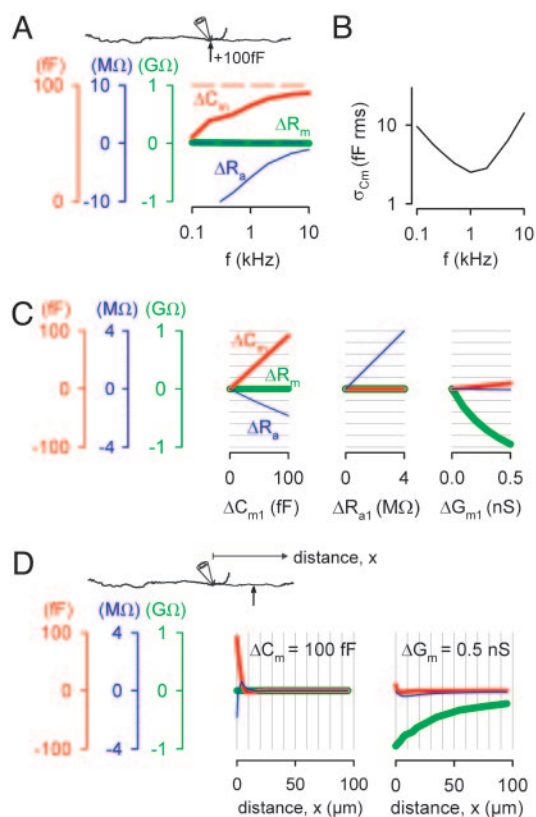


Fig. 2. High-frequency sine-wave techniques provide an accurate and specific assay of exocytosis from mossy fiber terminals. (A) Accuracy of ΔC_m (red), ΔR_a (blue), and ΔR_m (green) estimates, plotted against sine-wave frequency f , for a ΔC_m of 100 fF at the bouton in the morphology-based model. Model parameters were identical to those specified in the legend of Fig. 1B. (B) Predicted thermal noise of C_m estimates at a bandwidth of 5 kHz, plotted against sine-wave frequency. Noise was calculated from the complex admittance of the morphology-based model. (C) ΔC_m , ΔR_a , and ΔR_m , measured by a 5-kHz sine-wave technique after changes in membrane capacitance ΔC_{m1} (Left), access resistance ΔR_{a1} (Center), or membrane conductance ΔG_{m1} (Right) in the first compartment (bouton) of the morphology-based model. (D) ΔC_m , ΔR_a , and ΔR_m , measured by the sine-wave technique after changes in membrane capacitance ($\Delta C_m = 100$ fF; Left) and membrane conductance ($\Delta G_m = 0.5$ nS; Right) in different axonal compartments, plotted against the location of the change (x , measured from the point of emergence of the axon from the bouton). Similar calculations were performed to address three additional potential errors: (i) Errors in reversal potential setting ($E_{rev} = -50$ mV instead of 0 mV); results were almost identical. (ii) Phase errors (1°); results were very similar, except for a larger ΔR_a in C Center. (iii) Incomplete pipette compensation (first four cylinders of pipette model taken from ref. 59, 150 fF total pipette capacitance); results were similar except in C Left (smaller ΔR_a) and C Center (larger $-\Delta C_m$).

tected in the R_m trace. As the sign of ΔR_a reverses with distance, the ΔR_a signal provides information about the locus of the capacitance increase, with negative values indicating changes directly in the presynaptic terminal.

To probe fundamental properties of exocytosis, we applied the high-frequency sine-wave technique to whole-cell recorded mossy fiber terminals (Fig. 3). To induce transmitter release, Ca^{2+} inflow was evoked by 30-ms voltage pulses in the presence of blockers of voltage-gated Na^+ and K^+ channels; a stimulus amplitude of 0 mV was chosen to maximize the presynaptic Ca^{2+} current (23). In the presynaptic recording illustrated, the 30-ms stimulus evoked an increase of C_m by 23 fF, a decrease of R_a by 0.12 $M\Omega$, and a decrease of R_m by 0.037 $G\Omega$ (Fig. 3A). On average, a 30-ms pulse led to a mean ΔC_m of 101 ± 48 fF (Fig. 3B; $n = 12$). The size of ΔC_m was only weakly correlated with the

peak amplitude of the presynaptic Ca^{2+} current (Fig. 3C and D; $r = 0.24$, $P > 0.05$), indicating that the amplitude of ΔC_m was not limited by presynaptic Ca^{2+} inflow.

The results raise additional questions: Are the observed capacitance increases generated at the presynaptic terminal, and if so, are they unequivocally related to exocytosis? A highly significant correlation between ΔC_m and $-\Delta R_a$ was found ($r = 0.91$, $P < 0.001$), as quantitatively predicted from the bouton models (Fig. 3E, curves). This is consistent with the hypothesis that the capacitance increases were generated in the mossy fiber terminal rather than the axon or the filopodial extensions (47–49). Furthermore, 4 μM tetanus neurotoxin applied to the intracellular solution blocked the capacitance signals; ΔC_m in the presence of tetanus toxin was 18% of ΔC_m in interleaved controls under identical recording conditions (Fig. 3F; $P < 0.05$). Because tetanus toxin selectively cleaves synaptobrevin (45, 46), these experiments show that the capacitance signals were caused by exocytosis. In conclusion, our results indicate that voltage pulses evoke large exocytosis-related capacitance increases in hippocampal mossy fiber terminals, comparable in size to those recently reported in the calyx of Held (14, 19). With a single-vesicle ΔC_m of ≈ 70 aF, obtained from a mean clear vesicle diameter of 47 nm in mossy fiber terminals (figure 7D of ref. 52; see refs. 19 and 53) and a specific membrane capacitance of $1 \mu F cm^{-2}$, the ΔC_m evoked by 30-ms pulses corresponds to the fusion of $\approx 1,400$ vesicles. A potential caveat is that mossy fiber terminals contain a small proportion of large dense-core vesicles, which will lead to an overestimation of pool size.

Capacitance measurements allowed us to quantify rates in the synaptic vesicle cycle at hippocampal mossy fiber synapses (Fig. 3G–I). To determine the size of the releasable pool and the maximal rate of exocytosis, the length of the depolarizing pulse was varied between 0.2 and 100 ms, and ΔC_m was plotted against pulse duration (Fig. 3G). ΔC_m rose steeply for short pulses but approached saturation with longer pulses. In the experiment shown, the time course was biexponential, with time constants of 1.6 and 22 ms, suggesting that readily releasable and slowly releasable pools coexist at mossy fiber synapses (51). In the experiment illustrated, the amplitude-weighted time constant (τ_w) was 15 ms; on average, τ_w was 21 ± 3 ms ($n = 3$). The maximal release rate, determined as pool size (for 30-ms pulse) divided by τ_w , was ≈ 70 vesicles per millisecond. Thirty-millisecond pulses evoked near-maximal ΔC_m signals (Fig. 3G), indicating that the ΔC_m obtained with this pulse duration is an adequate measure of the size of the releasable pool of synaptic vesicles. After a stimulus that produced pool depletion, the capacitance signal decayed back to baseline within several seconds, presumably reflecting membrane retrieval by endocytosis (Fig. 3H and I). On average, the endocytosis time constant was 9.0 ± 5.5 s ($n = 3$) and the extent of endocytosis measured 10 s after the peak was $105 \pm 53\%$ ($n = 4$). With our estimate of a releasable pool size of $\approx 1,400$ vesicles, the time constant corresponds to a maximal rate of endocytosis of ≈ 160 vesicles per s.

Discussion

In the present paper, three major findings are reported. First, we define the conditions under which techniques for capacitance measurements can be applied to small presynaptic terminals comprised of multiple electrical compartments. Second, we report a direct presynaptic measurement of the size of the releasable vesicle pool at a cortical glutamatergic synapse. We estimate that the releasable vesicle pool in mossy fiber terminals is comprised of $\approx 1,400$ vesicles. Thus, the pool is substantially larger than previously reported for glutamatergic synapses in primary culture (27, 28). This apparent disagreement is probably due to differences between both synapse types and assays (pre-versus postsynaptic). Third, we made real-time measurements of endocytosis in mossy fiber terminals. Whereas exocytosis occurs

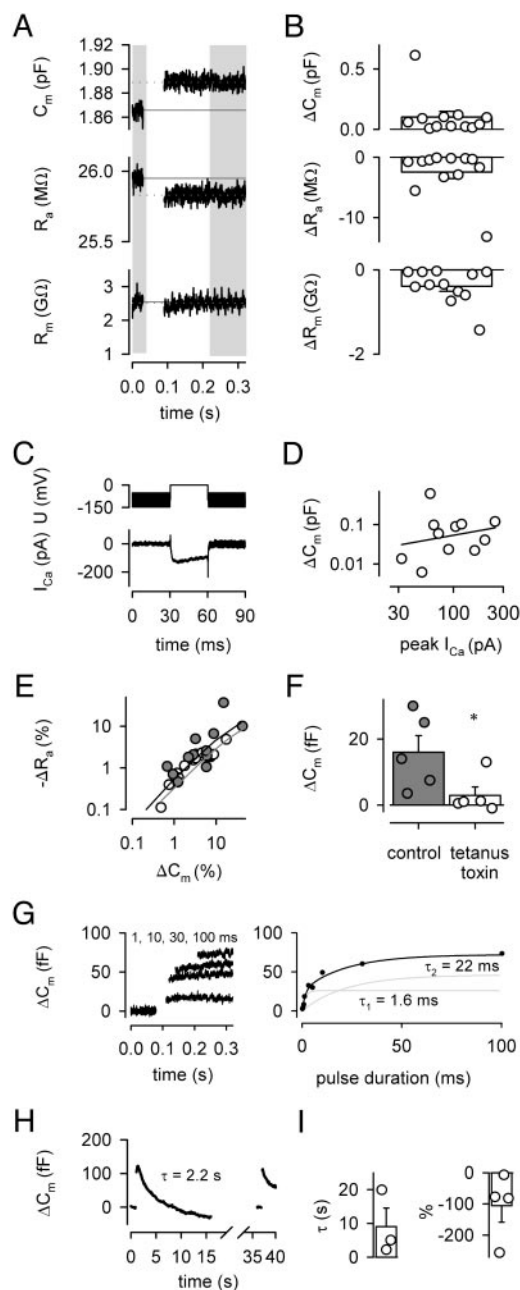


Fig. 3. Large pool size and rapid vesicle cycling in hippocampal mossy fiber terminals. (A) Changes in C_m , R_a , and R_m evoked by a 30-ms pulse. Vertical gray bars indicate regions for analysis. (B) Summary plots of ΔC_m , ΔR_a , and ΔR_m evoked by 30-ms pulses. Bars represent means \pm SEM; symbols indicate individual experiments ($n = 12$). In three experiments, sine-wave method SW₁ and square-pulse technique SQ₃ (100-mV amplitude) were applied in an interleaved manner at 2 Hz. In these experiments, SW₁ gave $\Delta C_m = 22$ fF, $\Delta R_a = -0.6$ M Ω , and $\Delta R_m = -0.6$ G Ω , in approximate agreement with the results of SQ₃ ($\Delta C_m = 41$ fF, $\Delta R_a = -0.3$ M Ω , and $\Delta R_m = -0.08$ G Ω); corresponding C_m and C_m noise values were 2.3 fF versus 18.4 fF. (C) Voltage-command and corresponding Ca^{2+} current (corrected for leak and capacitive current) in the same bouton shown in A. Note the sine-wave stimulation before and after the stimulus (5 kHz, ± 50 mV). (D) Double-logarithmic scatter plot of ΔC_m versus peak Ca^{2+} current. The line represents linear regression. (E) Double-logarithmic scatter plot of $-\Delta R_a$ versus ΔC_m . Filled circles represent data obtained with the 30-ms pulses shown in B; open circles illustrate experiments with different pulse durations (0.2–100 ms; $n = 33$ total; seven data points outside plotting range). Lines represent predictions of the morphology-based (black) and three-compartment models (gray). (F) ΔC_m signals evoked by 5-ms pulses in control conditions and in the presence of 4 μM tetanus toxin (recording temperature 34°C; *, $P < 0.05$). The peak Ca^{2+} current was not different

within milliseconds, endocytosis proceeds on a time scale of seconds.

Whereas sine-wave techniques for capacitance measurements were originally developed for single-compartment structures (25, 26), mossy fiber terminals are electrically complex. Presumably, the three compartments in our reduced representation (Fig. 1B) represent the presynaptic terminal, the axon, and the filopodial extensions (47–49). Extensive tests based on the morphology-based model show that high-frequency sine-wave techniques probe ΔC_m accurately. However, the structural complexity introduces a correlation between ΔC_m and $-\Delta R_a$. Intuitively, this apparent ΔR_a can be understood as follows. If a complex structure with distributed capacitances and resistors is approximated with a single-compartment formalism, the measured R_a is expected to be the weighted mean of R_{a1} , $R_{a1} + R_{a2}$, \dots , $R_{a1} + \dots + R_{an}$, with weights related to the capacitances C_{mi} of the i th compartment ($i = 1 \dots n$). If an increase in C_m occurs in the first compartment, the weight of R_{a1} increases and the measured R_a shifts toward R_{a1} . In contrast, if an increase of C_m occurs in higher compartments, R_a shifts in the opposite direction. Thus, the sign of ΔR_a provides information about the location of the change. For the mossy fiber terminals, the negative ΔR_a implies that the ΔC_m signal is generated at the presynaptic terminal rather than filopodial extensions or axon.

Using presynaptic capacitance measurements, we derived a quantitative picture of exo- and endocytosis at mossy fiber terminals. The releasable pool is comprised of $\approx 1,400$ vesicles. With 37 active zones per large mossy fiber terminal based on serial electron microscopy (47), this translates into ≈ 40 vesicles per active zone. Because these ≈ 40 vesicles are released within a 30-ms time interval (Fig. 3G), the present results argue strongly in favor of multivesicular release (31, 32) but against lateral inhibition (54) or fast adaptation of the Ca^{2+} sensor (55) at this synapse under our conditions. For 37 active zones (47), the maximal rate of endocytosis after complete pool depletion can be estimated as (≈ 160 vesicles per s)/37 = ≈ 4 vesicles per s per active zone. These quantitative results in mossy fiber terminals contrast with previous data at the calyx of Held. Although the size of the releasable pool is comparable at the two types of synapses ($\approx 1,400$ and ≈ 700 to $\approx 8,000$ vesicles, respectively; refs. 14, 19, 29, 30, and 32), the number of releasable vesicles per active zone is substantially larger (≈ 40 versus $\approx 4,000/554 = \approx 7$; ref. 53) and the rate of endocytosis per active zone after pool depletion is faster at the mossy fiber terminals than at the calyx (≈ 4 versus ≈ 0.5 vesicles per s; refs. 14 and 19).

Previous studies showed that the brief presynaptic action potential in mossy fiber terminals (22) is a highly efficient stimulus for activating presynaptic Ca^{2+} channels (23). The present results, however, suggest that the Ca^{2+} inflow associated with a single presynaptic action potential (half-duration 580 μs ; ref. 23) releases only a very small fraction of the vesicle pool (Fig. 3G). In contrast, high-frequency trains of presynaptic action potentials, perhaps in

in the two sets of measurements ($P > 0.5$). (G Left) ΔC_m signals evoked by 1-, 10-, 30-, and 100-ms test pulses, preceded by a 1.2-ms prepulse to 65 mV to maximally activate Ca^{2+} channels without Ca^{2+} inflow. A rapid component of endocytosis was not apparent under these conditions (19). (G Right) ΔC_m plotted against test-pulse duration. Note that ΔC_m saturates at a pulse duration of ≈ 30 ms. The continuous curve represents a biexponential function fitted to the data points ($\tau_1 = 1.6$ ms, $\tau_2 = 22$ ms); exponential components are shown superimposed. Data points represent single measurements, except for pulse durations < 1 ms (means of five measurements). (H) ΔC_m signals evoked by two 30-ms pulses shown on a slow time scale. The membrane capacitance decays back to baseline with a time constant of 2.2 s. (I) Summary plot of endocytosis time constants (Left; $n = 3$) and percentage of recovery after 10 s (Right; $n = 4$). Note the variable endocytosis time course and extent, as well as the excess endocytosis in one recording.

combination with action potential broadening (22), will be needed to release a larger fraction. At the mossy fiber–cornu ammonis area 3 (CA3) pyramidal neuron synapse, high-frequency stimulation leads to an almost 10-fold increase in synaptic strength, because of frequency facilitation, posttetanic potentiation, and long-term potentiation (56, 57). Because all of these activity-dependent changes are probably expressed presynaptically, the large number of vesicles per active zone at the mossy fiber synapse provides a straightforward explanation for their unique extent. The large pool may also

help to understand the impact of mossy fiber synaptic transmission during presynaptic spike trains *in vivo* (58).

We thank Drs. E. Neher and R. Schneggenburger for advice during the implementation of capacitance measurements, H. Bigalke for providing tetanus toxin, and J. Bischofberger, E. Neher, and G. Stuart for critically reading an earlier version of the manuscript. This work was supported by the Deutsche Forschungsgemeinschaft (SFB 505/C12) and the Alexander-von-Humboldt Foundation.

1. Katz, B. (1969) *The Release of Neural Transmitter Substances* (Liverpool Univ. Press, Liverpool, U.K.).
2. Betz, W. J. & Bewick, G. S. (1992) *Science* **255**, 200–203.
3. Beaumont, V. & Zucker, R. S. (2000) *Nat. Neurosci.* **3**, 133–141.
4. Linás, R. (1999) *The Squid Giant Synapse* (Oxford Univ. Press, New York).
5. Adler, E. M., Augustine, G. J., Duffy, S. N. & Charlton, M. P. (1991) *J. Neurosci.* **11**, 1496–1507.
6. Forsythe, I. D. (1994) *J. Physiol. (London)* **479**, 381–387.
7. Borst, J. G. G., Helmchen, F. & Sakmann, B. (1995) *J. Physiol. (London)* **489**, 825–840.
8. Wang, L.-Y. & Kaczmarek, L. K. (1998) *Nature* **394**, 384–388.
9. von Gersdorff, H. & Matthews, G. (1994) *Nature* **367**, 735–739.
10. von Gersdorff, H., Sakaba, T., Berglund, K. & Tachibana, M. (1998) *Neuron* **21**, 1177–1188.
11. Bliss, T. V. P. & Collingridge, G. L. (1993) *Nature* **361**, 31–39.
12. Zalutsky, R. A. & Nicoll, R. A. (1990) *Science* **248**, 1619–1624.
13. Yeckel, M. F., Kapur, A. & Johnston, D. (1999) *Nat. Neurosci.* **2**, 625–633.
14. Sun, J.-Y. & Wu, L.-G. (2001) *Neuron* **30**, 171–182.
15. Neher, E. & Sakaba, T. (2001) *J. Neurosci.* **21**, 444–461.
16. Ryan, T. A. (2003) *Proc. Natl. Acad. Sci. USA* **100**, 2171–2173.
17. Pyle, J. L., Kavalali, E. T., Piedras-Rentería, E. S. & Tsien, R. W. (2000) *Neuron* **28**, 221–231.
18. Gillespie, J. I. (1979) *Proc. R. Soc. London Ser. B* **206**, 293–306.
19. Sun, J.-Y., Wu, X.-S. & Wu, L.-G. (2002) *Nature* **417**, 555–559.
20. Hsu, S.-F. & Jackson, M. B. (1996) *J. Physiol. (London)* **494**, 539–553.
21. Mennerick, S., Zenisek, D. & Matthews, G. (1997) *J. Neurophysiol.* **78**, 51–62.
22. Geiger, J. R. P. & Jonas, P. (2000) *Neuron* **28**, 927–939.
23. Bischofberger, J., Geiger, J. R. P. & Jonas, P. (2002) *J. Neurosci.* **22**, 10593–10602.
24. Neher, E. & Marty, A. (1982) *Proc. Natl. Acad. Sci. USA* **79**, 6712–6716.
25. Lindau, M. & Neher, E. (1988) *Pflügers Arch.* **411**, 137–146.
26. Gillis, K. D. (1995) in *Single-Channel Recording*, eds. Sakmann, B. & Neher, E. (Plenum, New York), pp. 155–198.
27. Stevens, C. F. & Tsujimoto, T. (1995) *Proc. Natl. Acad. Sci. USA* **92**, 846–849.
28. Rosenmund, C. & Stevens, C. F. (1996) *Neuron* **16**, 1197–1207.
29. Schneggenburger, R., Meyer, A. C. & Neher, E. (1999) *Neuron* **23**, 399–409.
30. Bollmann, J. H., Sakmann, B. & Borst, J. G. G. (2000) *Science* **289**, 953–957.
31. Wadiche, J. I. & Jahr, C. E. (2001) *Neuron* **32**, 301–313.
32. Taschenberger, H., Leão, R. M., Rowland, K. C., Spirou, G. A. & von Gersdorff, H. (2002) *Neuron* **36**, 1127–1143.
33. Ryan, T. A., Reuter, H., Wendland, B., Schweizer, F. E., Tsien, R. W. & Smith, S. J. (1993) *Neuron* **11**, 713–724.
34. Geiger, J. R. P., Bischofberger, J., Vida, I., Fröbe, U., Pfitzinger, S., Weber, H. J., Haverkamp, K. & Jonas, P. (2002) *Pflügers Arch.* **443**, 491–501.
35. Tsien, R. & Pozzan, T. (1989) *Methods Enzymol.* **172**, 230–262.
36. Bartos, M., Vida, I., Frotscher, M., Meyer, A., Monyer, H., Geiger, J. R. P. & Jonas, P. (2002) *Proc. Natl. Acad. Sci. USA* **99**, 13222–13227.
37. Clements, J. D. & Redman, S. J. (1989) *J. Physiol. (London)* **409**, 63–87.
38. Hines, M. L. & Carnevale, N. T. (1997) *Neural Comput.* **9**, 1179–1209.
39. Major, G., Evans, J. D. & Jack, J. J. B. (1993) *Biophys. J.* **65**, 450–468.
40. Thompson, R. E., Lindau, M. & Webb, W. W. (2001) *Biophys. J.* **81**, 937–948.
41. Rohlicek, V. & Schmid, A. (1994) *Pflügers Arch.* **428**, 30–38.
42. Barnett, D. W. & Misler, S. (1997) *Biophys. J.* **72**, 1641–1658.
43. Horrigan, F. T. & Bookman, R. J. (1994) *Neuron* **13**, 1119–1129.
44. Kilic, G. & Lindau, M. (2001) *Biophys. J.* **80**, 1220–1229.
45. Xu, T., Binz, T., Niemann, H. & Neher, E. (1998) *Nat. Neurosci.* **1**, 192–200.
46. Südhof, T. C. (1995) *Nature* **375**, 645–653.
47. Chicurel, M. E. & Harris, K. M. (1992) *J. Comp. Neurol.* **325**, 169–182.
48. Acsády, L., Kamondi, A., Sik, A., Freund, T. & Buzsáki, G. (1998) *J. Neurosci.* **18**, 3386–3403.
49. Maccferri, G., Tóth, K. & McBain, C. J. (1998) *Science* **279**, 1368–1370.
50. Borst, J. G. G. & Sakmann, B. (1998) *J. Physiol. (London)* **506**, 143–157.
51. Sakaba, T. & Neher, E. (2001) *Neuron* **32**, 1119–1131.
52. Henze, D. A., McMahon, D. B. T., Harris, K. M. & Barrionuevo, G. (2002) *J. Neurophysiol.* **87**, 15–29.
53. Sätzler, K., Söhl, L. F., Bollmann, J. H., Borst, J. G. G., Frotscher, M., Sakmann, B. & Lübke, J. H. R. (2002) *J. Neurosci.* **22**, 10567–10579.
54. Abenavoli, A., Forti, L., Bossi, M., Bergamaschi, A., Villa, A. & Malgaroli, A. (2002) *J. Neurosci.* **22**, 6336–6346.
55. Hsu, S.-F., Augustine, G. J. & Jackson, M. B. (1996) *Neuron* **17**, 501–512.
56. Salin, P. A., Scanziani, M., Malenka, R. C. & Nicoll, R. A. (1996) *Proc. Natl. Acad. Sci. USA* **93**, 13304–13309.
57. Alle, H., Jonas, P. & Geiger, J. R. P. (2001) *Proc. Natl. Acad. Sci. USA* **98**, 14708–14713.
58. Henze, D. A., Wittner, L. & Buzsáki, G. (2002) *Nat. Neurosci.* **5**, 790–795.
59. Roth, A. & Häusser, M. (2001) *J. Physiol. (London)* **535**, 445–472.

3.2 Kole*, Hallermann* und Stuart, 2006, J Neurosci, 26:1677-1687

Seite 23-33

Single I_h Channels in Pyramidal Neuron Dendrites: Properties, Distribution, and Impact on Action Potential Output

Maarten H. P. Kole,^{1*} Stefan Hallermann,^{2*} and Greg J. Stuart¹

¹Division of Neuroscience, John Curtin School of Medical Research, Australian National University, Canberra 0200, Australian Capital Territory, Australia, and ²Physiologisches Institut I, Universität Freiburg, D-79104 Freiburg, Germany

The hyperpolarization-activated cation current (I_h) plays an important role in regulating neuronal excitability, yet its native single-channel properties in the brain are essentially unknown. Here we use variance-mean analysis to study the properties of single I_h channels in the apical dendrites of cortical layer 5 pyramidal neurons *in vitro*. In these neurons, we find that I_h channels have an average unitary conductance of 680 ± 30 fS ($n = 18$). Spectral analysis of simulated and native I_h channels showed that there is little or no channel flicker below 5 kHz. In contrast to the uniformly distributed single-channel conductance, I_h channel number increases exponentially with distance, reaching densities as high as ~ 550 channels/ μm^2 at distal dendritic sites. These high channel densities generate significant membrane voltage noise. By incorporating a stochastic model of I_h single-channel gating into a morphologically realistic model of a layer 5 neuron, we show that this channel noise is higher in distal dendritic compartments and increased threefold with a 10-fold increased single-channel conductance (6.8 pS) but constant I_h current density. In addition, we demonstrate that voltage fluctuations attributable to stochastic I_h channel gating impact on action potential output, with greater spike-timing precision in models with the experimentally determined single-channel conductance. These data suggest that, in the face of high current densities, the small single-channel conductance of I_h is critical for maintaining the fidelity of action potential output.

Key words: HCN; nonstationary fluctuation analysis; spike timing; noise; cortex; gain

Introduction

Nonselective hyperpolarization-activated currents in the heart (I_f) (Brown et al., 1979) and brain (I_h) (Halliwell and Adams, 1982) are crucial for a wide range of physiological processes, including rhythmogenesis, dendritic excitability, and synaptic transmission (Santoro and Tibbs, 1999; Robinson and Siegelbaum, 2003). These diverse functional roles are dependent, in part, on the elementary single-channel properties underlying I_f and I_h . At the molecular level, I_f and I_h are encoded by four distinct channel isoforms, called hyperpolarization-activated cyclic nucleotide-gated channels (HCN1–HCN4) (Ludwig et al., 1998; Santoro et al., 1998; Biel et al., 2002), each consisting of six membrane-spanning domains centered around a pore with a C terminus containing a cyclic nucleotide binding site (Santoro and Tibbs, 1999; Wainger et al., 2001; Zagotta et al., 2003). Whereas the first single-channel recordings of I_f in dissociated cardiac cells indicated a small unitary conductance of 0.98 pS (DiFrancesco,

1986), recent recordings of I_h in acutely dissociated CA1 neurons reported a 10-fold larger single-channel conductance of 10 pS (Simeone et al., 2005). Conflicting observations of HCN single-channel conductance have also been reported for heterologously expressed HCN subunits, with values of the HCN2 unitary conductance ranging from 2.5 pS (Johnson and Zagotta, 2005) to ~ 35 pS (Michels et al., 2005).

In this study, we aimed to resolve the unitary properties of single I_h channels in the brain in intact preparations (brain slices) using nonstationary fluctuation analysis (NSFA) (Sigworth, 1980) of macroscopic I_h currents recorded in cell-attached patches from the dendrites of cortical layer 5 pyramidal neurons. In these neurons, I_h is nonuniformly distributed with a significantly higher current density in the distal apical dendrites (Stuart and Spruston, 1998; Williams and Stuart, 2000; Berger et al., 2001; Lorincz et al., 2002; Notomi and Shigemoto, 2004), where it acts to shorten the duration of local dendritic postsynaptic events, diminishing distance-dependent effects on somatic EPSP and IPSP time course as well as temporal summation (Magee, 1998; Stuart and Spruston, 1998; Williams and Stuart, 2000, 2003; Berger et al., 2001).

Our observations indicate that I_h channels have a small unitary conductance of ~ 0.68 pS, which is uniform along the somatodendritic axis. Furthermore, we find that an exponential increase in single-channel number underlies the nonuniform spatial distribution of I_h , and show that stochastic gating of I_h

Received Aug. 30, 2005; revised Dec. 21, 2005; accepted Dec. 21, 2005.

This work was supported by the Alexander von Humboldt Foundation (G.J.S.) and the Förderkreis of the German Primate Center (Göttingen, Germany) (M.H.P.K.). We are grateful to M. Heckmann for critical reading of previous versions of this manuscript.

*M.H.P.K. and S.H. contributed equally to this work.

Correspondence should be addressed to Maarten H. P. Kole at the above address. E-mail: maarten.kole@anu.edu.au.

DOI:10.1523/JNEUROSCI.3664-05.2006

Copyright © 2006 Society for Neuroscience 0270-6474/06/261677-11\$15.00/0

channels leads to significant voltage membrane noise. Finally, we demonstrate using simulations that fluctuations in membrane potential attributable to I_h channel gating are sufficiently large to influence action potential (AP) fidelity in response to synaptic or weak periodic perithreshold inputs.

Materials and Methods

Patch-clamp recordings. Male Wistar rats (28–70 d) were deeply anesthetized by halothane inhalation. After decapitation, the brain was quickly removed, and sagittal brain slices (300 μm) of somatosensory cortex were prepared according to guidelines approved by the Animal Ethics Committee of the Australian National University. Throughout the preparation of slices, the brain was maintained in ice-cold artificial CSF (ACSF) of the following composition (in mM): 125 NaCl, 25 NaHCO_3 , 3 KCl, 1.25 NaH_2PO_4 , 25 glucose, 0.5 CaCl_2 , and 6 MgCl_2 , pH 7.4 (95% O_2 /5% CO_2). After cutting, slices were transferred to a holding chamber filled with the same ACSF maintained at 35°C for 45 min and subsequently stored at room temperature.

Individual slices were transferred to the stage of an upright microscope (BX51WI; Olympus Optical, Tokyo, Japan) equipped with differential interference contrast (DIC) optics, and the apical dendrites of layer 5 pyramidal neurons were visualized under infrared (IR) light (Stuart and Sakmann, 1994). The recording chamber was perfused with oxygenated (95% O_2 /5% CO_2) ACSF consisting of the following (in mM): 125 NaCl, 25 NaHCO_3 , 3 KCl, 1.25 NaH_2PO_4 , 25 glucose, 2 CaCl_2 , and 1 MgCl_2 . Somatic and dendritic cell-attached recordings were performed with borosilicate glass pipettes (Harvard Apparatus, Edenbridge, Kent, UK) pulled to a uniform resistance of $\sim 10\ \text{M}\Omega$, and filled with the following solution (in mM): 120 KCl, 20 tetraethylammonium-Cl, 10 HEPES, 5 EGTA, 5 4-AP, 1 MgCl_2 , 1 or 3 BaCl_2 , 1 NiCl_2 , 0.5 CdCl_2 , and 0.001 TTX, pH 7.4 (285 mOsm). For NSFA, a high concentration of BaCl_2 (3 mM) was included to block large-conductance channel openings of inward-rectifying K^+ channels. Somatic and dendritic whole-cell recordings were made with pipettes containing 135 mM K-gluconate, 7 mM NaCl, 2 mM MgCl_2 , 2 mM Na_2ATP , 0.3 mM NaGTP , 10 mM HEPES, pH 7.2 with KOH, and 0.2% biocytin (Invitrogen, Carlsbad, CA). All data were obtained at $34 \pm 1^\circ\text{C}$.

Currents were recorded with an Axopatch 200B amplifier (Molecular Devices, Union City, CA) in capacitive feedback mode and collected using an ITC-18 computer interface (InstruTech, Port Washington, NY). All signals were analog low-pass filtered at 10 kHz (eight-pole Bessel) and digitally sampled at 20 kHz using the data acquisition software Axograph (Molecular Devices). Ensemble traces were further digitally filtered at the indicated frequencies (see below). Baseline recording noise was $\sim 600\ \text{fA}$ root mean square (rms) at 5 kHz bandwidth and 1.0 pA at 10 kHz. The bath level of the recording chamber was kept to a minimum to reduce fast capacitance transients. Remaining transients were cancelled with capacitance compensation. Leak subtraction was generally performed off-line using scaled and averaged leak pulses (50 repetitions) using a P/10 protocol.

Voltage signals were recorded with a BVC-700 current-clamp amplifier (Dagan, Minneapolis, MN), filtered at 1 kHz, and sampled at 2 kHz. Capacitance transients and access resistance were compensated with the amplifier circuits. The instrumental noise from the electrode-amplifier circuit was estimated to be $\sim 40\ \mu\text{V}$ by replacing the electrode holder with a model cell (500 $\text{M}\Omega$ /33 pF; Molecular Devices). Synaptic conductances were blocked by bath application of 50 μM D-APV, 20 μM DNQX, and 50 μM bicuculline-methobromide, and Na^+ channels were blocked with 1 μM TTX (Tocris Bioscience, Bristol, UK). To investigate the impact of I_h channel gating on voltage noise, we bath applied the I_h antagonist ZD 7288 [4-(*N*-ethyl-*N*-phenylamino)-1,2-dimethyl-6-(methylamino)pyrimidinium chloride] in recordings in which somatic noise was $>100\ \mu\text{V}$. Cells with large spontaneous fluctuations in resting potential were disregarded from analysis. Some neurons (see Fig. 1A) were processed for biocytin and reconstructed *post hoc* with NeuroLucida (MicroBrightField, Williston, VT).

Data analysis. The patch holding potential was calculated assuming a resting potential at the soma of $-79\ \text{mV}$, estimated from perforated-patch recordings (Gulledge and Stuart, 2003). In addition, we corrected

for a distance-dependent depolarization of the membrane potential of $\sim 1\ \text{mV}/100\ \mu\text{m}$ (supplemental Fig. S1, available at www.jneurosci.org as supplemental material) and a liquid junction potential of the cell-attached solution of $-3\ \text{mV}$ (Williams and Stuart, 2000). Somatic whole-cell voltage was corrected for the $-14\ \text{mV}$ difference between the resting membrane potential during perforated-patch and whole-cell recordings (Gulledge and Stuart, 2003), primarily attributable to the liquid junction potential of the whole-cell pipette solution ($-12\ \text{mV}$). The distance of the dendritic recording site from the soma was measured *in situ* from the IR-DIC image and taken to be the linear distance between the recording site and the beginning of the apical trunk.

Steady-state activation curves (see Fig. 1C) were constructed from the amplitude of tail currents after voltage steps to different amplitudes (Williams and Stuart, 2000). These data were normalized to the maximum tail current amplitude and fitted with a single Boltzmann function. Activation time course of I_h onset was described by double-exponentials fits from which an amplitude weighed single exponential, $\tau_w = (A\tau_{\text{fast}} + B\tau_{\text{slow}})/(A + B)$, was calculated. The deactivation time course was well described by a single-exponential function. Average values are expressed as mean \pm SEM.

Nonstationary fluctuation analysis. NSFA of recorded, as well as simulated, I_h currents was performed according to recently described routines for voltage-dependent channels (Conti et al., 1980; Sigworth, 1980; Alvarez et al., 2002) written in and analyzed with Igor Pro 5.01 (WaveMetrics, Lake Oswego, OR). In brief, assuming that the macroscopic ionic current at a given time point (t) is dependent on the single-channel properties, such that $I(t) = N\gamma P_o(V, t)(V - V_{\text{REV}})$, where I is the current, and V the membrane voltage. The current is the product of N , the maximum number of channels, γ , the elementary single-channel conductance, P_o , the probability of channel opening at maximum steady-state current, and the electrical driving force, $V - V_{\text{REV}}$, where V_{REV} is the reversal potential.

The variance, σ_I^2 , in trial-to-trial fluctuations of the ensemble I_h current evoked by identical hyperpolarizing steps (-60 or $-100\ \text{mV}$; 400 ms duration) was calculated from sets of 80–140 consecutive sweeps. To correct for rundown of the ensemble I_h current, we followed procedures described previously (Conti et al., 1980; Alvarez et al., 2002). The variance was defined by:

$$\sigma_I^2(t) = \frac{2}{N_{\text{tr}} - 1} \sum_{i=1}^{N_{\text{tr}}} (y_i(t) - \bar{y}(t))^2$$

$$\text{with } y_i(t) = \frac{x_i(t) - x_{i+1}(t)}{2},$$

where N_{tr} is the number of evaluated traces (in most cases, 100), $x_i(t)$ are the values of the i th current trace, and \bar{y} is the average of all y_i . Variance-mean plots were fitted with a least-square algorithm to the following equation:

$$\sigma_I^2 = i\langle I \rangle - \frac{\langle I \rangle^2}{N} + B.$$

Here, B is a background noise offset, and $\langle I \rangle$ is the mean current. At the first root of the parabola, the slope equals the single-channel amplitude i . Variance-mean plots were calculated from data beginning 2 ms after the start of the voltage pulse to the maximum of the steady-state mean amplitude. Single-channel conductance, γ , was estimated by $i/(V - V_{\text{REV}})$, and the open probability, P_o , was determined by $P_o = I_{\text{max}}/(iN)$, where I_{max} is the average current amplitude at steady state. The reversal potential (V_{REV}) was experimentally measured to be $\sim 0\ \text{mV}$ ($0.5 \pm 2.6\ \text{mV}$; $n = 4$) with 120 mM external K^+ and zero Na^+ . For 60 mM external K^+ and Na^+ , and 2.5 mM external K^+ and 120 mM external Na^+ , we calculated a V_{REV} of -16 and $-45\ \text{mV}$, respectively, based on the Goldman-Hodgkin-Katz equation assuming an Na^+ to K^+ permeability ratio of 0.4 and 0.2 (Hestrin, 1987). Similar values of N , i , or P_o were obtained during NSFA of the first 200 ms ($n = 18$; $p > 0.3$) and also after exponential sampling ($n = 18$; $p > 0.7$), where mean current and variance were sampled in an exponentially manner based on τ_w .

I_h current simulations. Single I_h channel currents in the models shown in Figure 2 were simulated at 20 kHz temporal resolution (identical to the sampling frequency of recordings) with the high quality pseudorandom number generator in Igor Pro [compare with function ran2 by Press (2002)]. The uniformly distributed number, u , between 0 and 1 was used to generate an exponentially distributed interval $-(1/a) \times \ln(u)$, where a is the sum of the rate constants from one state to all neighboring states. Another random number was used to decide which state was visited next (Colquhoun et al., 2003). Simulated macroscopic I_h currents, with activation kinetics similar to the weighed activation time constant of experimental data ($\tau_w = 50$ ms), were generated by the addition of the appropriate number of single-channel currents. Realistic recording noise (1 pA rms at 10 kHz) was simulated by adding white noise (simulated with Igor Pro; Box-Müller transformation) with 1.22 pA rms to each point. Filtering with a low-pass Gaussian filter with a cutoff frequency of 10 kHz resulted in 1 pA rms, similar to that observed in patch-clamp recordings after low-pass filtering at 10 kHz using the eight-pole Bessel filter of the amplifier. As in the experimental situation, we repeated this procedure 100 times. The resulting 100 simulated macroscopic currents were analyzed with NSFA identical to the recorded data. Leak subtraction was implemented by subtracting a simulated empty leak current (an average of 50 traces of 1 pA rms noise scaled up by a factor of 10) from the mean current.

NEURON simulations. The impact of I_h channel fluctuations on AP output was simulated using a morphological realistic compartmental model of a large layer 5 pyramidal neuron (Stuart and Spruston, 1998, their Fig. 1A) in NEURON (version 5.7, available at <http://www.neuron.yale.edu/neuron/>). Spines were incorporated by decreasing R_m and increasing C_m twofold in spiny compartments. The passive properties R_m (15 k Ω /cm²), C_m (1 μ F/cm²), and R_i (100 Ω /cm) were uniformly distributed, and the resting membrane potential V_m was set at -89 mV, equivalent to the experimentally recorded V_m when I_h was blocked with 50 μ M ZD 7288. To account for active properties, voltage-gated channels (Schaefer et al., 2003) were incorporated at the following densities. The soma contained (in pS/ μ m²) $g_{Na} = 54$, $g_{Kv} = 200$, $g_{KAP} = 0.008$, $g_{Kca} = 3$, $g_{Km} = 0.1$, calcium $g_{Ca} = 0.3$, and $g_{Ca,T} = 0.0008$. In the dendrites the channel densities were as follows: $g_{Na} = 27$, $g_{Kv} = 25$, $g_{KAP} = 0.008$, $g_{Kca} = 1.5$, $g_{Km} = 0.05$, $g_{Ca} = 0.8$, and $g_{Ca,T} = 0.0005$. In the reconstructed axon, Na^+ and K^+ channels were included with a density of $g_{Na} = 30,000$ and $g_{Kv} = 400$. We set AP threshold to -63 mV (Gulledge and Stuart, 2003). Synaptic inputs were simulated as conductances with 0.2 ms rise and 2 ms decay time constants and a reversal potential of 0 mV (Häusser and Roth, 1997). The nominal temperature was set to 35°C.

The conductance density of I_h (g_h) was distributed across compartments using the following exponential function: $g_h = y_0 + A \exp(d/\lambda)$, with $y_0 = -2$ pS/ μ m², $A = 4.28$ pS/ μ m², $\lambda = 323$ μ m, and d is the distance from the soma. These values were obtained from an exponential fit to the experimental data in Figure 1B after correction for the 5.1-fold reduction in I_h conductance under physiological conditions in which the external potassium concentration is 2.5 mM (supplemental Fig. S2, available at www.jneurosci.org as supplemental material) and assuming a membrane area of 4.5 μ m² at the pipette tip (Engel and Jonas, 2005). The corrected and scaled g_h implemented in NEURON gave rise to a range of I_h densities between 2.3 pS/ μ m² at the soma to 93 pS/ μ m² in the distal apical dendrites ~ 1000 μ m from the soma and led to changes in V_m that were found experimentally (supplemental Fig. S1, available at www.jneurosci.org as supplemental material). The I_h reversal potential was set at -45 mV.

To investigate the impact of stochastic fluctuations attributable to probabilistic opening and closing of channels on AP output, we implemented stochastic channel gating in the NEURON-extension NMODL (Hines and Carnevale, 2000). For I_h , a simple two-state Hodgkin–Huxley scheme was used. In each segment, each closed single I_h channel had the chance to open within the iteration time, dt_{nrn} , with the probability, P_{open} :

$$P_{\text{open}} = \int_{t=0}^{dt_{\text{nrn}}} \alpha(v) \exp(-\alpha(v)t) dt = 1 - \exp(-\alpha(v)dt_{\text{nrn}}),$$

where $\alpha(v)$ is the rate of channel opening depending on the local membrane potential, v . Correspondingly, each open channel had the chance

to close with P_{close} depending on the rate of channel closing, $\beta(v)$. The opening rate $\alpha(v)$ was defined by

$$\alpha(v) = \frac{A(v+B)}{\exp\left(\frac{v+B}{C} - 1\right)},$$

and the closing rate $\beta(v)$ was defined by

$$\beta(v) = D \exp(v/E).$$

This led to Hodgkin–Huxley-type channel kinetics with single exponential activation kinetics (power = 1) and no inactivation (Hodgkin and Huxley, 1952). The five free parameters, A , B , C , D , and E , were determined by simultaneously fitting $1/(\alpha(v) + \beta(v))$ to the voltage dependence of the time constant of I_h activation and deactivation and $\alpha(v)/(\alpha(v) + \beta(v))$ to the activation curve (see Fig. 6A). The sum of squared errors was minimized using the Levenberg–Marquardt method (Mathematica 4.1; Wolfram Research, Champaign, IL), with the time constants of activation and deactivation weighed with the inverse of the maximum value in the dataset, and the voltage activation curve weighed with 10 times the inverse of the maximum value in the dataset. The resulting parameters were $A = 6.43$ s⁻¹, $B = 154$ mV, $C = 11.9$ mV, $D = 193$ s⁻¹, and $E = 33.1$ mV and predicted the data adequately (see fits in Fig. 6A).

Stochastic Na^+ channels (see Fig. 7E,F) were modeled with a kinetic reaction scheme of eight states describing the m^3h Hodgkin–Huxley activation kinetics (Hille, 1978, 2001). As with stochastic I_h channels, each Na^+ channel had the chance to move to one of its neighboring states within the iteration time, dt_{nrn} , with the appropriate probability. The kinetic rate constants were based on previously published Na^+ channel models (see <http://senselab.med.yale.edu/senselab/modeldb/>).

For both stochastic I_h and Na^+ channels, the number of channels in each segment, was calculated from the current density and the surface area. For each iteration time point dt_{nrn} , the numbers of channels in the open and the closed state were stored, and the “macroscopic” I_h and Na^+ current were determined by summation of the appropriate number of single-channel events. Simulations were performed on three Intel Pentium processors 2.6 GHz, one 64-bit opteron AMD processor (2×1.6 GHz), and one Linux Cluster that contained 18 machines, each with two 2.6 GHz Intel Xeon central processing units housed in two IBM Blade-Centers. The dt_{nrn} was set to 10 or 100 μ s for simulations using stochastic I_h or 1 μ s for simulations using stochastic Na^+ channels.

The power spectral density (PSD) of voltage (see Figs. 5, 6) was generated with Igor Pro from a 25 s sweep using the square-window method and fitted with a Lorentzian function, $S = A/(1 + (f/f_c)^2)$ (DeFelice, 1981). The predicted change in σ_v , when changing γ (see Fig. 6D), was based on theoretical work indicating that the variance of the macroscopic current, σ_I^2 , is proportional to $\gamma^2 N$ (for an example, see Diba et al., 2004, their Eq. 15). Because the current density was the same in models with different single-channel conductance (i.e., $\gamma N = \text{constant}$), σ_I^2 is proportional to γ . Thus, σ_I is proportional to $\sqrt{\gamma}$. The similarity between obtained and predicted voltage noise, $\sigma_{v,\text{predicted}}(\gamma) = \sigma_v(680 \text{ fS}) \sqrt{(\gamma/680 \text{ fS})}$, indicates a linear relationship between σ_v and σ_I in our model.

Stochastic resonance was assessed during weak sinusoidal somatic current injection (I_{sin}) in the presence of direct current (DC) adjusted to be just suprathreshold (one AP per cycle) or just subthreshold (zero APs per cycle) in models with deterministic I_h channels. A binary output of AP timing was derived from the membrane voltage of the model (V_m), which was set to zero until V_m crossed 0 mV, and was then set to 1 for 1 ms (Stacey and Durand, 2000). The PSD of this binary output trace was determined using Igor Pro. The signal-to-noise ratio (SNR) ratio was defined as $(S - B)/B$, where S was the peak of the PSD at 3 Hz, and B was the average of the baseline noise of the PSD before and after 3 Hz. Stochastic resonance curves were fitted according to the theory of monostable systems with excitable dynamics and after deterministic “rejection” to the resting state (Wiesenfeld et al., 1994):

$$\text{SNR} = \left(\frac{\epsilon \Delta U}{D}\right)^2 e^{-(\Delta U/D)},$$

where ϵ is the signal strength, ΔU is a constant related to the threshold barrier height, and D is noise intensity. For D , the variance of the somatic membrane potential was used (Wiesenfeld et al., 1994), calculated from the fit to Figure 6D. The two free parameters ϵ and ΔU were fitted with nonlinear least-squares regression with Igor Pro.

Input/output curves (see Fig. 7F) were normalized, aligned to the synaptic conductance that generated APs with a probability of 0.5, and fitted with the sigmoid function $AP_{\text{prob}}(\Delta g) = (1 + \exp(-\Delta g/s))^{-1}$, where Δg is the change in synaptic conductance, and s represents the steepness of the AP probability curve.

Results

Cell-attached patch-clamp recordings were made from the apical dendrites of large layer 5 pyramidal neurons up to 900 μm from the soma, and I_h currents evoked by hyperpolarizing pulses from a holding potential 25 mV depolarized to the resting membrane potential (Fig. 1A). These currents could be blocked by $82 \pm 7\%$ ($n = 3$) by bath application of 50 μM of the I_h antagonist ZD 7288 (BoSmith et al., 1993; Robinson and Siegelbaum, 2003), indicating adequate specificity for I_h (Fig. 1A). To determine the dendritic distribution of I_h current, we plotted I_h current density against distance of the recording site from the soma (Fig. 1B). The distribution was well described by a single-exponential function (Fig. 1B), from which it can be inferred that I_h current density increases e -fold with every 325 μm . The time course of I_h current onset during 100 mV hyperpolarizing steps was best fit with a double-exponential function, with a τ_{fast} of 27.0 ± 1.5 ms and τ_{slow} of 155 ± 8 ms ($n = 88$). The ratio of the amplitude of the fast to slow time constants was 4.9 ± 0.3 , indicating that fast activation kinetics dominate. The weighed single time constant of I_h activation was calculated to 49.7 ± 3.0 ms ($n = 88$). Steady-state voltage-activation curves were well described by a single Boltzmann function with a half-maximum activation (V_{half}) of, on average, -110 ± 1.5 mV and a slope constant of 10.1 ± 0.5 mV ($n = 9$) (Fig. 1C). At a few dendritic sites, cell-attached patch recordings were subsequently made with a saturating concentration of 8-Br-cAMP (100 μM , in the patch-pipette) to test for cyclic nucleotide modulation of I_h . On average, application of 8-Br-cAMP had no effect on the activation kinetics (τ_{fast} control, 22.0 ± 2.1 ms; cAMP, 21.4 ± 0.9 ms; paired t test, $p > 0.9$; $n = 10$) or the V_{half} (100 μM cAMP, -106 ± 0.9 mV; $n = 3$). These data are in good agreement with the relative insensitivity of the HCN1 isoform to cAMP regulation (Santoro and Tibbs, 1999) and an abundant expression of HCN1 in the layer 5 dendrites (Notomi and Shigemoto, 2004; Santoro et al., 2004).

Fluctuation analysis of I_h in cell-attached recordings

To examine the properties of single I_h channels, we used NSFA of macroscopic I_h currents (Conti et al., 1980; Sigworth, 1980; Alvarez et al., 2002). I_h currents in these experiments were activated by 400 ms hyperpolarizations to maximize the number of possible repetitions. Filtering of individual sweeps (Fig. 1D, top)

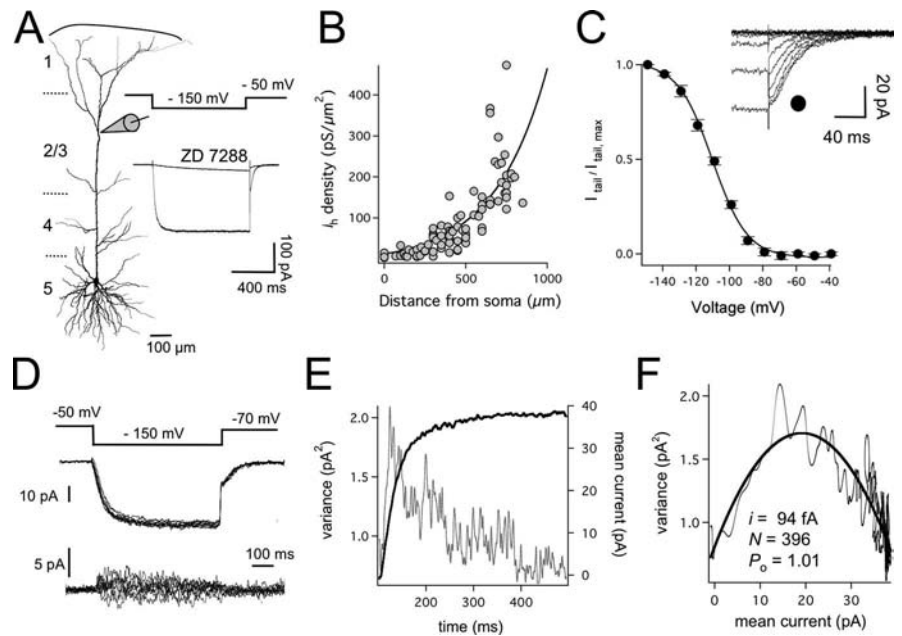


Figure 1. I_h current distribution, kinetics, and single-channel properties. **A**, Schematic of the experimental setup during dendritic cell-attached recording 700 μm from the soma of a layer 5 pyramidal neuron (reconstructed from a biocytin fill). The different cortical layers are indicated. An example of I_h current evoked by a 100 mV hyperpolarizing pulse from a holding potential 25 mV depolarized from rest is shown before and after bath application of ZD 7288 (50 μM). **B**, I_h current density plotted against distance from the soma ($n = 88$). Data fitted with a single-exponential function. **C**, I_h voltage-activation curve generated from tail currents (inset) during hyperpolarizing steps between -40 and -150 mV ($n = 9$; 680 ± 21 μm from the soma). Data fitted with a Boltzmann function. **D**, Superimposed successive single traces used for NSFA elicited by a 100 mV hyperpolarizing step (recorded 500 μm from the soma). Only 10 of 100 traces are shown. The corresponding subtracted differences from the 10 traces are given in the bottom panel. Currents were off-line digitally filtered at 100 Hz. **E**, Fluctuation analysis of data in **D**. Data of 100 successive sweeps were used to plot mean I_h current (black trace) and variance (gray trace) as a function of time. **F**, Variance-mean plot for the data in **E**. The data were well fitted by a parabola (black line) from which the single-channel amplitude i , the maximum number of channels N , and the open probability P_o were obtained.

performed with a digital Gaussian filter at 100 Hz and the current variance (σ^2) calculated from the difference between 100 consecutive sweeps (Fig. 1D, bottom). The plot of the current σ^2 versus time had a peak coinciding with half-maximal activation at ~ 25 ms (Fig. 1E). Plots of the current σ^2 against mean I_h current amplitude could be well fit with a parabolic function, from which the single-channel amplitude (i), the total number of channels (N), and open probability (P_o) can be estimated (Fig. 1F). On average, at dendritic sites ~ 500 μm from the soma, NSFA gave estimates of i of 88 ± 9.9 fA, N of 342 ± 24 , and P_o of 0.92 ± 0.03 ($n = 5$) during hyperpolarizing voltage steps of 100 mV from an estimated patch holding potential of approximately -50 mV.

Accuracy of parameters extracted using NSFA

How accurate are the values for i , N , and P_o obtained from NSFA? To assess this, we simulated I_h channels and performed NSFA on simulated macroscopic I_h currents. These simulations used I_h channels with activation kinetics similar to that observed experimentally (single exponential kinetics with τ of 50 ms). Two different channels were simulated, one without flicker (Fig. 2A, C–O) and one with channel flicker (Fig. 2B, C–C–O). In both cases, i was 100 fA and N was 500. In the case of the nonflickering channel, P_o was 1 (Fig. 2A), whereas P_o was 0.5 in the flickering channel (Fig. 2B, forward and backward rates, δ , into and out of the open state were equal). Simulated macroscopic I_h current traces were generated by adding 500 single-channel traces (Fig. 2A, B) and realistic recording noise. These currents were digitally filtered at frequencies ranging from 2 Hz to 10 kHz and subjected

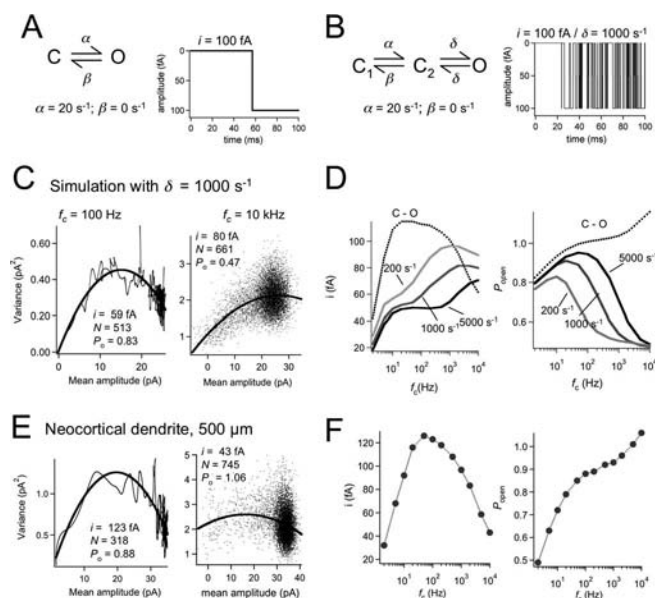


Figure 2. Accuracy of parameters extracted with NSFA. **A**, I_h channels simulated with a simple gating model. The rate from the closed (C) to the open (O) state was set to be 20 s^{-1} , and P_o was set to 1. The right panel shows an example of a simulated single-channel trace with amplitude i of 100 fA. **B**, Flickering I_h channels were simulated by adding an additional shut state C_2 to the scheme used in **A**. The rate into and out of the open state, δ , was equal, leading to $P_o = 0.5$. The other channel rates are not changed. The right panel shows an example of a simulated single-channel trace with the flicker frequency δ set to 1000 s^{-1} . For clarity, only 100 ms of the 400 ms trace is shown. **C**, Examples of variance-mean plots of simulated I_h channels with δ set to 1000 s^{-1} using a filter cutoff frequency, f_c , of 100 Hz (left) and 10 kHz (right). The parameters obtained from NSFA fitting (black lines) are indicated. **D**, The influence of filtering on the parameters extracted with NSFA was investigated systematically by varying f_c from 2 Hz to 10 kHz. The lines represent simulations with different flickering frequencies (δ ranging from 200 to 5000 Hz). With increasing flickering frequency, higher cutoff frequencies are required to extract the correct parameters using NSFA. The dotted lines represent the parameters obtained with the nonflickering C–O model. **E**, Variance-mean plots for experimental data recorded 500 μm from the soma and low-pass filtered at 100 Hz (left) or 10 kHz (right). The parameters obtained from NSFA are indicated. **F**, The single-channel parameters i , N , and P_o are plotted versus f_c for the experimental data shown in **E**. Note the high similarity to the nonflickering model (C–O) shown in **D**.

to NSFA. An example of the effect of filtering on variance-mean plots for simulated I_h channels using a model with 1 kHz flicker is shown in Figure 2C after filtering at 100 Hz or 10 kHz. A full analysis of the impact of filtering on the parameters extracted with NSFA for the nonflickering and flickering models is shown in Figure 2D. These plots indicate that, in the nonflickering model, i is underestimated during filtering at less than ~ 20 Hz or more than ~ 1 kHz (Fig. 2D, left), leading to overestimations of N (data not shown), whereas P_o increased monotonically with filter cutoff frequency (Fig. 2D, right). These simulations suggest that, in a situation in which there is no channel flicker, the best estimates of single I_h channel parameters are obtained after filter at ~ 100 Hz. The situation was reversed in models with channel flicker, with the estimated value of i increasing monotonically with cutoff frequency (Fig. 2D, left), whereas P_o increased and then decreased with increasing cutoff frequency and only converged to its appropriate value (0.5) at the highest cutoff frequencies tested (Fig. 2D, right). Thus, under conditions of high-frequency channel flickering, NSFA will only be accurate when the cutoff frequency is set at or above 10 kHz.

With these theoretical relationships in mind, we tested the impact of filtering on the parameters extracted with NSFA for native I_h currents. Macroscopic I_h currents recorded at 10 kHz

bandwidth were off-line digitally filtered at cutoff frequencies ranging from 2 Hz to 10 kHz. Variance-mean plots of recorded I_h currents after filtering at 100 Hz and 10 kHz are shown in Figure 2E. Figure 2F shows the estimated parameters obtained with NSFA for all cutoff frequencies tested. Similar to the nonflickering model, with increasing cutoff frequency i increased and then decreased, whereas P_o increased monotonically (similar results were observed in four other datasets). The impact of filtering on the single-channel parameters extract using NSFA of native I_h currents is therefore similar to that observed in the nonflickering model, suggesting that native I_h channels do not undergo significant flickering in the frequency range below ~ 5 kHz. Given this, these findings suggest that a cutoff filter frequency of ~ 100 Hz is optimal for obtaining the best estimates from NSFA. This is also consistent with theoretical work indicating that errors attributable to filtering will occur if the time constant of filtering (τ_{filter}) is more than $1/10$ of the time constant of channel activation (Alvarez et al., 2002). In neocortical dendrites, I_h has a weighted time constant of activation of ~ 50 ms. Thus, in our case, τ_{filter} should not be >5 ms, corresponding to a low-pass cutoff frequency (f_c) of $1/(2\pi\tau_{\text{filter}})$ or ~ 30 Hz.

Finally, we investigated the accuracy of the parameters extracted with NSFA under a large range of different signal-to-noise conditions in our nonflickering model filtered at 100 Hz by varying i and N systematically (supplemental Fig. S3, available at www.jneurosci.org as supplemental material). From these simulations, we found that, if the amplitude of macroscopic I_h currents is <1 pA or i is <10 fA, the errors in i , N , and P_o are large ($>50\%$) and thus highly inaccurate. However, if the macroscopic I_h current is >10 pA, as typically found in this study, the errors are $<20\%$. Together, these simulations indicate that NSFA has sufficient precision to accurately estimate the single-channel parameters of I_h channels under our recording conditions.

Dependence of I_h single-channel properties on voltage

Does NSFA of macroscopic I_h currents accurately describe the voltage-dependent properties of I_h ? To address this, hyperpolarizing pulses of -100 and -60 mV amplitude were alternated at 1 s intervals, and NSFA was performed on the obtained variance-mean relationships (Fig. 3A) (six patches ~ 570 μm from the soma). Because the total channel number N cannot be estimated precisely when channels are not fully activated, we fixed N during fitting of variance-mean plots for -60 mV steps to the value estimated during NSFA of -100 mV steps in the same patch. From this analysis, P_o was estimated to be, on average, 0.94 ± 0.03 during -100 mV steps and 0.55 ± 0.05 during -60 mV steps ($n = 6$). These estimates of P_o follow a voltage dependence similar to that obtained for the I_h activation curve determined from tail currents (Fig. 3B). The unitary amplitude, i , was significantly smaller during -60 mV steps compared with -100 mV steps (Fig. 3C, left) ($p < 0.001$), as expected because of the reduced driving force, whereas the unitary conductance, γ , was not statistically different (Fig. 3C, right) ($p > 0.13$). In conclusion, the results above indicate that NSFA of macroscopic I_h currents accurately describes the voltage-dependent properties of single I_h channels.

Dependence of I_h single-channel properties on location

Previous studies on I_h in layer 5 pyramidal dendrites have reported a significantly higher current density at distal dendritic locations (Williams and Stuart, 2000; Berger et al., 2001). Because the macroscopic I_h current is determined by the product of i , N , and P_o , we can now separate which of these factors underlies the

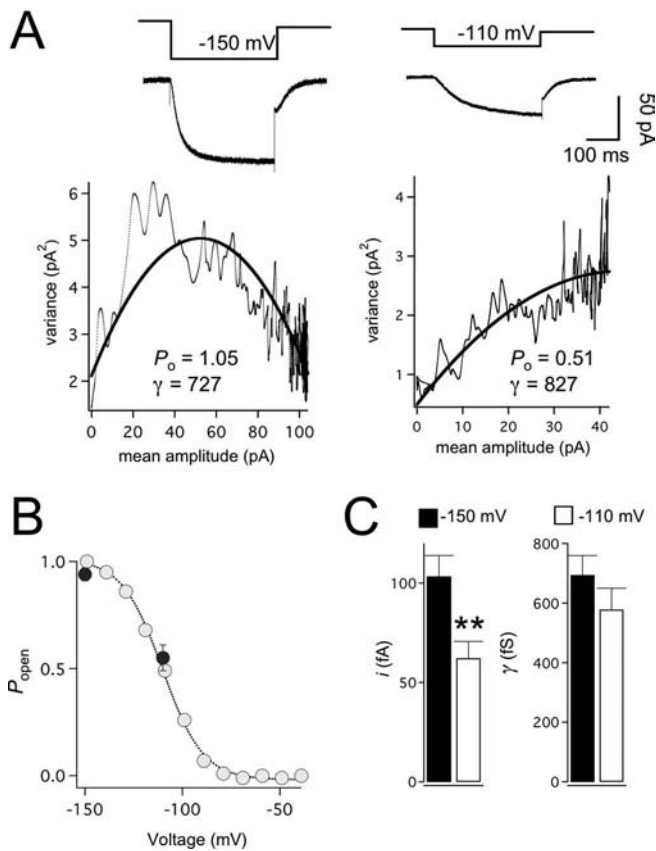


Figure 3. Voltage-dependent properties of I_h obtained with NSFA. **A**, Top, I_h currents evoked by hyperpolarizing steps to -150 mV (left) and -110 mV (right). Bottom, Fitting variance versus mean of the plots (black line) yielded a P_o of 1.05 with 889 channels and i of 109 fA during steps to -150 mV (left), whereas P_o was reduced to 0.51 and i to 91 fA during steps to -110 mV (right). N was fixed to that obtained during steps to -150 mV (889) during fitting of the NSFA data for steps to -110 mV (black line). **B**, Pooled data ($n = 5$) of P_o during steps to -150 mV (0.94 ± 0.03) and -110 mV (0.54 ± 0.05 ; filled circles) is consistent with the activation curves obtained from I_h tail-current amplitudes (open circles; same data as in Fig. 1C). **C**, Histogram of single-channel current amplitude i (left) and conductance γ (right) extracted with NSFA during steps to -150 and -110 mV. $**p < 0.001$ ($n = 6$).

highly nonuniform subcellular distribution of I_h in these neurons (Fig. 1B). Three examples of variance-mean plots obtained from recordings 270, 400, and 740 μm from the soma are shown in Figure 4A. Figure 4B shows that, when P_o is plotted as a function of recording location, for distances from ~ 120 to 900 μm from the soma, no clear dependence exists on dendritic site. Similarly, the I_h single-channel conductance, γ , was independent of the dendritic recording location (Fig. 4C). Plotting γ as a histogram indicates that γ represents a single population with average amplitude of 676 ± 35 fS (Fig. 4C, inset) ($n = 18$). In contrast, N was found to rise steeply with distance from the soma (Fig. 4D). An exponential fit to this data indicates that N increases e -fold for a 240 μm path length along the main apical dendrite of layer 5 pyramidal neurons, similar to the e -fold change in current density (Fig. 1B). At the most distal dendritic locations examined (900 μm from the soma), we observed as many as ~ 2500 I_h channels per dendritic patch, whereas at the most proximal sites (120 μm from the soma), as few as 40 channels per patch were observed. This gradient is essentially identical to the reported 60-fold increase in immunogold-labeled HCN1 particles in layer 5 dendritic membrane (Lorincz et al., 2002). These data correspond to I_h channel densities of 9–550/ μm^2 , assuming a membrane patch area of ~ 4.5 μm^2 (Engel and Jonas, 2005). The high

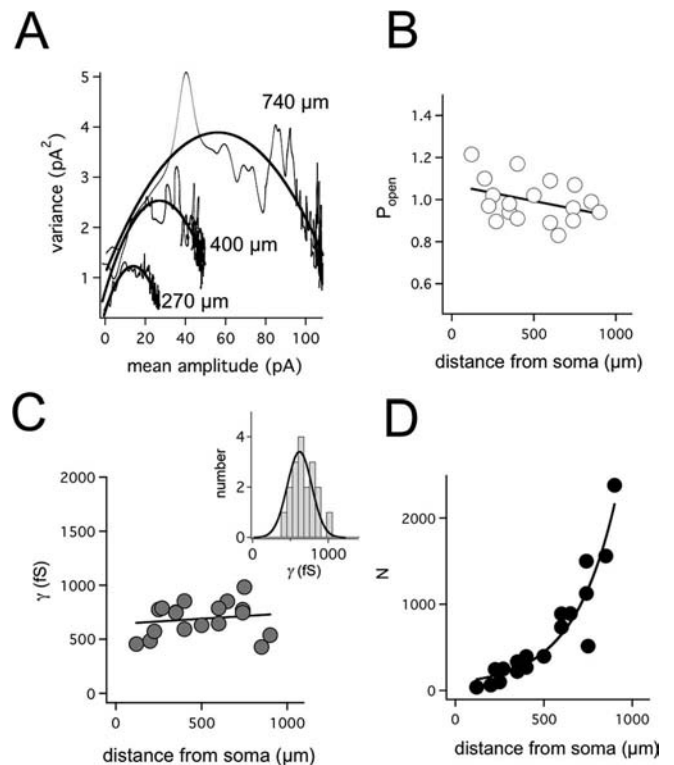


Figure 4. NSFA reveals a distance-dependent increase in N . **A**, Superimposed examples of variance-mean plots for three dendritic locations (270, 400, and 740 μm from the soma) with the variance-mean fits (black lines). **B**, Plot of open probability P_o versus recording distance from the soma. Data were fitted with a regression (slope of -0.015 ; $n = 18$). **C**, Plot of single-channel conductance γ versus distance from the soma. Data fitted with a linear regression (slope of $+0.11$; $n = 18$). Inset shows a histogram of γ revealing a single population well fitted with a Gaussian function ($n = 18$). **D**, Plot of the number of channels per patch (N) versus distance (d) from the soma. The data are well described by a single-exponential function of the form: $49 \times \exp(d/240) + 47$, indicating that the I_h channel number increases e -fold for a 240 μm change in distance.

density of I_h in the distal dendrites of layer 5 pyramidal neurons is comparable with the density of voltage-activated Na^+ channels found at nodes of Ranvier (Hille, 2001). In conclusion, these data indicate that the nonuniform scaling of I_h current density is generated by an exponential increase in channel number per dendritic membrane area, leading to high channel densities in distal dendrites.

Contribution of stochastic I_h channel gating to membrane noise

The results above indicate that I_h channels have a very small single-channel conductance yet can be expressed at very high densities. Why is the single-channel conductance of I_h so small? Clearly, it would be energetically more efficient to increase single-channel conductance, for example by 10-fold to 6.8 pS, thereby reducing channel number by a factor of 10 for the same current density. One possible explanation for the small single-channel conductance of I_h is that there are other constraints on the system, such as voltage noise. Previous work indicates that the stochastic opening and closing of voltage-dependent channels can generate fluctuations in membrane potential, which could be a significant source of voltage noise in excitable cells (DeFelice, 1981; White et al., 2000). To directly address whether the stochastic gating of single I_h channels contributes to membrane noise, we recorded voltage noise at the resting membrane potential in the

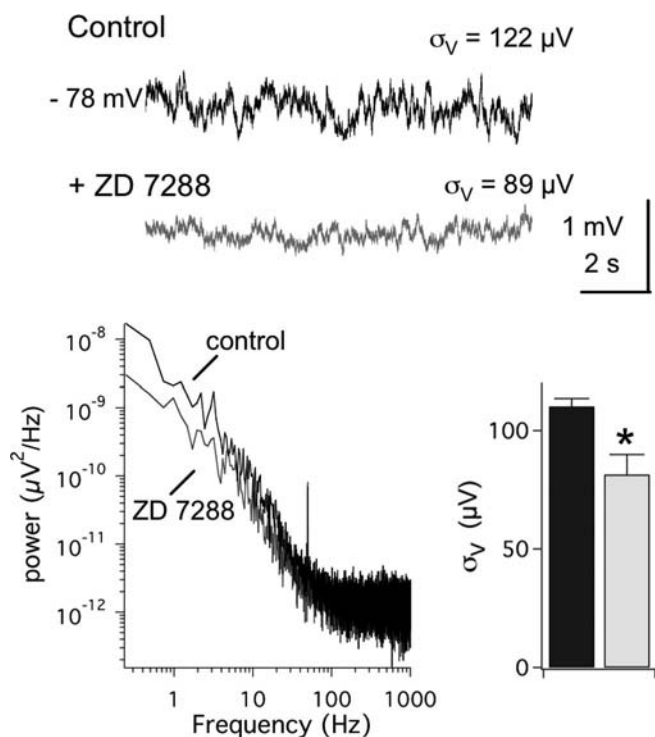


Figure 5. Impact of I_h channel gating on somatic voltage noise. Whole-cell somatic voltage recordings before (top trace; black) and after (bottom trace; gray) I_h channel block by bath application of ZD 7288 ($50 \mu\text{M}$). All data were recorded in the presence of synaptic blockers and TTX. DC injection was used to maintain the same membrane potential in control and ZD 7288. Left, Power spectrum of the same traces indicating that ZD 7288 attenuates voltage fluctuations in the low-frequency range. Right, Population data of the average SD, σ_V , of the somatic voltage noise in control (black bar) and ZD 7288 (gray bar).

presence of blockers for NMDA, AMPA, GABA_A, and Na⁺ channels. In Figure 5, an example is shown of control membrane potential fluctuations at the soma with an SD, σ_V , of 122 μV (Fig. 5, black trace). To isolate the contribution of I_h channels to these voltage fluctuations, we bath applied $50 \mu\text{M}$ ZD 7288 (BoSmith et al., 1993). This led to a hyperpolarization of the somatic resting membrane by 11 mV (average change, $-10.3 \pm 0.5 \text{ mV}$; $n = 6$), which was corrected for by positive DC injection to obtain a similar resting membrane potential as in control (-77.9 mV). Under these conditions, σ_V was reduced to 89 μV (Fig. 5, gray trace). Spectral analysis of traces before and after ZD 7288 showed that I_h noise is particularly dominant in the low-frequency range (Fig. 5, left). On average, application of ZD 7288 lead to a reduction of σ_V by $33 \pm 7 \mu\text{V}$ (Fig. 5, right) ($n = 6$; paired t test, $p < 0.01$), showing that native I_h channels contribute significantly to voltage noise at resting membrane potentials.

Impact of I_h single-channel conductance on membrane noise

Next we investigated the impact of I_h single-channel properties on membrane voltage noise using a model in which single-channel conductance and number could be varied in a controlled manner. A stochastic Hodgkin–Huxley model of I_h based on our experimental data (Fig. 6A) was introduced into a morphologically realistic model of a layer 5 pyramidal neuron (Fig. 6B). The model contained voltage-activated Na⁺, K⁺, and Ca²⁺ conductances distributed uniformly throughout the dendritic tree, together with a stochastic I_h channel model distributed exponentially to mimic the experimentally observed increase in I_h current density with distance from the soma (Fig. 1B). Addition of I_h

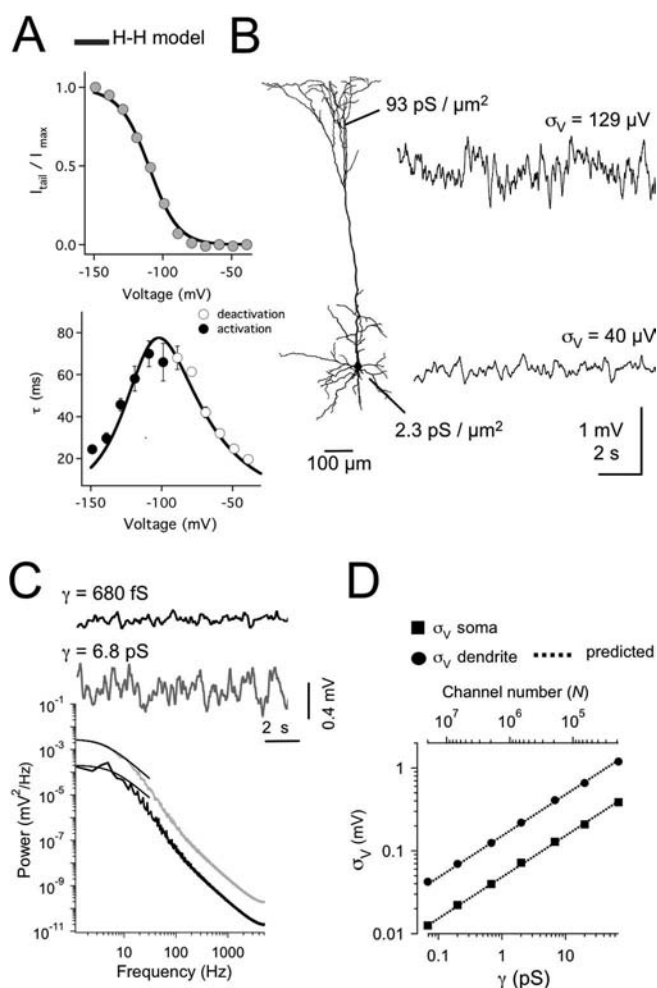


Figure 6. Impact of I_h channel single-channel conductance on voltage noise in a model. **A**, Modeling of I_h kinetics using Hodgkin–Huxley (H–H) formalism. Steady-state voltage-activation curve (top) and the voltage dependence of activation (weighted single time constant; filled circles, bottom) together with the predictions from the Hodgkin–Huxley I_h model (lines). **B**, Left, Morphology of the compartmental layer 5 neuron. Conductance densities at the soma and a distal dendritic location, together with representative examples (right) of the resting membrane potential at the soma (-79 mV ; bottom trace) and distal dendrites (-63 mV ; $1000 \mu\text{m}$ from the soma; top trace) using a model with single-channel conductance γ of 680 fS. **C**, The power of somatic membrane potential fluctuations versus frequency for models with γ of 680 fS (black) and 6.8 pS (gray). Data fitted with a Lorentzian function (see Materials and Methods) from 1 to 30 Hz giving a cutoff frequency f_c of 6.0 and 4.2 Hz, respectively, in the models with γ of 680 fS and 6.8 pS. **D**, The SD of the resting membrane potential σ_V plotted against γ and total N used in the simulations. The squares represent σ_V at the soma and the circles σ_V at a dendritic position $1000 \mu\text{m}$ from the soma. The lines are the predicted relationship between σ_V and γ (see Materials and Methods).

depolarized the soma by 10 to -79 mV and set the membrane potential in the very distal tuft branches to -65 mV . This effect of I_h on the resting membrane potential was quantitatively similar to experimentally observed changes in membrane potential with distance from the soma (supplemental Fig. S1, available at www.jneurosci.org as supplemental material).

We first performed simulations using I_h channels with a single-channel conductance of 680 fS, the experimentally determined value. Figure 6B shows that, using this model, small fluctuations in somatic membrane potential occur with a σ_V of 40 μV (Fig. 6B, bottom trace). As expected, because of the higher density of I_h in distal dendrites, as well as their small diameter, fluctuations in membrane potential at distal dendritic locations

(1000 μm from the soma) were significantly larger than at the soma, with σ_V being 129 μV (Fig. 6B, top trace). We next performed simulations with a single-channel conductance of 6.8 pS, 10-fold greater than observed experimentally while maintaining the same current density by scaling down N . Note that 6.8 pS is still in the low range compared with the single-channel conductance of most other ion channels (Hille, 2001). Increasing the I_h single-channel conductance, γ , to 6.8 pS increased σ_V to 129 μV at the soma (Fig. 6C, bottom, gray trace) and up to 408 μV in dendritic compartments ~ 1000 μm from the soma (data not shown). Analysis of the PSD of voltage fluctuations indicated that this increase in membrane noise was similar at all frequencies of the power spectrum (Fig. 6C). The cutoff frequency of the PSD was slightly lower at the soma than in the dendrites (~ 5 vs ~ 8 Hz), presumably because of greater “filtering” of voltage fluctuations at the soma by the larger somatic capacitance (data not shown).

To compare the voltage noise introduced by I_h with that generated by channel noise from voltage-activated Na^+ channels, we performed simulations using a stochastic Na^+ channel model with $\gamma_{\text{Na}} = 10$ pS. In these simulations, we used a deterministic I_h model to allow us to isolate the contribution of voltage-activated Na^+ channels to membrane noise independent of I_h channel noise. At resting membrane potentials, stochastic Na^+ channels generated membrane noise with $\sigma_V = 7.3$ μV at the soma, significantly smaller than the observed $\sigma_V = 40$ μV in models with stochastic I_h channel ($\gamma = 680$ fS). In dendritic compartments ~ 1000 μm from the soma, σ_V increased to 47 μV (compared with 129 μV for I_h channels). These data indicate that, at resting membrane potentials, the voltage noise attributable to stochastic gating of I_h channels is significantly larger than that mediated by Na^+ channels.

Despite the uniform dendritic Na^+ channel density in the model, the Na^+ channel voltage noise was greatest at distal dendritic locations. Given recent experimental evidence that Na^+ channel noise is greater at depolarized potentials (Jacobson et al., 2005), we reasoned that the larger membrane fluctuations at distal dendritic locations were generated by increased activation of voltage-dependent Na^+ channels as a consequence of the depolarizing action of nonuniform I_h (supplemental Fig. S1, available at www.jneurosci.org as supplemental material). Consistent with this idea, when the I_h density in our model was set to be low and uniform, leading to a homogeneous resting potential of -83 mV, the σ_V of Na^+ channel-induced membrane noise was 2.7 μV in both distal dendritic and somatic compartments. This suggests a dual role for I_h on membrane noise in the distal dendrites: increasing membrane noise via the high density of distal dendritic I_h channels, as well as via depolarization-induced activation of dendritic Na^+ channels.

The relationship between γ , N , and σ_V is depicted in a log–log plot in Figure 6D. Previous theoretical work indicates that the current variance, σ_I^2 , is proportional to N and the square of γ (White et al., 2000; Diba et al., 2004). Consistent with this idea, the observed change in σ_V was well predicted by the expected change in current noise, with σ_V proportional to the square root of γ (Fig. 6D). These simulations indicate that the impact of I_h single-channel conductance on voltage noise follows known theoretical descriptions of the contribution of single-channel properties to current noise. From this, it follows that, for a given current density, reducing I_h single-channel conductance, rather than channel number, is the most effective means to reduce the impact of stochastic gating of I_h on membrane noise.

Impact of I_h channel noise on action potential fidelity

To assess the functional implications of I_h channel noise, we first analyzed the probability and timing of AP generation in response to weak periodic suprathreshold inputs. A small sinusoidal current (3 Hz; 4 pA peak-to-peak) was injected into the soma together with a larger DC adjusted to elicit one AP per sine-wave cycle in models with deterministic I_h . These current injections elicited, on average, one AP per sine-wave cycle in models with stochastic I_h with a single-channel conductance, γ , of 680 fS (Fig. 7A). The ability to detect the sinusoidal signal (the SNR) was quantified from the 3 Hz peak in the PSD (see Materials and Methods). The temporal precision of AP output was quantified from the SD of the temporal jitter in AP timing (σ_t) (Fig. 7A). Increasing γ 10-fold to 6.8 pS led to an increase in AP failures and spontaneous APs not phase locked to the peak of the weak input signal (Fig. 7B), leading to a decrease in both the SNR (Fig. 7C, black diamonds) and temporal precision (Fig. 7C, blue diamonds). Systematic variation of γ between 0.4 and 400 pS showed that, as γ increases, there is an ~ 100 -fold decrease in SNR and a qualitatively similar decrease in temporal precision (Fig. 7C, diamonds).

Can the detection of subthreshold periodic signals, however, be facilitated by membrane noise via stochastic resonance (Wiesenfeld et al., 1994; Wiesenfeld and Moss, 1995; Stacey and Durand, 2000)? To examine the impact of I_h channel noise on stochastic resonance, the amplitude of DC injected into the soma was adjusted so that small sinusoidal currents (3 Hz; 4 pA peak-to-peak) were just subthreshold in models with deterministic I_h . In models with stochastic I_h , these current injections elicited stochastic resonance, with the SNR dependent on the amplitude of the I_h single-channel conductance, γ (Fig. 7C). In the example shown in Figure 7C (red circles), the SNR peaked in I_h models in which γ was ~ 10 pS. According to classical stochastic resonance theory (Wiesenfeld and Moss, 1995), the SNR peak is expected at half of the threshold barrier height (ΔU). Consistent with this expectation, reducing ΔU by using larger DCs, which brings subthreshold sinusoidal currents closer to AP threshold, led to SNR peaks at smaller values of γ (e.g., < 1 pS; data not shown). Decreasing the amplitude of sinusoidal currents from 4 to 1 pA with identical values of ΔU resulted in SNR peaks at approximately the same value of γ but smaller SNR amplitude. These findings indicate that, although detection of small periodic signals can be improved by voltage noise from stochastic gating of I_h channels, the optimal I_h single-channel conductance critically depends on the characteristics of the signal that is to be detected.

We also investigated the impact of I_h channel noise on AP output during EPSPs of varying amplitude located 400 μm from the soma (Fig. 7D–F). For all EPSP amplitudes, ~ 25 trials were repeated while changing only the values for the random number generator used to generate stochastic gating of simulated I_h channels. In models with γ of 680 fS, the variance in spike timing was small ($\sigma_t \leq 1$ ms), and the precision ($1/\sigma_t$) increased linearly with synaptic strength (Fig. 7E, black diamonds). In comparison, considerable more jittering in AP latency was observed in models with γ of 6.8 pS, and precision increased only weakly with EPSP amplitude (Fig. 7E, blue circles). Simulations with stochastic Na^+ channels, but deterministic I_h channels, indicated that stochastic gating of Na^+ channels introduces similar reductions in temporal precision to that seen in models with stochastic I_h with γ of 6.8 pS (Fig. 7E, open circles).

The reduced precision of AP generation in models with larger I_h channel noise was associated with a shallower slope of the input–output relationship of EPSP amplitude versus the proba-

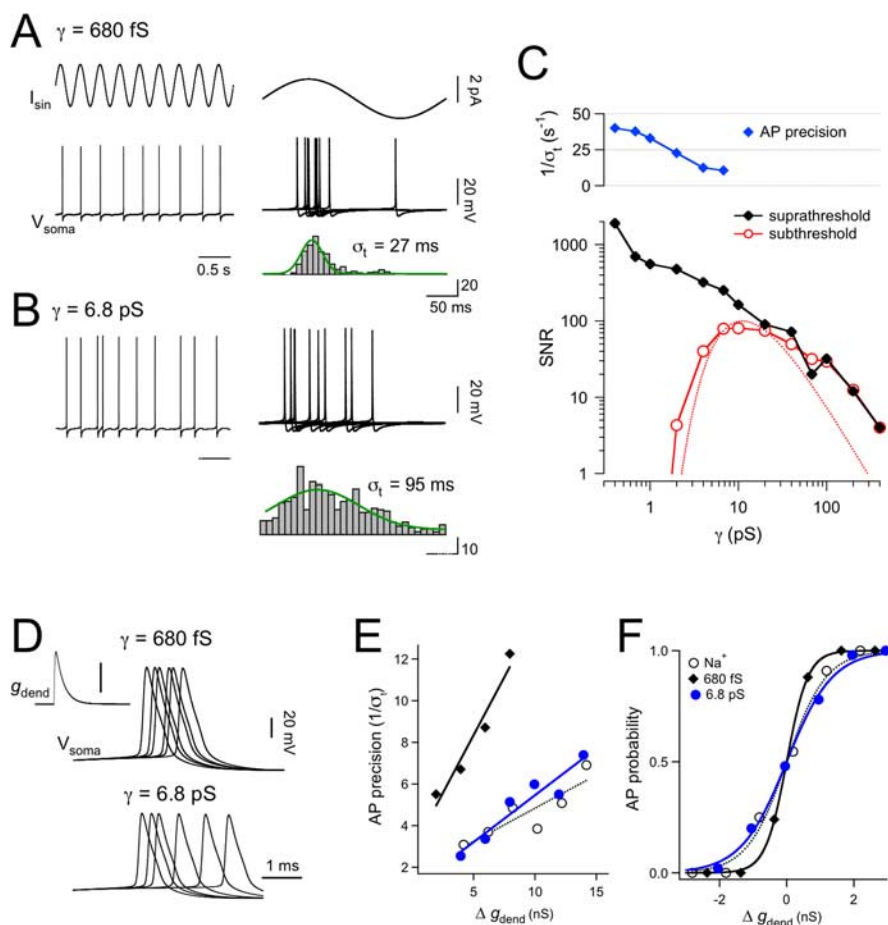


Figure 7. Impact of I_h single-channel noise on the fidelity of AP output in the model. **A**, Somatic injection of a small suprathreshold sinusoidal current signal ($I_{\text{sin}} = 4$ pA; 3 Hz; top trace) elicited, on average, one AP per sine-wave cycle (bottom trace) in a model with γ of 680 fS. Right, Superimposed responses on an expanded time scale. Bottom, Histogram of AP onset latency relative to the phase of the sine wave for 400 consecutive sine-wave cycles. Data were fitted with a Gaussian function (green line) with SD σ_t . **B**, Corresponding plots as in **A** but with increased γ to 6.8 pS. Note the threefold increase in AP jitter. **C**, SNR determined from the 3 Hz peak in the power-spectrum density, and temporal precision (blue diamonds, $1/\sigma_t$) are plotted as a function of γ (range, 0.4–400 pS). Subthreshold sinusoidal current injections (red; $I_{\text{sin}} = 4$ pA) and suprathreshold injections (black; $I_{\text{sin}} = 4$ pA) were analyzed for stochastic resonance. The dotted lines are fits according to stochastic resonance theory (see Materials and Methods). **D**, Superimposed sweeps of APs evoked by a simulated excitatory synaptic conductance (g_{dend} ; left trace; calibration bar, 60 nS) injected 400 μm from the soma in models with single-channel conductance γ of 680 fS (top) and 6.8 pS (bottom). Note the larger trial-to-trial variability (jittering) in models with large γ . **E**, Spike precision defined as $1/\sigma$ and plotted versus the change in amplitude of the excitatory synaptic conductance in models with γ of 680 fS (black diamonds) and 6.8 pS (blue circles). For comparison, a model with deterministic I_h and stochastic Na^+ channels with $\gamma_{\text{Na}} = 10$ pS is shown (open circles). **F**, Input–output relationship showing the probability of AP generation versus the change in amplitude of the excitatory synaptic conductance in models with $\gamma = 680$ fS (black line; steepness of the sigmoid fit, $s = 0.31$ nS) and $\gamma = 6.8$ pS (blue line; $s = 0.68$ nS). For comparison, a model with deterministic I_h and stochastic Na^+ channels with $\gamma_{\text{Na}} = 10$ pS is shown (open circles; $s = 0.59$ nS).

bility of AP generation (Fig. 7F). A change in slope of this input–output function indicates that models with higher I_h single-channel conductance have a larger threshold uncertainty (White et al., 2000). Simulations with stochastic Na^+ channels but deterministic I_h channels also showed a larger threshold uncertainty (Fig. 7F, open circles). Note that the change in the input–output function during EPSPs in models with stochastic I_h did not translate into a change in slope of the AP firing frequency (f) versus input current (I) relationship (f/I curve) during long (1 s) pulses (data not shown). This was presumably the case because the level of background noise generated by stochastic gating of I_h ($\text{SD} < 1$ mV) was too small to cause a change in f/I gain, as observed by others during balanced synaptic noise (Chance et al., 2002).

Discussion

Using NSFA of native I_h currents combined with simulations of their biophysical properties, we provide, to our knowledge, the first estimation of the single-channel properties of I_h channels in the brain *in situ*. To explore the precision of NSFA, we analyzed simulated I_h currents with predetermined single-channel properties and studied the impact of filtering, indicating a high stability of the extracted single-channel parameters, as well as little if any channel flicker. Indeed, the observed unitary conductance of I_h of 680 fS is in good agreement with the previous estimate of 980 fS for I_f in the sinoatrial node of the heart (DiFrancesco, 1986). We go on to show both experimentally and in simulations that stochastic openings of I_h generate voltage noise, which impacts on the fidelity of action potential output.

Comparisons with previous studies

Although our data provide compelling evidence for small-conducting I_h channels, a recent study in acutely dissociated CA1 pyramidal neurons using excised patches from the soma has proposed a >10-fold higher single-channel conductance of 10 pS (Simeone et al., 2005). Such large single-channel openings (~ 1 pA), however, were not observed in previous cell-attached studies of native I_h currents in CA1 pyramidal neurons (Magee, 1998). In addition, it is also unclear how I_h currents were observed at all in the study of Simeone et al. (2005), given the evidence that I_h is very sensitive to enzymatic procedures for acute dissociation (Budde et al., 1994). Our findings in brain slices are also at odds with estimates of HCN single-channel conductance based on heterologously expressed HCN subunits (2.5–35 pS) (Johnson and Zagotta, 2005; Michels et al., 2005). Although the explanation for these discrepancies are also unclear, a number of proteins are known to interact with HCN subunits, such as Filamin A or TRIP8b (Gravante et al., 2004; Santoro et al., 2004). Additional experiments will be needed to address whether interaction of these proteins with HCN channels leads to modification of channel properties, such as single-channel conductance. Given this possibility, it is worth noting that the studies that used cell-attached recording configuration (the present study) (DiFrancesco, 1986) consistently observed a small single-channel conductance < 1 pS. This may suggest that excised patch-clamp recordings disturb the single-channel properties of I_h , perhaps via removal of accessory or loss of interactions between HCN channels and critical cytosolic proteins.

I_h channel noise

Given the wide spectrum of observed unitary conductances for voltage-dependent channels (from ~ 1 to 300 pS) (Hille, 2001),

we asked why is the single-channel conductance of I_h so small? A growing number of studies indicate that noise generated by random channel opening limits neuronal response reliability (Schneidman et al., 1998; White et al., 2000), influences the energy efficiency of channels (Schreiber et al., 2002), and constrains the physical dimensions of axon diameters (Faisal et al., 2005). Conversely, noise can have a beneficial role by enhancing the detection of weak periodic signals via a stochastic resonance mechanism (Wiesenfeld and Moss, 1995) or via enhancing sub-threshold oscillations (Dorval and White, 2005). Based on these studies, it seems likely that the magnitude of channel noise is under evolutionary pressure in biological systems seeking energy-efficient coding systems (Laughlin and Sejnowski, 2003). We show here that native I_h channels generate between ~ 40 and $130 \mu\text{V}$ of voltage noise (rms) spatially distributed from the soma to distal dendrites, with most of the power below 10 Hz (Figs. 5, 6). Although most recent studies have focused on the role of stochastic openings of Na^+ channels (Schneidman et al., 1998; Diba et al., 2004; Dorval and White, 2005; Faisal et al., 2005; Jacobson et al., 2005), we propose that I_h is also likely to be an important source of intrinsic channel noise in neurons. This would be expected to be the case for a number of reasons. First, channel noise is greater for voltage-dependent channels, like I_h , that have slow activation kinetics (Diba et al., 2004). Second, channel noise increases linearly with channel number (Diba et al., 2004), and, as we show, I_h channel densities can be very high, particularly at distal dendritic locations (Fig. 4). Third, channel noise would be expected to lead to larger voltage noise in smaller compartments in which I_h channel densities are maximal. Finally, the depolarizing gradient generated by I_h will enhance Na^+ channel noise. These observations indicate that the dynamic interplay between I_h and Na^+ channel noise will need to be considered in future studies investigating the impact of membrane noise in neuronal computation.

Functional implications of I_h channel gating on action potential output

We asked whether I_h noise is large enough to impact on AP output. This was shown to be the case both for perithreshold weak periodic stimuli and single EPSPs (Fig. 7). In models with high I_h single-channel conductance (6.8 pS), larger AP jitter and lower phase reliability were observed compared with models with the experimentally observed I_h single-channel conductance of 680 fS. In contrast to these negative aspects of I_h noise, models with stochastic I_h also showed stochastic resonance for very weak (1–4 pA) oscillatory inputs. Whether such noise-enhanced signal detection is functionally relevant in cortical layer 5 pyramidal neurons is presently unclear, because, under *in vivo* conditions, it seems likely that voltage noise will be dominated by the large fluctuations of ongoing, spatially distributed, synaptic activity at dendritic sites (Destexhe et al., 2003). Furthermore, although I_h noise could improve detection of weak sinusoidal signals, the optimal single-channel conductance was critically dependent on the characteristics of the input signal to be detected. Thus, it seems unlikely that stochastic resonance mechanisms have worked as a selection factor for I_h single-channel conductance. Rather, our results suggest that such selection, favoring small-conducting I_h channels, is more likely to depend on the influence of stochastic channel noise on the reliability of spike timing (Fig. 7C, top, E, F).

Although our studies concentrate on cortical layer 5 pyramidal neurons, which express I_h channels primarily in their dendrites, many of the results can be generalized in other neuronal

and cell types. For example, expression of I_h in small-diameter compartments such as axons (Notomi and Shigemoto, 2004) would be expected to increase channel noise and limit the axonal conduction reliability (Faisal et al., 2005). In addition, because the magnitude of channel noise is further increased by slower channel activation kinetics (Diba et al., 2004), it seems likely that spike-time jitter will be even greater in cells in which HCN activation is slower, such as in the cardiac cells (DiFrancesco, 1984) and thalamic relay neurons (McCormick and Pape, 1990). Such predictions remain to be tested.

Given that theoretical relationships indicate that current noise is linearly dependent on single-channel number but changes with the square root of channel conductance (White et al., 2000; Diba et al., 2004), reducing single-channel conductance is an efficient means to reduce membrane noise attributable to stochastic channel gating. This result may well explain the small single-channel conductance of I_h channels in the brain and suggests that the single-channel conductance of I_h is evolutionarily constrained to be small to reduce its impact on both membrane noise and AP output.

In conclusion, our results indicate that native I_h channels in the brain have a small single-channel conductance, comparable in size with the single-channel conductance of I_f in the heart, which is likely to be critical for reducing membrane noise attributable to stochastic gating, thereby maintaining the fidelity of temporal patterns of AP output.

References

- Alvarez O, Gonzalez C, Latorre R (2002) Counting channels: a tutorial guide on ion channel fluctuation analysis. *Adv Physiol Educ* 26:327–341.
- Berger T, Larkum ME, Luscher H-R (2001) High I_h channel density in the distal apical dendrite of layer V pyramidal cells increases bidirectional attenuation of EPSPs. *J Neurophysiol* 85:855–868.
- Biel M, Schneider A, Wahl C (2002) Cardiac HCN channels: structure, function, and modulation. *Trends Cardiovasc Med* 12:206–212.
- BoSmith RE, Briggs I, Sturgess NC (1993) Inhibitory actions of ZENECA ZD7288 on whole-cell hyperpolarization activated inward current (I_f) in guinea-pig dissociated sinoatrial node cells. *Br J Pharmacol* 110:343–349.
- Brown HF, DiFrancesco D, Noble SJ (1979) How does adrenaline accelerate the heart? *Nature* 280:235–236.
- Budde T, White JA, Kay AR (1994) Hyperpolarization-activated Na^+ - K^+ current (I_h) in neocortical neurons is blocked by external proteolysis and internal TEA. *J Neurophysiol* 72:2737–2742.
- Chance FS, Abbott LF, Reyes AD (2002) Gain modulation from background synaptic input. *Neuron* 35:773–782.
- Colquhoun D, Hatton CJ, Hawkes AG (2003) The quality of maximum likelihood estimates of ion channel rate constants. *J Physiol (Lond)* 547:699–728.
- Conti F, Neumcke B, Nonner W, Stämpfli R (1980) Conductance fluctuations from the inactivation process of sodium channels in myelinated nerve fibres. *J Physiol (Lond)* 308:217–239.
- DeFelice LJ (1981) Introduction to membrane noise. New York: Plenum.
- Destexhe A, Rudolph M, Pare D (2003) The high-conductance state of neocortical neurons *in vivo*. *Nat Rev Neurosci* 4:739–751.
- Diba K, Lester HA, Koch C (2004) Intrinsic noise in cultured hippocampal neurons: experiment and modeling. *J Neurosci* 24:9723–9733.
- DiFrancesco D (1984) Characterization of the pace-maker current kinetics in calf Purkinje fibres. *J Physiol (Lond)* 348:341–367.
- DiFrancesco D (1986) Characterization of single pacemaker channels in cardiac sino-atrial node cells. *Nature* 324:470–473.
- Dorval Jr AD, White JA (2005) Channel noise is essential for perithreshold oscillations in entorhinal stellate neurons. *J Neurosci* 25:10025–10028.
- Engel D, Jonas P (2005) Presynaptic action potential amplification by voltage-gated Na^+ channels in hippocampal mossy fiber boutons. *Neuron* 45:405–417.
- Faisal AA, White JA, Laughlin SB (2005) Ion-channel noise places limits on the miniaturization of the brain's wiring. *Curr Biol* 15:1143–1149.
- Gravante B, Barbuti A, Milanese R, Zappi I, Viscomi C, DiFrancesco D

- (2004) Interaction of the pacemaker channel HCN1 with filamin A. *J Biol Chem* 279:43847–43853.
- Gulledge AT, Stuart GJ (2003) Excitatory actions of GABA in the cortex. *Neuron* 37:299–309.
- Halliwel JV, Adams PR (1982) Voltage-clamp analysis of muscarinic excitation in hippocampal neurons. *Brain Res* 250:71–92.
- Häusser M, Roth A (1997) Estimating the time course of the excitatory synaptic conductance in neocortical pyramidal cells using a novel voltage jump method. *J Neurosci* 17:7606–7625.
- Hestrin S (1987) The properties and function of inward rectification in rod photoreceptors of the tiger salamander. *J Physiol (Lond)* 390:319–333.
- Hille B (1978) Ionic channels in excitable membranes. Current problems and biophysical approaches. *Biophys J* 22:283–294.
- Hille B (2001) Ion channels of excitable membranes, Ed 3. Sunderland, MA: Sinauer.
- Hines ML, Carnevale NT (2000) Expanding NEURON's repertoire of mechanisms with NMODL. *Neural Comput* 12:995–1007.
- Hodgkin AL, Huxley AF (1952) A quantitative description of membrane current and its application to conduction and excitation in nerve. *J Physiol (Lond)* 117:500–544.
- Jacobson GA, Diba K, Yaron-Jakobovitch A, Oz Y, Koch C, Segev I, Yarom Y (2005) Subthreshold voltage noise of rat neocortical pyramidal neurons. *J Physiol (Lond)* 564:145–160.
- Johnson Jr JP, Zagotta WN (2005) The carboxyl-terminal region of cyclic nucleotide-modulated channels is a gating ring, not a permeation path. *Proc Natl Acad Sci USA* 102:2742–2747.
- Laughlin SB, Sejnowski TJ (2003) Communication in neuronal networks. *Science* 301:1870–1874.
- Lorincz A, Notomi T, Tamas G, Shigemoto R, Nusser Z (2002) Polarized and compartment-dependent distribution of HCN1 in pyramidal cell dendrites. *Nat Neurosci* 5:1185–1193.
- Ludwig A, Zong X, Jeglitsch M, Hofmann F, Biel M (1998) A family of hyperpolarization-activated mammalian cation channels. *Nature* 393:587–591.
- Magee JC (1998) Dendritic hyperpolarization-activated currents modify the integrative properties of hippocampal CA1 pyramidal neurons. *J Neurosci* 18:7613–7624.
- McCormick DA, Pape HC (1990) Properties of a hyperpolarization-activated cation current and its role in rhythmic oscillation in thalamic relay neurons. *J Physiol (Lond)* 431:291–318.
- Michels G, Er F, Khan I, Südkamp M, Herzig S, Hoppe UC (2005) Single-channel properties support a potential contribution of hyperpolarization-activated cyclic nucleotide-gated channels and I_f to cardiac arrhythmias. *Circulation* 111:399–404.
- Notomi T, Shigemoto R (2004) Immunohistochemical localization of I_h channel subunits, HCN1–4, in the rat brain. *J Comp Neurol* 471:241–276.
- Press WH (2002) Numerical recipes in C++: the art of scientific computing, Ed 2. Cambridge, UK: Cambridge UP.
- Robinson RB, Siegelbaum SA (2003) Hyperpolarization-activated cation currents: from molecules to physiological function. *Annu Rev Physiol* 65:453–480.
- Santoro B, Tibbs GR (1999) The HCN gene family: molecular basis of the hyperpolarization-activated pacemaker channels. *Ann NY Acad Sci* 868:741–764.
- Santoro B, Liu DT, Yao H, Bartsch D, Kandel ER, Siegelbaum SA, Tibbs GR (1998) Identification of a gene encoding a hyperpolarization-activated pacemaker channel of brain. *Cell* 93:717–729.
- Santoro B, Wainger BJ, Siegelbaum SA (2004) Regulation of HCN channel surface expression by a novel C-terminal protein–protein interaction. *J Neurosci* 24:10750–10762.
- Schaefer AT, Larkum ME, Sakmann B, Roth A (2003) Coincidence detection in pyramidal neurons is tuned by their dendritic branching pattern. *J Neurophysiol* 89:3143–3154.
- Schneidman E, Freedman B, Segev I (1998) Ion channel stochasticity may be critical in determining the reliability and precision of spike timing. *Neural Comput* 10:1679–1703.
- Schreiber S, Machens CK, Herz AV, Laughlin SB (2002) Energy-efficient coding with discrete stochastic events. *Neural Comput* 14:1323–1346.
- Sigworth FJ (1980) The variance of sodium current fluctuations at the node of Ranvier. *J Physiol (Lond)* 307:97–129.
- Simeone TA, Rho JM, Baram TZ (2005) Single channel properties of hyperpolarization-activated cation currents in acutely dissociated rat hippocampal neurons. *J Physiol (Lond)* 568:371–380.
- Stacey WC, Durand DM (2000) Stochastic resonance improves signal detection in hippocampal CA1 neurons. *J Neurophysiol* 83:1394–1402.
- Stuart G, Spruston N (1998) Determinants of voltage attenuation in neocortical pyramidal neuron dendrites. *J Neurosci* 18:3501–3510.
- Stuart GJ, Sakmann B (1994) Active propagation of somatic action potentials into neocortical pyramidal cell dendrites. *Nature* 367:69–72.
- Wainger BJ, DeGennaro M, Santoro B, Siegelbaum SA, Tibbs GR (2001) Molecular mechanism of cAMP modulation of HCN pacemaker channels. *Nature* 411:805–810.
- White JA, Rubinstein JT, Kay AR (2000) Channel noise in neurons. *Trends Neurosci* 23:131–137.
- Wiesenfeld K, Moss F (1995) Stochastic resonance and the benefits of noise: from ice ages to crayfish and SQUIDS. *Nature* 373:33–36.
- Wiesenfeld K, Pierson D, Pantazelou E, Dames C, Moss F (1994) Stochastic resonance on a circle. *Phys Rev Lett* 72:2125–2129.
- Williams SR, Stuart GJ (2000) Site independence of EPSP time course is mediated by dendritic I_h in neocortical pyramidal neurons. *J Neurophysiol* 83:3177–3182.
- Williams SR, Stuart GJ (2003) Voltage- and site-dependent control of the somatic impact of dendritic IPSPs. *J Neurosci* 23:7358–7367.
- Zagotta WN, Olivier NB, Black KD, Young EC, Olson R, Gouaux E (2003) Structural basis for modulation and agonist specificity of HCN pacemaker channels. *Nature* 425:200–205.

3.3 Schmid*, Hallermann* *et al.*, 2008, Nat Neurosci, 11:659-666

Seite 35-42

Activity-dependent site-specific changes of glutamate receptor composition *in vivo*

Andreas Schmid^{1-3,5}, Stefan Hallermann^{1,4,5}, Robert J Kittel^{1,3,4}, Omid Khorramshahi^{1,2}, Andreas M J Frölich³, Christine Quentin¹⁻³, Tobias M Rasse³, Sara Mertel¹⁻³, Manfred Heckmann^{1,4} & Stephan J Sigrist¹⁻³

The subunit composition of postsynaptic non-NMDA-type glutamate receptors (GluRs) determines the function and trafficking of the receptor. Changes in GluR composition have been implicated in the homeostasis of neuronal excitability and synaptic plasticity underlying learning. Here, we imaged GluRs *in vivo* during the formation of new postsynaptic densities (PSDs) at *Drosophila* neuromuscular junctions coexpressing GluRIIA and GluRIIB subunits. GluR composition was independently regulated at directly neighboring PSDs on a submicron scale. Immature PSDs typically had large amounts of GluRIIA and small amounts of GluRIIB. During subsequent PSD maturation, however, the GluRIIA/GluRIIB composition changed and became more balanced. Reducing presynaptic glutamate release increased GluRIIA, but decreased GluRIIB incorporation. Moreover, the maturation of GluR composition correlated in a site-specific manner with the level of Bruchpilot, an active zone protein that is essential for mature glutamate release. Thus, we show that an activity-dependent, site-specific control of GluR composition can contribute to match pre- and postsynaptic assembly.

Synapse formation and maturation are highly regulated, multi-step processes that require bidirectional communication across the synaptic cleft^{1,2}. Neurotransmitter receptors are enriched in the PSD, a specialized membrane microdomain located opposite the active zones³ of presynaptic terminals, where transmitter release occurs. Mechanisms matching pre- and postsynaptic structure and function during synapse maturation are subjects of intense research. Notably, alterations in the postsynaptic receptor subunit composition are important for the developmental maturation of cholinergic mouse endplates⁴, as well as GABAergic and glutamatergic central synapses⁵.

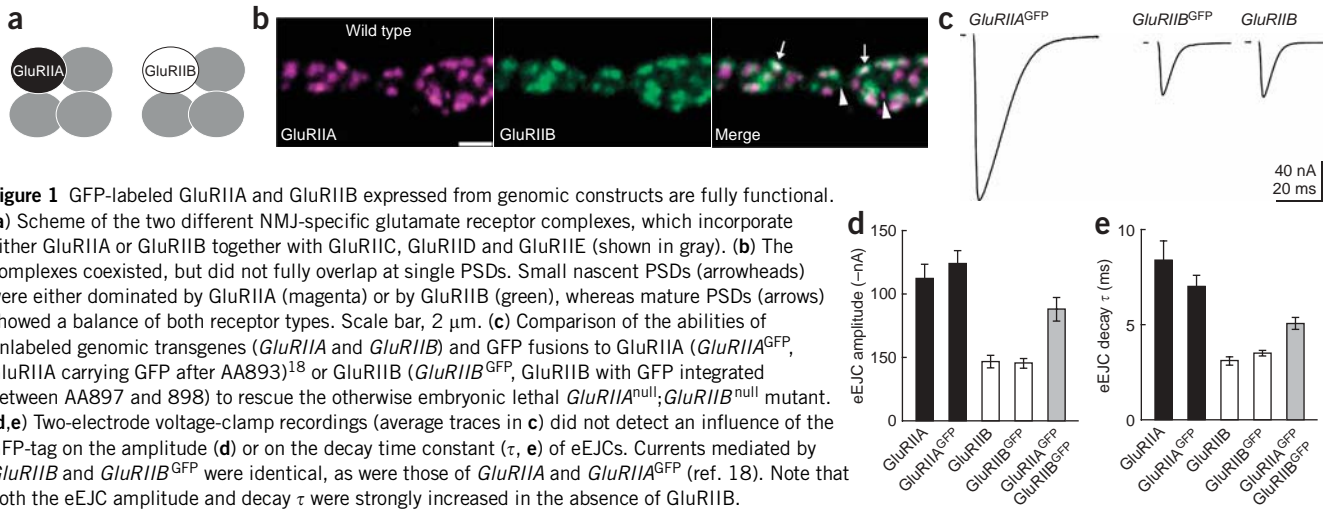
Glutamatergic synapses dominate excitatory transmission in the brain, and changes in the composition of synaptic GluRs mediate learning-related potentiation or depression events⁶ and operate in homeostatic controls of excitability⁷. Finally, glutamatergic synapse numbers change during development and during learning-related long-term plasticity. The question of how cell-wide and synapse-specific mechanisms are linked *in vivo* to integrate these processes remains unanswered.

At the *Drosophila* neuromuscular junction (NMJ), ionotropic glutamate receptors mediate the postsynaptic response to glutamate⁸⁻¹⁰. These receptors appear to assemble as heteromeric tetramers by selecting from five subunits (Fig. 1a)¹¹⁻¹³. Three of these subunits, GluRIIC, IID and IIE are essential for receptor formation and function (Fig. 1a). Each receptor also includes a fourth subunit,

which can be either GluRIIA or GluRIIB (Fig. 1a). These two receptor types differ in their single channel properties, which lead to large (at GluRIIB-lacking NMJs, referred to as GluRIIA-NMJs) or small (at GluRIIA-lacking NMJs, or GluRIIB-NMJs) glutamate-gated currents¹⁴⁻¹⁶. Glutamate receptor composition also controls the morphological size of the NMJ and the number of individual synaptic contacts^{16,17} (defined as a single presynaptic active zone opposite a PSD, referred to here as 'synapse'). Our previous analysis showed that immature PSDs typically form at a distance from existing synapses and then grow until reaching a stable mature size in several hours¹⁸.

We analyzed the *in vivo* dynamics of GluRIIA and GluRIIB complexes during PSD maturation at developing NMJs. GluR incorporation was controlled on the level of individual PSDs. During PSD maturation, presynaptic glutamate release shaped GluR composition. Notably, a GluRIIA- and Ca²⁺-mediated retrograde signal has previously been identified at NMJ synapses, which adapts presynaptic release to postsynaptic sensitivity homeostatically^{9,19,20}. The regulation described here may act in concert with this retrograde signal to enable effective integration of pre- and postsynaptic assembly. Moreover, as GluR composition also controls the number of PSDs formed per NMJ^{16,17,21}, our results show how cell-wide structural synaptic plasticity may be coordinated with short-lived forms of plasticity at individual synapses.

¹Institute for Clinical Neurobiology, Medical Faculty, University of Würzburg, Zinklesweg 10, 97080 Würzburg, Germany. ²Rudolf Virchow Center, Deutsche Forschungsgemeinschaft Research Center for Experimental Biomedicine, University of Würzburg, Versbacher Str. 9, 97078 Würzburg, Germany. ³European Neuroscience Institute-Göttingen, University of Göttingen, Grisebachstr. 5, 37077 Göttingen, Germany. ⁴Carl Ludwig Institute of Physiology Medical Faculty, University of Leipzig, Liebigstr. 27, 04103 Leipzig, Germany. ⁵These authors contributed equally to this work. Correspondence should be addressed to S.J.S. (stephan.sigrist@virchow.uni-wuerzburg.de).



RESULTS

Endogenous GluRIIB and GluRIIA are differentially localized on the level of individual PSDs (Fig. 1b)¹³. To study the principles of PSD formation at the *Drosophila* NMJ *in vivo*, we previously expressed a GFP-labeled GluRIIA subunit (*GluRIIA*^{GFP}) using its endogenous promoter¹⁸. This construct rescued the otherwise lethal *GluRIIA*^{null}, *GluRIIB*^{null} mutant and restored large evoked junctional currents (eEJC amplitude: *GluRIIA*, -112.6 ± 11.1 nA, $n = 9$; *GluRIIA*^{GFP}, -124.3 ± 10.0 nA, $n = 9$; $P = 0.45$) with slow decay kinetics, as are typical for GluRIIA-NMJs (eEJC decay τ : *GluRIIA*, 8.4 ± 1.1 ms, $n = 9$; *GluRIIA*^{GFP}, 7.0 ± 0.6 ms, $n = 9$; $P = 0.40$; Fig. 1c–e)¹⁸. A similarly constructed *GluRIIB*^{GFP} also rescued the *GluRIIA*^{null}/*GluRIIB*^{null} mutant (GluRIIB 50% and *GluRIIB*^{GFP} 55% of expected Mendelian ratio, $n > 300$) and restored the small evoked postsynaptic currents (*GluRIIB*, -47 ± 5 nA, $n = 10$; *GluRIIB*^{GFP}, -46 ± 4 nA, $n = 10$; $P = 0.97$) with fast decay kinetics^{9,14}, as are typical for GluRIIB-NMJs (*GluRIIB*, 3.1 ± 0.2 ms, $n = 10$; *GluRIIB*^{GFP}, 3.5 ± 0.1 ms, $n = 10$; $P = 0.08$; Fig. 1c–e). NMJs coexpressing *GluRIIA*^{GFP} and *GluRIIB*^{GFP} showed intermediate values (eEJC amplitude, -88.3 ± 9.3 nA; eEJC decay τ , 5.1 ± 0.3 ms; $n = 6$).

Miniature excitatory junctional currents (mEJCs) reflect synaptic currents that are mediated by the GluR population present at individual PSDs in response to spontaneously occurring fusions of single vesicles. Patch-clamp recordings from *Drosophila* embryonic muscles^{22,23} deliver excellent signal-to-noise conditions for the examination of even very small mEJCs (Fig. 2). As expected, *GluRIIB*^{GFP}-mediated mEJCs were markedly smaller than those mediated by *GluRIIA*^{GFP} (*GluRIIA*^{GFP}, -132 ± 13 pA, $n = 6$; *GluRIIB*^{GFP}, -40 ± 1.4 pA, $n = 7$; $P = 0.001$; Fig. 2). Taken together, the GFP-labeling strategy fully conserved the specific functional differences between GluRIIA and GluRIIB, with GluRIIA complexes largely dominating post-synaptic currents.

In vivo imaging of GluR composition at the single PSD level

As described, we previously imaged *GluRIIA*^{GFP} *in vivo* to show that new PSDs form independent of existing PSDs¹⁸. To visualize GluRIIA and GluRIIB dynamics *in vivo*, we generated equally functional fusions of GluRIIA and GluRIIB with monomeric red fluorescent protein (mRFP)²⁴ (Fig. 3). Identified NMJs of larvae coexpressing *GluRIIB*^{GFP} and *GluRIIA*^{mRFP} (in the *GluRIIA*^{null}/*GluRIIB*^{null} background) were subjected to repetitive *in vivo* imaging (Fig. 3a). Early third-instar larvae were imaged at 12-h intervals at 25 °C. *In vivo* imaging

showed that small, immature PSDs were typically enriched with GluRIIA (Fig. 3a). During further PSD maturation, however, GluRIIA and GluRIIB levels tended to shift toward a balanced composition (Fig. 3a,c). Notably, GluR composition often changed in opposite directions at directly neighboring PSDs located within less than a micrometer (Fig. 3a).

To ensure that fluorophore choice was not affecting the apparent development of GluR composition, we exchanged GFP and mRFP in a separate experiment to create larvae coexpressing *GluRIIA*^{GFP} and *GluRIIB*^{mRFP}. The development of GluR composition that we then observed was essentially identical to that described above (data not shown).

The *in vivo* GluRIIA and GluRIIB fluorescence signals were processed and the number (N_{IIA} and N_{IIB}) of GluRIIA and GluRIIB complexes was estimated (Supplementary Fig. 1 online; for detailed protocol, see Supplementary Methods online). This estimate is based on the integrated fluorescence intensity of a single PSD in intensity-normalized images and the assumption that a PSD contains, on average, ~ 60 GluRIIA and ~ 60 GluRIIB complexes, as determined by electrophysiological recordings¹⁵. N_{IIA} and N_{IIB} are meant to be proportional (but not necessarily identical) to the real number of GluRs per PSD. Moreover, to allow a symmetrical measure of the contribution of GluRIIA and GluRIIB at a PSD, we calculated the relative difference, $\frac{N_{IIB} - N_{IIA}}{N_{IIA} + N_{IIB}}$. We chose this term because the ‘simple ratio’ (N_{IIA}/N_{IIB}) can range from 0 to 1 (balanced) and from 1 to ∞ . In contrast, the above defined relative difference is symmetrically distributed around 0 at balanced PSDs, -1 at GluRIIA-PSDs and $+1$ at GluRIIB-PSDs. For simplicity, this is referred to as the ratio and is depicted by *GluRIIA* \leftarrow *GluRIIB* in the figures (for example, see Fig. 3b,c).

We analyzed 505 individual PSDs (from 8 NMJs, muscle 27) that were identified at 0 h and were re-identified at 12 h. We plotted the initial status at $t = 0$ of all PSDs in terms of size ($N = N_{IIA} + N_{IIB}$) and ratio (*GluRIIA* \leftarrow *GluRIIB*) (Fig. 3b). GluRIIA levels were typically dominant over GluRIIB levels at immature, small PSDs, whereas GluR levels were typically more balanced at larger, mature PSDs. This became obvious when we plotted the average ratio as a function of the size (Fig. 3b), which showed that the distribution was skewed toward GluRIIA for PSDs with low GluR numbers, but less so for PSDs with high GluR numbers. To illustrate the development of PSDs over 12 h, each PSD was plotted as an arrow, pointing from its initial size and ratio at 0 h to its size and ratio at 12 h (Fig. 3c). PSDs substantially

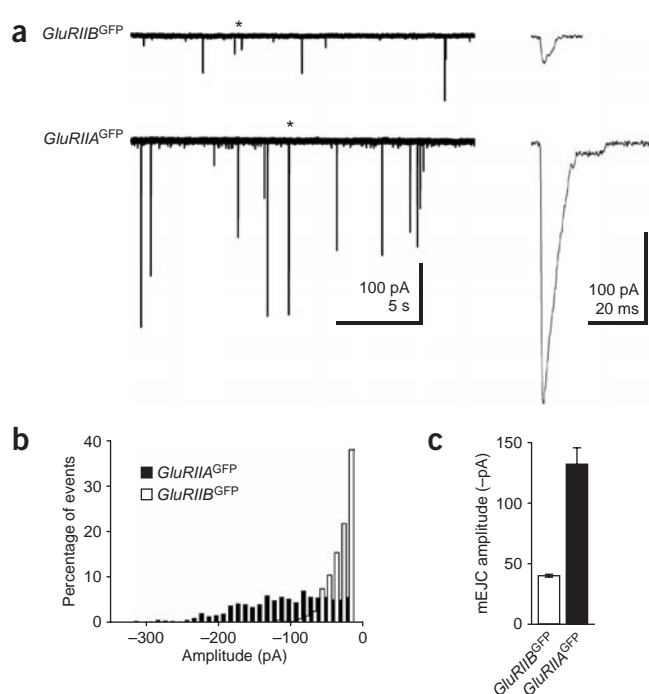


Figure 2 Patch-clamp recordings of NMJs expressing only GluRIIA^{GFP} or GluRIIB^{GFP}. **(a)** Representative traces of mEJCs from whole-cell patch-clamp recordings of GluRIIA^{GFP}- and GluRIIB^{GFP}-rescued embryonic NMJs. **(b,c)** Quantification of the mEJC amplitudes clearly shows the larger postsynaptic sensitivity of GluRIIA^{GFP} rescued NMJs.

increased their GluR numbers (N ; $N_{t=0} = 132 \pm 4$, $N_{t=12} = 177 \pm 5$, $P < 0.0001$), and the small PSDs nearly invariably developed toward a balanced GluRIIB and GluRIIA composition over these 12 h. This was found for both the typical small GluRIIA-rich PSDs and, notably, for the less-frequent small, GluRIIB-rich PSDs (**Fig. 3a**). This shift in GluR composition also became obvious in a histogram plot, where the PSDs at 12 h were no longer skewed toward GluRIIA, as opposed to when they were first identified ($t = 0$ h; **Fig. 3b,d**). Notably, the very small new synapses that first appeared after 12 h ($n = 144$) were, on average, balanced (**Fig. 3e**, see also balanced ratio of smallest PSDs in **Fig. 3b**). Taken together, nascent PSDs began with a heterogeneous and, on average, balanced ratio, but rapidly became rich in GluRIIA during their initial, immature stage of development. With further growth and maturation, however, a balanced receptor composition was reached, apparently irrespective of their initial GluR composition.

In vivo FRAP analysis of GluRIIA and GluRIIB dynamics

We were interested in describing GluR subtype dynamics in detail during synaptic maturation at the level of a single PSD. The extent to which the differential development of PSDs (**Fig. 3**) is determined by differences in the incorporation of receptors into PSDs or by differences in dissociation of receptors from PSDs cannot be derived from the above data. To learn about the PSD incorporation characteristics of GluRIIA and GluRIIB during synaptic maturation, we visualized and bleached GluRIIB^{GFP} and GluRIIA^{mRFP} (coexpressed in the *GluRIIA*^{null};*GluRIIB*^{null} background, *GluRIIB*^{GFP};*GluRIIA*^{mRFP}), and then re-imaged them after 24 h of recovery (**Fig. 4a**). As expected¹⁸, fluorescence recovery after photobleaching (FRAP) of GluRIIA^{mRFP} was strong at a few PSDs (**Fig. 4a**), but faint at the remaining PSDs

(**Fig. 4a**). In contrast, FRAP of GluRIIB^{GFP} appeared to be more uniform over the PSDs. Indeed, quantification indicated a broader FRAP distribution for GluRIIA^{mRFP} than for GluRIIB^{GFP} (**Fig. 4b,c**). To determine whether the choice of the fluorophore affected FRAP behavior, larvae coexpressing GluRIIA^{GFP} and GluRIIB^{mRFP} were imaged as well. We observed an essentially identical difference in the FRAP behavior of GluRIIA and GluRIIB (data not shown).

Thus, GluRIIA incorporation appears to be strongly regulated at the level of individual PSDs and typically decreased with PSD maturation. Incorporation of GluRIIB, in contrast, was more uniform over PSDs and was still ongoing in mature PSDs. Notably, however, the less-frequent small PSDs that were dominated by GluRIIB developed a more homogenous GluR composition over time as well. This observation prompted us to search for a self-regulating element in the maturation of PSD GluR composition.

Glutamate release shapes maturation of GluR composition

As mentioned, GluRIIA and GluRIIB differ strongly in their functional features; GluRIIA receptor clusters mediate a larger ionic current, as their desensitization kinetics are slower than those of GluRIIB (**Figs. 1 and 2**)¹⁴. We speculated that differences in the GluR composition between PSDs should translate into differences in the glutamate-gated current between PSDs, and that these differences might, in turn, steer further GluR incorporation. If so, blocking presynaptic glutamate release might affect the maturation of GluR composition. To test our hypothesis, we expressed tetanus toxin light chain (TNT), which effectively suppresses evoked glutamate release²⁵, in motor neurons with GluRIIA^{mRFP} and GluRIIB^{GFP} for *in vivo* FRAP experiments (**Fig. 4d–f**). In contrast with controls, a higher proportion of PSDs showed GluRIIA-FRAP incorporation after TNT expression (**Fig. 4d**). However, the amount of GluRIIA-FRAP was particularly high in only a subset of synapses (**Fig. 4d**). At the same time, GluRIIB-FRAP signals appeared to be atypically low after TNT expression. In fact, quantification of FRAP signals showed that the relative number of PSDs with low GluRIIA incorporation was reduced after motor neuron-driven TNT expression (compare **Fig. 4b,e**) and that the number of newly incorporated GluRIIA complexes increased after TNT expression, whereas the number of newly incorporated GluRIIB complexes decreased (**Fig. 4e**). As a result, the PSD incorporation profile shifted toward GluRIIA (compare **Fig. 4c,f**), which was also evident in a cumulative plot comparing incorporation profiles with and without TNT (**Fig. 4f**). Thus, suppressing endogenous glutamate release by TNT promoted additional GluRIIA incorporation, but suppressed GluRIIB incorporation. It is reasonable to assume that GluRIIA incorporation might outcompete GluRIIB for PSD slots after suppressing glutamate release. However, as GluRIIB-FRAP was comparable between animals expressing only GluRIIB^{GFP} and animals expressing both GluRIIB^{GFP} and GluRIIA (data not shown), the decrease of GluRIIB seems to occur, at least in part, independent of the increase in GluRIIA incorporation after TNT expression. In conclusion, glutamate release from the presynapse is important for shaping GluR composition during PSD maturation.

In an attempt to further dissect the kinetics of GluR changes during PSD maturation, we built quantitative models of GluR kinetics (**Supplementary Fig. 2** online). This analysis suggested that the further incorporation of GluRIIA at maturing PSDs strongly depends on both presynaptic glutamate release and the already established status of GluR composition. As GluRIIA complexes have more impact on the postsynaptic current, limiting GluRIIA incorporation via presynaptic glutamate release also limits the current that is mediated per PSD during its maturation. In turn, differences between presynaptic active

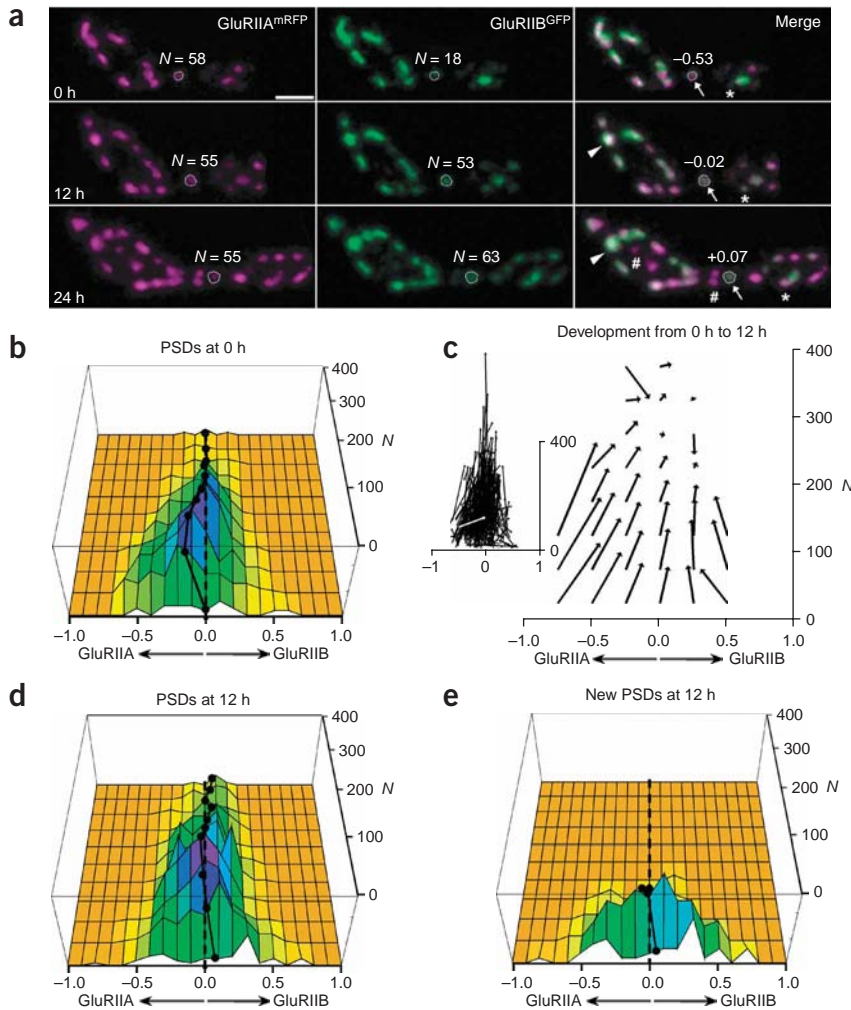


Figure 3 *In vivo* imaging of GluR composition during PSD maturation of developing *Drosophila* NMJs. **(a)** Confocal *in vivo* imaging (at 25 °C) of third-instar larvae expressing both *GluRIIB^{GFP}* and *GluRIIA^{mRFP}* to rescue the *GluRIIA^{null};GluRIIB^{null}* mutant (*GluRIIB^{GFP};GluRIIA^{mRFP}*). Single PSDs were imaged and re-identified after 12 and 24 h. Nascent PSDs were particularly rich in *GluRIIA^{mRFP}* (magenta, see # in merged channel). During maturation, PSDs dominated by *GluRIIA^{mRFP}* tended to specifically integrate *GluRIIB^{GFP}* (green) and vice versa (arrows and asterisks, respectively), while both PSD types grew substantially in size. Large PSDs maintained a rather stable net receptor content and barely increased their size (arrowheads). *N* indicates estimated GluR numbers (see **Supplementary Fig. 1**) of *GluRIIA* (left) and *GluRIIB* (middle). Right, estimated ratios of GluR composition expressed as the relative difference $(N_{IIB}-N_{IIA})/N$, with $N = N_{IIA} + N_{IIB}$. Scale bar, 2 μ m. **(b)** Distribution of the GluR ratio and the size of all PSDs at 0 h ($n = 505$, 8 NMJs). Colors indicate relative amount of GluRs (increasing from orange to blue). The black circles indicate the average ratio at PSDs as a function of the size, and the dashed line indicates a balanced GluR ratio. **(c)** Development of GluR number and ratio over 12 h. PSDs were binned to overlapping areas of ± 50 *N* and ratios of ± 0.25 (unbinned plot see inset; white arrow represents PSD encircled in **a**). **(d)** Distribution of GluR ratio and the size of all PSDs observed at 12 h. **(e)** Distribution of the GluR ratio and the size of all new PSDs observed for the first time at 12 h.

zones might contribute to the differences in the development of receptor composition (**Fig. 5**).

Active zone-specific control of GluR composition

Presynaptic active zones at the NMJ are suggested to differ in their glutamate release status depending on whether they form a presynaptic dense body (T bar)²⁶. Bruchpilot (BRP) is homologous to the mammalian CAST/ERC family of active-zone proteins. BRP-deficient synapses do not form T bars and suffer from inefficient evoked glutamate release, whereas their spontaneous release is fully sustained^{26,27}.

We previously combined *in vivo* imaging of GluRIIA with retrospective immunolabeling of BRP to show that BRP accumulation lagged behind GluRIIA accumulation during maturation of NMJ synapses¹⁸. To directly compare maturation of the presynaptic active zone with maturation of GluR composition at individual sites, we carried out *in vivo* imaging of BRP with GluRIIA and GluRIIB. To this end, BRP was visualized using a fragment of the protein (BRP-short, corresponding to amino acids 473–1226 of the 1,740-amino acid BRP protein) fused to cyan fluorescent protein (CFP) (BRP-short^{CFP}; **Fig. 5a**). Although BRP-short was not recognized by the monoclonal antibody Nc82, it colocalized perfectly with endogenous BRP (**Supplementary Fig. 3** online), which is recognized by Nc82 (ref. 27). We imaged BRP-short with GluRIIA^{mRFP} and GluRIIB^{GFP} *in vivo* over an

8-h interval (**Fig. 5a**) to determine the relationship between the maturation of individual presynaptic active zones and the GluR composition of the corresponding PSDs. In addition, part of the NMJ was subjected to FRAP analysis after specifically bleaching the GluRIIA and GluRIIB signals. Synapses with a strong BRP signal were nearly inevitably rich in GluRIIB, which is characteristic of mature PSDs. Newly formed synapses were rich in GluRIIA, but were very weak in BRP, and GluRIIA-FRAP appeared to be maximal at locations lacking BRP. Quantification of the FRAP data showed that the absolute incorporation of GluRIIA decreased with increasing levels of BRP (**Fig. 5b**). These data imply that the accumulation of GluRIIA is reduced as soon as an efficient accumulation of BRP occurs at the active zone during synaptic maturation.

If the maturation of BRP-dependent release is important for the maturation of GluR composition, *brp* mutant synapses should be defective in restricting GluRIIA incorporation. Indeed, GluR composition was strongly shifted toward GluRIIA in the absence of BRP (**Fig. 5d**), which is consistent with the substantially increased amplitude and decay time constant of *brp* mutant mEJCs²⁶.

Most *Drosophila* muscles are innervated by two motor neurons with distinct morphological and physiological properties (**Fig. 5c**). Type Ib and Is terminals are reminiscent of tonic and phasic terminals at the crayfish NMJ, respectively²⁸, as type Ib terminals possess a lower release probability at their active zones than Is terminals and facilitate on higher-frequency stimulation. Consistent with a previous report on endogenous GluRs¹³, we observed a shift toward fluorescently labeled GluRIIA at PSDs of type Ib terminals (**Fig. 5c,d**). Afferent-specific

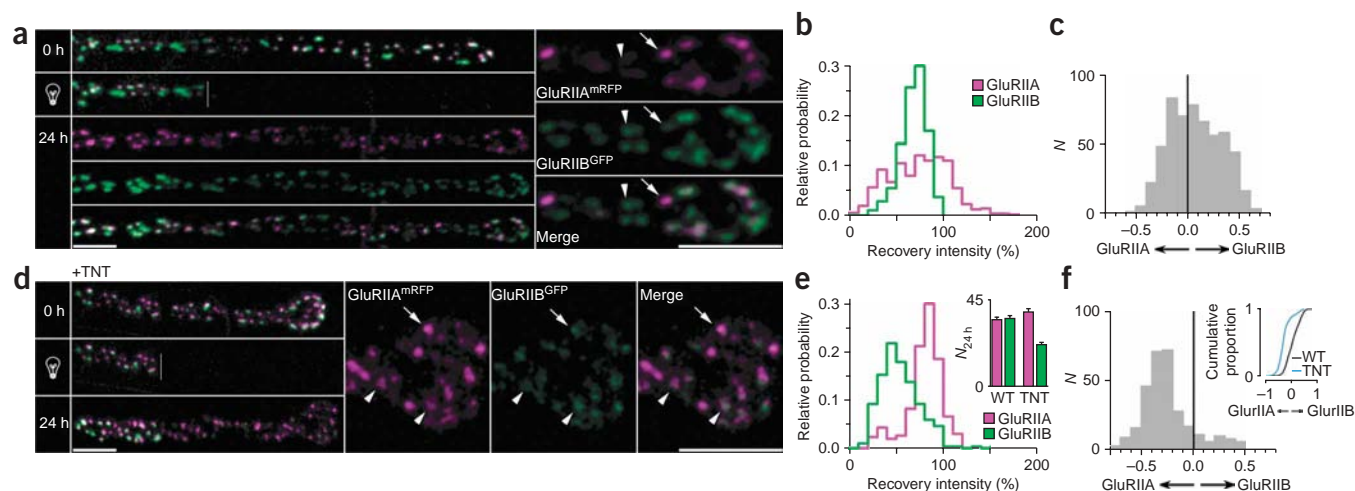


Figure 4 FRAP of GluRIIA and GluRIIB during synapse formation and maturation. **(a)** FRAP experiment of *GluRIIB*^{GFP};*GluRIIA*^{mRFP} NMJ (green and magenta, respectively; recovery time of 24 h). Both GFP and mRFP signals were bleached at 0 h and the FRAP images after 24 h are shown (the latter also at a higher magnification). FRAP after 24 h uncovered differential incorporation of *GluRIIA*^{mRFP} (magenta) and *GluRIIB*^{GFP} (green). Scale bars, 5 μ m. **(b)** Distribution of the average pixel intensity in individual PSDs ($n = 563$, 7 NMJs, $\Delta t = 24$ h) relative to the average pixel intensity of the unbleached PSDs at 24 h for *GluRIIA* (magenta) and *GluRIIB* (green). **(c)** Distribution of the ratio of incorporated N_{IIA} and N_{IIB} at individual PSDs after 24 h. **(d)** FRAP of *GluRIIB*^{GFP};*GluRIIA*^{mRFP} combined with TNT (concomitant expression of TNT with the mosaic motor neuron driver *ok319-gal4*; neuromuscular junction 14). Compared with the situation without activity block **(a)**, FRAP of *GluRIIA*^{mRFP} appeared to be more generalized, while FRAP of *GluRIIB*^{GFP} appeared to be weaker. Scale bars, 5 μ m. **(e)** Distribution of the recovery of average pixel intensity after 24 h during expression of TNT in the nerve terminal ($n = 303$, 7 NMJs). Inset, average number of incorporated *GluRIIA* and *GluRIIB* receptors after 24 h. WT, wild type. **(f)** Distribution of the ratio of incorporated N_{IIA} and N_{IIB} at individual PSDs after 24 h of TNT expression in the nerve terminal. Inset, cumulative proportion of the ratio distribution shown in **c** and **f**.

utilization of glutamate receptors could, in principle, be mediated via distinct molecular cues or, alternatively, by differences in activity between the two different classes of motor neurons¹³. Consistent with the latter, TNT expression shifted both terminals toward *GluRIIA* (**Fig. 5d**). Taken together, the inability to develop mature glutamate release at active zones shifts the composition of the corresponding PSD toward *GluRIIA*.

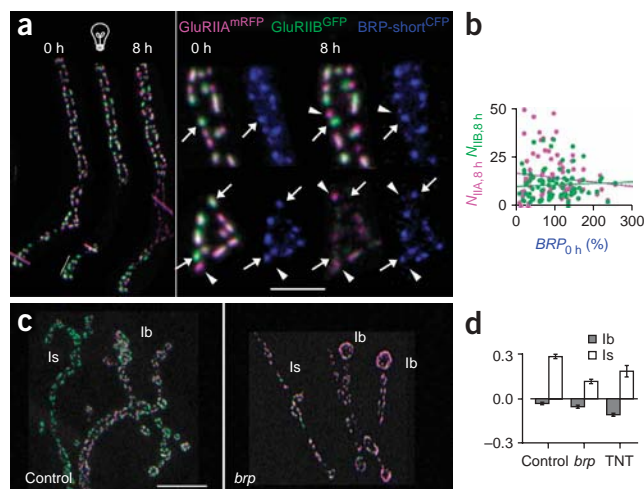
Intracellular C termini and control of GluR composition

Intracellular C-terminal domains (CTDs) have been broadly implicated in the subunit-specific targeting behavior of GluRs during synaptic plasticity processes in the CNS^{29–31}. We addressed the extent to which the GluR incorporation behavior described here is controlled by the

subtype-specific nature of the CTD. To this end, we produced genomic transgenes encoding CTD chimeras of *GluRIIA* and *GluRIIB* (*GluRIIA* with *GluRIIB* CTD, *GluRIIA*_B^{GFP} termed chimera 2; *GluRIIB* with *GluRIIA* CTD, *GluRIIB*_A^{GFP} termed chimera 1; only sequences directly encoding the CTDs were exchanged, with the 3' UTR sequences remaining unchanged). Both chimeras rescued the otherwise embryonic lethal *GluRIIA*^{null};*GluRIIB*^{null} background, giving rise to adult flies.

In the first FRAP experiment (chimera 1; **Fig. 6a,b**), *GluRIIB*_A^{GFP} was expressed together with *GluRIIA*^{mRFP}. PSD incorporation of the *GluRIIB*_A^{GFP} chimera was strongly suppressed relative to the control *GluRIIB*^{GFP}, leading to a *GluRIIA*-shifted PSD ratio in the chimera 1 combination (**Fig. 6b**). Thus, transferring the *GluRIIA* CTD to the 'body' of *GluRIIB* (replacing its normal CTD) impaired PSD

Figure 5 The BRP-dependent release component controls the maturation of GluR composition. **(a)** *In vivo* imaging of *GluRIIA*^{mRFP} (magenta), *GluRIIB*^{GFP} (green) and BRP-short^{CFP} (blue). Left, images of the whole NMJ at 0 h, before and after specifically bleaching *GluRIIA*^{mRFP} and *GluRIIB*^{GFP}, and at 8 h. Right, detail of unbleached area and FRAP in bleached area. Arrows indicate mature synapses, characterized by large *GluRIIB* and large BRP signals. Arrowheads show synapses characterized by large *GluRIIA* and small BRP signals. Scale bar, 5 μ m. **(b)** Quantification of the relationship between *GluRIIA* (magenta) or *GluRIIB* (green) FRAP at 8 h and the normalized BRP signal of that synapse at 0 h, with linear regression lines in magenta and green. **(c,d)** GFP and mRFP signals at NMJs (muscle 4, abdominal segment 2) expressing *GluRIIB*^{GFP};*GluRIIA*^{mRFP} in the *GluRIIA*^{null};*GluRIIB*^{null} background, combined with the *brp* mutant or with TNT expression (for exact genotypes see Methods). **(c)** At Is terminal innervations, GluR composition was shifted toward *GluRIIB* in controls. In the *brp*-mutant background, terminals were shifted toward *GluRIIA*. Scale bar, 10 μ m. **(d)** Quantification showed that GluR composition is shifted toward *GluRIIA* in both *brp*-deficient animals and after TNT expression. In *brp*-deficient animals, this effect was particularly strong at Is terminals.



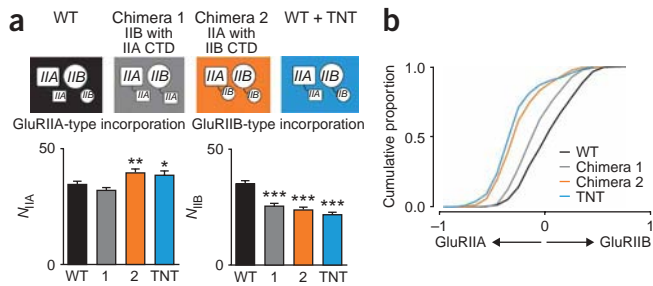


Figure 6 Influence of intracellular C-terminal domains on FRAP behavior *in vivo*. (a,b) Shown are N_{IA} and N_{IB} (a) and the respective cumulative histogram of the ratio $(N_{IB} - N_{IA})/N$ of incorporated receptors (b) for several two-channel FRAP experiments. WT, $GluRIIA^{GFP}; GluRIIB^{mRFP}$ ($n = 656$, 6 NMJs); chimera 1, $GluRIIB_A^{GFP}; GluRIIA^{mRFP}$ ($n = 377$, 7 NMJs); chimera 2, $GluRIIA_B^{GFP}; GluRIIB^{mRFP}$ ($n = 326$, 6 NMJs); TNT, $GluRIIB^{GFP}; GluRIIA^{mRFP}$ combined with TNT ($n = 303$, 7 NMJs). All genomic constructs were expressed in the $GluRIIA^{null}; GluRIIB^{null}$ background; FRAP recovery was 24 h. In all situations, GluRIIB-type incorporation was strongly reduced compared with the control (N_{IB}) (WT, 35.2 ± 1.2 ; chimera 1, 25.5 ± 1.0 ; chimera 2, 23.8 ± 1.0 ; TNT, 21.8 ± 1.0). In contrast, GluRIIA-type incorporation was significantly increased when presynaptic activity was suppressed or GluRIIA lacked its C terminus (N_{IA}) (WT, 34.7 ± 1.3 ; chimera 1, 32.0 ± 1.4 ; chimera 2, 39.5 ± 1.8 , $P < 0.01$; TNT, 38.7 ± 1.8 , $P < 0.001$).

incorporation compared with unmodified GluRIIB. In the second FRAP experiment (chimera 2; **Fig. 6a,b**), $GluRIIA_B^{GFP}$ was expressed together with $GluRIIB^{mRFP}$. The PSD incorporation of the $GluRIIA_B^{GFP}$ chimera was significantly increased relative to control $GluRIIA^{GFP}$ ($P < 0.01$), while $GluRIIB^{mRFP}$ incorporation simultaneously decreased relative to control. This also resulted in a GluRIIA-shifted incorporation profile (**Fig. 6b**). Notably, expressing TNT gave nearly identical results as the chimera 2 combination in the absence of TNT (**Fig. 6b**). Thus, the CTD of GluRIIA appears to convey signals that mediate the glutamate release dependence of GluR composition during PSD maturation. At immature PSDs, however, GluRIIA with the CTD of GluRIIB still dominated over GluRIIB (data not shown), and GluRIIA and GluRIIB did not behave identically when equipped with the same CTD (chimera 1 and 2). Our results thus also emphasize additional subtype-specific roles for the GluR bodies in the control of PSD GluR composition (see Discussion).

Site-specific GluR composition control and synapse formation

The level of GluRIIA (but not of GluRIIB) is directly associated with the number of PSDs and active zones formed at the NMJ^{16,17}, indicating that GluRIIA is a rate-limiting component. Correspondingly, PSD numbers were clearly and significantly increased at $GluRIIA^{GFP}$ -NMJs when compared with $GluRIIB^{GFP}$ -NMJs ($P < 0.001$; **Fig. 7a,b**). Our previous study demonstrated that the GluRIIA population contributing to PSD assembly resides in a cell-wide pool, potentially in the muscle plasma membrane¹⁸. Thus, synapse-specific consumption of GluRIIA complexes might directly control the amount of GluRIIA that is available to promote the formation of new synapses. Consistent with this, TNT-expressing NMJs (data not shown) and BRP-lacking NMJs^{26,27} form fewer synapses. This may represent a simple mechanism contributing to match PSD numbers to levels of presynaptic activity, as has been shown in this system^{32–34} (**Fig. 7c**).

DISCUSSION

Imaging at *Drosophila* neuromuscular junctions enabled us to track the amount and composition of glutamate receptors in intact animals over

days with single synapse resolution. As we have shown previously¹⁸, new synapses form distinct from preexisting synapses and then mature in several hours to finally reach a size typical of both their presynaptic (active zones) and postsynaptic (PSDs) specializations. In these PSDs, two glutamate receptor complexes coexist, containing either the GluRIIA or GluRIIB subunit^{9,11–13}. Our results indicate that GluR-subtype dynamics are controlled at a submicron scale (**Fig. 3**).

Our FRAP experiments indicated that there was a principal difference between GluRIIA and GluRIIB incorporation at individual PSDs (**Fig. 4a–c**), showed that a genetically evoked suppression of presynaptic glutamate release results in an increase in GluRIIA and a decrease in GluRIIB incorporation (**Fig. 4d–f**), and suggested that the amount of the presynaptic active zone protein BRP correlates with a shift toward GluRIIB incorporation (**Fig. 5**). Thus, when PSDs begin to mediate mature current amplitudes, they shift their composition toward the rapidly desensitizing GluRIIB complex (**Fig. 5**). Put differently, a synaptic site will stop GluRIIA incorporation only if both relevant parameters, presynaptic release of glutamate (sufficient amount of BRP) and sufficient levels of efficiently conducting glutamate receptors (GluRIIA), coincide.

Newly formed PSDs possess a rather balanced composition (**Fig. 3d**) and then become rich in GluRIIA, before finally balancing the GluR composition again (**Fig. 3b**). Potentially, a positive feedback initially promotes GluRIIA incorporation, whereas a negative feedback dominates with further maturation. It has been suggested that postsynaptic Ca^{2+} influx through GluRIIA controls retrograde signaling²⁰. Similarly, GluR composition could be controlled during PSD maturation by such a signal through GluRIIA (**Fig. 7c**). Metabotropic glutamate receptors³⁵ or nonvesicular glutamate release³⁶ may also be involved. Moreover, the role of Ca^{2+} -activated kinase/phosphatase signaling in GluR composition dynamics should be studied. Notably, postsynaptic stimulation of aPKC activity has been shown to reduce the PSD levels of GluRIIA³⁷. It is tempting to speculate that differences in presynaptic glutamate release might steer postsynaptic GluR composition through spatio-temporal modulation of Ca^{2+} signals.

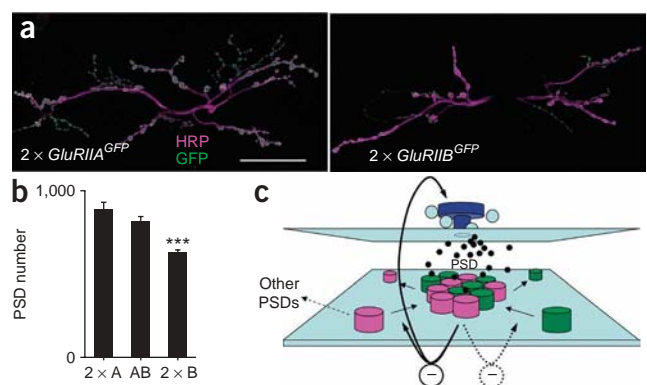


Figure 7 Control of GluR composition and structural plasticity at the NMJ. (a) Shown are immunostainings for HRP (magenta) and GFP (green) in third-instar larvae (NMJ 6/7) expressing two copies of either $GluRIIA^{GFP}$ or $GluRIIB^{GFP}$ in the $GluRIIA^{null}; GluRIIB^{null}$ background. $GluRIIA$ -NMJs are clearly larger than $GluRIIB$ -NMJs. Scale bar, 20 μ m. (b) Quantification of a. The absolute number of PSDs was significantly reduced in NMJs of $2 \times GluRIIB^{GFP}$ ($2 \times B$) when compared with $2 \times GluRIIA^{GFP}$ ($2 \times A$) and $GluRIIB^{GFP}; GluRIIA^{GFP}$ (AB) ($2 \times A$, 888 ± 46 ; AB, 815 ± 31 ; $2 \times B$, 628 ± 19). (c) Model connecting activity-dependent GluR dynamics at single PSDs with the rate of PSD formation via the amount of GluRIIA available for the maturation of new PSDs. Green, GluRIIB; magenta, GluRIIA.

In vivo mobility of synaptic acetylcholine receptors fluorescently labeled with bungarotoxin has been elegantly studied at the mouse NMJ. There, activity-evoked changes in Ca^{2+} influx through these receptors seem to control receptor lifetime in the postsynaptic compartment³⁸. Mechanistic similarities between these two systems are now open for analysis.

The cytoplasmic C termini of mammalian GluRs are considered to be important in the control of activity-dependent GluR targeting³¹. Notably, we found that subtype-specific differences were not fully switched after genetically switching the CTDs (Fig. 6) and subtype-specific behaviors were not fully eliminated after deprivation of presynaptic glutamate release. Thus, differences in the affinities of the GluRIIA and GluRIIB ectodomains and differences in their ionic transmission and signals conveyed by the CTDs seem to affect PSD assembly synergistically. In fact, we have recently shown that PSD assembly is greatly disrupted in the absence of all GluRs³⁹ and is severely compromised without GluRIIA (data not shown). Thus, potential protein interactions⁴⁰, which specifically allow GluRIIA to incorporate into immature PSDs, might be particularly important for efficient PSD assembly.

Positive feedback mechanisms clearly operate during long-term potentiation (LTP). Indeed, it was demonstrated that LTP increased the amount of glutamate receptors containing the GluR1 subunit at glutamatergic synapses in the vertebrate CNS^{30,31}. On the single-molecule level, local activity restricts the mobility of the GluR1 subunit on a submicron scale⁴¹. In addition, mechanisms must exist that stabilize the total synaptic strength of a neuron during exposure to synaptic plasticity^{7,42}. Recently, it was shown that adaptation to prolonged AMPAR blockade in cultivated hippocampal neurons increases the amount of GluR1 per PSD and elevates the presynaptic efficacy^{43,44}, which is consistent with our findings. According to our model (Fig. 7c), a blockade of receptors would lead to an omission of the negative feedback loop on GluRIIA incorporation and BRP accumulation. Notably, large synapses would be affected most⁴³, but diffusion of receptors in the spine and the spine neck would also have to be considered⁴⁵. It will be interesting to investigate how positive and negative feedback during development are related to positive feedback during LTP^{30,31} and negative feedback during homeostatic control^{43,46}, and how these mechanisms interact in terms of metaplasticity⁴⁴.

Recently⁴⁶, pharmacological blockade of glutamate receptors at the *Drosophila* NMJ was shown to trigger a fast negative-feedback mechanism involving presynaptic $Ca_v2.1$ calcium channels. This negative feedback, however, was independent of presynaptic action potentials⁴⁶. Here we used presynaptic TNT expression to suppress synaptic activity, resulting in a complete block of evoked glutamate release and a reduced frequency of mEPSCs²⁵. However, although mEPSC frequency is unaltered in BRP mutants²⁶, clear changes occurred in GluR composition (Fig. 5c,d). Thus, evoked glutamate release, rather than mEPSCs, might be mainly responsible for determining GluR composition at larval NMJs⁴⁷ over extended periods. Therefore, these observations may be reconciled by differences in the duration of activity suppression and/or the site of intervention. Similarly, in cultured hippocampal neurons, AMPA receptor blockade or action potential suppression lead to different synaptic responses to inactivity^{43,48}.

Taken together, our analysis indicates that the incorporation rate of GluRIIA is high at immature PSDs, but increasing levels of GluRIIA establish a negative feedback, reducing PSD incorporation of this complex (Figs. 3, 5 and 6) and further growth of the presynaptic site^{9,14,19,46} (Fig. 7c). In addition, we hypothesize that high levels of glutamate release lower the consumption of GluRIIA at maturing PSDs, and thereby support the growth of additional nascent synapses.

In this manner, synapse-specific control of GluR composition can also execute cell-wide control over activity-dependent synapse formation in a long-term fashion. Indeed, experience-dependent increases in the number of NMJ synapses^{21,33} depend on GluRIIA, but not GluRIIB.

METHODS

Molecular biology. A genomic *EcoRI/XhoI* fragment, which served as a *GluRIIA* rescue construct, has recently been used to clone *GluRIIA*^{GFP893} and *GluRIIA*^{mRFP893} (ref. 18). Previously, a genomic *HindIII/SalI* fragment that covers the whole open reading frame of *GluRIIB* and the 3' end of *GluRIIA* was used as a genomic *GluRIIB* rescue construct¹⁴. In this study, the *GluRIIA* 3' end, which is potentially translatable, was cleaved off, leaving a genomic *NsiI/NcoI* construct of *GluRIIB* (*GluRIIB* coding region with ~700 bp upstream and ~500 bp downstream) with unaltered rescue capability. The fluorescently tagged *GluRIIB*^{GFP897} and *GluRIIB*^{mRFP897} (fluorophore insertion after AA897), based on a recent *in vitro* transposition screen (Sheridan 2002), were designed similarly to *GluRIIA*^{GFP893} and *GluRIIA*^{mRFP893} (ref. 18). Genomic constructs of the chimeric EGFP-tagged receptor subunits *GluRIIA*_B^{GFP} and *GluRIIB*_A^{GFP} were produced by a three-step overlap extension PCR (Elongase, Stratagene) with 30 ± 2 overlapping bases. To produce *GluRIIA*_B^{GFP}, the C-terminal domain of *GluRIIB*^{GFP897} was integrated into the *GluRIIA* backbone via *HpaI/XhoI*. The product was inserted into pUAST via *EcoRI/XhoI*. *GluRIIB*_A^{GFP} was cloned by integrating the C-terminal domain of *GluRIIA*^{GFP893} into the *GluRIIB* backbone via *KpnI/NsiI*. The product was inserted into a pUAST derivative via *NotI/NaeI*. All constructs were double-strand sequenced. Primer sequences and exact protocols can be requested.

Genetics. Activity suppression was performed combining mosaic driver line *ok319-gal4* with *UAS-tetanus toxin light chain (UAS-TNT)* as described³⁹. The *GluRIIA;GluRIIB* double-mutant background (*GluRIIA*^{null}, *GluRIIB*^{null})^{9,11,14} was established by crossing *df(2L)c^{h4}* (*dfc^{h4}*) flies with *df(2L)GluRIIA;GluRIIB*^{SP22} (*A22*) flies. The following genotypes were used: *GluRIIA*: *dfc^{h4}/A22;UAS-GluRIIA/+*. *GluRIIA*^{GFP}: *dfc^{h4}/A22;UAS-GluRIIA*^{GFP893}/*+*. $2 \times$ *GluRIIA*^{GFP}: *dfc^{h4}/A22;UAS-GluRIIA*^{GFP893}. *GluRIIA*^{GFP}, *GluRIIB*^{mRFP}: *dfc^{h4}/A22;UAS-GluRIIA*^{GFP893}/*UAS-GluRIIB*^{mRFP897}. *GluRIIB*: *dfc^{h4}/A22;UAS-gluRIIB/+*. *GluRIIB*^{GFP}: *dfc^{h4}/A22;UAS-GluRIIB*^{GFP897}/*+*. $2 \times$ *GluRIIB*^{GFP}: *dfc^{h4},UAS-GluRIIB*^{GFP897}/*A22;UAS-GluRIIB*^{GFP897}/*+*. *GluRIIB*^{GFP}, *GluRIIA*^{mRFP}: *dfc^{h4},UAS-GluRIIB*^{GFP897}/*A22;UAS-GluRIIA*^{mRFP893}/*+*. *GluRIIB*^{GFP}, *GluRIIA*^{mRFP} combined with *TNT*: *dfc^{h4}, ok319-gal4/A22, UAS-TNT;UAS-GluRIIB*^{GFP897}/*UAS-GluRIIA*^{mRFP893}. *GluRIIA*_B^{GFP}, *GluRIIB*^{mRFP}, *dfc^{h4},UAS-GluRIIA*_B^{GFP}/*A22;UAS-GluRIIB*^{mRFP897}/*+*. *GluRIIB*^{GFP}, *GluRIIA*^{GFP}: *dfc^{h4},UAS-GluRIIB*^{GFP}/*A22;UAS-GluRIIA*^{GFP}/*+*. *GluRIIB*_A^{GFP}, *GluRIIA*^{mRFP}: *dfc^{h4},UAS-GluRIIB*_A^{GFP}/*A22;UAS-GluRIIA*^{mRFP893}/*+*. Fluorescent GluR expression in *brp*-deficient background: *brp*⁶⁹/*df(2R)BSC29;UAS-GluRIIB*^{GFP897}/*UAS-GluRIIA*^{mRFP893}. The *UAS-BRP-short*^{CFP} construct was expressed with *ok6-gal4* in the background of *UAS-GluRIIB*^{GFP897}/*UAS-GluRIIA*^{mRFP893}. Larvae of indicated genotypes were selected from crosses using Black cell- or GFP-marked balancer chromosomes. Animals were raised at 25 °C in high-density vials.

Immunohistochemistry. We used mouse antibody to GluRIIA (1:100, 8B4D2; Developmental Studies Hybridoma Bank, University of Iowa), rabbit antibody to GluRIIB (1:2,000, a gift from A. DiAntonio, Washington University School of Medicine), rabbit antibody to GluRIID (1:500), goat antibody to HRP cyanine 5 (1:200), mouse Nc82 (1:100, a gift from E. Buchner, University of Würzburg) and rabbit antibody to GFP (1:500, Molecular Probes) as primary antibodies. Larval dissections (third instar) were carried out as recently described¹¹.

Electrophysiology. See detailed protocols in the **Supplementary Methods**.

***In vivo* imaging.** Early third-instar larvae of standardized size were *in vivo* imaged as previously described¹⁸. For FRAP experiments, only a subpopulation of the PSDs at the NMJ were bleached. For detailed protocols of quantitative imaging analysis, see **Supplementary Methods**.

Statistical analysis. The nonparametric Mann-Whitney rank sum test was used for statistical analysis. The data are reported as mean \pm s.e.m., *n* indicates the

sample number and *P* denotes the significance (* *P* < 0.05, ** *P* < 0.01 and *** *P* < 0.001).

Note: Supplementary information is available on the Nature Neuroscience website.

ACKNOWLEDGMENTS

We would like to thank D.E. Featherstone for help with establishing patch-clamp recordings from *Drosophila* embryos and A. DiAntonio for fly stocks. This work was supported by grants from the Deutsche Forschungsgemeinschaft to S.J.S. (SI849/2-1 and 2-2, TP A16/SFB 406, TP B25/SFB581, SFB487) and to M.H. (HE 2621/4-1 and TP B22/SFB 581), and by *formel.1* grants to S.H. and R.J.K. from the Medical Faculty of the University of Leipzig.

Published online at <http://www.nature.com/natureneuroscience>

Reprints and permissions information is available online at <http://npg.nature.com/reprintsandpermissions>

- McAllister, A.K. Dynamic aspects of CNS synapse formation. *Annu. Rev. Neurosci.* **30**, 425–450 (2007).
- Garner, C.C., Zhai, R.G., Gundelfinger, E.D. & Ziv, N.E. Molecular mechanisms of CNS synaptogenesis. *Trends Neurosci.* **25**, 243–251 (2002).
- Zhai, R.G. & Bellen, H.J. The architecture of the active zone in the presynaptic nerve terminal. *Physiology (Bethesda)* **19**, 262–270 (2004).
- Witzemann, V. *et al.* Acetylcholine receptor epsilon-subunit deletion causes muscle weakness and atrophy in juvenile and adult mice. *Proc. Natl. Acad. Sci. USA* **93**, 13286–13291 (1996).
- Takahashi, T. Postsynaptic receptor mechanisms underlying developmental speeding of synaptic transmission. *Neurosci. Res.* **53**, 229–240 (2005).
- Derkach, V.A., Oh, M.C., Guire, E.S. & Soderling, T.R. Regulatory mechanisms of AMPA receptors in synaptic plasticity. *Nat. Rev. Neurosci.* **8**, 101–113 (2007).
- Turrigiano, G. Homeostatic signaling: the positive side of negative feedback. *Curr. Opin. Neurobiol.* **17**, 318–324 (2007).
- Schuster, C.M. *et al.* Molecular cloning of an invertebrate glutamate receptor subunit expressed in *Drosophila* muscle. *Science* **254**, 112–114 (1991).
- Petersen, S.A., Fetter, R.D., Noordermeer, J.N., Goodman, C.S. & DiAntonio, A. Genetic analysis of glutamate receptors in *Drosophila* reveals a retrograde signal regulating presynaptic transmitter release. *Neuron* **19**, 1237–1248 (1997).
- DiAntonio, A. Glutamate receptors at the *Drosophila* neuromuscular junction. *Int. Rev. Neurobiol.* **75**, 165–179 (2006).
- Qin, G. *et al.* Four different subunits are essential for expressing the synaptic glutamate receptor at neuromuscular junctions of *Drosophila*. *J. Neurosci.* **25**, 3209–3218 (2005).
- Featherstone, D.E. *et al.* An essential *Drosophila* glutamate receptor subunit that functions in both central neuropil and neuromuscular junction. *J. Neurosci.* **25**, 3199–3208 (2005).
- Marrus, S.B., Portman, S.L., Allen, M.J., Moffat, K.G. & DiAntonio, A. Differential localization of glutamate receptor subunits at the *Drosophila* neuromuscular junction. *J. Neurosci.* **24**, 1406–1415 (2004).
- DiAntonio, A., Petersen, S.A., Heckmann, M. & Goodman, C.S. Glutamate receptor expression regulates quantal size and quantal content at the *Drosophila* neuromuscular junction. *J. Neurosci.* **19**, 3023–3032 (1999).
- Pawlu, C., DiAntonio, A. & Heckmann, M. Postfusional control of quantal current shape. *Neuron* **42**, 607–618 (2004).
- Sigrist, S.J., Thiel, P.R., Reiff, D.F. & Schuster, C.M. The postsynaptic glutamate receptor subunit DGLuR-IIA mediates long-term plasticity in *Drosophila*. *J. Neurosci.* **22**, 7362–7372 (2002).
- Sigrist, S.J. *et al.* Postsynaptic translation affects the efficacy and morphology of neuromuscular junctions. *Nature* **405**, 1062–1065 (2000).
- Rasse, T.M. *et al.* Glutamate receptor dynamics organizing synapse formation *in vivo*. *Nat. Neurosci.* **8**, 898–905 (2005).
- Davis, G.W., DiAntonio, A., Petersen, S.A. & Goodman, C.S. Postsynaptic PKA controls quantal size and reveals a retrograde signal that regulates presynaptic transmitter release in *Drosophila*. *Neuron* **20**, 305–315 (1998).
- Yoshihara, M., Adolfsen, B., Galle, K.T. & Littleton, J.T. Retrograde signaling by Syt 4 induces presynaptic release and synapse-specific growth. *Science* **310**, 858–863 (2005).
- Reiff, D.F., Thiel, P.R. & Schuster, C.M. Differential regulation of active zone density during long-term strengthening of *Drosophila* neuromuscular junctions. *J. Neurosci.* **22**, 9399–9409 (2002).
- Broadie, K.S. & Bate, M. Development of the embryonic neuromuscular synapse of *Drosophila melanogaster*. *J. Neurosci.* **13**, 144–166 (1993).
- Nishikawa, K. & Kidokoro, Y. Junctional and extrajunctional glutamate receptor channels in *Drosophila* embryos and larvae. *J. Neurosci.* **15**, 7905–7915 (1995).
- Campbell, R.E. *et al.* A monomeric red fluorescent protein. *Proc. Natl. Acad. Sci. USA* **99**, 7877–7882 (2002).
- Sweeney, S.T., Broadie, K., Keane, J., Niemann, H. & O’Kane, C.J. Targeted expression of tetanus toxin light chain in *Drosophila* specifically eliminates synaptic transmission and causes behavioral defects. *Neuron* **14**, 341–351 (1995).
- Kittel, R.J. *et al.* Bruchpilot promotes active zone assembly, Ca²⁺ channel clustering, and vesicle release. *Science* **312**, 1051–1054 (2006).
- Wagh, D.A. *et al.* Bruchpilot, a protein with homology to ELKS/CAST, is required for structural integrity and function of synaptic active zones in *Drosophila*. *Neuron* **49**, 833–844 (2006).
- Atwood, H.L. & Karunanithi, S. Diversification of synaptic strength: presynaptic elements. *Nat. Rev. Neurosci.* **3**, 497–516 (2002).
- Barry, M.F. & Ziff, E.B. Receptor trafficking and the plasticity of excitatory synapses. *Curr. Opin. Neurobiol.* **12**, 279–286 (2002).
- Malinow, R. & Malenka, R.C. AMPA receptor trafficking and synaptic plasticity. *Annu. Rev. Neurosci.* **25**, 103–126 (2002).
- Bredt, D.S. & Nicoll, R.A. AMPA receptor trafficking at excitatory synapses. *Neuron* **40**, 361–379 (2003).
- Zhong, Y., Budnik, V. & Wu, C.F. Synaptic plasticity in *Drosophila* memory and hyperexcitable mutants: role of cAMP cascade. *J. Neurosci.* **12**, 644–651 (1992).
- Sigrist, S.J., Reiff, D.F., Thiel, P.R., Steinert, J.R. & Schuster, C.M. Experience-dependent strengthening of *Drosophila* neuromuscular junctions. *J. Neurosci.* **23**, 6546–6556 (2003).
- Zhong, Y. & Wu, C.F. Neuronal activity and adenylyl cyclase in environment-dependent plasticity of axonal outgrowth in *Drosophila*. *J. Neurosci.* **24**, 1439–1445 (2004).
- Bogdanik, L. *et al.* The *Drosophila* metabotropic glutamate receptor DmGluRA regulates activity-dependent synaptic facilitation and fine synaptic morphology. *J. Neurosci.* **24**, 9105–9116 (2004).
- Featherstone, D.E. *et al.* Presynaptic glutamic acid decarboxylase is required for induction of the postsynaptic receptor field at a glutamatergic synapse. *Neuron* **27**, 71–84 (2000).
- Ruiz-Canada, C. *et al.* New synaptic bouton formation is disrupted by misregulation of microtubule stability in aPKC mutants. *Neuron* **42**, 567–580 (2004).
- Akaaboune, M., Grady, R.M., Turney, S., Sanes, J.R. & Lichtman, J.W. Neurotransmitter receptor dynamics studied *in vivo* by reversible photo-unbinding of fluorescent ligands. *Neuron* **34**, 865–876 (2002).
- Schmid, A. *et al.* Non-NMDA-type glutamate receptors are essential for maturation, but not for initial assembly of synapses at *Drosophila* neuromuscular junctions. *J. Neurosci.* **26**, 11267–11277 (2006).
- Chen, K., Merino, C., Sigrist, S.J. & Featherstone, D.E. The 4.1 protein coracle mediates subunit-selective anchoring of *Drosophila* glutamate receptors to the postsynaptic actin cytoskeleton. *J. Neurosci.* **25**, 6667–6675 (2005).
- Ehlers, M.D., Heine, M., Groc, L., Lee, M.C. & Choquet, D. Diffusional trapping of GluR1 AMPA receptors by input-specific synaptic activity. *Neuron* **54**, 447–460 (2007).
- Turrigiano, G.G., Leslie, K.R., Desai, N.S., Rutherford, L.C. & Nelson, S.B. Activity-dependent scaling of quantal amplitude in neocortical neurons. *Nature* **391**, 892–896 (1998).
- Thiagarajan, T.C., Lindskog, M. & Tsien, R.W. Adaptation to synaptic inactivity in hippocampal neurons. *Neuron* **47**, 725–737 (2005).
- Thiagarajan, T.C., Lindskog, M., Malgaroli, A. & Tsien, R.W. LTP and adaptation to inactivity: overlapping mechanisms and implications for metaplasticity. *Neuropharmacology* **52**, 156–175 (2007).
- Holcman, D. & Triller, A. Modeling synaptic dynamics driven by receptor lateral diffusion. *Biophys. J.* **91**, 2405–2415 (2006).
- Frank, C.A., Kennedy, M.J., Gooled, C.P., Marek, K.W. & Davis, G.W. Mechanisms underlying the rapid induction and sustained expression of synaptic homeostasis. *Neuron* **52**, 663–677 (2006).
- Verstreken, P. *et al.* Endophilin mutations block clathrin-mediated endocytosis, but not neurotransmitter release. *Cell* **109**, 101–112 (2002).
- Bacci, A. *et al.* Chronic blockade of glutamate receptors enhances presynaptic release and downregulates the interaction between synaptophysin-synaptobrevin vesicle-associated membrane protein 2. *J. Neurosci.* **21**, 6588–6596 (2001).

3.4 Fouquet *et al.*, 2009, J Cell Biol, 186:129-145

Seite 44-60

Maturation of active zone assembly by *Drosophila* Bruchpilot

Wernher Fouquet,^{1,2} David Oswald,^{1,2} Carolin Wichmann,^{1,3} Sara Mertel,¹ Harald Depner,¹ Marcus Dyba,⁴ Stefan Hallermann,⁵ Robert J. Kittel,^{3,5} Stefan Eimer,⁶ and Stephan J. Sigrist^{1,2}

¹Institute for Biology/Genetics, Free University Berlin, 14195 Berlin, Germany

²Biolmaging Center and ³Institute for Clinical Neurobiology, Universität Würzburg, 97078 Würzburg, Germany

⁴Research & Development, Leica Microsystems CMS GmbH, 68165 Mannheim, Germany

⁵Carl-Ludwig-Institut für Physiologie, Medizinische Fakultät, Universität Leipzig, 04103 Leipzig, Germany

⁶European Neuroscience Institute and Center for Molecular Physiology of the Brain, 37077 Göttingen, Germany

Synaptic vesicles fuse at active zone (AZ) membranes where Ca^{2+} channels are clustered and that are typically decorated by electron-dense projections. Recently, mutants of the *Drosophila melanogaster* ERC/CAST family protein Bruchpilot (BRP) were shown to lack dense projections (T-bars) and to suffer from Ca^{2+} channel-clustering defects. In this study, we used high resolution light microscopy, electron microscopy, and intravital imaging to analyze the function of BRP in AZ assembly. Consistent with truncated BRP variants forming shortened

T-bars, we identify BRP as a direct T-bar component at the AZ center with its N terminus closer to the AZ membrane than its C terminus. In contrast, *Drosophila* Liprin- α , another AZ-organizing protein, precedes BRP during the assembly of newly forming AZs by several hours and surrounds the AZ center in few discrete punctae. BRP seems responsible for effectively clustering Ca^{2+} channels beneath the T-bar density late in a protracted AZ formation process, potentially through a direct molecular interaction with intracellular Ca^{2+} channel domains.

Introduction

The arrival of action potentials mediates Ca^{2+} influx through strategically localized clusters of voltage-operated Ca^{2+} channels at the synaptic active zone (AZ) membrane. Ca^{2+} triggers exocytosis of synaptic vesicles, and tight coupling between release-ready vesicles and Ca^{2+} channels seems important for efficient neurotransmitter release (Neher and Sakaba, 2008). AZs are further characterized by macromolecular cytomatrices named dense bodies (Zhai and Bellen, 2004; Siksou et al., 2007). The role of these electron-dense specializations and of AZ-enriched proteins in the assembly of the AZ and/or the synaptic vesicle exo-endocytosis cycle is under intense investigation (Oswald and Sigrist, 2009). Protein architectures constituting and controlling dense bodies remain to be revealed, and their contributions to AZ assembly in general and Ca^{2+} channel clustering in particular must be defined genetically.

The most straightforward approach would be to use immunolabeling combined with light microscopy. However, individual AZs measure only a few hundred nanometers in diameter, rendering this approach difficult. Recently, stimulated emission depletion (STED) microscopy (Hell, 2007) has proven valuable for high resolution light microscopic studies of synapse architectures (Kittel et al., 2006; Jin and Garner, 2008; Westphal et al., 2008).

The *Drosophila melanogaster* neuromuscular junction (NMJ) is a leading model for genetic analyses of synapse structure and assembly (Featherstone et al., 2000; Koh et al., 2000; Collins and DiAntonio, 2007). In this preparation, dense body structures termed T-bars may take part in activity-dependent changes of synaptic performance (Prokop and Meinertzhagen, 2006). Furthermore, the Ca^{2+} channel $\alpha 1$ subunit Cacophony (Cac) was shown to dominate neurotransmitter release at NMJ synapses (Kawasaki et al., 2000).

Proteins of the conserved CAST (CAZ-associated structural protein)/ERC (ELKS–Rab6-interacting protein CAST)

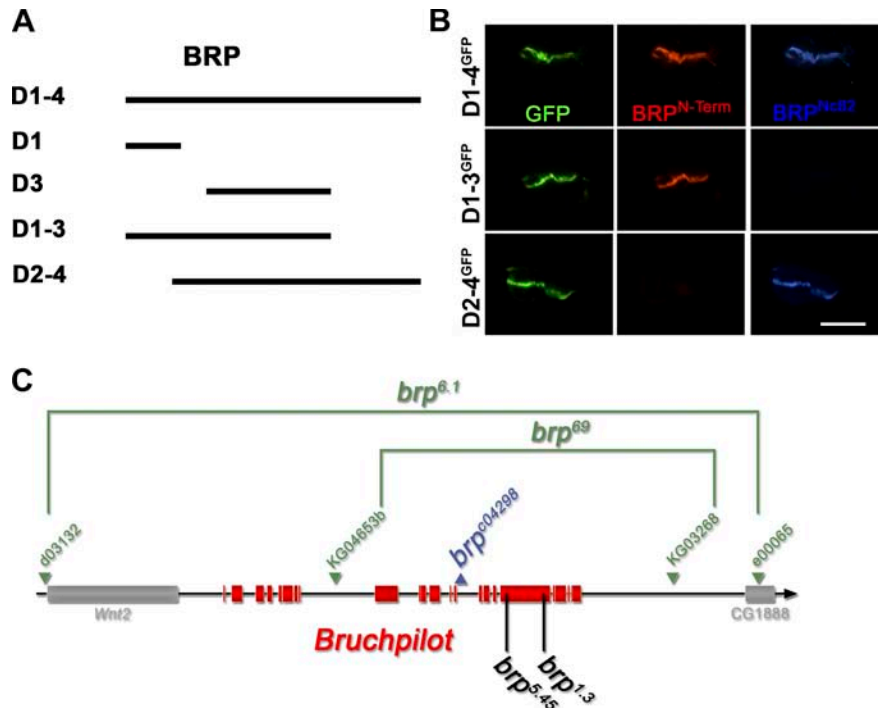
W. Fouquet and D. Oswald contributed equally to this paper.

Correspondence to Stephan J. Sigrist: stephan.sigrist@fu-berlin.de

Abbreviations used in this paper: au, arbitrary units; AZ, active zone; BRP, Bruchpilot; Cac, Cacophony; DGluR, *Drosophila* glutamate receptor subunit; DLiprin- α , *Drosophila* Liprin- α ; EMS, ethyl methyl sulfonate; FS, freeze substitution; HPF, high pressure freezing; IP, immunoprecipitation; mStraw, mStrawberry; NMJ, neuromuscular junction; PSD, postsynaptic density; PSF, point spread function; STED, stimulated emission depletion; UAS, upstream activator sequence.

© 2009 Fouquet et al. This article is distributed under the terms of an Attribution–Noncommercial–Share Alike–No Mirror Sites license for the first six months after the publication date [see <http://www.jcb.org/misc/terms.shtml>]. After six months it is available under a Creative Commons License [Attribution–Noncommercial–Share Alike 3.0 Unported license, as described at <http://creativecommons.org/licenses/by-nc-sa/3.0/>].

Figure 1. Epitope mapping for mAb Nc82 and genetic analysis of *brp*. (A) BRP fragments used for transgenic expression experiments. (B) Ectopic expression (in wing imaginal discs) of GFP-tagged BRP fragments missing either N- (D2-4) or C-terminal (D1-3) regions. Wing discs were costained for BRP^{N-Term} (red), BRP^{Nc82} (blue), and GFP (green). The D2-4 construct shows no BRP^{N-Term} reactivity, whereas the D1-3 construct lacks BRP^{Nc82} staining. Bar, 300 μ m. (C) Genomic analysis of the *brp* locus. The deletion mutants (*brp*⁶⁹ and *brp*^{6.1}) and their parental transposon insert lines are shown in green, and the pBac transposon insert line is shown in blue. Position of EMS-induced stop codons of *brp*^{1.3} and *brp*^{5.45} are shown in black.



family are generic AZ proteins. In mice, CAST/ERC proteins have been shown to localize to AZs of various synapses and to bind other AZ proteins such as RIM (Rab3a-interacting molecule) and Liprin- α (Ohtsuka et al., 2002; Wang et al., 2002; Ko et al., 2003; Deguchi-Tawarada et al., 2004). In *Caenorhabditis elegans*, the CAST/ERC family member ELKS (glutamine-, leucine-, lysine-, and serine-rich protein) appears to operate genetically downstream of Syd-2/Liprin- α during the assembly of AZs at vulval synapses (Dai et al., 2006; Patel et al., 2006). Recently, the CAST/ERC family member Bruchpilot (BRP), a coiled-coil rich protein of nearly 200 kD, was identified via its localization to *Drosophila* AZs. Mutants of *brp* lacked T-bars, and Ca²⁺ channels were mislocalized at AZs, leading to inefficient vesicle release and changes in synaptic short-term plasticity (Kittel et al., 2006; Wagh et al., 2006).

In this study, we provide evidence that BRP takes up an elongated conformation and is a direct component of the T-bar. The N terminus of BRP is found superimposed on the Ca²⁺ channel clusters at the AZ center. BRP and Cac arrive at an advanced stage of the protracted synapse assembly process, and both proteins interact in vitro. In contrast, a further AZ-organizing protein, *Drosophila* Liprin- α (DLiprin- α), localizes to a different subcompartment of the AZ and enters nascent AZs substantially earlier than BRP. Thus, the assembly of the T-bar is instructed by BRP, which seems essential for clustering higher numbers of Ca²⁺ channels at an advanced stage of AZ maturation.

Results

The AZ protein BRP was recently shown to be crucial for efficient neurotransmission at *Drosophila* NMJs. Presynaptic AZs missing BRP lacked dense bodies (T-bars), and Ca²⁺ channel

densities were compromised within AZs (Kittel et al., 2006). However, whether BRP performs an essential signaling role in T-bar formation or whether the protein itself is an essential building block of T-bars remained to be clarified. Thus, we entered into a structure-function analysis of BRP.

mAb Nc82 maps toward the C-terminal end of BRP

mAb Nc82 is derived from a *Drosophila* head extract-directed library (Hofbauer et al., 2009) and allowed the first identification of the BRP protein. mAb Nc82 is a widely used marker in *Drosophila*, both for neuropil in general and for AZs in particular (Wucherpfennig et al., 2003; Kittel et al., 2006; Wagh et al., 2006). Previously, we had loosely mapped the epitope of Nc82 to the region between aa 635 and the end of the 1,740-aa BRP protein (based on cDNA AT09405; Wagh et al., 2006). To define the Nc82 epitope more precisely, various BRP fragments (Fig. 1 A and Table I) were ectopically expressed in wing discs using *dpp-Gal4* (Fig. 1 B). In this manner, the mAb Nc82 epitope (hereafter BRP^{Nc82}) could be mapped to the region between aa 1,227 and 1,740. Additionally, an antibody directed against an N-terminal peptide (BRP^{N-Term} antibody; aa 62–75; Fig. 1 B) was produced.

Table I. BRP-reexpressing constructs

BRP fragments	Start (aa)	End (aa)
Domain 1 (D1)	1	320
Domain 2 (D2)	268	617
Domain 3 (D3)	473	1,226
Domain 4 (D4)	1,152	1,740

The predicted lengths in aa of the UAS-BRP fragments (relative to full-length BRP [1,740 aa]) are shown.

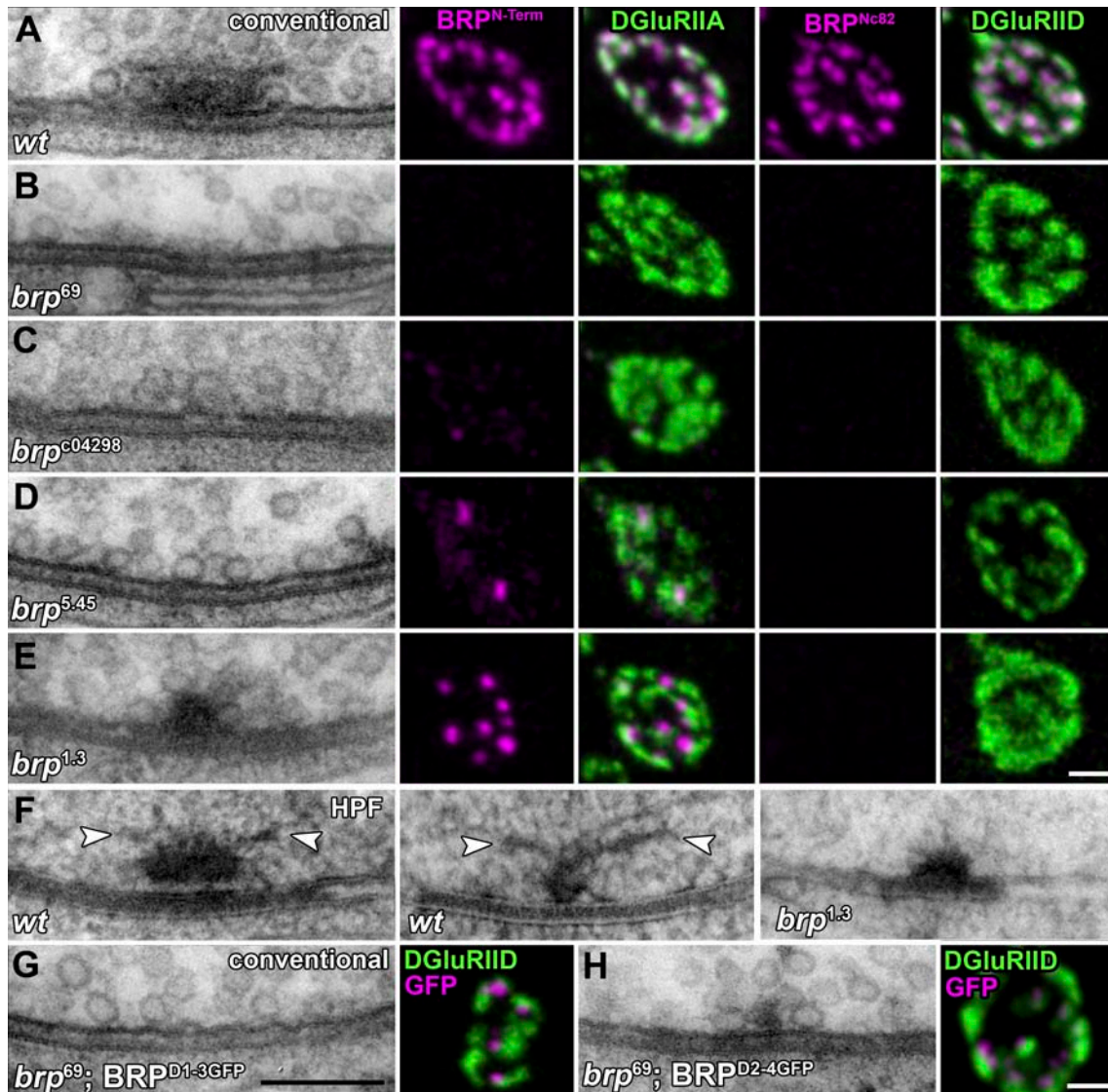


Figure 2. Combined electron and light microscopic analysis of AZ organization at NMJs of different *brp* alleles. (A–E, left) Ultrastructure of *Drosophila* NMJ AZs preserved with conventional room temperature embedding for transmission EM. The following genotypes are depicted: wild-type (*wt*; A), *brp*⁶⁹ (B), *brp*^{c04298} (C), *brp*^{5.45} (D), and *brp*^{1.3} (E). (right) Corresponding confocal images of boutons costained for either BRP^{N-Term} or BRP^{Nc82} (magenta) and DGlurIIA or DGlurIID (green). (F) Wild-type and *brp*^{1.3} T-bars preserved using HPF followed by FS. For controls, long (left) and short axis (middle) views of T-bars are depicted; arrowheads indicate filaments emerging from the T-bar pedestal. (G and H, left) Conventionally embedded AZs after expression of BRP^{D1-3GFP} and BRP^{D2-4GFP} in the *brp*⁶⁹ mutant background. In BRP^{D1-3GFP}, T-bar formation could not be observed. For BRP^{D2-4GFP}, electron-dense structures much smaller than T-bars were observed. (right) Corresponding confocal images of the reexpression constructs costained for GFP (magenta) and DGlurIID (green). Bars: (G) 200 nm; (E and H) 500 nm.

Structure-function analysis of BRP in T-bar formation

So far, the analysis of BRP function was based on the *brp*⁶⁹ allele in which most of the protein-coding sequence (corresponding to aa 283–1,740) is deleted (Fig. 1 C, green). As previously reported, T-bars were missing at *brp*⁶⁹ AZs (Fig. 2, compare A and B), and the BRP^{Nc82} label (Fig. 2, A and B) was absent (Kittel et al., 2006). The BRP^{N-Term} label was also completely absent (Fig. 2 B), indicating that the predicted residual protein (corresponding to aa 1–282) is unstable or at least does not localize to the NMJ. To ensure that *brp*⁶⁹ reflects a true null phenotype, we produced the deletion mutant *brp*^{6.1} (Fig. 1 C, green) in which all genomic sequences of *brp* were removed (see

Materials and methods). This led to a complete loss of BRP^{Nc82}/BRP^{N-Term} labels and T-bars, whereas some traces of residual electron-dense material appeared at the same frequency as in *brp*⁶⁹ (Kittel et al., 2006; unpublished data). As *brp*^{6.1} and *brp*⁶⁹ (Kittel et al., 2006) behaved identically in all aspects, our previous analysis based on *brp*⁶⁹ reflected a true null situation.

BRP is a large protein (1,740 aa). To enter into a structure-function analysis of BRP in T-bar assembly, additional *brp* alleles were looked into. First, a piggyBac-transposon insert (*brp*^{c04298}; Fig. 1 C, blue; Bellen et al., 2004) located toward the middle of the locus was characterized. At *brp*^{c04298} NMJs, the BRP^{Nc82} label was absent, whereas the BRP^{N-Term} label was dramatically reduced (Fig. 2 C). Comparable with our observations

for *brp*⁶⁹ (Kittel et al., 2006), electron microscopic analysis of *brp*^{c04298} showed a complete lack of T-bars (Fig. 2 C), and only traces of electron-dense material remained at AZ membranes. Thus, as this allele is a site-specific insertion but not a deletion (which in principle might eliminate control elements of genes other than *brp*), this allele provides further proof that BRP is essential for T-bar assembly. However, as the molecular alterations of *brp*^{c04298} cannot be predicted easily, we sought to analyze aa point mutations in *brp*. To do so, a chemical mutagenesis screen (ethyl methyl sulfonate [EMS]) selecting for reduced viability over *brp*-null alleles was performed.

The *brp*^{5.45} allele is characterized by a stop codon at aa position 867 (~50% protein length), which leads to pupal lethality over *brp* null with weak escapers (Fig. 1 C). As expected, the BRP^{Nc82} label was absent from *brp*^{5.45} NMJs. Although the number of BRP^{N-Term} clusters was reduced over the whole NMJ (Fig. S1 A), those remaining in *brp*^{5.45} were slightly smaller, although of comparable intensity as in controls (Fig. 2 D; and Fig. S1, B and C). Despite extensive analysis, T-bars were not detected at *brp*^{5.45} NMJs (Fig. 2 D).

The EMS allele *brp*^{1.3} delivered paralyzed adult escapers over *brp* null as the result of a premature stop codon at aa 1,390 (generating a protein 523 aa longer than predicted for *brp*^{5.45}; Fig. 1 C). Although the number of BRP^{N-Term} clusters was reduced to ~40% (Fig. S1 A), their sizes and intensities were comparable with controls. At the same time, the BRP^{Nc82} label was absent (Fig. 2 E). T-bar-like structures were observed at *brp*^{1.3} NMJs (Fig. 2 E), although at lower frequency than in controls (not depicted). However, upon closer inspection, the T-bar-like structures typically appeared truncated (Fig. 2).

For EM, conventional room temperature embedding procedures, including aldehyde fixation and dehydration of the tissue (Fig. 2, A–E), are prone to shrinkage artifacts. To use an alternative conservation method for the analysis of *brp*^{1.3}, we introduced high pressure freezing (HPF)/freeze substitution (FS) EM (Gray et al., 2006; Rostaing et al., 2006; Siksou et al., 2007) to larval NMJs. With HPF/FS, NMJ tissue appeared well preserved, as judged by the smooth membrane surfaces of, for example, mitochondria (Fig. S2, A and B) or presynaptic boutons (not depicted). Furthermore, electron-dense structures appeared taller, which was likely caused by a reduced loss of material during HPF/FS embedding (e.g., the synaptic cleft; Fig. 2 F). Unlike T-bars visualized in conventionally embedded tissues, HPF/FS-processed T-bars were characterized by filamentous elements at their distal ends (Fig. 2 F, arrowheads). At *brp*^{1.3} NMJs, HPF/FS EM (similarly to our observations obtained with standard EM) typically revealed shortened T-bars (Fig. S2 C, quantification). In conclusion, elimination of aa 1,390–1,740 of BRP did not prevent the formation of T-bar-like assemblies per se. However, these assemblies were significantly smaller than in controls. This result is in line with the assumption that BRP operates as a building block shaping the T-bar.

To both confirm and extend our results, BRP-encoding cDNA fragments (C-terminally GFP tagged for in vivo visualization) were expressed in motoneurons of *brp*⁶⁹ larvae (Fig. 2, G and H). As expected (Kittel et al., 2006), full-length BRP localized to AZs and restored T-bar formation (not depicted). The

C-terminally truncated fragment D1-3^{GFP} (BRP^{D1-3GFP}; Δ aa 1,227–1,740; Fig. 1 A and Table I) localized to presynaptic sites but was not sufficient for T-bar formation (Fig. 2 G). Thus, expression of BRP^{D1-3GFP} further suggests that the C-terminal region of BRP (distal of aa 1,226; Table I) is important for T-bar formation.

By expressing D2-4^{GFP} (BRP^{D2-4GFP}; Δ aa 1–267; Fig. 1 A and Table I), the role of the N-terminal region of BRP was tested. The expressed protein was found close to individual AZs (Fig. 2 H). Although T-bars were never observed, small electron-dense aggregates (clearly smaller than T-bars) localized to the AZ membrane at high frequency (Fig. 2 H). Thus, the N-terminal region of BRP seems important for the formation of proper, full-sized T-bars, whereas the C-terminal region is required for the assembly of T-bars by itself. Thus, the entire BRP protein appears to take part in configuring the T-bar structure.

BRP epitopes reside at the electron-dense T-bar matrix

To monitor whether BRP epitopes are associated with the electron-dense T-bar matrix, HPF/FS samples were subjected to immuno-EM. The antibodies to both epitopes, BRP^{N-Term} and BRP^{Nc82}, bound to the T-bar matrix (Fig. 3). Notably, the BRP^{N-Term} antibody showed higher labeling efficacy (Fig. 3, compare B with C) and was found throughout cross-sectional views of T-bars in vertical sections (Fig. 3 B, right).

In contrast, BRP^{Nc82}-conjugated gold particles were typically found at the most distal edge of electron-dense structures in vertical sections (Fig. 3 C, right). From the expression of ectopic BRP fragments (Fig. 1, A and B) and *brp*^{1.3} (Fig. 2 E), it is clear that the Nc82 epitope must be located distal to aa 1,390 in the C-terminal quarter of the protein. When comparing BRP^{N-Term} and BRP^{Nc82}, the BRP^{N-Term} label appeared significantly closer to the AZ membrane than the BRP^{Nc82} label (Fig. 3 D). Thus, the N-terminal region of BRP seems to reside closer to the AZ membrane than the C-terminal region. However, it should be noted that because of the moderate membrane contrast possible with the immuno-EM technique used, the angle at which AZs are observed cannot be exactly determined. This complicates a quantitative analysis. Collectively, both BRP epitopes are found at the T-bar matrix, and the ultrastructural analysis supports the notion that BRP is a direct component of the T-bar.

BRP^{Nc82} and BRP^{N-Term} epitopes are vertically segregated relative to the AZ membrane

To validate and extend our findings concerning the localization of BRP^{N-Term} and BRP^{Nc82}, further light microscopic experiments were performed. Conventional fluorescence microscopy is highly compatible with protein-specific labeling and enables the processing of high sample numbers. Importantly, confocal sectioning of *Drosophila* NMJ boutons allows for a reliable definition of the orientation of synapses relative to the optical axis because bouton surfaces are nearly spherical. Hereafter, tangentially imaged AZs are called planar AZs, whereas vertically imaged AZs are referred to as vertical AZs.

We were interested in visualizing the BRP protein with its distinct epitopes in relation to the remainder of the AZ and

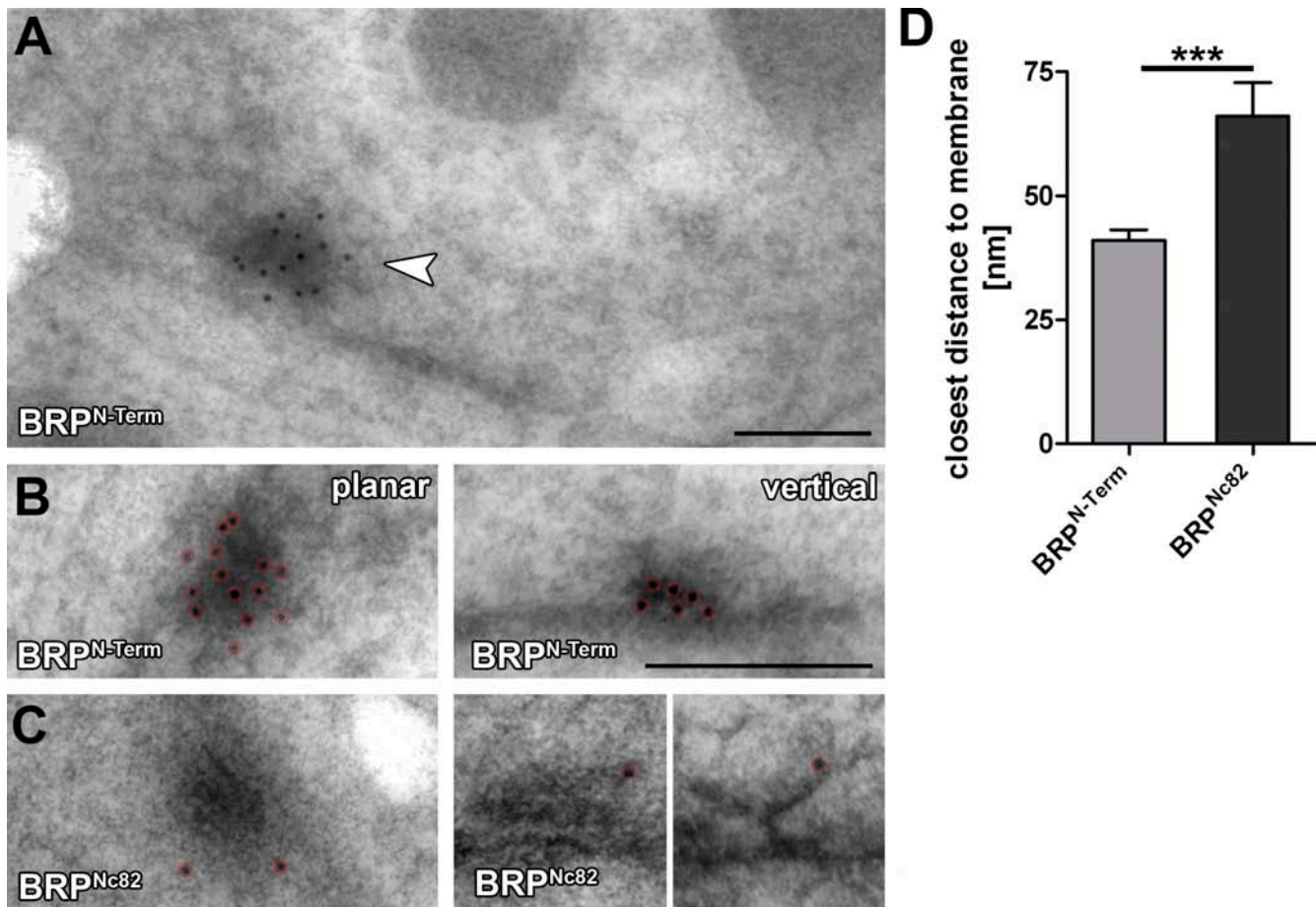


Figure 3. **Immuno-EM versus two BRP epitopes at *Drosophila* NMJ AZs.** (A) High pressure frozen bouton prepared for immunogold labeling, indicating a T-bar labeled for BRP^{N-Term} (arrowhead). (B and C) Magnifications of individual planar (left) and vertically (right) imaged T-bars labeled (after embedding) for either BRP^{N-Term} (B) or BRP^{Nc82} (C). Gold particles are highlighted by red circles. (D) Quantification of BRP^{N-Term} and BRP^{Nc82} signals of the closest distance of individual gold particles to the AZ membrane. Error bars indicate mean \pm SEM. ***, $P < 0.005$. Bars: (A) 150 nm; (B) 200 nm.

the synapse. Therefore, center of mass distances at vertical AZs (along an axis perpendicular to the AZ membrane) were performed with standard confocal microscopy. First, to test this approach, the distance between postsynaptic glutamate receptors (intracellular epitope on *Drosophila* glutamate receptor subunit IID [DGluRIID]; Qin et al., 2005) and presynaptic Ca²⁺ channels (Cac^{GFP} [GFP at intracellular C terminus of Cac]; Kawasaki et al., 2004) was measured. A value of 40 nm was determined (Fig. 4 A), which is compatible with a distance of ~ 35 nm between the cytoplasmic leaflets of pre- and postsynaptic membranes, as measured with EM at NMJ synapses (not depicted).

As expected, mAb Nc82 identified diffraction-limited spots opposite the center of postsynaptic densities (PSDs; Fig. 4 B). Notably, BRP^{Nc82} and DGluRIID signals were separated by ~ 155 nm (Fig. 4, A and B), and BRP^{Nc82} and Cac^{GFP} were separated by ~ 110 nm (Fig. 4, A and C). Thus, the epitope recognized by BRP^{Nc82} is clearly localized at a distance away from the presynaptic AZ membrane, which is consistent with our immuno-EM findings (Fig. 3, C and D). Next, we colabeled BRP^{N-Term} and BRP^{Nc82} (Fig. 4 D). The BRP^{N-Term} label was found ~ 70 nm closer to the plasma membrane than the C-terminal label (Fig. 4 A).

Our measurements were performed using sandwiches of primary antibodies and labeled secondary antibodies. For distances in the double-digit nanometer range, the size of individual Ig molecules (used for the detection of epitopes) might be relevant. Thus, we sought to independently validate the distance between BRP N and C termini. To do so, BRP^{D1-4GFP} was expressed in the *brp*⁶⁹ background, and the distance between the BRP C terminus (endogenous GFP fluorescence) and the N terminus (BRP^{N-Term} antibody) was determined (Fig. 4 A). Again, ~ 70 nm was measured. Finally, the center to center distance between BRP^{N-Term} and Cac^{GFP} was measured as ~ 60 nm (Fig. 4 A). Collectively, we conclude that the BRP^{Nc82} and BRP^{N-Term} epitopes are segregated along an axis perpendicular to the AZ membrane.

The BRP N terminus displays a confined distribution close to the AZ membrane

We proceeded to study the molecular organization of AZs at the *Drosophila* NMJ with STED microscopy to obtain improved optical resolution in xy coordinates. Previously, it was demonstrated that BRP^{Nc82} forms doughnut-shaped structures when visualized at AZs arranged planar to the optical axis (Kittel et al., 2006). BRP^{Nc82} doughnuts were reproduced from planar AZs (Fig. 5, A [arrow] and B) with a resolution displaying an

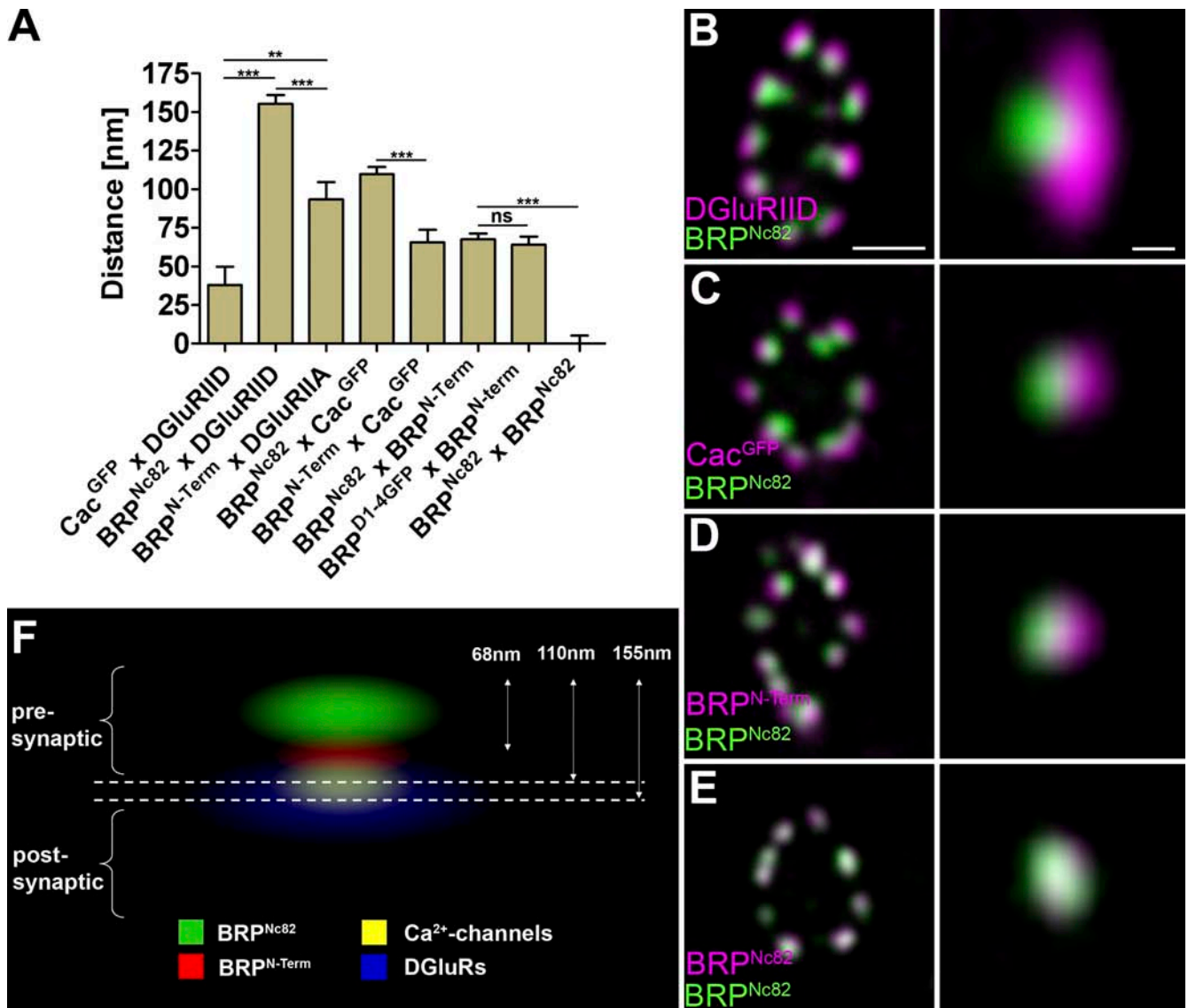


Figure 4. Polarized orientation of BRP at AZs. (A) Distances of center to center intensity maxima for different synaptic labels are as follows: Cac^{GFP} × DGlurIID, 37.9 ± 11.9 nm ($n = 30$); BRP^{Nc82} × DGlurIID, 155.2 ± 5.7 nm ($n = 30$); BRP^{N-Term} × DGlurIID, 93.4 ± 11.3 nm ($n = 30$); BRP^{Nc82} × Cac^{GFP}, 109.8 ± 4.6 nm ($n = 30$); BRP^{N-Term} × Cac^{GFP}, 65.6 ± 7.9 nm ($n = 30$); BRP^{Nc82} × BRP^{N-Term}, 67.5 ± 3.8 nm ($n = 70$); D1-4^{GFP} × BRP^{N-Term}, 64.2 ± 5.1 nm ($n = 40$); BRP^{Nc82} × BRP^{Nc82}, 0.0 ± 5.2 nm ($n = 30$). Error bars indicate mean ± SEM. **, $P < 0.01$; ***, $P < 0.005$. (B–E) Confocal images of midsections through the bouton (left) and single vertically imaged synapses (right) with the bouton lumen facing left. (B) Magenta, DGlurIID; green, BRP^{Nc82}. Bars: 500 nm (left) and 100 nm (right). (C) Magenta, Cac^{GFP}; green, BRP^{Nc82}. (D) Magenta, BRP^{N-Term}; green, BRP^{Nc82}. (E) Magenta, BRP^{Nc82}; green, BRP^{Nc82}. (F) Schematic model of protein epitope distribution at an individual NMJ AZ.

effective point-spread function (PSF) of 80-nm full-width half-maximum. Other than BRP^{Nc82}, BRP^{N-Term} did not show a doughnut-shaped distribution when imaged with STED (Fig. 5 C). Instead, the BRP^{N-Term} signal appeared centered within the “doughnut hole” of the BRP^{Nc82} signal at planar AZs, as also apparent after averaging STED signals from individually aligned AZs (Fig. 5 D). The combination of STED resolution (confined to one channel in our experiments) for BRP^{Nc82} and confocal resolution for BRP^{N-Term} revealed a polarized and funnel-like distribution of BRP epitopes (Fig. 5, A–C). Notably, the BRP^{Nc82} signal did not appear fully continuous but instead consisted of discrete foci (Fig. 5, B and F) within an overall circular array. In an additional experiment, we expressed full-length BRP^{D1-4} (Wagh et al., 2006) in *brp*⁶⁹ mutants. The distance between BRP^{N-Term}

and BRP^{Nc82} was similar to that observed at control AZs (Fig. 5 E). This suggests that individual BRP molecules can adopt an elongated conformation.

The N terminus of BRP overlays the Ca²⁺ channels at the AZ core

How does the molecular architecture of BRP relate to Ca²⁺ channels at AZs? Ca²⁺ channel spots (Cac^{GFP}) imaged at standard confocal resolution were found to cocenter with the BRP^{N-Term} label and BRP^{Nc82} doughnuts at planar AZs. At vertical AZs, the Cac^{GFP} signal localized toward the AZ membrane relative to both BRP^{N-Term} (Fig. 5 C) and BRP^{Nc82} (Fig. 5, F and G). When imaged with STED resolution, Ca²⁺ channels consistently localized to small, typically slightly elliptical patches (~100–150 nm

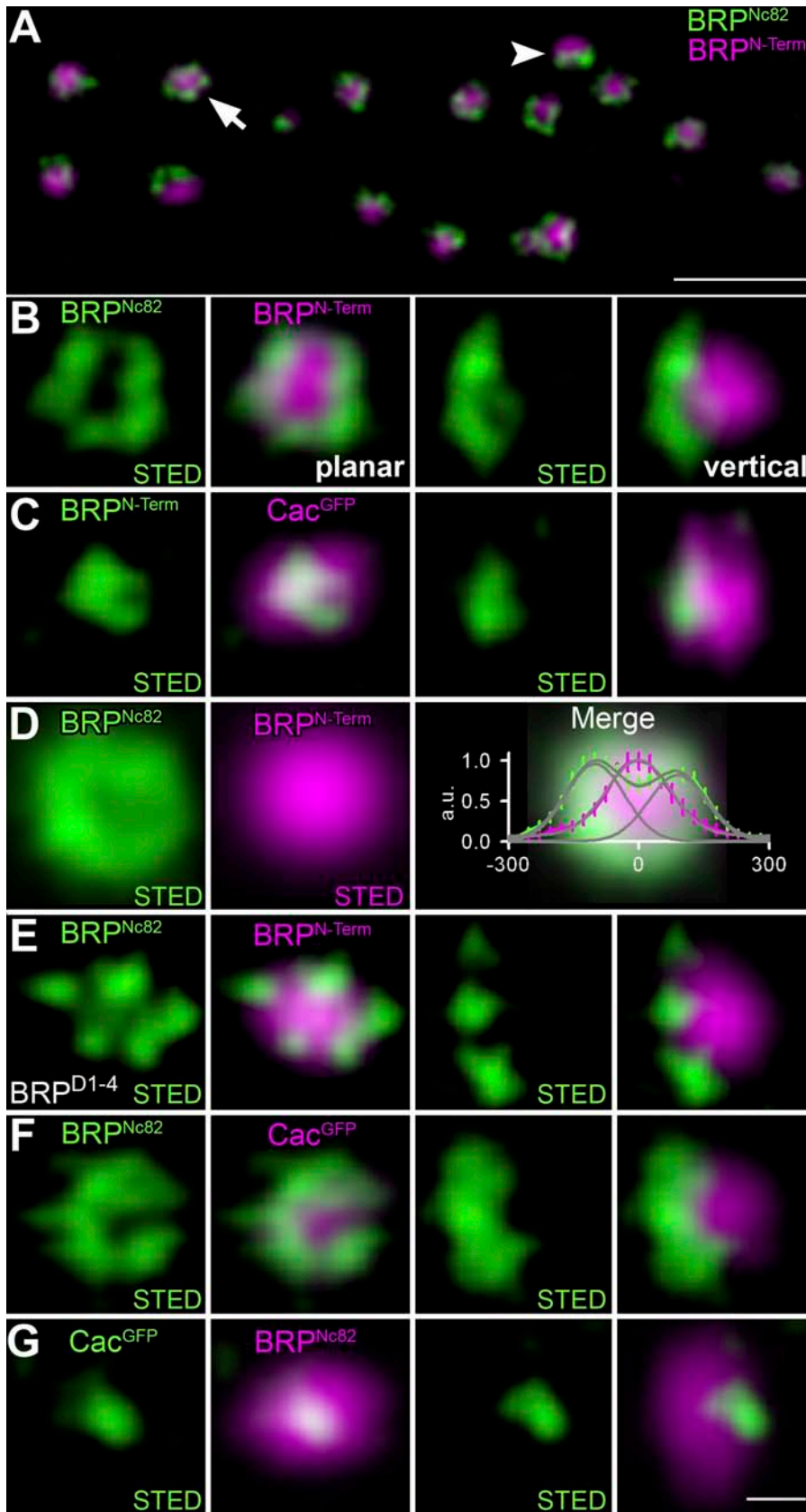
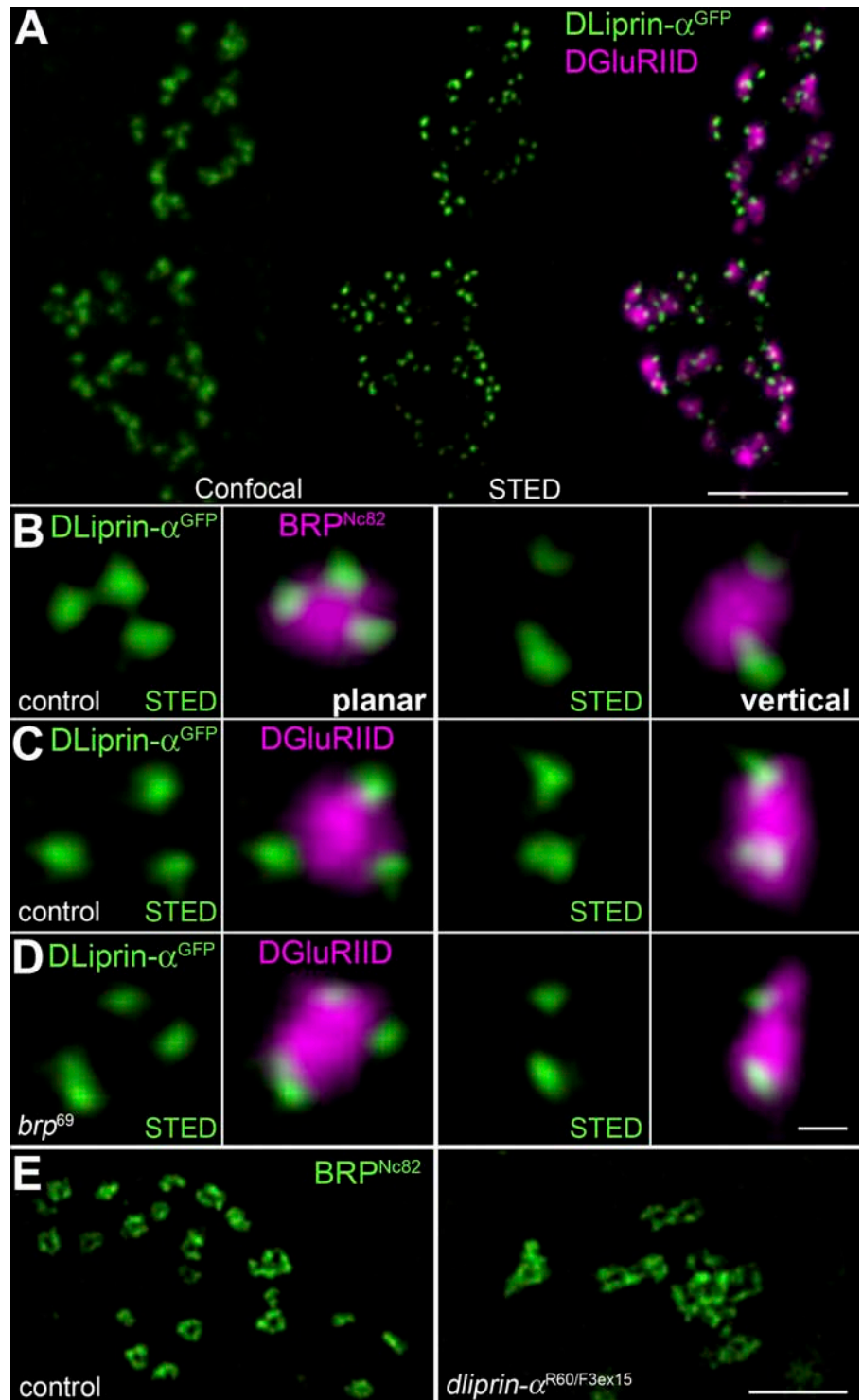


Figure 5. **STED analysis of AZ organization at *Drosophila* NMJ synapses.** (A) Overview of a bouton stained for BRP^{N-Term} (confocal; magenta) and BRP^{Nc82} (STED; green) showing planar (arrow) and vertical (arrowhead) AZs. (B and C) Magnifications of individual planar (left) and vertical (right) AZs stained for BRP^{Nc82} (STED) and BRP^{N-Term} (confocal; B) and BRP^{N-Term} (STED) and Cac^{GFP} (confocal; C). (D) Mean normalized planar BRP^{N-Term} (magenta) and BRP^{Nc82} (green) arrangement shown with STED resolution (BRP^{N-Term}, n = 14; BRP^{Nc82}, n = 47). (right) The merge superimposed with the intensity profile along one axis through the midpoint for BRP^{N-Term} (magenta) and BRP^{Nc82} (green) is shown. Error bars indicate ± SEM. (E) BRP^{Nc82} (STED) and BRP^{N-Term} (confocal) after expression of full-length BRP cDNA in *brp*⁶⁹ background (BRP^{D1-4}). (F and G) Individual planar (left) and vertical (right) AZs stained for BRP^{Nc82} (STED) and Cac^{GFP} (confocal; F) and Cac^{GFP} (STED) and BRP^{Nc82} (confocal; G). All images were deconvolved using lmspector software. Bars: (A) 1 μm; (G) 100 nm.

Figure 6. STED microscopic analysis of DLiprin- α^{GFP} at AZs. (A) Single confocal sections of NMJs colabeled for DLiprin- α^{GFP} (green, confocal resolution in left image and STED resolution in middle image) and DGluRIID (magenta, confocal overlay in right image). STED images of DLiprin- α^{GFP} reveal substructures beyond the diffraction limit of confocal microscopy. (B–D) STED images of an individual AZ. Discrete dots of DLiprin- α^{GFP} are arranged at the AZ edge (magenta, BRP^{Nc82} [B] and DGluRIID [C and D]). Left, planar AZ; right, vertical AZ. B and C show controls, and D shows *brp*⁶⁹. (E) Single confocal slices of control (left) and *dliprin- α* (right) junctions labeled for BRP^{Nc82} with STED resolution. Atypical clusters of BRP doughnuts are observed at *dliprin- α* mutant NMJs. Bars: (A) 1.5 μ m; (D) 100 nm; (E) 1 μ m.



along the longest axis) at the AZ center (Fig. 5 G). Thus, the T-bar organized by BRP overlays the field of Ca²⁺ channels at the AZ center.

DLiprin- α localizes to discrete compartments surrounding the AZ center

Liprin- α localizes to the AZ and has been shown to be important for the formation of AZs in both *Drosophila* and *C. elegans* (Kaufmann et al., 2002; Dai et al., 2006; Patel et al., 2006). To extend our “AZ

map,” DLiprin- α^{GFP} was expressed in motoneurons and visualized via α GFP stainings with STED microscopy (Fig. 6 A). DLiprin- α localized to presynaptic AZs opposite DGluRIID-positive PSDs. However, as opposed to BRP, DLiprin- α clustered somewhat lateral from the AZ center. STED resolution revealed that DLiprin- α formed discrete “quantal” clusters at the edge of a single AZ colabeled with BRP^{Nc82} (Fig. 6 B) or DGluRIID (Fig. 6 C).

Discrete DLiprin- α clusters were still observable at *brp*⁶⁹ NMJs, suggesting that the presence of BRP is not essential for

the recruitment of DLiprin- α to the AZ (Fig. 6 D). However, the localization of BRP, as imaged with STED, appeared aberrant at *dliprin- α* NMJs (Fig. 6 E). Strikingly, individual BRP doughnuts seemed interconnected, which is directly consistent with the previous observation of complex, multi-T-bar AZs at *dliprin- α* mutant NMJs (Kaufmann et al., 2002).

BRP and Ca²⁺ channels accumulate late during AZ assembly

So far, we have provided evidence that BRP operates as an essential building block of the T-bar. Notably, fast assembly of T-bars might drive experience-dependent changes of synaptic transmission in the fly central nervous system (Brandstatter et al., 1991; Rybak and Meinertzhagen, 1997). Thus, to learn about the T-bar assembly process in the frame of synapse reorganization, we visualized BRP accumulation in vivo during the developmental formation of individual synapses (Rasse et al., 2005; Fuger et al., 2007; Schmid et al., 2008). Previously, we found that neuromuscular accumulation of glutamate receptors (as DGluRIAs) in PSDs typically form at a distance from existing PSDs and then grow over several hours before reaching a final mature size (Rasse et al., 2005; Schmid et al., 2008). Thus, for the analysis of AZ assembly in vivo, DGluRIIA was coimaged to serve as a reference point for our temporal analysis (Fig. 7, A, B, and D; and Table II).

Larvae coexpressing two fluorescently tagged synaptic proteins were imaged (Fig. 7), and quantitative data were obtained to analyze the temporal sequence of protein arrival at developing AZs. For a given larval NMJ, two in vivo images were acquired with a time interval of 12 h. Sites were regarded as new synapses if protein labels exceeded the mean background by a factor of 2.5 at the second ($t = 12$ h) but not at the first time point ($t = 0$ h). This way, a temporal sequence of molecular AZ assembly was extracted.

We first compared BRP and DGluRIIA accumulation. For visualization of BRP, we used a fragment of the protein (BRP-short), which delivered a label that fully matched the label of endogenous BRP (Schmid et al., 2008). When BRP-short^{GFP} was examined with STED, doughnuts were detected that resembled those found with BRP^{Nc82} (unpublished data). As previously described (Schmid et al., 2008), the accumulation of DGluRIIA clearly preceded BRP arrival in vivo (Fig. 7 A and Table II). Moreover, all postsynaptic DGluRIIA accumulations eventually

incorporated presynaptic BRP, demonstrating that DGluRIIA accumulation reliably indicates the formation of new synapses.

As described in the previous section, presynaptic DLiprin- α localization seems to be largely independent of BRP (Fig. 6 D), which is compatible with DLiprin- α functioning upstream of BRP in AZ assembly. Consistently, DLiprin- α incorporation invariably preceded BRP accumulation (Fig. 7 C and Table II).

BRP is crucial for either the initial formation or the maintenance of Ca²⁺ channel clusters. Thus, we analyzed Cac localization at individual developing AZs. Cac and BRP appeared highly correlated, and the timing of Cac accumulation at AZs was typically very close to the advent of BRP with a slight tendency of Cac to precede BRP (Fig. 7 E and Table II).

Collectively, we show that newly forming AZs, similar to PSDs (Rasse et al., 2005), are small to begin with and then increase in size over many hours in vivo before accumulating detectable levels of BRP and reaching a final mature size at developing NMJs. This assembly process of individual new synapses is protracted over hours and is characterized by the contribution of pre- and postsynaptic proteins in a defined, overlapping sequence. DLiprin- α appears to be a very early player involved in initializing AZ assembly, whereas BRP, together with Cac, follows only after postsynaptic DGluRIIA incorporation is already clearly detectable (Fig. 7, A and D).

BRP controls Ca²⁺ channel accumulation at maturing AZs

If Cac slightly precedes BRP during assembly, how can the Cac-clustering defects described in *brp*⁶⁹ (Kittel et al., 2006) be explained? To exclude allele-specific effects, we first scored Cac clustering at AZs (opposite DGluRIID receptor fields) in the *brp* alleles *brp*^{6.1}, *brp*⁶⁹, *brp*^{c04298}, and *brp*^{1.3} (Fig. 8 A). A Cac-clustering defect identical to that found in *brp*⁶⁹ was observed in the full-deletion *brp*^{6.1}. As expected, *brp*^{c04298} also showed an identical clustering defect (Fig. 8 A). Previously, we provided evidence that the Cac delocalization in *brp*⁶⁹ is responsible for reduced neurotransmitter release. In this study, we took the opportunity to test the influence of BRP on neurotransmission independently of *brp*⁶⁹ and recorded from *brp*^{c04298} NMJs. All electrophysiological features of *brp*^{c04298}, including the alterations of short-term plasticity connected to defective Ca²⁺ channel clustering, were similar to

Table II. Quantification of protein accumulation during AZ assembly using NMJ in vivo imaging

Coexpressed proteins (A × B)	Both A and B	A before B	B before A
BRP × DGluRIIA	BRP ⁺ /IIA ⁺ 17/39 (44%)	BRP ⁺ /IIA ⁻ 0/39 (0%)	BRP ⁻ /IIA ⁺ 22/39 (56%)
DLiprin- α × DGluRIIA	DLiprin- α ⁺ /IIA ⁺ 16/39 (41%)	DLiprin- α ⁺ /IIA ⁻ 23/39 (59%)	DLiprin- α ⁻ /IIA ⁺ 0/39 (0%)
BRP × DLiprin- α	BRP ⁺ /DLiprin- α ⁺ 8/31 (26%)	BRP ⁺ /DLiprin- α ⁻ 0/31 (0%)	BRP ⁻ /DLiprin- α ⁺ 23/31 (74%)
DGluRIIA × Cac	IIA ⁺ /Cac ⁺ 36/62 (58%)	IIA ⁺ /Cac ⁻ 21/62 (34%)	IIA ⁻ /Cac ⁺ 5/62 (8%)
BRP × Cac	BRP ⁺ /Cac ⁺ 42/62 (68%)	BRP ⁺ /Cac ⁻ 7/62 (11%)	BRP ⁻ /Cac ⁺ 13/62 (21%)

Quantification of the relative accumulation of the indicated synaptic proteins at newly forming AZs ($\Delta t = \sim 12$ h). A synaptic site was scored positive (+) or negative (-) for a specific protein depending on whether protein fluorescence signals exceeded the mean background level by >2.5-fold. For example, when comparing BRP and DGluRIIA (at synapses forming newly over 12 h), 44% were positive for both proteins, 0% for BRP only, and 56% for DGluRIIA only.

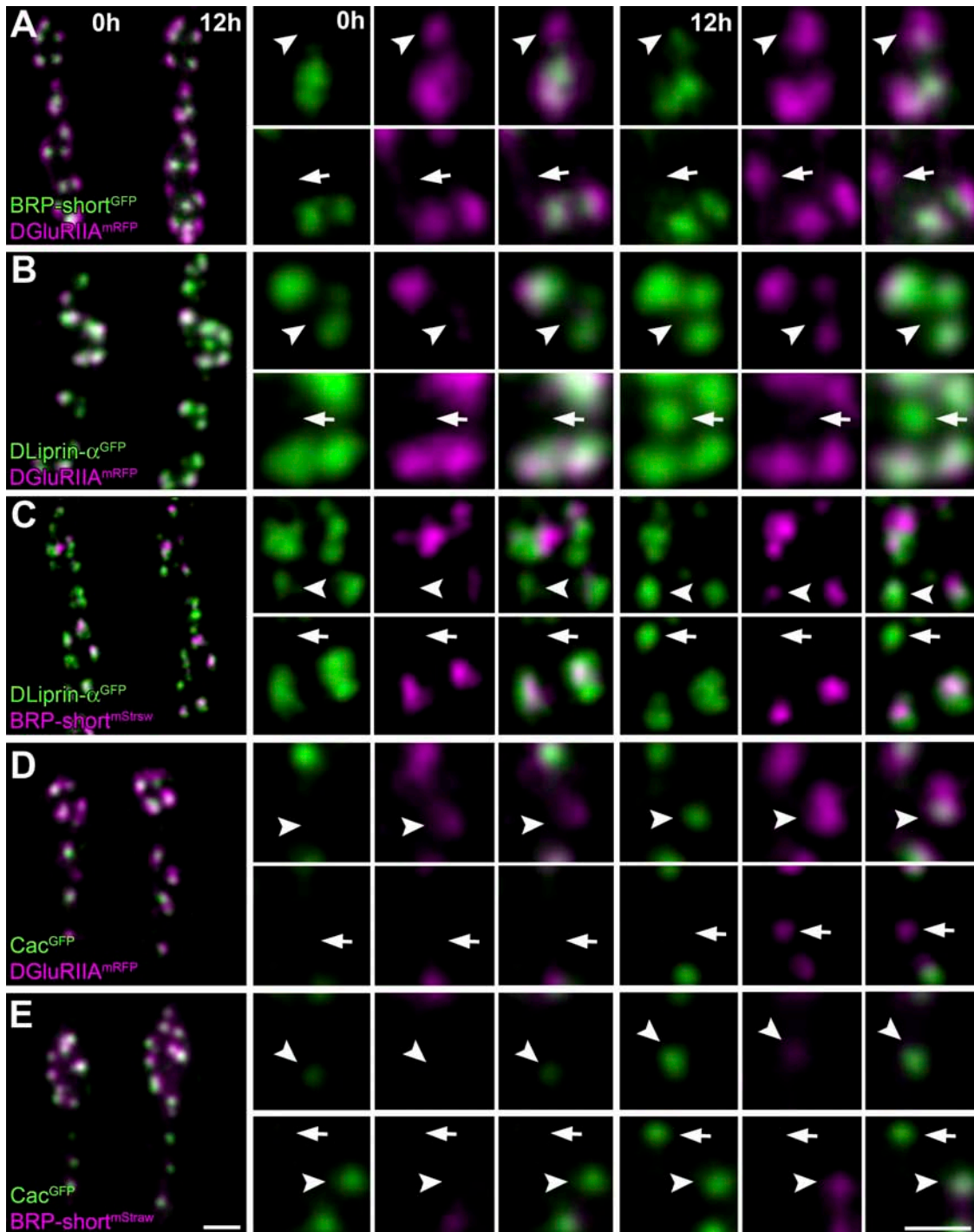
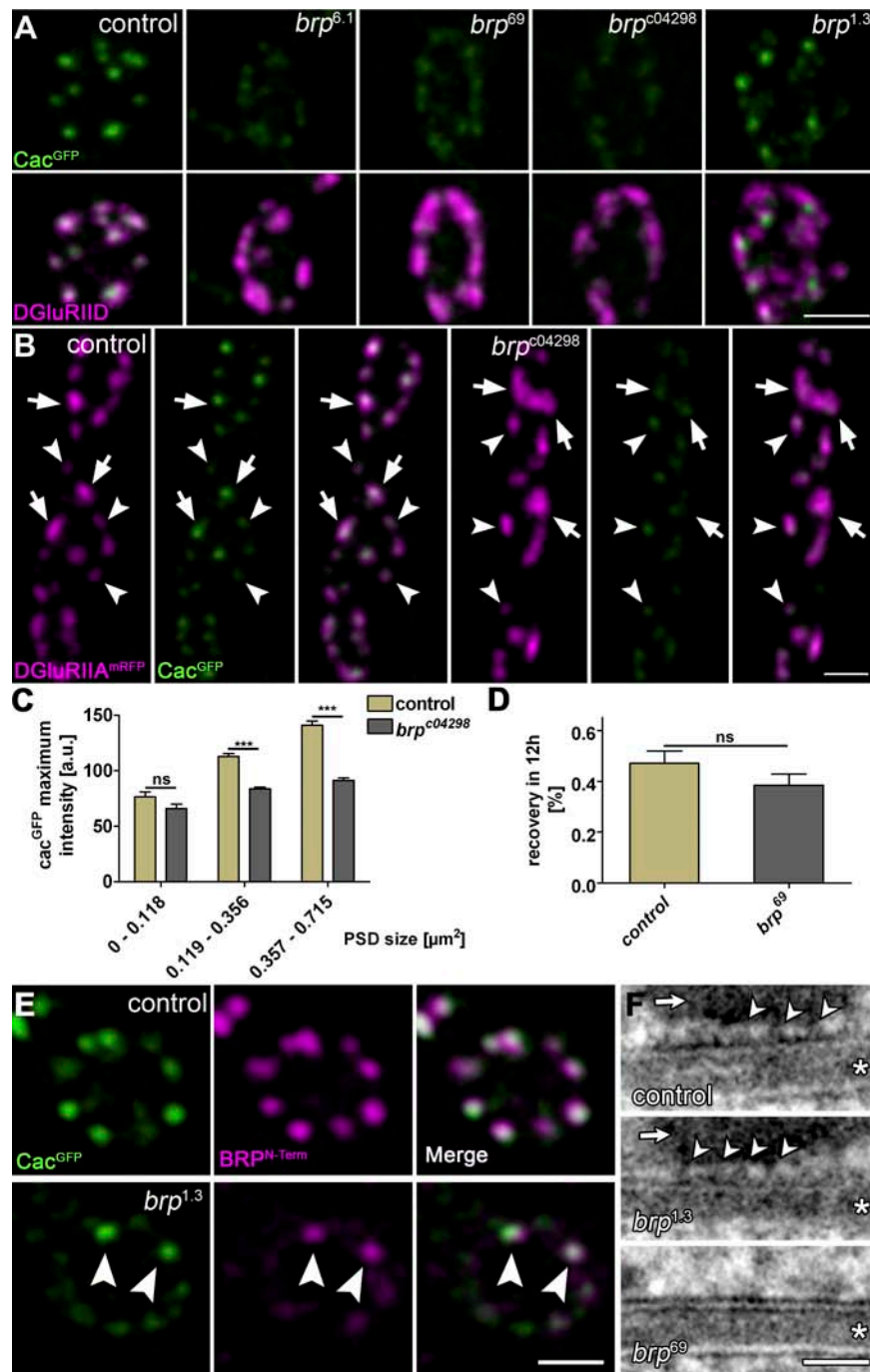


Figure 7. **In vivo analysis of synaptic protein accumulation.** (A–E) Confocal stacks of sequentially in vivo-imaged NMJs (muscle 26) at $\Delta t = 12$ h. NMJs coexpress the indicated labels (green, GFP constructs; magenta, mRFP constructs). (top) Individual in vivo-imaged synapses (arrowheads) positive for only one label at $t = 0$ h but positive for both labels at $t = 12$ h are shown. (bottom) A prospective synapse (arrows) positive for only one label at $t = 12$ h is shown. Bars, 1 μ m.

those observed in *brp*⁶⁹ (Fig. S3; Kittel et al., 2006). Thus, several independent alleles clearly demonstrate that loss of BRP results in defective clustering of Cac at the AZ, which in turn provokes defects in transmitter release.

Notably, the mislocalization of Cac is not absolute, but instead, a certain degree of Cac remained clustered at AZs in *brp* null. As our in vivo imaging experiments show (Fig. 7), AZs go through a long, protracted assembly process before finally

reaching their fully mature size. Thus, we wondered whether BRP may be more important for maturation and potentially less so for initialization of Cac clustering. To address this, we visualized Cac in intact, living *brp*^{c04298} mutant larvae together with DGluRIIA as a reference for synapse maturation (Fig. 8 B). In *brp*^{c04298} larvae, nascent synapses, identified by their small DGluRIIA accumulations, seemed to accumulate Cac at normal density (Fig. 8, B and C). However, larger, more mature synapses



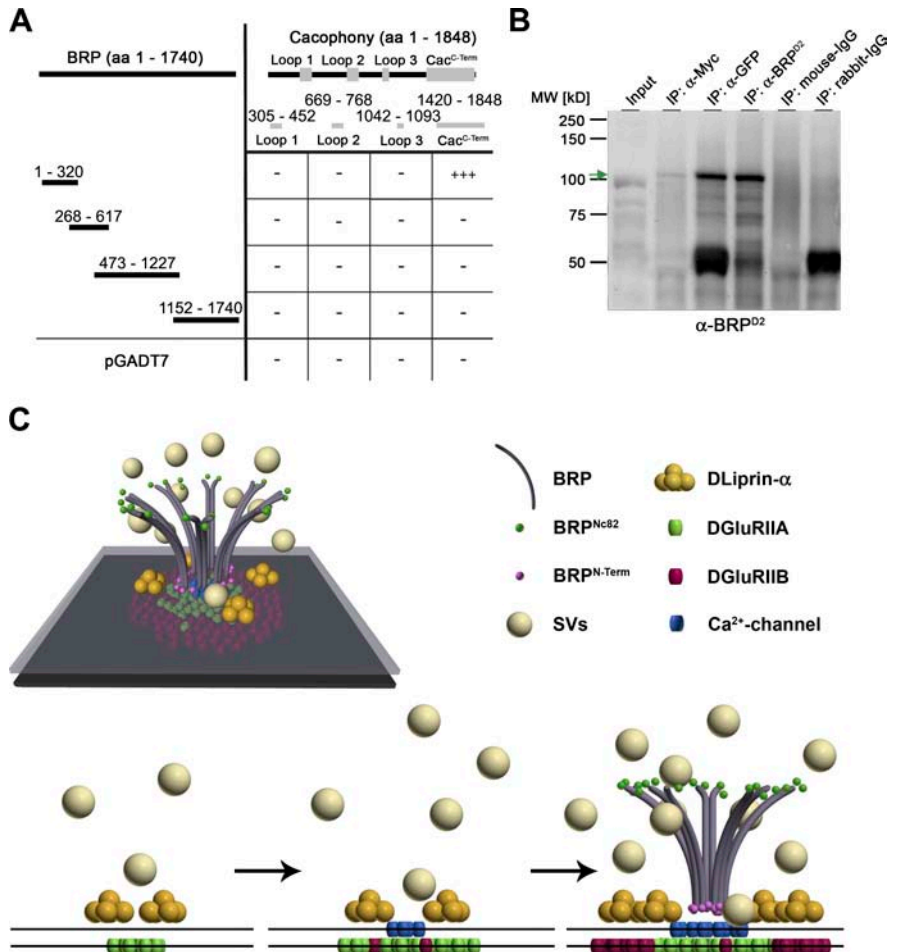
with more substantial DGLuRIIA accumulations showed reduced *Cac* density in the absence of BRP (Fig. 8, B and C). In clear contrast, the recruitment of *Cac*^{GFP} to AZs appears to be independent of presynaptic DLiprin-α, as the localization of Ca²⁺ channels appears normal in *dliprin-α* mutants (Fig. S4).

Our data imply the following scenario: BRP, an integral component of the T-bar, is recruited to AZs later than DLiprin-α. BRP seems largely dispensable for the initial Ca²⁺ channel accumulation. However, the matrix organized by BRP is required for maintaining the continuous clustering of Ca²⁺ channels beneath the T-bar base during the maturation process, which lasts several hours.

Alternatively, the Ca²⁺ channel-clustering defect in *brp* could be caused by impaired *Cac* transport. To address this, *Cac* trafficking dynamics were measured using FRAP experiments. Notably, *Cac* FRAP was slow, with a recovery half-time of ~12 h (Fig. 8 D), which is similar to other synaptic membrane proteins such as DGLuRIIA (Schmid et al., 2008). Importantly, however, *Cac* FRAP was essentially unaltered at *brp* boutons, indicating that the long-range transport of *Cac* to the AZ is not affected by the loss of BRP (Fig. 8 D). Thus, BRP seems to be directly required for Ca²⁺ channel clustering at AZs but not for its recruitment to the terminal. We aimed to further address the relation between T-bar assembly and Ca²⁺ channel clustering. Notably,

Figure 9. The N terminus of BRP physically interacts with the C terminus of Cac in vitro.

(A) Scheme of yeast two-hybrid analysis using Cac bait constructs and overlapping BRP prey constructs. Full-length Cac protein comprises three large intracellular loops (aa are indicated) and its intracellular C-terminal region (aa 1,420–1,848). The N terminus of BRP (aa 1–320) interacts with the C-terminal region of Cac (83% of the reported cytoplasmic C terminus, sparing the EF hand and most of its IQ motif; Kawasaki et al., 2002). –, no interaction; +++, interaction of high confidence. (B) Co-IPs from Schneider cell extracts cotransfected with a GFP-tagged N-terminal construct of BRP (D1-2^{GFP}; aa 1–617) and Myc-tagged Cac^{C-Term}. Western blotting shows the pull-down of the BRP construct in the anti-Myc IP at ~100 kD (arrow). The corresponding band is not detected in the control lanes (IgGs). The slightly different migration of the band in the input lane and in the IP lanes is the result of differences in sample buffer. MW, molecular weight. (C) Spatiotemporal model of AZ assembly and organization at *Drosophila* NMJs. SVs, synaptic vesicles.



brp^{1.3} (Fig. 8 A) showed partially restored Cac clustering. Moreover, those AZs positive for BRP^{N-Term} in *brp*^{1.3} corresponded to the AZs of restored Cac clustering (Fig. 8 E). Thus, AZ accumulation of the C-terminally truncated but N-terminally intact BRP protein seems to permit the assembly of a distally truncated T-bar, which still functions in clustering Cac.

To further explore this, we prepared larval NMJ AZs via HPF/FS. In this study, a gap between the AZ membrane and the T-bar pedestal (Fig. 8 F, arrows) was observed, where peg-like (Harlow et al., 2001) structures extended from the AZ membrane and distally contacted (or even slightly penetrated) the T-bar pedestal (Fig. 8 F, top, arrowheads). Such pegs were also observed at *brp*^{1.3} AZs (Fig. 8 F, middle, arrowheads) but not at AZ membranes of the *brp*⁶⁹-null allele (Fig. 8 F, bottom). Thus, these data further support the notion that Cac clustering beneath the T-bar pedestal is restored at *brp*^{1.3} AZs. Moreover, the cytoplasmic domains of Ca²⁺ channels might well extend from the AZ membrane, possibly allowing for a direct interaction with BRP.

Possible direct interaction between the C terminus of Cac and the N terminus of BRP

To address a possible interaction between BRP and Ca²⁺ channels, we tested for protein–protein interactions in vitro. First, all intracellular loops of Cac were tested with BRP

constructs in a yeast two-hybrid assay. Only the C-terminal domain of Cac and the N-terminal domain of BRP showed positive for interaction (Fig. 9 A). Thus, in agreement with our hypothesis concerning the orientation of BRP within the T-bar, the BRP N terminus may interact with the Cac C-terminal domain. To further investigate this interaction, we double transfected Schneider S2R+ cells with a GFP-tagged N-terminal construct of BRP (aa 1–617) and Myc-Cac^{C-Term} (aa 1,420–1,848). Pull-downs directed against Myc, GFP, and BRP (using a polyclonal antibody directed against aa 268–617 of BRP; see Materials and methods) confirmed a direct interaction (Fig. 9 B).

We are presently unable to (genetically) test whether this physical interaction of BRP with the Cac C terminus (and not other functions downstream of BRP-mediated T-bar assembly) is essential for Cac clustering. However, we tested whether Cac was important for BRP localization by staining *cac*-null embryos (Kawasaki et al., 2002). In this study, BRP signals were not reduced compared with controls (Fig. S5). Thus, BRP might be involved in providing slots in the AZ cytomatrix, which define sites of stable Ca²⁺ channel incorporation, whereas the Ca²⁺ channels themselves are not involved in clustering BRP. Collectively, our results suggest a model as depicted in Fig. 9 C for the spatiotemporal assembly process of the AZ at the glutamatergic *Drosophila* NMJ.

Discussion

Efficient neurotransmission is believed to crucially depend on the structural and functional integrity of the presynaptic AZ compartment (Schoch and Gundelfinger, 2006). An ancestral set of AZ components is conserved between *Drosophila*, *C. elegans*, and mammals (Stryker and Johnson, 2007; Jin and Garner, 2008). The strong phenotype we observed at *Drosophila* NMJs in the absence of the ERC/CAST member BRP, lacking T-bar–dense bodies and defective Ca²⁺ channel clustering (Kittel et al., 2006; Wagh et al., 2006), forms an entry point for studying AZ assembly, which is often complicated by redundant and cooperative interactions between AZ components (Jin and Garner, 2008).

BRP and dense body formation

We addressed whether BRP signals T-bar formation (without being a direct component of the T-bar) or whether the protein itself is an essential building block of this electron-dense structure. In this study, we provide evidence that BRP is a direct T-bar component. Immuno-EM identifies the N terminus of BRP throughout the whole cross section of the T-bar (Fig. 3, A and B), and genetic approaches show that a truncated BRP, lacking the C-terminal 30% of the protein's sequence, forms truncated T-bars (Fig. 2, E and F). Immuno-EM and light microscopy consistently demonstrate that N- and C-terminal epitopes of BRP are segregated along an axis vertical to the AZ membrane and suggest that BRP is an elongated protein, which directly shapes the T-bar structure (Fig. 9 C).

In *brp*^{5.45} (predicted as aa 1–866), T-bars were not detected, whereas *brp*^{1.3} (aa 1–1,389) formed T-bar–like structures, although fewer and smaller than normal (Fig. 2, E and F; and Fig. S2 C). Moreover, the BRP^{D1-3GFP} construct (1–1,226) did not rescue T-bar assembly. Thus, domains between aa 1,226 and 1,390 of BRP may also be important for the formation of T-bars. Clearly, however, the assembly scheme for T-bars is expected to be controlled at several levels (e.g., by phosphorylation) and might involve further protein components. Nonetheless, it is highly likely that the C-terminal half of BRP plays a crucial role.

BRP, the dense body, and Ca²⁺ channel clustering

As BRP represents an essential component of the electron-dense T-bar subcompartment at the AZ center, it might link Ca²⁺ channel–dependent release sites to the synaptic vesicle cycle (Neher and Sakaba, 2008). Interestingly, light and electron microscopic analysis has located CAST at mammalian synapses both with and without ribbons (tom Dieck et al., 2005; Deguchi-Tawarada et al., 2006; Siksou et al., 2007). Overall, this study is one of the first to genetically identify a component of an electron-dense synaptic specialization and thus paves the way for further genetic analyses of this subcellular structure.

The N terminus of BRP is found significantly closer to the AZ membrane than the C terminus, where it covers a confined area very similar to the area defined by the Cac^{GFP} epitope. Electron tomography of frog NMJs suggested that the cytoplasmic domains of Ca²⁺ channels, reminiscent of pegs, are concentrated directly beneath a component of an electron-dense AZ matrix

resembling ribs (Harlow et al., 2001). In addition, freeze-fracture EM identified membrane-associated particles at flesh fly AZs, which, as judged by their dimensions, might well be Ca²⁺ channels (Feeney et al., 1998). We observed peg-like structures beneath the T-bar pedestal. Similar to fly T-bars, the frog AZ matrix extends up to 75 nm into the presynaptic cytoplasm. Based on the amount of cytoplasmic Ca²⁺ channel protein (Catterall, 1998), Harlow et al. (2001) concluded that Ca²⁺ channels are likely to extend into parts of the ribs. Thus, physical interactions between cytoplasmic domains of Ca²⁺ channels and components of ribs/T-bars might well control the formation of Ca²⁺ channel clusters at the AZ membrane. However, a short N-terminal fragment of BRP (aa 1–320) expressed in the *brp*-null background was unable to localize to AZs efficiently and consistently failed to restore Cac clustering (unpublished data).

The mean Ca²⁺ channel density at AZs is reduced in *brp*-null alleles. In vitro assays indicate that the N-terminal 20% of BRP can physically interact with the intracellular C terminus of Cac. Notably, we found that the GFP epitope at the very C terminus of Cac^{GFP} was closer to the AZ membrane than the N-terminal epitope of BRP (Fig. 4 A). It is conceivable that parts of the Cac C terminus extend into the pedestal region of the T-bar cytomatrix to locally interact with the BRP N terminus. This interaction might play a role in clustering Ca²⁺ channels beneath the T-bar pedestal.

Clearly, additional work will be needed to identify the contributions of discrete protein interactions in the potentially complex AZ protein interaction scheme. Our study should pave the way for a genetic analysis of spatial relationships and structural linkages within the AZ organization. Moreover, we aim to integrate our findings in the framework of mechanisms for Ca²⁺ channel trafficking, clustering, and functional modulation (Cao et al., 2004; Evans and Zamponi, 2006; Catterall and Few, 2008).

Timing of AZ assembly, Ca²⁺ channel accumulation, and synapse maturation

Our imaging assays allowed a temporally resolved analysis of AZ assembly in vivo (Fig. 7). BRP is a late player in AZ assembly, arriving hours after DLiprin- α and also clearly after the postsynaptic accumulation of DGluRIIA. Accumulation of Cac was late as well, although it slightly preceded the arrival of BRP, and impaired Cac clustering at AZs lacking BRP became apparent only from a certain synapse size onwards (Fig. 8, B and C). In this study, we report that new AZs, similar to PSDs (Rasse et al., 2005), form at sites distant from preexisting ones and grow to reach a mature, fixed size. Thus, the late, BRP-dependent formation of the T-bar seems to be required for maintaining high Ca²⁺ channel levels at maturing AZs but not for initializing Ca²⁺ channel clustering at newly forming sites. As the dominant fraction of neuromuscular AZs is mature at a given time point, the overall impression is that of a general clustering defect in *brp* mutants. In reverse, it will be of interest to further differentiate the molecular mechanisms governing early Ca²⁺ channel clustering. Pre- to postsynaptic communication via neurexin–neuroligin (Missler et al., 2003; Li et al., 2007; Zeng et al., 2007) interactions might well contribute to this process. A further candidate involved in early Ca²⁺ channel clustering is the Fuseless protein, which was recently shown to be crucial for proper Cac localization at AZs (Long et al., 2008).

In summary, during the developmental formation of *Drosophila* NMJ synapses, the emergence of a presynaptic dense body, which is involved in accumulating Ca^{2+} channels, appears to be a central aspect of synapse maturation. This is likely to confer mature release probability to individual AZs (Kittel et al., 2006) and contribute to matching pre- and postsynaptic assembly by regulating glutamate receptor composition (Schmid et al., 2008). Whether similar mechanisms operate during synapse formation and maturation in mammals remains an open question.

Outlook: dense body architectures and synaptic plasticity

In this study, we concentrated on developmental synapse formation and maturation. The question arises whether similar mechanisms to those relevant for AZ maturation might control activity-dependent plasticity as well and whether maturation-dependent changes might be reversible at the level of individual synapses. Notably, experience-dependent, bidirectional changes in the size and number of T-bars (occurring within minutes) were implied at *Drosophila* photoreceptor synapses by ultrastructural means (Brandstatter et al., 1991; Rybak and Meinertzhagen, 1997). Moreover, at the crayfish NMJ, multiple complex AZs with double-dense body architecture were produced after stimulation and were associated with higher release probability (Wojtowicz et al., 1994). In fact, a recent study has correlated the ribbon size of inner hair cell synapses with Ca^{2+} microdomain amplitudes (Frank et al., 2009). Thus, a detailed understanding of the AZ architecture might permit a prediction of functional properties of individual AZs.

Materials and methods

Genetics

All fly strains were reared under standard laboratory conditions (Sigrist et al., 2003). Either w^1 or w^{1118} was used as background for transgenesis (BestGene Inc.).

Chemical mutagenesis

The EMS screen was performed according to standard protocols. In brief, isogenic w^{1118} males were mutagenized with 25 mM EMS solution and crossed to virgins carrying a second chromosomal balancer. For initial mapping, male F1 offspring were crossed with *Df(2R)BSC29* virgins, and candidate flies were tested with different *brp* mutant lines. Genomic DNA was extracted from positive candidate flies, and PCR amplicons containing *brp* exon clusters were double-strand sequenced to identify the mutations.

Generation of *brp* deletions

brp chromosomal deletions were constructed using the Flp recombinase system as previously described (Parks et al., 2004). The different parental lines were provided by the Exelixis collection at Harvard Medical School (Boston, MA).

The following genotypes were used for the ectopic expression of the BRP constructs (Fig. 1 A; Fig. 2, G and H; and Fig. 5): for wing disc expression, upstream activator sequence (UAS)-BRP^{D1-3GFP/+}; *dpp-Gal4/+*. UAS-BRP^{D2-4GFP}/*dpp-Gal4*. UAS-BRP^{D1-4GFP}/*dpp-Gal4*. For expression of BRP constructs at NMJs in the *brp* mutant background, UAS-BRP^{D1-3GFP/+}; *Df(2R)BSC29/brp⁶⁹*, *ok6-Gal4*. *Df(2R)BSC29/brp⁶⁹*, *ok6-Gal4*; UAS-BRP^{D2-4GFP/+}. *Df(2R)BSC29/brp⁶⁹*, *ok6-Gal4*; UAS-BRP^{D1-4/+}. *Df(2R)BSC29/brp⁶⁹*, *ok6-Gal4*. The *Gal4* lines and *Df(2R)BSC29* were provided by the Bloomington *Drosophila* Stock Center. For experiments in the *dliprin- α* mutant background (Fig. 6 D), we used *dliprin- α ^{R60}/dliprin- α ^{F3ex15}* animals (Kaufmann et al., 2002).

Antibodies

For the N-terminal BRP (BRP^{N-term}) antibody, a rabbit polyclonal antibody was raised (SeqLab) against a synthetic peptide (CREPRDRSRDRSLER). The specificity of the affinity-purified α -BRP antibody was confirmed by immunofluorescence analysis of larval muscle fillet preparations.

The BRP^{D2} antibody was raised against the BRP domain D2 (aa 268–617; SeqLab) in rabbits. The immunogen was expressed recombinantly as 6xHis-tagged fusion protein in *Escherichia coli* and purified using a protocol including denaturing and refolding of the protein. The antibody containing serum was affinity purified versus the same protein as used for immunization.

Transmission EM

For HPF, about one to three *Drosophila* late second/early third instar larvae were placed in aluminum specimen carrier of 200- μm depth (type A; Bal-Tec), filled with yeast paste, and covered with a lid. The samples were frozen immediately in an HPM machine (HPM010; Bal-Tec) and rapidly transferred to liquid nitrogen for storage.

FS and embedding were performed in acetone in either an EM AFS (automatic freeze substitution; for morphology; Leica) or an EM AFS2 (for immunocytochemistry; Leica). Two separate protocols were used for morphological and immunocytochemical analysis (Rostaing et al., 2006; Sikso et al., 2007). For immunocytochemistry, the substitution was performed in pure acetone without uranyl acetate.

For morphology, 55–60-nm (gray silver) sections, and for immunocytochemistry, 85-nm (silver gold) sections were cut using an EM Ultracut 6 (Leica). Sections were collected on formvar-coated 100 mesh grids. For morphological experiments, sections were dried and poststained with uranyl acetate and lead citrate as described previously (Schmid et al., 2006). For immunocytochemistry, grids were placed in droplets of PBS, pH 7.2, until labeling procedure started. Immunocytochemistry was performed as described previously (Rostaing et al., 2006; Sikso et al., 2007). Rb α -BRP^{N-term} (1:500) and M α -BRP^{Nc82} (Nc82; 1:2; provided by E. Buchner, Universität Würzburg, Würzburg, Germany) antibodies were used. Micrographs were taken with a 1,024 × 1,024 charge-coupled device detector (HSS 512/1024; Proscan Electronic Systems) in an electron microscope (EM 902A; Carl Zeiss, Inc.) operated in bright field mode.

Conventional room temperature embedding was essentially performed as described previously (Wagh et al., 2006). Images were obtained from dissected preparations of third instar larvae (NMJ 6/7; segments A2/A3). Instead of 1-h fixation in 1% osmium tetroxide, the fixation was performed in 1% osmium tetroxide and 0.8% KFeCN in 0.1 M cacodylate buffer. After infiltration in epon resin, muscles were cut out (six animals for each genotype) and embedded in a single block.

For T-bar size quantification, T-bars or residual T-bars were taken from vertical AZs. The electron density of the T-bar was measured from the AZ membrane to the T-bar platform if present (height) or along the AZ membrane (width).

Molecular cloning

For expression constructs of Dliprin- α ^{GFP}, a 3.6-kb fragment of pOT2 LD27334 was subcloned into pBluescript KS(+) (Agilent Technologies) using the Sall and EcoRI restriction sites introduced by PCR primers and subsequently double-strand sequenced. The insert was excised and inserted into pENTR4 (Invitrogen) via Sall and NotI sites. The final expression construct of Dliprin- α ^{GFP} was obtained using the Gateway system (Invitrogen). In brief, pENTR4 Dliprin- α was recombined with pTWG (a *Drosophila* pUAS Gateway vector developed in the laboratory of T. Murphy, The Carnegie Institution of Washington, Baltimore, MD).

The BRP constructs used for expression in *Drosophila* flies and *Drosophila* Schneider cell culture were obtained by PCR using the corresponding cDNA as template (*brp* cDNA; Wagh et al., 2006) and cloned into pENTER, a modified version of pENTR4 using the SpeI and Asp718I restriction sites.

The pUbiP Gateway destination vectors, used for coexpression experiments in S2R+ cell culture, were obtained from A. Hertzog (Max Planck Institute, Göttingen, Germany). These contained a ubiquitin promoter and either an N- or C-terminal tag.

Yeast two-hybrid constructs for *cac* and *brp* were obtained by PCR using the corresponding cDNA as template (*cac* cDNA was provided by R.W. Ordway, The Pennsylvania State University, Philadelphia, PA; *brp* cDNA; Wagh et al., 2006) and cloned into the bait vector pGBKT7 (Clontech Laboratories, Inc.) or the prey vector pGADT7 (Clontech Laboratories, Inc.) using the restriction sites introduced with the PCR primers.

Vectors used for fusion protein expression in *Drosophila* Schneider cell culture were made from respective modified pENTR4 clones containing truncated *brp* or truncated *cac* using the Gateway system.

Molecular cloning in detail

pENTER. The multiple cloning site of pENTR4 (Invitrogen) was modified by oligonucleotide annealing using two primers with a 5'-phosphate modification (MWG-Biotech AG): 5'-CATGGGAAGTACTCCCGGGCGCGCCGCGG-

CCGCGGTACCAGC-3' and 5'-TCGAGCTGGTACC GCGGCCGCGGCGCGCCCGGGACTAGTCC-3'. The annealed oligonucleotides were ligated into a previously cut pENTER4 vector using the NcoI and XhoI restriction sites. This modification resulted in a loss of the *ccdB* gene and a new multiple cloning site.

pTWmStrawberry. In short, the *Drosophila* Gateway vector pTWG containing an EGFP tag placed downstream of the Gateway cassette was used as a template to replace the EGFP by mStrawberry (mStraw; pRSETB mStraw was provided by R. Y. Tsien, University of California, San Diego, La Jolla, CA). For general information about the *Drosophila* Gateway vector collection, please visit http://www.ciwemb.edu/labs/murphy/Gateway%20vectors.html#_Copyright_2003,_Carnegie. The following fragments were amplified by PCR using either pTWG (α - and γ -mStraw) or pRSETB mStraw (β -mStraw) as templates: α -mStraw, 5'-CTCCATGTCGGCAGAATGCT-3' and 5'-GTTATTCTCTCGCCCTTGCTCACCAT-3'; β -mStraw, 5'-ACCGGCGGCATGGACGAGCTGTACAAG-3' and 5'-TGGATCCGATCCAGACATGA-3'; and γ -mStraw, 5'-ATGGTGAGCAAGGGCAGAGGA-3' and 5'-CTGTACAGCTCGTCCATGC-3'.

In two independent PCRs using the Elongase Enzyme Mix (Invitrogen), the three fragments were fused and subsequently ligated into a previously cut pTWG backbone using XbaI-HpaI. After transformation into *E. coli* strain DB3.1, the cells were plated on selective media containing ampicillin and chloramphenicol. Digestion and double-strand sequencing confirmed the successful replacement of the fluorophore.

pENTER4 and pENTER cloning. All final plasmids of pENTER4 or pENTER constructs were double-strand sequenced before any Gateway recombination with destination vectors.

pENTER4 DLiprin- α . 5'-GAGCGTCGACATGTGGAACATGATGTGCGACGTA-3' and 5'-GGAATTCGCGCGCGAAGCACTGCGCTGCTCA-3'; recombined with pTWG (C-terminal EGFP tag).

pENTER BRP D1-2 (aa 1–617). 5'-GAGTACTAGTATGGGCAGTCCATACTACCGC-3' and 5'-GTCTGGTACCTGCTCTTCCGCATCCGAC-3'; recombined with pUbiP-rfa-EGFP (C-terminal EGFP).

pENTER BRP D1-3 (aa 1–1,226). 5'-GAGTACTAGTATGGGCAGTCCATACTACCGC-3' and 5'-GTCTGGTACCCATTGCGCCTTCTCCAGTTC-3'; recombined with pTWG (C-terminal EGFP tag).

pENTER BRP D2-4 (aa 269–1,740). 5'-GAGTACTAGTGAGGAGGAGCGTCAGATGTTCC-3' and 5'-GTCTGGTACCGAAAAAGCTCTTCAAGAAGCCAGC-3'; recombined with pTWG (C-terminal EGFP tag).

pENTER BRP D1-4 (aa 1–1,740). 5'-GAGTACTAGTATGGGCAGTCCATACTACCGC-3' and 5'-GTCTGGTACCGAAAAAGCTCTTCAAGAAGCCAGC-3'; recombined with pTWG (C-terminal EGFP tag).

pENTER BRP D2 (aa 269–617). 5'-GAGTACTAGTGAGGAGGAGCGTCAGATGTTCC-3' and 5'-GTCTGGTACCTGCTCTTCCGCATCCGAC-3'; recombined with pDEST17 (N-terminal 6 \times His tag; Invitrogen) for antibody production.

pENTER BRP D3 (BRP short; aa 473–1,226). 5'-GAGTACTAGTATGGGCAGTCCATACTACCGC-3' and 5'-GTCTGGTACCCATTGCGCCTTCTCCAGTTC-3'; recombined with pTWG (C-terminal EGFP tag) and pTWmStraw.

pENTER Cac C terminus (aa 1,420–1,848). pGADT7 Cac C terminus was NcoI-XhoI digested, and the 2.2-kb insert was ligated into pENTER using the same restriction sites. The double-strand-sequenced plasmid was recombined with pUbiP-10xmyc-rfa (N-terminal 10 \times Myc tag).

pGBKT7 Cac Loop 1 (aa 305–452). 5'-GATGCCATGGTGCTCAACTAGTCTTGGTGTGTC-3' and 5'-GATGCTCGAGGAAAGACGAGGACGATCACG-3' were used. The PCR product was cut using NcoI-XhoI and ligated into pGBKT7 using NcoI-Sall.

pGBKT7 Cac Loop 2 (aa 669–768). 5'-GATGCCATGGATAATTTGGCGAATGCCAAGAA-3' and 5'-GATGGAATCCAAAATAACCACCCAATGGGC-3' were used. The PCR product was cut and ligated into pGBKT7 using NcoI-EcoRI.

pGBKT7 Cac Loop 3 (aa 1,042–1,093). 5'-GATGCCATGGTTACGTTTCAAGAGCAAGGCGAA-3' and 5'-GATGCTCGAGACACCACAATTCGCCACACTTTATA-3' were used. The PCR product was cut using NcoI-XhoI and ligated into pGBKT7 using NcoI-Sall.

pGBKT7 Cac C terminus (aa 1,420–1,848). 5'-GATGCCATGGCGTTATCGCTTGTATCGTGA-3' and 5'-GATGCTCGAGACCAATCCTCCTCATCCGAA-3' were used. The PCR product was cut using NcoI-XhoI and ligated into pGBKT7 using NcoI-Sall and into pGADT7 using NcoI-XhoI.

pGADT7 BRP D1 (aa 1–320). 5'-GAGTCATATGGGCAGTCCATACTACCGC-3' and 5'-GTCTATCGATGCGCGCTGGTAGTCTG-3' were used. The PCR product was cut using ClaI-NdeI and ligated into pGADT7.

pGADT7 BRP D2 (aa 268–617). 5'-GAGTCATATGGAGGAGGAGCGTCAGATGTTCC-3' and 5'-GTCTATCGATTGCTCTTCCGCATCCGAC-3' were used. The PCR product was cut using ClaI-NdeI and ligated into pGADT7.

pGADT7 BRP D3 (aa 473–1,226). pENTER BRP D3 was digested with SpeI-Asp718I, and the insert was subcloned into pSL1180fa. The insert was released again using NcoI-NdeI and ligated into a modified version of pGADT7 (pGADT7 IIB). Within the pGADT7 IIB vector, a point mutation deleting the first NcoI restriction site was introduced.

pGADT7 BRP D4 (aa 1,152–1,740). 5'-GAGTCATATGCATGAGAAGCTACTGAAGAAGGTCG-3' and 5'-GTCTATCGATGAAAAAGCTCTTCAAGAAGCCAGC-3' were used. The PCR product was cut using ClaI-NdeI and ligated into pGADT7.

Yeast two hybrid

In principle, all cotransformation experiments were conducted according to the yeast two-hybrid protocols of Clontech Laboratories, Inc. using the strain AH109. To ensure the presence of both cotransformed plasmids, the yeast was plated on minimal synthetic-defined/–Leu/–Trp medium plates. After growing for 2–3 d, at least 10 clones each were analyzed on synthetic-defined/–Ade/–His/–Leu/–Trp/X- α galactosidase medium plates to select for positive interaction. If >90% of the clones grew and turned blue in color, this was regarded as a positive interaction of high confidence (+++). As a positive control, pGBKT7-p53 was cotransformed with pGADT7 containing the SV40 large T antigen. Negative controls consisted either of laminin as bait together with the prey to be tested or the corresponding bait together with the empty prey vector.

Biochemistry

Drosophila Schneider S2R+ cells were provided by A. Herzig and cultured at 25°C in an ambient atmosphere in Schneider's *Drosophila* medium (Bio-West) supplemented with 10% FCS + 2 mM L-glutamine, 100 U/ml penicillin, and 100 μ g/ml streptomycin (Invitrogen). Medium was exchanged every 3–4 d. Cell cultures were split every 10–14 d. Cell cotransfection was conducted using the Effectene transfection reagent kit (QIAGEN). Cell lysis was performed with lysis buffer containing 25 mM Tris-HCl, pH 7.5, 150 mM NaCl, 2 mM EDTA, 2 mM EGTA, 10% glycerol (vol/vol), 1% NP-40 (vol/vol), and complete protease inhibitor (Roche) for 45 min at 0°C. Total protein concentrations were determined by bicinchoninic acid protein assay (Thermo Fisher Scientific).

For coimmunoprecipitations (co-IPs), 350 μ g total protein extract from whole cell lysates was mixed with 20 μ l protein A agarose bead suspension (Affi-prep protein A support; Bio-Rad Laboratories) precoupled with either monoclonal M α -Myc antibody (9E10; Santa Cruz Biotechnology, Inc.), polyclonal Rb- α GFP (A11122; Invitrogen), Rb- α BRP^{D2}, or the respective IgG control from mouse or rabbit (Dianova). After incubation at room temperature, the coupled beads were thoroughly washed repeatedly and eluted by boiling in 40 μ l of Laemmli buffer.

10 μ l IP eluates and 30 μ g whole cell lysates were subjected to denaturing SDS-PAGE using Tris-HCl NuPAGE 4–12% gradient gels and then transferred to a nitrocellulose membrane (iBlot; Invitrogen). The membrane was probed with Rb- α BRP^{D2} (1:500).

Image acquisition

Conventional confocal images were acquired at room temperature with a 63 \times 1.4 NA oil objective suited in a confocal microscope (TCS-SP5; Leica). Images taken from fixed samples were from third instar larval NMJs 6/7 (segments A2 and A3). NMJs depicted in live experiments derive from muscles 26 and 27 in segments A2 and A3. The fluorescence detection was set with the acousto optical beam splitter between 500 and 530 nm for GFP and between 575 and 620 nm for mRFP and mStraw. Photomultiplier gain was set to 1,250 V. GFP was excited using the 488-nm ArKr laser line, whereas mRFP and mStraw were excited with a 561-nm diode-pumped solid-state laser. For STED images, the STED setup (TCS; Leica) was used in combination with a 100 \times 1.4 NA oil objective at 20°C (Leica). Dye (Atto647N; Atto-Tec) was excited with a pulsed laser at 635 nm and depleted with a laser adjusted to 760 nm (Mai Tai Ti:Sapphire; Newport Spectra-Physics). Detection of the Atto-647N was performed with avalanche photodiodes and optical filters permeable for light of wavelengths between 650 and 710 nm. Diode gain was continuously set to 310 V. Excitation laser power varied according to the sample but always ranged between 5.0 and 5.6 V.

Immunostainings

Immunostainings and dissections were performed as described previously (Qin et al., 2005). Larvae were incubated with antibody solutions overnight at 4°C. Larvae were mounted either in Vectashield (Vector Laboratories) or

Mowiol. The following antibody dilutions were used: α -Nc82 (provided by E. Buchner), 1:200; α -DGLuRIIA (8B4D2; Developmental Studies Hybridoma Bank), 1:100; Rb α -BRP^{N-Term}, 1:250; Rb α -DGLuRIID (Qin et al., 2005), 1:500; α -GFP (Invitrogen), 1:500; Rb α -GFP (Invitrogen), 1:500; and HRP-Cy5 (Dianova), 1:250. For standard immunostainings, secondary antibodies were diluted 1:500. For STED stainings, dye (Atto647N) conjugation to secondary antibodies giving sheep α -M-Atto647N and sheep α -Rb-Atto647N were performed according to producer protocols (<http://www.atto-tec.com>) and used 1:100. Embryos (*w*¹¹¹⁸ and *elav-Gal4, l(1)l13HC129*; Kawasaki et al., 2002) were staged by time (22–24 h after egg laying) and morphology, dissected, and stained as described for larvae.

Live imaging

The following strains were used for in vivo imaging experiments: for Ca²⁺ channels, *ok6-Gal4/+; Cac^{GFP}, DGLuRIIA^{mRFP}/+* (control); *Df(2R)BSC29, ok6-Gal4/brp; Cac^{GFP}, DGLuRIIA^{mRFP}/+* (*brp* mutant background). For temporal analysis of AZ assembly, *ok6-Gal4/+; BRP-short^{GFP}/DGLuRIIA^{mRFP}, ok6-Gal4/+; DLiprin- α ^{GFP}/DGLuRIIA^{mRFP}, ok6-Gal4, BRP-short^{mStraw}/+; DLiprin- α ^{GFP}/+, ok6-Gal4/+; Cac^{GFP}, DGLuRIIA^{mRFP}/+, ok6-Gal4, BRP-short^{mStraw}/+; Cac^{GFP}/+.*

Imaging of intact *Drosophila* larvae along with larval anaesthetization was performed as described previously (Rasse et al., 2005; Fuger et al., 2007; Schmid et al., 2008). For FRAP experiments, intense 488-nm laser light was applied inside a region of interest of $\sim 10 \mu\text{m}$ of edge length (zoom, 25) bleaching both green and red fluorescent dyes. After an incubation of 12 h at 25°C, the junctions were imaged and compared with the prebleached pictures. Control regions were conserved at the junctions for internal control of intensity levels.

Image processing

Images were acquired using Application Suite Advanced Fluorescence (LAS-AF; Leica) software.

Confocal imaging

Confocal stacks were processed with ImageJ software (National Institutes of Health). Single slices and confocal stacks were deconvolved using the ImageJ plug-ins iterative deconvolution and iterative deconvolution 3D, respectively (provided by B. Dougherty, OptiNav, Inc., Redmond, WA). To generate the PSF for deconvolution, the ImageJ plug-in diffraction PSF 3D (provided by B. Dougherty) was used. The PSF settings were adjusted according to our hardware parameters, emission wavelengths, and image dimensions.

For analysis of FRAP data, intensity ratios between bleached areas and control nonbleached regions were retrieved. To compare several experiments, prebleached ratios were set to 1, and postbleached images were normalized accordingly. Recoveries were calculated by subtracting ratios generated immediately after the bleaching from ratios acquired 12 h after bleaching.

For quantification of areas and intensities, maximum projections, acquired with comparable confocal settings, were thresholded at 30 arbitrary units (au), and remaining areas were measured via the analyze particle function of ImageJ.

To obtain unbiased mean BRP^{Nc82} and BRP^{N-Term} distributions with STED resolution (Fig. 5 D), we used STED images of BRP^{Nc82}-Atto647N (or BRP^{N-Term}-Atto647N), which were simultaneously recorded with confocal images of the BRP^{N-Term}-Alexa Fluor 488 (or BRP^{Nc82}-Alexa Fluor 488). From these images, AZs were selected, which appeared planar to the optical slice. The confocal channel of each image of a planar AZ was automatically fitted with a 2D Gaussian function with Mathematica (version 5.0; Wolfram Research). The peaks of the Gaussian functions were used to automatically align and subsequently average the corresponding STED signal. The averaged STED images (BRP^{Nc82} and BRP^{N-Term}) were finally aligned according to the corresponding confocal counterpart. The BRP^{N-Term} signal was fitted with a single Gaussian (standard deviation = 52 nm), and the BRP^{Nc82} signal was fitted with the sum of two Gaussians (standard deviation = 48 nm and peak distance Δx = 189 nm).

STED imaging

STED images were processed using a linear deconvolution software integrated into the Inspector Software package (Max-Planck Innovations GmbH). Regularization parameters ranged from $1e^{-10}$ to $1e^{-12}$. The PSF was generated by using a 2D Lorentzian function with its half-width and half-length fitted to the half-width and half-length obtained by images of 25-nm crimson beads conjugated to Atto647N.

Electrophysiology

Two electrode voltage clamp recordings were essentially conducted as previously described (Kittel et al., 2006). All experiments were performed on male third instar larval NMJs (muscle 6; segments A2 and A3) in HL3

(70 mM NaCl, 5 mM KCl, 20 mM MgCl₂, 10 mM NaHCO₃, 5 mM trehalose, 115 mM sucrose, 5 mM HEPES, and 1 mM CaCl₂, pH 7.2). Muscle cells had an input resistance $\geq 4 \text{ M}\Omega$. Intracellular electrodes were filled with 3 M KCl, and resistances ranged from 10–25 M Ω . Stimulation artifacts of evoked excitatory junctional currents were removed for clarity. Genotypes used were *brp*^{CO4298}/*Df(2R)BSC29* and *w*¹¹¹⁸ as controls.

Statistics

Data were analyzed using the Mann-Whitney rank sum test for linear independent data groups (Prism; GraphPad Software, Inc.). Means are annotated \pm SEM. Asterisks are used to denote significance (*, $P < 0.05$; **, $P < 0.01$; ***, $P < 0.005$; not significant, $P > 0.05$).

Online supplemental material

Fig. S1 shows a quantification of BRP^{N-Term} expression levels in several *brp* mutants. Fig. S2 shows a comparison of mitochondrion ultrastructure either preserved using conventional room temperature embedding with aldehyde fixation and dehydration or HPF/FS along with T-bar size quantification of conventional and HPF/FS-prepared control and *brp*^{1,3} larvae. Fig. S3 shows amplitude and rise time of evoked excitatory junctional current recorded from *brp*^{CO4298} NMJs. Fig. S4 shows that *diprin- α* AZs do not suffer from Cac-clustering defects. Fig. S5 shows that BRP clustering is not disturbed at *cac* AZs. Online supplemental material is available at <http://www.jcb.org/cgi/content/full/jcb.200812150/DC1>.

We thank Christine Quentin, Claudia Wirth, and Franziska Zehe for excellent technical assistance. Furthermore, we thank all colleagues who provided us with reagents.

This work was supported by grants from the Deutsche Forschungsgemeinschaft to S.J. Sigrist (grants Exc 257, S1849/2-1 and 2-2, TP A16/SFB 551, TP B23/SFB581), by funds of the Max Planck Society to D. Oswald, and by *formel.1* grants to S. Hallermann and R.J. Kittel from the Medical Faculty of the University of Leipzig.

Submitted: 23 December 2008

Accepted: 10 June 2009

References

- Bellen, H.J., R.W. Levis, G. Liao, Y. He, J.W. Carlson, G. Tsang, M. Evans-Holm, P.R. Hiesinger, K.L. Schulze, G.M. Rubin, et al. 2004. The BDGP gene disruption project: single transposon insertions associated with 40% of *Drosophila* genes. *Genetics*. 167:761–781.
- Brandstatter, J.H., S.R. Shaw, and I.A. Meinertzhagen. 1991. Terminal degeneration and synaptic disassembly following receptor photoablation in the retina of the fly's compound eye. *J. Neurosci.* 11:1930–1941.
- Cao, Y.Q., E.S. Piedras-Renteria, G.B. Smith, G. Chen, N.C. Harata, and R.W. Tsien. 2004. Presynaptic Ca²⁺ channels compete for channel type-prefering slots in altered neurotransmission arising from Ca²⁺ channelopathy. *Neuron*. 43:387–400.
- Catterall, W.A. 1998. Structure and function of neuronal Ca²⁺ channels and their role in neurotransmitter release. *Cell Calcium*. 24:307–323.
- Catterall, W.A., and A.P. Few. 2008. Calcium channel regulation and presynaptic plasticity. *Neuron*. 59:882–901.
- Collins, C.A., and A. DiAntonio. 2007. Synaptic development: insights from *Drosophila*. *Curr. Opin. Neurobiol.* 17:35–42.
- Dai, Y., H. Taru, S.L. Deken, B. Grill, B. Ackley, M.L. Nonet, and Y. Jin. 2006. SYD-2 Liprin- α organizes presynaptic active zone formation through ELKS. *Nat. Neurosci.* 9:1479–1487.
- Deguchi-Tawarada, M., E. Inoue, E. Takao-Rikitsu, M. Inoue, T. Ohtsuka, and Y. Takai. 2004. CAST2: identification and characterization of a protein structurally related to the presynaptic cytomatrix protein CAST. *Genes Cells*. 9:15–23.
- Deguchi-Tawarada, M., E. Inoue, E. Takao-Rikitsu, M. Inoue, I. Kitajima, T. Ohtsuka, and Y. Takai. 2006. Active zone protein CAST is a component of conventional and ribbon synapses in mouse retina. *J. Comp. Neurol.* 495:480–496.
- Evans, R.M., and G.W. Zamponi. 2006. Presynaptic Ca²⁺ channels—integration centers for neuronal signaling pathways. *Trends Neurosci.* 29:617–624.
- Featherstone, D.E., E.M. Rushton, M. Hilderbrand-Chae, A.M. Phillips, F.R. Jackson, and K. Broadie. 2000. Presynaptic glutamic acid decarboxylase is required for induction of the postsynaptic receptor field at a glutamatergic synapse. *Neuron*. 27:71–84.
- Feeney, C.J., S. Karunanithi, J. Pearce, C.K. Govind, and H.L. Atwood. 1998. Motor nerve terminals on abdominal muscles in larval flesh flies,

- Sarcophaga bullata*: comparisons with *Drosophila*. *J. Comp. Neurol.* 402:197–209.
- Frank, T., D. Khimich, A. Neef, and T. Moser. 2009. Mechanisms contributing to synaptic Ca²⁺ signals and their heterogeneity in hair cells. *Proc. Natl. Acad. Sci. USA.* 106:4483–4488.
- Fuger, P., L.B. Behrends, S. Mertel, S.J. Sigrist, and T.M. Rasse. 2007. Live imaging of synapse development and measuring protein dynamics using two-color fluorescence recovery after photo-bleaching at *Drosophila* synapses. *Nat. Protoc.* 2:3285–3298.
- Gray, N.W., R.M. Weimer, I. Bureau, and K. Svoboda. 2006. Rapid redistribution of synaptic PSD-95 in the neocortex in vivo. *PLoS Biol.* 4:e370.
- Harlow, M.L., D. Ress, A. Stoschek, R.M. Marshall, and U.J. McMahan. 2001. The architecture of active zone material at the frog's neuromuscular junction. *Nature.* 409:479–484.
- Hell, S.W. 2007. Far-field optical nanoscopy. *Science.* 316:1153–1158.
- Hofbauer, A., T. Ebel, B. Waltenspiel, P. Oswald, Y.C. Chen, P. Halder, S. Biskup, U. Lewandrowski, C. Winkler, A. Sickmann, et al. 2009. The Wuerzburg hybridoma library against *Drosophila* brain. *J. Neurogenet.* 23:78–91.
- Jin, Y., and C.C. Garner. 2008. Molecular mechanisms of presynaptic differentiation. *Annu. Rev. Cell Dev. Biol.* 24:237–262.
- Kaufmann, N., J. DeProto, R. Ranjan, H. Wan, and D. Van Vactor. 2002. *Drosophila* liprin-alpha and the receptor phosphatase Dlar control synapse morphogenesis. *Neuron.* 34:27–38.
- Kawasaki, F., R. Felling, and R.W. Ordway. 2000. A temperature-sensitive paralytic mutant defines a primary synaptic calcium channel in *Drosophila*. *J. Neurosci.* 20:4885–4889.
- Kawasaki, F., S.C. Collins, and R.W. Ordway. 2002. Synaptic calcium-channel function in *Drosophila*: analysis and transformation rescue of temperature-sensitive paralytic and lethal mutations of cacophony. *J. Neurosci.* 22:5856–5864.
- Kawasaki, F., B. Zou, X. Xu, and R.W. Ordway. 2004. Active zone localization of presynaptic calcium channels encoded by the cacophony locus of *Drosophila*. *J. Neurosci.* 24:282–285.
- Kittel, R.J., C. Wichmann, T.M. Rasse, W. Fouquet, M. Schmidt, A. Schmid, D.A. Wagh, C. Pawlu, R.R. Kellner, K.I. Willig, et al. 2006. Bruchpilot promotes active zone assembly, Ca²⁺ channel clustering, and vesicle release. *Science.* 312:1051–1054.
- Ko, J., M. Na, S. Kim, J.R. Lee, and E. Kim. 2003. Interaction of the ERC family of RIM-binding proteins with the liprin-alpha family of multidomain proteins. *J. Biol. Chem.* 278:42377–42385.
- Koh, Y.H., L.S. Gramates, and V. Budnik. 2000. *Drosophila* larval neuromuscular junction: molecular components and mechanisms underlying synaptic plasticity. *Microsc. Res. Tech.* 49:14–25.
- Li, J., J. Ashley, V. Budnik, and M.A. Bhat. 2007. Crucial role of *Drosophila* neurexin in proper active zone apposition to postsynaptic densities, synaptic growth, and synaptic transmission. *Neuron.* 55:741–755.
- Long, A.A., E. Kim, H.T. Leung, E. Woodruff III, L. An, R.W. Doerge, W.L. Pak, and K. Broadie. 2008. Presynaptic calcium channel localization and calcium-dependent synaptic vesicle exocytosis regulated by the Fuseless protein. *J. Neurosci.* 28:3668–3682.
- Missler, M., W. Zhang, A. Rohmann, G. Kattenstroth, R.E. Hammer, K. Gottmann, and T.C. Sudhof. 2003. Alpha-neurexins couple Ca²⁺ channels to synaptic vesicle exocytosis. *Nature.* 423:939–948.
- Neher, E., and T. Sakaba. 2008. Multiple roles of calcium ions in the regulation of neurotransmitter release. *Neuron.* 59:861–872.
- Ohtsuka, T., E. Takao-Rikitsu, E. Inoue, M. Inoue, M. Takeuchi, K. Matsubara, M. Deguchi-Tawarada, K. Satoh, K. Morimoto, H. Nakanishi, and Y. Takai. 2002. Cast: a novel protein of the cytomatrix at the active zone of synapses that forms a ternary complex with RIM1 and munc13-1. *J. Cell Biol.* 158:577–590.
- Oswald, D., and S.J. Sigrist. 2009. Assembling the presynaptic active zone. *Curr. Opin. Neurobiol.* doi:10.1016/j.conb.2009.03.003.
- Parks, A.L., K.R. Cook, M. Belvin, N.A. Dompe, R. Fawcett, K. Huppert, L.R. Tan, C.G. Winter, K.P. Bogart, J.E. Deal, et al. 2004. Systematic generation of high-resolution deletion coverage of the *Drosophila melanogaster* genome. *Nat. Genet.* 36:288–292.
- Patel, M.R., E.K. Lehrman, V.Y. Poon, J.G. Crump, M. Zhen, C.I. Bargmann, and K. Shen. 2006. Hierarchical assembly of presynaptic components in defined *C. elegans* synapses. *Nat. Neurosci.* 9:1488–1498.
- Prokop, A., and I.A. Meinertzhagen. 2006. Development and structure of synaptic contacts in *Drosophila*. *Semin. Cell Dev. Biol.* 17:20–30.
- Qin, G., T. Schwarz, R.J. Kittel, A. Schmid, T.M. Rasse, D. Kappei, E. Ponimaskin, M. Heckmann, and S.J. Sigrist. 2005. Four different subunits are essential for expressing the synaptic glutamate receptor at neuromuscular junctions of *Drosophila*. *J. Neurosci.* 25:3209–3218.
- Rasse, T.M., W. Fouquet, A. Schmid, R.J. Kittel, S. Mertel, C.B. Sigrist, M. Schmidt, A. Guzman, C. Merino, G. Qin, et al. 2005. Glutamate receptor dynamics organizing synapse formation in vivo. *Nat. Neurosci.* 8:898–905.
- Rostaing, P., E. Real, L. Siksou, J.P. Lechaire, T. Boudier, T.M. Boeckers, F. Gertler, E.D. Gundelfinger, A. Triller, and S. Marty. 2006. Analysis of synaptic ultrastructure without fixative using high-pressure freezing and tomography. *Eur. J. Neurosci.* 24:3463–3474.
- Rybak, J., and I.A. Meinertzhagen. 1997. The effects of light reversals on photoreceptor synaptogenesis in the fly *Musca domestica*. *Eur. J. Neurosci.* 9:319–333.
- Schmid, A., G. Qin, C. Wichmann, R.J. Kittel, S. Mertel, W. Fouquet, M. Schmidt, M. Heckmann, and S.J. Sigrist. 2006. Non-NMDA-type glutamate receptors are essential for maturation but not for initial assembly of synapses at *Drosophila* neuromuscular junctions. *J. Neurosci.* 26:11267–11277.
- Schmid, A., S. Hallermann, R.J. Kittel, O. Khorramshahi, A.M. Frolich, C. Quentin, T.M. Rasse, S. Mertel, M. Heckmann, and S.J. Sigrist. 2008. Activity-dependent site-specific changes of glutamate receptor composition in vivo. *Nat. Neurosci.* 11:659–666.
- Schoch, S., and E.D. Gundelfinger. 2006. Molecular organization of the presynaptic active zone. *Cell Tissue Res.* 326:379–391.
- Sigrist, S.J., D.F. Reiff, P.R. Thiel, J.R. Steinert, and C.M. Schuster. 2003. Experience-dependent strengthening of *Drosophila* neuromuscular junctions. *J. Neurosci.* 23:6546–6556.
- Siksou, L., P. Rostaing, J.P. Lechaire, T. Boudier, T. Ohtsuka, A. Fejtova, H.T. Kao, P. Greengard, E.D. Gundelfinger, A. Triller, and S. Marty. 2007. Three-dimensional architecture of presynaptic terminal cytomatrix. *J. Neurosci.* 27:6868–6877.
- Stryker, E., and K.G. Johnson. 2007. LAR, liprin alpha and the regulation of active zone morphogenesis. *J. Cell Sci.* 120:3723–3728.
- tom Dieck, S., W.D. Altmock, M.M. Kessels, B. Qualmann, H. Regus, D. Brauner, A. Fejtova, O. Bracko, E.D. Gundelfinger, and J.H. Brandstatter. 2005. Molecular dissection of the photoreceptor ribbon synapse: physical interaction of Bassoon and RIBEYE is essential for the assembly of the ribbon complex. *J. Cell Biol.* 168:825–836.
- Wagh, D.A., T.M. Rasse, E. Asan, A. Hofbauer, I. Schwenkert, H. Durrbeck, S. Buchner, M.C. Dabauvalle, M. Schmidt, G. Qin, et al. 2006. Bruchpilot, a protein with homology to ELKS/CAST, is required for structural integrity and function of synaptic active zones in *Drosophila*. *Neuron.* 49:833–844.
- Wang, Y., X. Liu, T. Biederer, and T.C. Sudhof. 2002. A family of RIM-binding proteins regulated by alternative splicing: implications for the genesis of synaptic active zones. *Proc. Natl. Acad. Sci. USA.* 99:14464–14469.
- Westphal, V., S.O. Rizzoli, M.A. Lauterbach, D. Kamin, R. Jahn, and S.W. Hell. 2008. Video-rate far-field optical nanoscopy dissects synaptic vesicle movement. *Science.* 320:246–249.
- Wojtowicz, J.M., L. Marin, and H.L. Atwood. 1994. Activity-induced changes in synaptic release sites at the crayfish neuromuscular junction. *J. Neurosci.* 14:3688–3703.
- Wucherpfennig, T., M. Wilsch-Brauninger, and M. Gonzalez-Gaitan. 2003. Role of *Drosophila* Rab5 during endosomal trafficking at the synapse and evoked neurotransmitter release. *J. Cell Biol.* 161:609–624.
- Zeng, X., M. Sun, L. Liu, F. Chen, L. Wei, and W. Xie. 2007. Neurexin-1 is required for synapse formation and larvae associative learning in *Drosophila*. *FEBS Lett.* 581:2509–2516.
- Zhai, R.G., and H.J. Bellen. 2004. The architecture of the active zone in the presynaptic nerve terminal. *Physiology (Bethesda).* 19:262–270.

3.5 Geis et al., 2010, Brain 133:3166-3180

Seite 62-76

Stiff person syndrome-associated autoantibodies to amphiphysin mediate reduced GABAergic inhibition

Christian Geis,¹ Andreas Weishaupt,¹ Stefan Hallermann,^{2,3} Benedikt Grünewald,¹ Carsten Wessig,¹ Thomas Wultsch,⁴ Andreas Reif,⁴ Nadiya Byts,⁵ Marcus Beck,¹ Sibylle Jablonka,² Michael K. Boettger,^{1,6} Nurcan Üçeyler,¹ Wernher Fouquet,^{2,7} Manfred Gerlach,⁸ Hans-Michael Meinck,⁹ Anna-Leena Sirén,⁵ Stephan J. Sigrist,^{2,7} Klaus V. Toyka,¹ Manfred Heckmann^{1,2,3,7,10,*} and Claudia Sommer^{1,*}

1 Department of Neurology, University of Würzburg, Würzburg 97080, Germany

2 Institute of Clinical Neurobiology, University of Würzburg, Würzburg 97080, Germany

3 Carl-Ludwig-Institute of Physiology, University of Leipzig, Leipzig 04103, Germany

4 Department of Psychiatry, University of Würzburg, Würzburg 97080, Germany

5 Department of Neurosurgery, University of Würzburg, Würzburg 97080, Germany

6 Institute of Physiology I, University Hospital Jena, Jena 07743, Germany

7 Rudolf-Virchow-Center, Deutsche Forschungsgemeinschaft-Research Center for Experimental Biomedicine, Würzburg 97080, Germany

8 Department of Child and Adolescent Psychiatry, Psychosomatics and Psychotherapy, University of Würzburg, Würzburg 97080, Germany

9 Department of Neurology, University of Heidelberg, Heidelberg 69120, Germany

10 Institute for Physiology, University of Würzburg, Würzburg 97080, Germany

*These authors contributed equally to this work.

Correspondence to: Claudia Sommer,
Department of Neurology,
University of Würzburg,
Josef-Schneider-Str. 11,
97080 Würzburg,
Germany
E-mail: sommer@uni-wuerzburg.de

Synaptic inhibition is a central factor in the fine tuning of neuronal activity in the central nervous system. Symptoms consistent with reduced inhibition such as stiffness, spasms and anxiety occur in paraneoplastic stiff person syndrome with autoantibodies against the intracellular synaptic protein amphiphysin. Here we show that intrathecal application of purified anti-amphiphysin immunoglobulin G antibodies induces stiff person syndrome-like symptoms in rats, including stiffness and muscle spasms. Using *in vivo* recordings of Hoffmann reflexes and dorsal root potentials, we identified reduced presynaptic GABAergic inhibition as an underlying mechanism. Anti-amphiphysin immunoglobulin G was internalized into neurons by an epitope-specific mechanism and colocalized *in vivo* with presynaptic vesicular proteins, as shown by stimulation emission depletion microscopy. Neurons from amphiphysin deficient mice that did not internalize the immunoglobulin provided additional evidence of the specificity in antibody uptake. GABAergic synapses appeared more vulnerable than glutamatergic synapses to defective endocytosis induced by anti-amphiphysin immunoglobulin G, as shown by increased clustering of the endocytic protein AP180 and by defective loading of FM 1–43, a styryl dye used to label cell membranes. Incubation of cultured neurons with anti-amphiphysin immunoglobulin G reduced basal and stimulated release of γ -aminobutyric acid substantially more than that of glutamate. By whole-cell patch-clamp analysis of GABAergic inhibitory transmission in hippocampus granule cells we

Received January 24, 2010. Revised July 23, 2010. Accepted July 25, 2010.

© The Author (2010). Published by Oxford University Press on behalf of the Guarantors of Brain. All rights reserved.

For Permissions, please email: journals.permissions@oxfordjournals.org

showed a faster, activity-dependent decrease of the amplitude of evoked inhibitory postsynaptic currents in brain slices treated with antibodies against amphiphysin. We suggest that these findings may explain the pathophysiology of the core signs of stiff person syndrome at the molecular level and show that autoantibodies can alter the function of inhibitory synapses *in vivo* upon binding to an intraneuronal key protein by disturbing vesicular endocytosis.

Keywords: stiff person syndrome; GABA; amphiphysin; patch clamp; STED microscopy

Abbreviations: DAPI = 4',6-diamidino-2-phenylindole; dep-amphAB = patient IgG depleted of anti-amphiphysin antibodies; IgG = immunoglobulin G; native-amphAB = native IgG fraction containing high-titre anti-amphiphysin antibodies; spec-amphAB = affinity purified and reconstituted patient anti-amphiphysin antibodies; SPS = stiff person syndrome; VGAT = vesicular GABA transporter; VGLUT = vesicular glutamate transporter

Introduction

Synaptic inhibition is a key-coordinative force in the CNS that is mediated predominantly by gamma-aminobutyric acid (GABA)-ergic and glycinergic interneurons. While the pathogenesis of some inherited and toxin-mediated diseases involving disturbed synaptic inhibition is well understood (Shiang *et al.*, 1993; Lalli *et al.*, 2003), it is unclear whether an antibody-mediated autoimmune process may also specifically affect synaptic inhibition. The pathogenic role of antibodies to ion channel-associated transmitter receptors has long been demonstrated in disorders of neuromuscular transmission (Toyka *et al.*, 1975; Buchwald *et al.*, 1998a, b, 2005). Furthermore, antibodies against membrane proteins, e.g. glutamate receptors, can alter excitatory transmission in the CNS (Sillevis Smitt *et al.*, 2000; Coesmans *et al.*, 2003; Dalmau *et al.*, 2008).

Paraneoplastic stiff person syndrome (SPS) associated with antibodies to amphiphysin (Folli *et al.*, 1993) is one of the few autoimmune diseases of the CNS with evidence for a direct pathogenic effect of autoantibodies. Clinical improvement correlates with lowering of antibody titres by therapeutic plasmapheresis (Wessig *et al.*, 2003) and symptoms can be reproduced in rats by systemic passive transfer of patient immunoglobulin G (IgG) containing high-titre antibodies to amphiphysin (Sommer *et al.*, 2005). Mechanistically, the typical core symptoms of SPS, i.e. stiffness, intermittent muscle spasms and anxiety (Murinson and Vincent, 2001; Meinck and Thompson, 2002; Vasconcelos and Dalakas, 2003), and the therapeutic effects of benzodiazepines are consistent with a disorder of GABAergic inhibition.

Amphiphysin is an intracellular protein involved in the synaptic vesicle cycle that promotes cleavage of clathrin-coated vesicles via binding of its Src homology 3 (SH3)—domain to dynamin (Wigge and McMahon, 1998). Acute blocking of the function of amphiphysin impairs synaptic vesicle endocytosis *in vitro*, leading to stimulation and frequency-dependent alteration of the presynaptic architecture with an increased number of clathrin coat intermediates and a decrease in the releasable vesicle pool. This results in a functionally relevant synaptic transmission failure, particularly at higher frequencies (Shupliakov *et al.*, 1997; Evergren *et al.*, 2004). In knockout mice with amphiphysin 1 deficiency, stimulus-dependent vesicle recycling is reduced, resulting in learning deficits and an increased susceptibility to seizures, consistent with reduced CNS inhibition (Di Paolo *et al.*, 2002).

We describe a combined immunological, neurophysiological and molecular approach to investigating the specific pathogenic role of IgG antibodies toward amphiphysin and elucidating the disease mechanism. From our findings we propose a disorder affecting predominantly, but not exclusively, GABAergic inhibition.

Materials and methods

Patients and therapeutic plasma exchange

Two SPS patients with antibodies against amphiphysin suffered from a paraneoplastic SPS related to breast cancer. The clinical details of Patient 1 who had a complex paraneoplastic syndrome have been reported (Wessig *et al.*, 2003). Patient 2 is a 52-year-old housewife whose initial symptoms included painful stiffness and spasms in the right arm. Symptoms deteriorated over time, resulting in impaired limb movements, stiff gait and eventually ataxia and cranial nerve pathology. Plasma exchange therapy (Cobe Spectra Apheresis System, CaridianBCT, Lakewood, Colorado, USA) involving roughly one plasma volume per session resulted in transient improvement of stiffness and muscle spasms. Titres of anti-amphiphysin antibodies were measured by means of a commercial enzyme immunodot assay with rabbit antisera raised against recombinant amphiphysin I as a positive control (H.P. Seelig, Karlsruhe, Germany). Titres before the first plasma exchange were $1-2 \times 10^8$ in Patient 1 and $1-5 \times 10^5$ in Patient 2, with a typical fall in titres upon plasma exchange.

Amphiphysin expression and IgG preparation

For expression and purification of recombinant human glutathione S-transferase-amphiphysin and glutathione S-transferase-SH3 domain fusion protein, the gene encoding for amphiphysin protein and the construct containing its wild-type SH3 domain (Grabs *et al.*, 1997) were sub-cloned into the pGEX-6P expression vector system (GE Healthcare, Munich, Germany) to generate a glutathione S-transferase fusion protein (GE Healthcare) which was transformed into *Escherichia coli* BL21(DE3)-pRILP cells (Stratagene, La Jolla, CA, USA). The fusion proteins were expressed and purified as described earlier (David *et al.*, 1994) and were cleaved by PreScission protease and separated from the glutathione S-transferase-tag according to the manufacturer's instructions. For the generation of columns to use in amphiphysin affinity chromatography, amphiphysin protein

was coupled to Cyanogen bromide-activated-Sepharose (GE Healthcare) as described by the manufacturer. Human immunoglobulins were purified from patient plasma filtrates as described earlier (Buchwald *et al.*, 1998b; Sommer *et al.*, 2005), including a control patient with chronic inflammatory polyneuropathy. For depletion of amphiphysin antibodies by affinity chromatography, purified IgG from Patient 1 that contained high titres of amphiphysin antibodies was dissolved in phosphate buffered saline and loaded onto an amphiphysin-sepharose affinity column. After washing, the amphiphysin-specific antibodies were eluted from the matrix with 0.1 M glycine, pH 2.5. Serial fractions of 2 ml each were collected and adjusted to pH 7.4 with 1 M Tris-HCl, pH 9.0. The amphiphysin antibody-depleted fractions and the amphiphysin antibody containing eluates were then dialysed separately against distilled water, freeze dried and stored at -20°C . Lyophilized IgG was dissolved in normal saline just before use and checked by western blotting.

Animals and surgery

Female Lewis rats were purchased from Harlan-Winkelmann (Borchen, Germany). All experiments were approved by the Bavarian State authorities. Intrathecal catheters (0.28 mm inner diameter; 0.61 mm outer diameter; intrathecal length: 7.0 cm; [Supplementary Fig. 3A](#)) were placed as described previously (Yaksh and Rudy, 1976). Rats that developed signs of paralysis after catheter placement were sacrificed immediately. After allowing recovery for 5 days, animals were randomized to receive either purified patient IgG with the highest titre of anti-amphiphysin antibodies without further processing (native-amphAB from Patients 1 and 2 at a concentration of 100 mg/ml, $n=10$ and 6, respectively) or an IgG fraction that had been depleted of anti-amphiphysin antibodies by affinity chromatography (dep-amphAB, 100 mg/ml, $n=4$, from Patient 1 only), or the specific anti-amphiphysin antibodies re-eluted from the affinity columns (spec-amphAB, diluted 1:10, concentration 10 mg/ml, $n=11$, from Patient 1 only), the IgG fraction of plasmapheresis material from a control patient (control IgG, 100 mg/ml, $n=9$ and $n=10$ in two different experiments), and normal saline ($n=7$). Intrathecal injections of 10 μl of patient IgG or saline with a subsequent flush of 10 μl saline were performed daily for 5 days, every other day for the next five injections and every third day for two following injections.

In parts of experiments we used amphiphysin knockout mice and their wild-type counterpart (kindly provided by P. deCamilli, Yale University, New Haven).

Behavioural analysis

Behavioural analyses were done by an investigator blinded to the treatment allocation of the rats. Animals were observed daily for at least 1 h while in their cages and when moving freely over a table with tunnels and obstacles. Each animal was videotaped for 3 min ([Supplementary Videos](#)) for documentation and blinded analysis. Stiffness was rated semi-quantitatively, similar to the clinical testing performed in humans with SPS (Dalakas *et al.*, 2000). The following parameters were documented as abnormal signs on a scale of 0–3: slowing when in free motion, trunk stiffness during walking, reduced climbing ability, muscle spasms and dystonic movements ([Fig. 1B](#)). RotaRod testing and gait analysis were performed as described in [Supplementary Methods](#).

Hoffmann reflex testing

Rats were anesthetized with intraperitoneal injections of ketamin and xylazin (80–100 mg/kg and 5 mg/kg, respectively). Hoffmann reflex recordings were performed as described earlier (Lee *et al.*, 2005) using a Toennies electromyograph and NeuroScreen^{plus} software (Erich Jaeger GmbH, Hoechberg, Germany). For analysis of post-activation depression, the ratio of the Hoffmann reflex and motor response (H/M ratio) was determined with serial single stimuli applied at the tibial nerve at frequencies ranging from 0.1 to 10 Hz with stimulation currents 30% above that needed for a maximal response (supramaximal) (Lee *et al.*, 2005). H/M values of the tenth stimulation were taken for further analysis. The H/M ratio was fitted with an exponential decay: $a = a_0 + a_1 \cdot \exp(-f/f_1)$, where a is the amplitude in percent (normalized to 100% at 0.1 Hz stimulation frequency) and f is the frequency in hertz ($a_0 + a_1$ were determined as 100%). The analysis of the D1/D2 inhibition is described in [Supplementary Methods](#).

Dorsal root potential recording

Dorsal root potentials were recorded from dorsal roots L4 and L5 bilaterally with an ELC-03X amplifier (NPI Electronic, Tamm, Germany) after stimulation of the tibial nerve using a Grass S88 stimulator (stimulus duration 0.2 ms, single stimulation and trains of three stimuli at 100 Hz; Grass Technologies, West Warwick, Rhode Island, USA) as described earlier (Barron and Matthews, 1938; Schmidt, 1971). In a subset of animals, the dependence of the dorsal root potential amplitude on GABAergic transmission was tested by applying bicucullin locally to the dorsal root entry zone of the spinal cord.

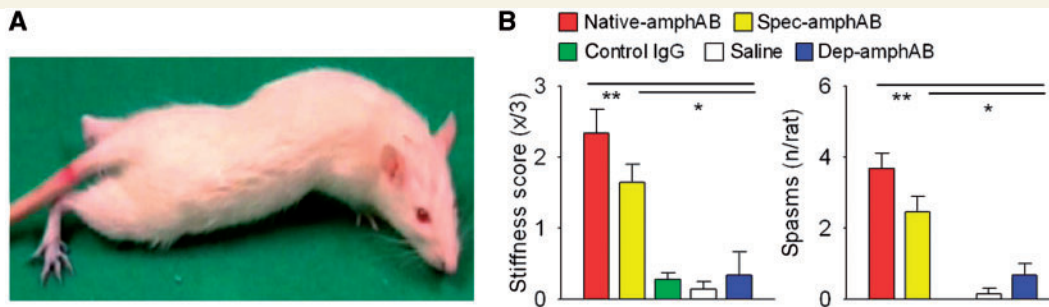


Figure 1 SPS-like symptoms after intrathecal passive transfer of anti-amphiphysin antibodies. (A and B) Rats treated with native-amphAB ($n=8$) and purified spec-amphAB ($n=10$), but none with control IgG ($n=9$), or saline ($n=7$) developed muscle stiffness and spasms with extension of the hind limbs and contraction of abdominal muscles. IgG fractions specifically depleted of the anti-amphiphysin antibodies (dep-amphAB, $n=4$) had none of these effects. * $P < 0.05$; ** $P < 0.01$.

Histological and immunohistochemical analysis

At the end of the experiment, rats were sacrificed, blood was withdrawn and the lumbar spinal cord was rapidly removed, mounted in Tissue-Tec optimal-cutting-temperature embedding compound and then deep frozen in liquid nitrogen. For details on histological and immunohistochemical procedures, see [Supplementary Methods](#).

Stimulation emission depletion microscopy

Ten-micrometer spinal cord sections or dissociated hippocampal neurons were viewed with a Leica SP5 true confocal scanner stimulation emission depletion microscope (Hell, 2007) using a 100× oil immersion lens (Leica Microsystems, Wetzlar, Germany) with the following filter and wavelength settings: for visualization of Cy-3 secondary antibodies excitation, 543 nm and emission 575–620 nm; for stimulation emission depletion imaging with the Atto-conjugated secondary antibody excitation, 635 nm and emission 645–715 nm.

Imaging with quantum dot-coupled antibodies

Three hundred microlitre spec-amphAB and control IgG antibodies (1 mg/mg) were coupled to the activated quantum dots according to manufacturer's instructions, resulting in an IgG concentration of $344 \pm 3.6 \mu\text{g/ml}$. For live cell imaging, 2.5 μl of each tagged antibody solution was dissolved in 200 μl cell culture medium and incubated with dissociated hippocampal neurons cultured from wild-type and amphiphysin knockout mice for 10 min, 1.5, 3 and 6 h, respectively. For detection of internalized antibodies, nanocrystal-tagged antibodies (130 nmol) were incubated with the cell cultures for 6 h at 37°C. After fixation, cells were incubated overnight at 4°C with antibodies against calnexin, a protein of the endoplasmic reticulum (Abcam, Cambridge, UK), followed by Cy2 secondary antibodies (1:100) and 4',6-diamidino-2-phenylindole (DAPI) nuclear staining. Stacks of confocal images were recorded in the multi-track mode and examples of single optical slices are shown in Fig. 5A. Images were analysed with Image Pro Plus version 4.5 software (MediaCybernetics, Bethesda, Maryland, USA).

Antibody internalization assays

To reveal epitope specificity, a defined amount (46 nmol) of quantum dot-tagged spec-amphAB was pre-incubated with recombinant amphiphysin in concentrations from 388 nmol to 0.8 fmol in the cell culture medium at room temperature for 1 h followed by incubation with dissociated mouse hippocampal neurons for 6 h at 37°C. For each concentration, five randomly distributed square fields of 375 μm side length were analysed by counting internalized quantum dot profiles and overall number of neurons (mean count of neurons was 92.2 ± 6.4 per profile). Means of internalized quantum dot counts per profile were plotted against the antigen concentration using Sigma-Plot 9.0 Software (Systat Software, San Jose, CA, USA). Other hippocampal neurons were incubated with 46 nmol tagged spec-amphAB and unlabelled spec-amphAB in various concentrations (ranging from 1.8 μmol to 0.34 nmol) for 6 h at 37°C, and then processed and analysed as described earlier. To investigate the temperature dependence of the internalization process, hippocampal neurons were incubated at 37°C or 25°C for 6 h in additional experiments. Mean numbers of internalized

quantum dots were plotted against the concentration of unlabelled spec-amphAB. All experiments were performed in duplicate.

Analysis of defects in vesicle endocytosis

To analyse the influence of anti-amphiphysin antibodies on vesicle recycling and endocytic function in GABAergic and glutamatergic synapses, dissociated hippocampal neurons were incubated with native-amphAB and control IgG at 100 $\mu\text{g/ml}$ for 6 h at 37°C. In a separate set of experiments, cell cultures were additionally incubated with 1 μmol of tetrodotoxin (TTX, Sigma, St. Louis, Missouri, USA). Neurons were then fixed with ice-cold methanol (100%) for 20 min at -20°C and subsequently washed three times with phosphate buffered saline. For confocal imaging, cells were incubated at 4°C with the following antibodies: mouse monoclonal anti-bassoon antibodies (Stressgen, 1:1000), rabbit polyclonal anti-AP180 antibodies (Synaptic Systems, 1:2000) followed by the respective Cy-3 conjugated secondary antibodies (Dianova, 1:300) for 2 h at room temperature and DAPI nuclear staining. For high-resolution stimulation emission depletion microscopy, double immunofluorescence staining was performed with anti-AP180 and polyclonal guinea pig anti-vesicular glutamate transporter (VGLUT) or anti-vesicular GABA transporter (VGAT) antibodies (both Synaptic Systems, Goettingen, Germany, 1:2000, 1:1000, respectively) followed by anti-guinea-pig Cy-3 secondary antibodies and anti-rabbit IgG conjugated to Atto 647N (Atto-Tec, Siegen, Germany). Clustering of the synaptic proteins was analysed by counting immunoreactive puncta per 300 μm^2 in six randomly chosen areas in each of six single-culture incubations according to previous reports (Ferguson *et al.*, 2007; Hayashi *et al.*, 2008). Colocalization with VGAT and VGLUT was determined in each of 10 randomly chosen areas using Image Pro Plus version 4.5 software.

High-performance liquid chromatography analysis of GABA and glutamate release

Hippocampal cell cultures were incubated with native-amphAB and control IgG as described earlier. After 6 h, medium was removed and neurons were pre-incubated for 90 s at 37°C with 200 μl of 119 mM NaCl, 2.5 mM KCl, 2 mM CaCl_2 , 2 mM MgCl_2 , 25 mM Hepes and 30 mM glucose (artificial CSF). Thereafter, cell cultures were either stimulated by depolarization with 200 μl of a high-potassium solution (31.5 mM NaCl, 90 mM KCl, 2 mM CaCl_2 , 2 mM MgCl_2 , 25 mM Hepes and 30 mM glucose) or 200 μl artificial CSF for 90 s at 37°C (Ferguson *et al.*, 2007; Hayashi *et al.*, 2008) ($n=6$ for each condition). GABA and glutamate concentrations were analysed by high-performance liquid chromatography as described in the [Supplementary Methods](#). To assess structural integrity, subsets of cells were stained with rabbit anti- β -tubulin antibodies (Sigma, 1:1000) followed by anti-rabbit Cy-3 secondary antibodies.

Analysis of vesicle endo- and exocytosis with FM dye imaging

Dissociated hippocampal neurons were grown on glass cover-slips with a grid (Science Services, Munich, Germany) until Day 10 *in vitro* and were then incubated for 3 h with all IgG fractions at a concentration of 100 $\mu\text{g/ml}$. Thereafter, cells were superfused with artificial CSF. Synaptic boutons were loaded with 10 μM FM[®] dye 1–43 (Molecular Probes,

Eugene, Oregon, USA) in the presence of 90 mM KCl and 2 mM CaCl₂ for 90 s at room temperature according to published protocols (Klingauf *et al.* 1998). Individual boutons were imaged after 15 min perfusion with artificial CSF. Destaining of the synaptic boutons was performed with brief pulses of 90 mM KCl and 2 mM CaCl₂. Boutons were viewed with a Zeiss Axioskop 2 microscope using a 63× water immersion lens (Zeiss, Wetzlar, Germany). FM dyes were excited at 470 nm wavelength with a shutter-controlled X-Cite[®] 120PC fluorescence lamp (Exfo Life Sciences Division, Ontario, Canada) every 2 s and images were taken with an Axiocam MRm camera (Zeiss). After imaging, a bright-field image was taken for later identification of the depicted neurons and cells were fixed with ice-cold 100% methanol as described. Cells were then stained for VGAT and VGLUT using Cy-3 and Cy-2 secondary antibodies, respectively. The pixel intensities of fluorescent spots in the live-imaging episode were analysed using Image Pro Plus version 4.5 software. GABAergic and glutamatergic boutons were identified after the live-imaging experiments by comparison with the VGAT and VGLUT staining, respectively (Fig. 7B).

Whole-cell patch-clamp analysis

GABAergic miniature potentials and single evoked GABAergic inhibitory postsynaptic currents were recorded in granule cells of acute hippocampal slice preparations after pre-incubation with 1 mg/ml native-amphAB or control-IgG at 32°C for at least 30 min. For further details see [Supplementary Methods](#).

Primary cell cultures

Rat embryonic spinal neuron co-cultures (motor neurons and interneurons), mouse embryonic motor neuron cultures and mouse embryonic hippocampal cultures were prepared as described in [Supplementary Methods](#).

Data analysis

All data are presented as means and standard errors of the means. Statistical analyses were performed using SPSS software version 11.5 (SPSS Inc., Munich, Germany) with ANOVA and Bonferroni *post hoc* test for the behavioural analyses, analysis of Hoffmann reflex data ([Supplementary Fig. 6](#)), dorsal root potentials and immunohistochemical quantifications. The FM dye evoked fluorescence intensity was assessed for each time point, and the intergroup differences were analysed with a one-way ANOVA with Bonferroni *post hoc* analysis. Hoffmann reflex data (Fig. 3A; [Supplementary Fig. 2](#)) and *in vitro* electrophysiological data (mean inhibitory postsynaptic current in steps of 10 stimuli throughout the train and mean inhibitory postsynaptic current in the recovery phase) were analysed using the Mann–Whitney U-test.

Results

Intrathecal passive transfer of anti-amphiphysin antibodies to the spinal cord induces long-lasting SPS-like symptoms in rats

To investigate the functional impact of amphiphysin autoantibodies, we used native-amphAB which was obtained from plasma filtrates of Patient 1 in passive transfer experiments. Following this, we performed experiments with specific antibodies to amphiphysin

purified by affinity chromatography from Patient 1 IgG, with this patient's IgG specifically depleted of amphiphysin antibodies with a control patient's IgG and with the IgG fraction of Patient 2, who had anti-amphiphysin antibody positive SPS but with lower titres. We repetitively applied intrathecal injections of these IgG fractions to the subarachnoid space of rats via implanted spinal catheters. After six or seven injections of IgG containing anti-amphiphysin antibodies, all rats treated with native-amphAB (8/8 from Patient 1 and 6/6 from Patient 2) and with affinity-purified spec-amphAB (10/10 from Patient 1) developed stiffness of trunk and limb muscles with intermittent muscle spasms and gait abnormalities (Fig. 1A and B; [Supplementary Figs 1 and 2A](#) and [Supplementary Videos 1–3](#)). In contrast, none of the four rats injected with the same amounts of IgG depleted of specific antibodies (dep-amphAB) and none of the 19 rats injected with control IgG developed SPS-like symptoms. Very rarely, animals of the control groups showed short-lasting truncal stretching without twisting, possibly due to transient local irritation of the spinal cord by the catheters ([Supplementary Fig. 3](#)). Footprint analysis showed increased outward rotation of the hind paws in rats treated with native-amphAB and spec-amphAB ([Supplementary Fig. 1A and B](#)). The grip force test of the forelimbs did not reveal differences between groups (data not shown), indicating no detectable effects of anti-amphiphysin antibodies on forelimb muscle strength. On the accelerating RotaRod, rats in the native-amphAB group showed a marked and significant decrease in forced walking time ([Supplementary Fig. 1C](#) and [Supplementary Video 2](#)).

Purified human anti-amphiphysin antibodies bind specifically to neuronal structures and recognize the amphiphysin SH3 domain

The various IgG preparations of Patient 1 used in the passive transfer experiments were tested by western blotting with homogenized rat spinal cord and with a 45 kDa glutathione S-transferase fusion protein containing the amphiphysin SH3 domain, the high-affinity binding partner for dynamin (Shupliakov *et al.*, 1997; Evergren *et al.*, 2004). The native-amphAB and spec-amphAB showed clear and strong bands, equivalent to blots with polyclonal rabbit anti-amphiphysin antibodies. In the depleted fraction (dep-amphAB), only a faint band at 128 kDa was present, equivalent to a purification efficiency of ~99.9% (Fig. 2A and B).

In spinal cord sections from untreated rats, only incubation with native-amphAB and spec-amphAB but not with dep-amphAB and control IgG resulted in perineuronal staining in the ventral horn (Fig. 2C). When primary motor neuron and interneuron co-cultures were immunoreacted with the IgG fractions at a 10 µg/ml concentration, only native-amphAB but not control IgG resulted in a strong-sprinkled-staining pattern of neuronal cell bodies and dendrites (Fig. 2D). To further substantiate the specificity of binding to amphiphysin, we switched species and incubated motor neurons or spinal cord sections of wild-type mice with the IgG preparations. An identical staining pattern was observed as in rat tissue, whereas cells and sections from

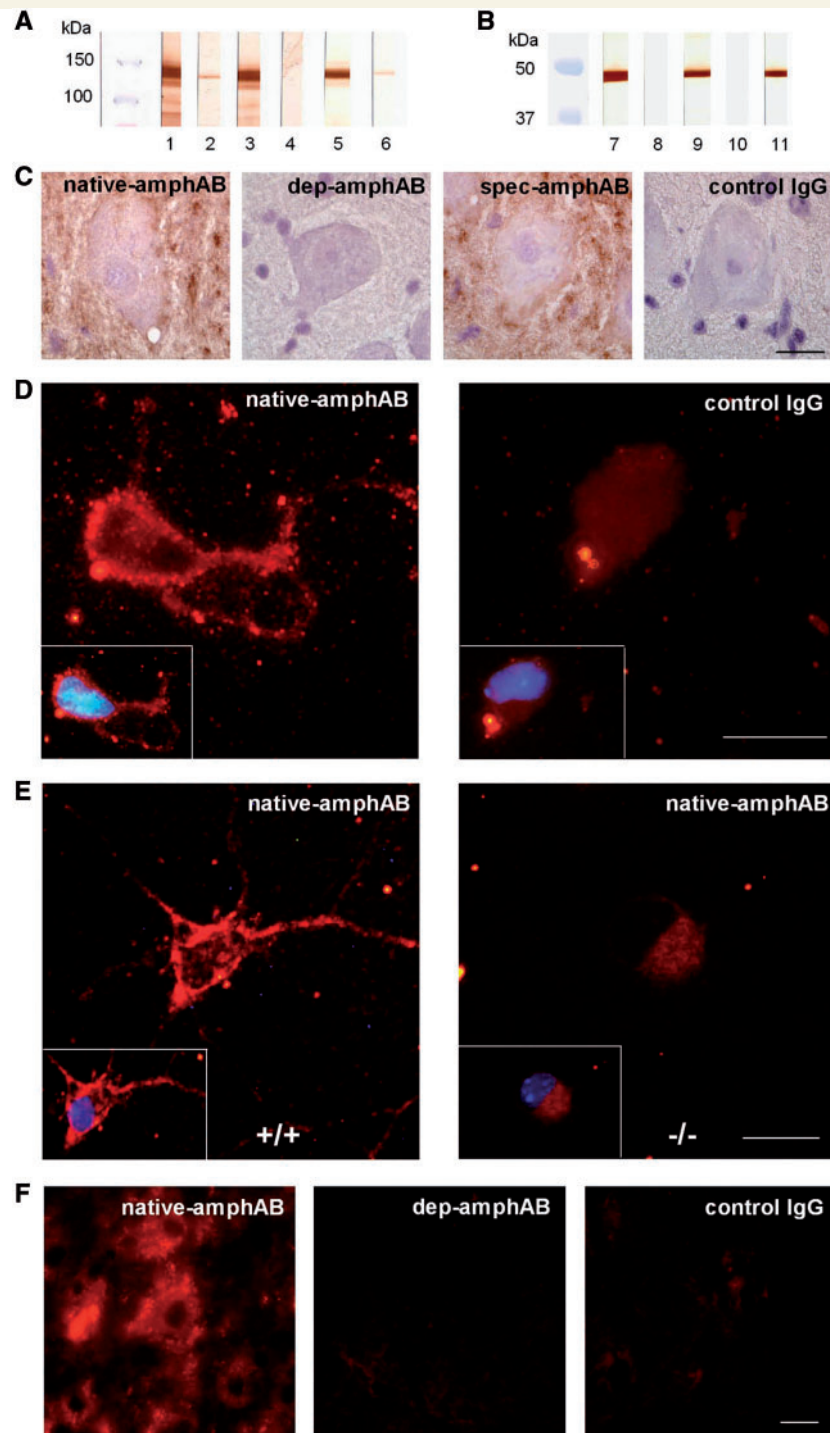


Figure 2 Selective binding of anti-amphiphysin antibodies to neuronal tissue. Western blotting of purified IgG (1 mg/ml) on rat spinal cord tissue (A) and on a glutathione S-transferase SH3 domain fusion protein (B) displayed specific binding of anti-amphiphysin antibodies (lanes 1 and 7: native-amphAB IgG; 3 and 9: spec-amphAB from Patient 1; 4 and 10: control IgG; 5 and 11: commercial, polyclonal anti-amphiphysin antibodies). Affinity chromatography resulted in almost complete depletion of anti-amphiphysin antibodies (lanes 2 and 8: dep-amphAB; 6: native-amphAB at 1000× lower concentration). (C) Naïve rat spinal cord sections were incubated with IgG ($n=3$ for each IgG preparation). Incubation with native-amphAB and with spec-amphAB from Patient 1 resulted in distinct staining of neuronal plasma membranes and dendrites, indicating specific binding to neuronal surface structures. After depletion of anti-amphiphysin antibodies these staining properties were completely absent. Control IgG at the same concentration showed no immunoreactivity (scale bar: 30 μ m). (D) Incubation of a rat spinal motor neuron-interneuron co-culture with native-amphAB IgG and subsequent immunoreaction against human IgG antibodies resulted in an intense punctate staining of the cell membrane, soma and dendrites, whereas control IgG elicited only faint staining of cell bodies (representative sample out of three for each IgG preparation; scale bar: 20 μ m). Inset shows overlay of the same neurons with DAPI. (E) Incubation of wild-type (+/+) mouse motor neurons with native-amphAB revealed a similar staining pattern as in D (left panel), whereas motor neurons from amphiphysin knockout mice (-/-) did not (scale bar: 20 μ m). (F) Treatment of rats with pathogenic native-amphAB, but not with dep-amphAB or control IgG, resulted in intense staining of spinal motor neurons in lumbar spinal cord sections (scale bar: 30 μ m).

amphiphysin knockout mice showed only faint background staining (Fig. 2E; [Supplementary Fig. 4](#)).

Human IgG was detected in the homogenized spinal cord of rats that had been injected intrathecally with native-amphAB (120 μ l at a concentration of 100 mg/ml resulting in $135 \pm 23 \mu$ g/ml tissue, $n=3$) and in the group injected with specific antibodies (spec-amphAB, 120 μ l at a concentration of 10 mg/ml resulting in $67 \pm 9 \mu$ g/ml tissue, $n=4$), indicating relatively higher binding of spec-amphAB and thus pointing to a possible enrichment at the respective binding sites. Plasma levels of human IgG in the rats were usually below the detection threshold, which made a systemic effect of the administered antibodies unlikely (data not shown).

Immunofluorescence staining for human IgG showed intense immunoreactivity of neurons in the ventral horn and in the centromedullary region in spinal cord cryosections from rats treated *in vivo* with the pathogenic native-amphAB or spec-amphAB but not with control IgG (Fig. 2F). Taken together, these findings suggest specific binding of anti-amphiphysin antibodies to neuronal structures containing amphiphysin.

Anti-amphiphysin antibodies disturb spinal synaptic pathways by reduction of GABAergic presynaptic inhibition

The abnormal continuous motor activity and hyperexcitability in monosynaptic reflexes (Floeter et al., 1998) suggest disordered

spinal inhibitory mechanisms in SPS. To assess this in our rat model, we investigated spinal inhibition in antibody treated animals *in vivo*. We examined an established monosynaptic pathway by measuring changes of Hoffmann reflex amplitude (the electrically elicited deep tendon reflex). Hoffmann reflexes are normally inhibited during high-frequency stimulation, which is due to post-activation depression at the afferent neuron-motor neuron synapse (Lev-Tov and Pinco, 1992; Lee et al., 2005) ([Supplementary Fig. 5A](#)). Indeed, in animals treated with control IgG ($n=9$ and 10 in separate experiments), frequency-dependent depression of the Hoffmann reflex was observed as expected. However, after application of native-amphAB or spec-amphAB, post-activation depression of the Hoffmann reflex amplitude was significantly diminished. This effect was not seen in rats injected with dep-amphAB (Fig. 3A and [Supplementary Fig. 2B](#)).

Another pathophysiologically relevant feature associated with the typical stiffness of SPS is incomplete inhibition of antagonistic muscles leading to co-activation of agonistic and antagonistic muscles. Therefore, we investigated the modulation of the Hoffmann reflex amplitude by applying a conditioning volley with different latencies at a nerve supplying an antagonistic muscle (Eccles et al., 1961; Lee et al., 2005; Chen et al., 2006) ([Supplementary Fig. 5B](#)). No depression in Hoffmann reflex was found in the rats treated with the pathogenic native-amphAB ($n=8$) and spec-amphAB ($n=7$) (for details see [Supplementary Fig. 6](#)).

The reduction in frequency-dependent depression of Hoffmann reflex amplitudes and depression after antagonistic stimulation may also involve polysynaptic pathways. Therefore we examined

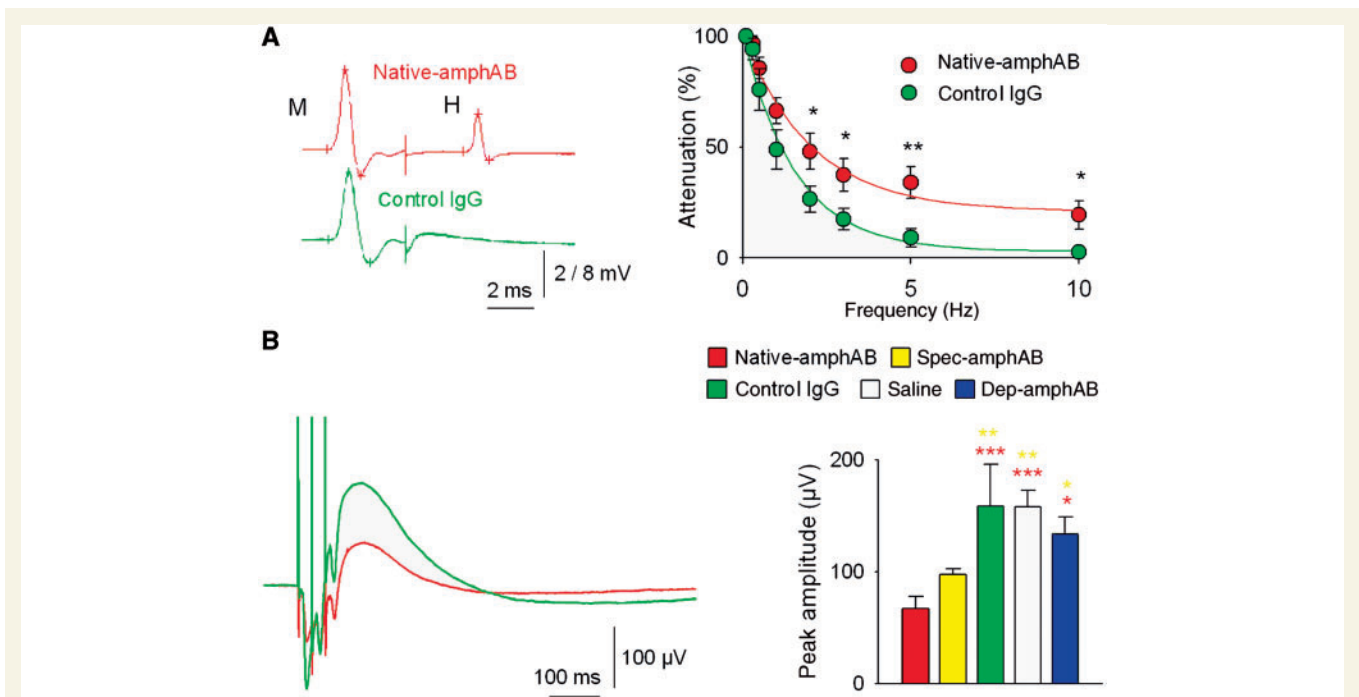


Figure 3 Reduced GABAergic spinal inhibition. (A) Left: in Hoffmann reflex recordings at 10 Hz stimulation, native-amphAB treated rats ($n=8$) reached a plateau of H-wave amplitudes at 21% of the initial amplitude in contrast to the almost complete (3%) amplitude reduction in the control IgG group ($n=9$). Right: representative Hoffmann reflex recordings with native-amphAB (upper trace) and with control IgG. (B) GABAergic dorsal root potentials evoked after a train of three stimuli (100 Hz) were significantly lowered in the native-amphAB ($n=10$, red asterisks) and spec-amphAB groups ($n=17$, yellow asterisks) compared with the control IgG ($n=15$) and saline groups ($n=12$) and rats treated with IgG depleted of anti-amphiphysin antibodies ($n=17$) ($*P<0.05$; $**P<0.01$; $***P<0.001$).

presynaptic inhibition, one of the most potent spinal inhibitory mechanisms (Eccles *et al.*, 1962a, b, 1963; Hultborn, 2006) mediated by depolarization of primary afferent presynaptic terminals through selective GABAergic axo-axonal synapses of inhibitory interneurons (termed 'last order primary afferent depolarization' interneurons). Dorsal root potentials are electrotonically conducted potentials generated by primary afferent depolarization interneurons that can be recorded from lumbar dorsal roots *in vivo* (Barron and Matthews, 1938; Eccles *et al.*, 1963; Hultborn, 2006) (Supplementary Fig. 5C and D). Dorsal root potentials showed a characteristic uniform course and could be blocked by local superfusion of bicucullin (De Koninck and Henry, 1994) (Supplementary Fig. 7A and C). After single and repetitive stimulation, dorsal root potential amplitudes were significantly reduced in rats treated with any of the anti-amphiphysin antibody fractions as compared with animals treated with control IgG (Fig. 3B; Supplementary Fig. 2C, 7B and Table 1), which is best explained by a marked reduction of presynaptic GABAergic inhibition in animals treated with pathogenic anti-amphiphysin antibodies. However, a possible influence of a decreased excitatory feed-forward input to spinal inhibitory interneurons cannot be excluded. These effects on GABAergic inhibition were not seen when IgG depleted of the specific antibodies (dep-amphAB) was used. Of note, the effects on dorsal root potential amplitudes and on Hoffmann reflex depression were less pronounced when native-amphAB from Patient 2 was used. This might be explained by the lower antibody titres (10^5 versus 10^8) of these fractions.

Patient anti-amphiphysin antibodies are specifically internalized *in vivo* and *in vitro* and bind to presynaptic nerve terminals

To address the question of whether the amphiphysin-specific antibodies enter neurons, the site of antibody binding and internalization at the sub-cellular level was studied. Spinal cord sections from rats treated with native-amphAB and spec-amphAB were double immunoreacted with antibodies to anti-human IgG and to presynaptic antigens including VGAT, VGLUT, bassoon and clathrin. High-resolution stimulation emission depletion light microscopy (Kittel *et al.*, 2006; Hell, 2007) revealed staining in punctuate structures around motor neurons and dendrites. Human IgG showed close colocalization with the presynaptic vesicle-associated VGAT, partial colocalization with VGLUT and clathrin, and a juxtaposed but not overlapping distribution with the presynaptic active zone protein bassoon, suggesting accumulation in presynaptic terminals at the sites of the vesicle cycle (Fig. 4).

In contrast to autoantibodies directed at membrane-bound receptors (Toyka *et al.*, 1975; Lang *et al.*, 1983; Sillevis Smitt *et al.*, 2000; Coesmans *et al.*, 2003), it has been discussed controversially whether antibodies to an intracellular antigen can be pathogenic, and if so, how they reach their target antigen (Kissel and Elble, 1998; Levin *et al.*, 2002). To further study binding and internalization, we incubated dissociated mouse hippocampal neurons with spec-amphAB tagged with fluorescent nanocrystals. We observed a strong and time-dependent binding followed by

internalization of the antibody complexes (Supplementary Fig. 8). After incubation of wild-type neurons with tagged control IgG or after incubation of amphiphysin knockout neurons with spec-amphAB, only scarce if any binding was observed. Intracellular binding of tagged anti-amphiphysin antibodies was verified with confocal microscopy and colocalization with the intracellular marker calnexin (linked to the endoplasmic reticulum) (Fig. 5A). Pre-incubation of tagged spec-amphAB at increasing concentrations of recombinant amphiphysin inhibited the internalization of antibodies in a concentration-dependent manner (Fig. 5B), suggesting an epitope-specific process. Internalization of labelled antibodies was inhibited with a calculated EC_{50} of 15.7 nmol by adding unlabelled spec-amphAB in increasing concentrations to a constant amount of tagged antibodies (57.5 nmol) (Fig. 5C). Reducing temperature led to a marked reduction of internalization (Fig. 5D), consistent with a temperature-dependent mechanism of internalization, e.g. clathrin-mediated endocytosis (Smith *et al.*, 2008).

Endocytic function of inhibitory synapses is preferentially affected by anti-amphiphysin antibodies

The clinical signs of SPS and our experimental results reported above are in line with defective GABAergic inhibition. Since amphiphysin is expressed in most CNS synapses, and not just in GABAergic presynaptic terminals, we set out to investigate the effects of patient IgG on inhibitory and excitatory synapses directly. In dissociated hippocampal neurons, incubation with native-amphAB but not with control IgG resulted in an increased clustering of the endocytic protein AP180 (Fig. 6A and B), which is known to result from defective endocytosis (Ferguson *et al.*, 2007; Hayashi *et al.*, 2008). Blocking the continuous neuronal background activity with TTX led to a redistribution of AP180 clustering, indicating a significant endocytic defect already at basal network activity. Stimulation emission depletion microscopy revealed a significantly increased clustering of AP180 at GABAergic synapses, marked with VGAT, as compared with glutamatergic synapses, marked with VGLUT (Fig. 6C and D). When measuring the neurotransmitter release in cell culture supernatants with high-performance liquid chromatography, incubation with native-amphAB resulted in a significant decrease of neurotransmitter release at basal levels and even more so after stimulation with 90 mmol KCl (Fig. 6E and F). Thereby the GABA release (78% compared with incubation with control IgG) and glutamate release (53% of control IgG) were both decreased. Notably, after incubation with anti-amphiphysin antibodies, brief stimulation with 90 mmol KCl no longer resulted in a significant increase in GABA release. The structural integrity of dissociated hippocampal neurons after high-potassium stimulation was ascertained by visual inspection after staining against β -tubulin (Supplementary Fig. 9).

Next we investigated the functional effect of anti-amphiphysin antibodies on the vesicle cycle. When synaptic boutons of dissociated hippocampal neurons were loaded with FM dyes (Fig. 7A and B), subsequent destaining with 90 mmol KCl pulses was faster after pre-incubation with native-amphAB and spec-amphAB as compared with dep-amphAB and control IgG ($\tau = 14, 12, 25$

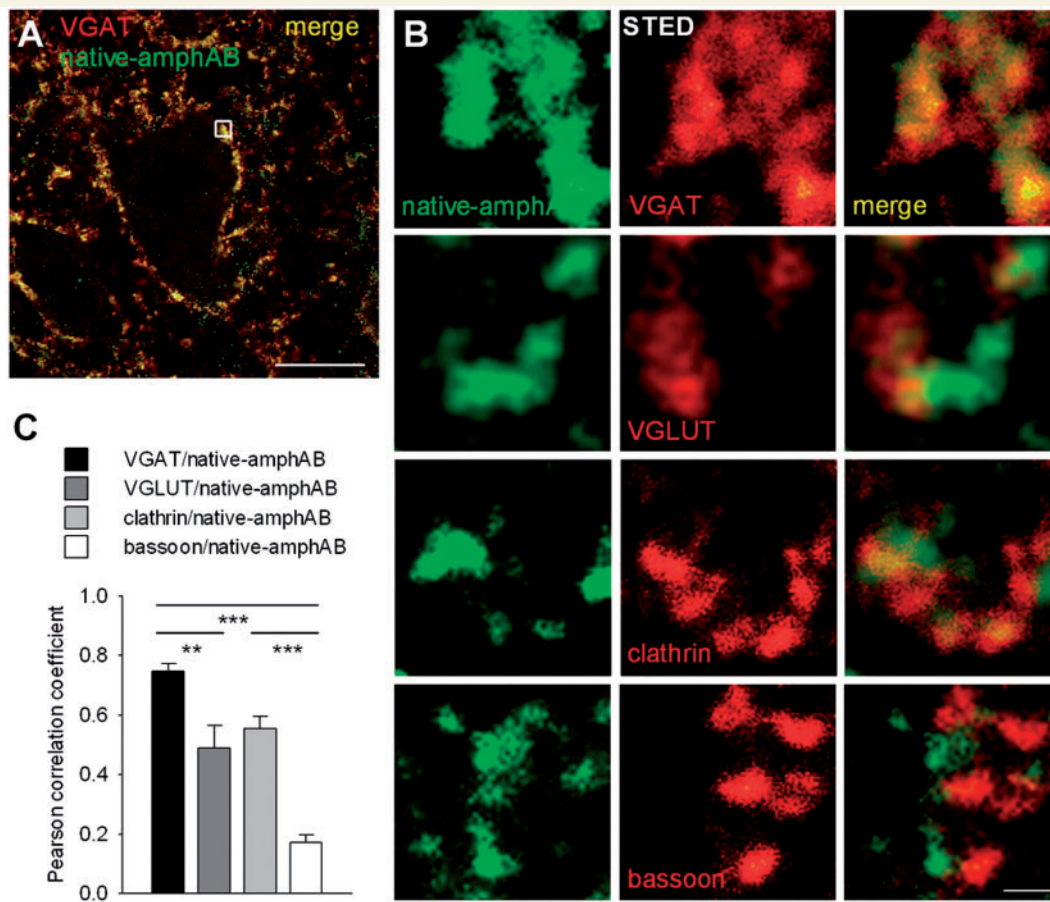


Figure 4 Presynaptic localization of intrathecally injected anti-amphiphysin antibodies. (A) Double immunofluorescence labelling anti-human IgG and the presynaptic markers VGAT, showed punctate staining around motor neurons and dendrites in the anterior horn of the spinal cord (scale bar: 20 μ m). Staining for VGLUT, clathrin and bassoon gave similar patterns. (B) Stimulation emission depletion high-resolution microscopy from an area of interest (small square in the left panel) revealed almost complete overlay of human IgG with VGAT, partial overlay with VGLUT and clathrin, and largely adjacent staining with the active zone marker bassoon, indicating presynaptic enrichment of injected anti-amphiphysin antibodies (scale bar: 500 nm). (C) The amount of colocalization was determined using volumetric data and calculating Pearson's correlation coefficient (** $P < 0.01$; *** $P < 0.001$).

and 48 s, respectively), whereby the first phase of rapid destaining was preferentially affected (Fig. 7C). Since loading of synaptic boutons with FM dye-stained vesicles depends on effective endocytosis, the faster destaining of boutons by anti-amphiphysin antibodies may be explained by defective endocytosis leading to fewer releasable vesicles. We then compared the FM dye destaining kinetics separately in GABAergic and glutamatergic synapses (Fig. 7B). Treatment with spec-amphAB but not with dep-amphAB led to a faster destaining also in glutamatergic synapses ($\tau = 19$ versus 51 s). The loading capacity of GABAergic boutons was markedly reduced to 59% as compared with glutamatergic boutons within the same experiments (Fig. 7D), corroborating a substantial defect in vesicular endocytosis, preferentially in GABAergic synapses.

Since studying GABAergic transmission in spinal cord slices requires differentiation between monosynaptic and polysynaptic input (Torsney and MacDermott, 2006), we turned to a well-defined, simple model synapse which is capable of high-frequency

synaptic transmission with known high turnover of presynaptic vesicles (Kraushaar and Jonas, 2000). We performed whole-cell patch-clamp analysis of a monosynaptic GABAergic inhibitory transmission on hippocampal granule cells in acute slice preparations after incubation with native-amphAB and control IgG (Fig. 8A; Supplementary Fig. 10). The analysis of spontaneous GABAergic miniature potentials and of single evoked inhibitory postsynaptic currents revealed no difference between groups in amplitudes, rise time and decay time, indicating no relevant synaptic transmission defect at resting conditions. In contrast, when GABAergic afferents were stimulated at high frequencies, the amplitude of evoked inhibitory postsynaptic currents decreased faster in slices treated with antibodies against amphiphysin ($\tau = 0.9$ versus 1.7 s), and it was significantly smaller throughout the first phase of train stimulation. Additionally, pre-incubation with native-amphAB led to lower absolute amplitude of GABAergic inhibitory postsynaptic currents in the recovery phase (Fig. 8B).

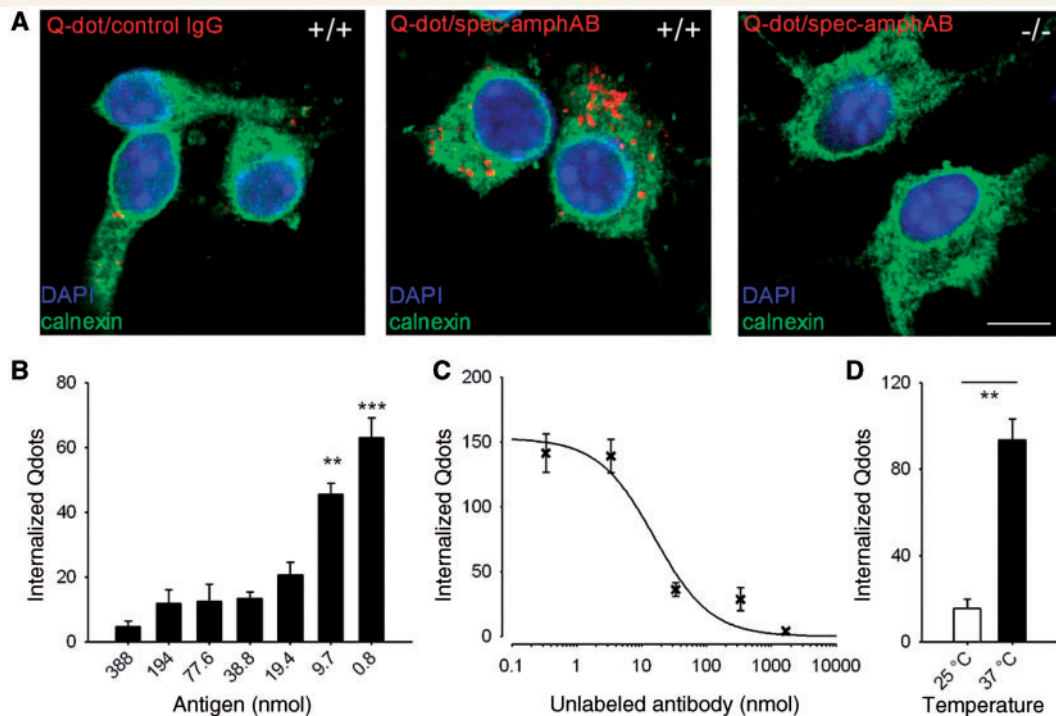


Figure 5 Specific neuronal uptake of anti-amphiphysin antibodies. (A) Confocal microscopy of dissociated hippocampal neurons incubated with quantum dot (Qdot) and stained with the intracellular marker calnexin showed internalization of anti-amphiphysin antibodies in wild-type neurons (+/+), but only minimal neuronal uptake of tagged control IgG. No specific internalization of anti-amphiphysin antibodies was observed with neurons from amphiphysin knockout mice (-/-) (scale bar: 10 μ m). (B) Preabsorption with the antigen by pre-incubation of tagged spec-amphAB with recombinant amphiphysin resulted in a concentration dependent decrease of free binding sites of the antibodies and lead to diminished uptake of anti-amphiphysin antibodies (saturated conditions from 38.8 nmol). (C) Pre-incubation with tagged spec-amphAB (46 nmol) and various amounts of unlabelled spec-amphAB revealed a decrease of internalized antibodies with increasing amounts of unlabelled antibodies, confirming the epitope-specific binding and subsequent uptake of anti-amphiphysin antibodies. Fitting a Hill equation, $Q = Q_{max} \times EC_{50}/(EC_{50} + Ab)$ resulted in an EC_{50} of 15.7 nmol (Q , number of internalized Qdots; Ab , concentration of unlabelled antibody). (D) Reducing temperature resulted in a marked decrease of internalized tagged spec-amphAB (** $P < 0.01$; *** $P < 0.001$) indicating a temperature-sensitive uptake mechanism.

Discussion

The principal finding of our study is that human disease-related antibodies against the SH3 domain of amphiphysin, an intracellular protein involved in synaptic transmission, are capable of inducing a disorder of synaptic inhibition. We provide experimental evidence for the concept that these effects are brought about by binding of the antibodies to CNS neurons with subsequent internalization, in turn leading to a disturbance of synaptic vesicle endocytosis and, consequently, to diminished transmitter release.

The behavioural observations in rats treated with antibodies to amphiphysin from two patients with SPS were strikingly similar to the core signs of these and other SPS patients and are consistent with reduced synaptic inhibition.

Specificity of the antibody effects

We used several strategies to test the amphiphysin specificity of the observed effects: (i) the effects observed *in vivo* were strictly related to anti-amphiphysin antibodies; (ii) as shown with

high-resolution stimulation emission depletion microscopy, injected antibodies accumulated in presynaptic terminals at the site of vesicle endocytosis, consistent with the known distribution of the target antigen and the anatomical site of the functional defects identified by electrophysiology; (iii) internalization of anti-amphiphysin antibodies into hippocampal neurons was dependent on the presence of amphiphysin, as shown by competition experiments. Corroborating this notion, no specific internalization could be observed in neurons from amphiphysin-deficient mice. Collectively, these findings make it unlikely that an additional antibody of unknown specificity within the patients' polyclonal IgG fraction might have been responsible for the observed effects on synaptic inhibition.

The pathogenic role of circulating autoantibodies associated with diseases of the CNS has long been a matter of debate, unlike in autoimmune disorders of the neuromuscular junction (Toyka *et al.*, 1975; Vincent *et al.*, 1995; Buchwald *et al.*, 1998a, 2005) and peripheral nerves (Fukunaga *et al.*, 1983; Roberts *et al.*, 1994; Buchwald *et al.*, 1998a). In only few conditions, pathogenic effects of autoantibodies in CNS diseases were

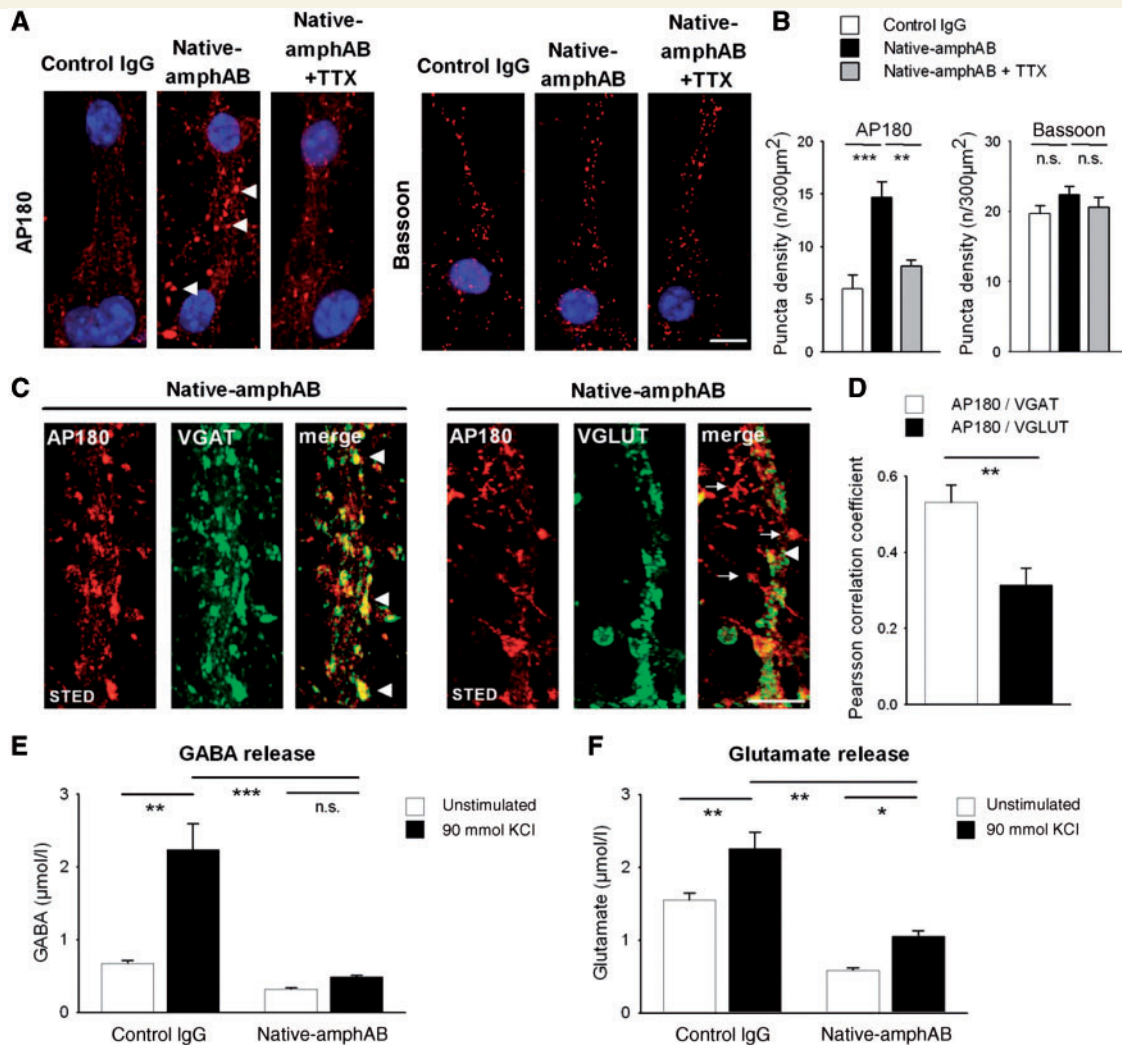


Figure 6 Functional effects of autoantibodies on GABAergic and glutamatergic synapses. (A and B) Confocal imaging of mouse hippocampal neurons treated either with native-amphAB or control IgG revealed enhanced clustering (arrowheads) of the endocytic protein AP180, but not of the active-zone protein bassoon in neurons pre-incubated with anti-amphiphysin antibodies as compared with control IgG. AP180 was redistributed in cultures when synaptic network activity was blocked by tetrodotoxin (TTX; $^{***}P < 0.01$; scale bar $10 \mu\text{m}$). (C and D) Clustering of the endocytic protein AP180 occurs preferentially at GABAergic synapses. High-resolution stimulation emission depletion microscopy revealed significantly more overlay of GABAergic synapses (stained with VGAT) with clusters of AP180 (arrowheads), as compared with glutamatergic synapses (stained with VGLUT) (arrows; scale bar $5 \mu\text{m}$; $^{***}P < 0.01$). (E and F) Following incubation with native-amphAB high-performance liquid chromatography analysis of cell culture supernatant revealed a substantial decrease of GABA release (down to 21.8% compared with incubation with control IgG) and, to a lesser extent, of glutamate release (down to 46.6%; $P < 0.01$). Stimulation with 90 mM K^+ in anti-amphiphysin IgG treated cell cultures did not result in an increase of GABA release, but did increase glutamate release. This indicates a more pronounced alteration of inhibitory as compared with excitatory synaptic activity ($^{*}P < 0.05$; $^{**}P < 0.01$; $^{***}P < 0.001$).

proposed (Rogers *et al.*, 1994; Silveis Smitt *et al.*, 2000; Coesmans *et al.*, 2003; Lennon *et al.*, 2005) and very recently shown for the disorder neuromyelitis optica (Bennett *et al.*, 2009; Bradl *et al.*, 2009; Saadoun *et al.*, 2010). In all these conditions, the crucial antigen is a receptor or ion channel on the cell membrane, or a protein adjacent or linked to such receptors or channels. In contrast, it has usually been considered unlikely that antibodies to an intracellular protein antigen might become pathogenic, and if they were, it remained unclear how they would reach their target antigen (Kissel and Elble, 1998;

Levin *et al.*, 2002). We here show data suggesting that patient antibodies can be internalized into neurons and colocalize with other intracellular proteins *in vivo* and *in vitro* by an epitope-specific process.

Deficient GABAergic inhibition as a pathophysiologic mechanism in SPS

Several lines of argumentation lead to the hypothesis of disturbed GABAergic inhibition in SPS. (i) Electromyography shows persistent

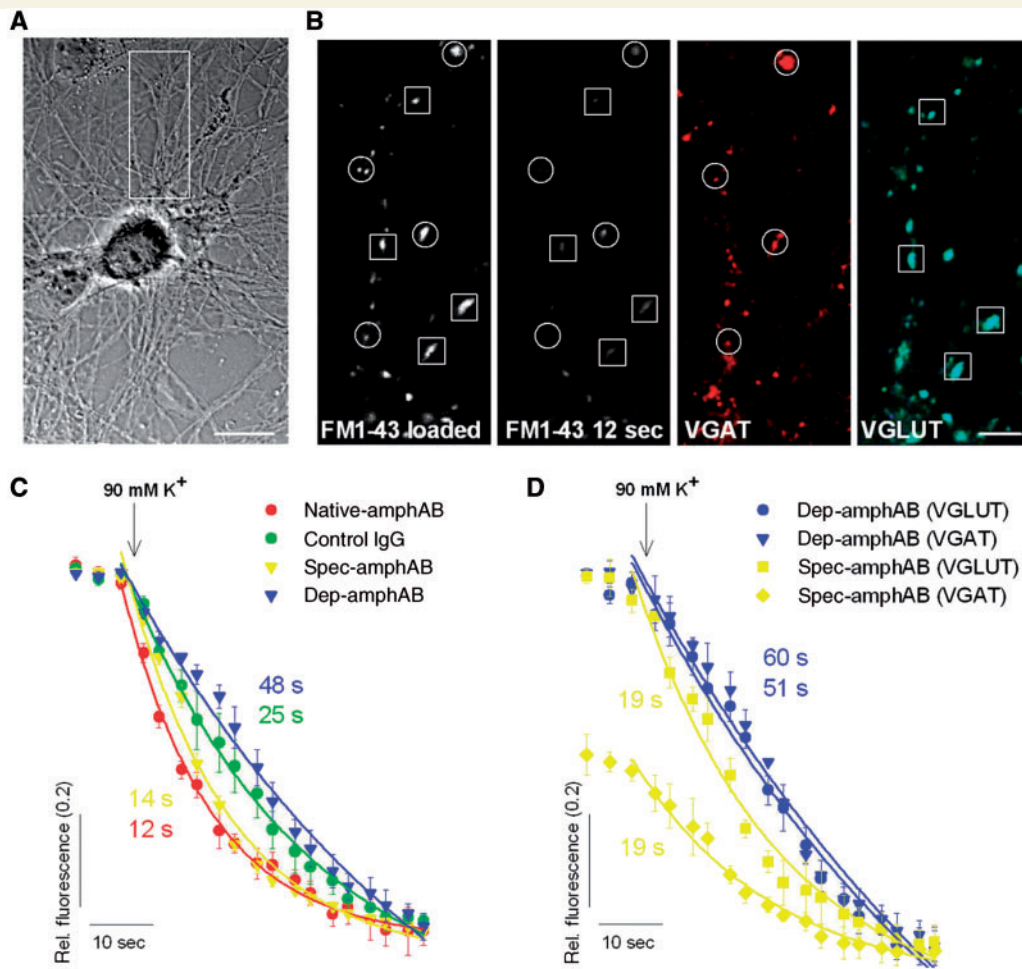


Figure 7 Vesicle endocytosis and subsequent transmitter release is preferentially affected in GABAergic synapses. (A and B) Synaptic boutons of dissociated hippocampal neurons were loaded with FM dye 1–43. Destaining by vesicle exocytosis was elicited using brief stimulation with 90 mM K^+ and images were taken every 2 s. GABAergic (circles) and glutamatergic (squares) synapses were identified after the live imaging by VGAT and VGLUT immunofluorescence [inset in (A); scale bar: 20 μ m (A), 50 μ m (B)]. (C) Analysis revealed a faster-destaining time course of synapses treated with native-amphAB ($n=3$ experiments; 116 boutons analysed) or spec-amphAB ($n=4$; 133 boutons) compared with dep-amphAB ($n=4$; 134 boutons) or control IgG ($n=4$; 164 boutons) ($P<0.05$). (D) Differentiating between GABA- and glutamatergic synapses-revealed slightly faster destaining of glutamatergic synapses after pretreatment with spec-amphAB ($n=3$; 61 boutons) compared with dep-amphAB ($n=3$; 63 boutons) ($P<0.01$, 15–18 s after the start of destaining). However, in GABAergic synapses ($n=3$; 66 boutons), the initial FM dye loading intensity was markedly reduced ($P<0.001$) compared with glutamatergic synapses (within the same experiments) and to both kinds of synapses pre-treated with dep-amphAB ($n=3$, 64 boutons for GABAergic synapses). This indicates insufficient endocytosis resulting in a diminished number of releasable vesicles.

motor activity in patients and in the animal model (Meinck *et al.*, 1984; Sommer *et al.*, 2005); (ii) patients usually respond to GABAergic drugs like benzodiazepines; (iii) all three other types of autoantibodies associated with SPS to date directly target GABAergic structures: glutamate decarboxylase (Solimena *et al.*, 1988), GABA-receptor-associated protein (GABARAP) (Raju *et al.*, 2006) and gephyrin (Butler *et al.*, 2000). It is unclear why GABAergic synapses should be preferentially affected by anti-amphiphysin antibodies, since amphiphysin has a widespread distribution in the CNS with a preferential occurrence in presynaptic terminals around synaptic vesicles (Lichte *et al.*, 1992; David *et al.*, 1996). Recently, a striking heterogeneity in synaptic vesicle recycling and functional properties between inhibitory and

excitatory synapses was shown in a mouse model of defective endocytosis due to dynamin 1 deficiency (Ferguson *et al.*, 2007; Hayashi *et al.*, 2008). Inhibitory GABAergic synapses were selectively affected by endocytic deficiency, which was attributed to their intrinsic properties, in particular to their higher level of tonic activity and spiking frequency with a fast synaptic vesicle turnover (Kraushaar and Jonas, 2000; Luthi *et al.*, 2001).

To test spinal pathways in our experimental rats treated intrathecally with the purified patient IgG preparations, we used similar paradigms as were used previously by others in patients with SPS (Floeter *et al.*, 1998). In animals injected with anti-amphiphysin antibodies, frequency-dependent Hofmann reflex depression, Hofmann reflex depression after antagonistic stimulation and

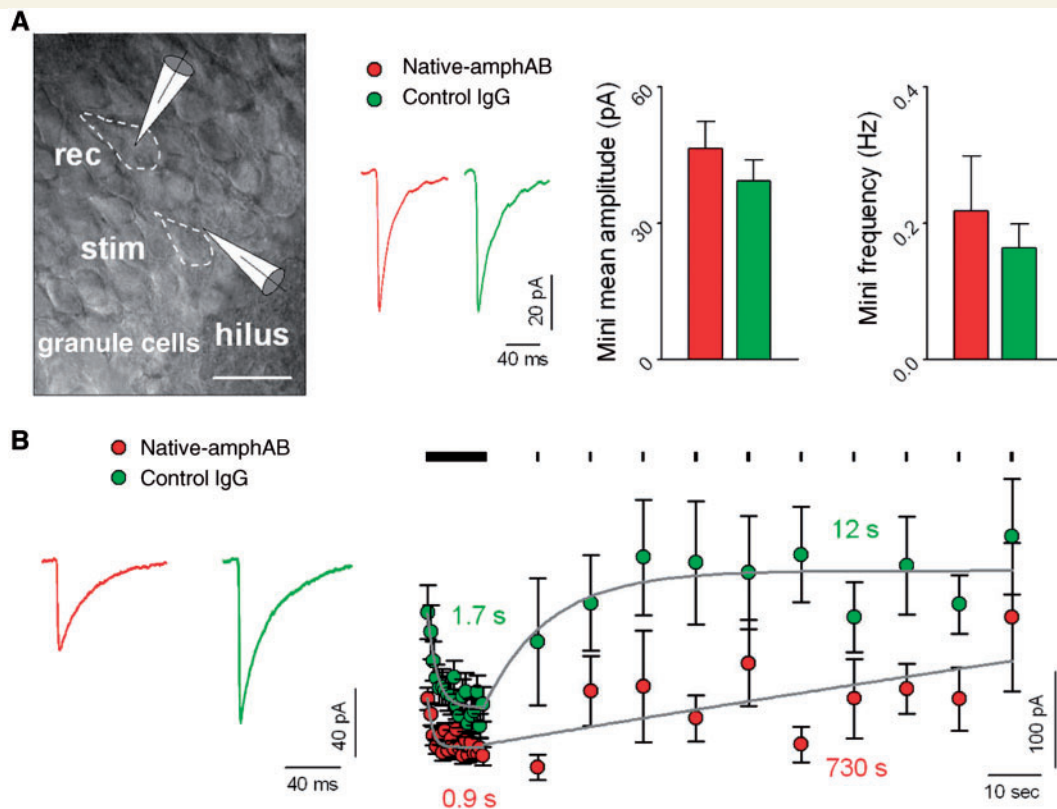


Figure 8 (A) Whole-cell recording of granule cells (cell margins marked by dashed lines) in the hippocampal dentate gyrus showed only minor and not significant differences in amplitude or frequency of GABAergic miniature inhibitory postsynaptic currents when slices were pre-incubated with native-amphAB or control IgG (examples are averaged traces from single experiments; stim, stimulating electrode; rec, recording electrode; scale bar: 20 μ m). (B) Analysis of mean inhibitory postsynaptic currents amplitudes during high frequency stimulation (10 Hz) showed significantly lower amplitudes in native-amphAB treated slices during the first phase of the train response ($P < 0.001$ for stimuli 10–20, $P < 0.05$ for stimuli 20–30) and in the recovery period ($P < 0.05$; native-amphAB: $n = 7$, control IgG: $n = 10$). Traces show averaged responses from two single experiments during train stimulation. After high-frequency stimulation, GABAergic inhibitory postsynaptic currents decline faster in native-amphAB treated cells compared with control IgG ($\tau = 0.9$ s versus 1.7 s) and also the recovery of inhibitory postsynaptic currents amplitudes is substantially slower after the train stimulation ($\tau = 730$ s versus 12 s).

dorsal root potential peak amplitudes were all significantly lowered, which is best explained by a frequency-dependent reduction in inhibitory spinal synaptic function. Taken together, this makes antibody mediated reduction of GABAergic inhibition a likely disease mechanism in anti-amphiphysin associated SPS. In support of these findings, our *in vitro* experiments showed that the endocytic and consecutively exocytic function of GABAergic synapses were clearly more affected than that of glutamatergic synapses upon incubation with antibodies against amphiphysin: (i) enhanced clustering of the endocytotic protein AP180; (ii) a decrease of neurotransmitter release and faster destaining and (iii) decreased initial vesicle staining of FM dyes are all consistent with a defect of endocytosis and a subsequent decrease in the releasable vesicle pool resulting in reduced synaptic transmission. Moreover, our patch-clamp analysis revealed a substantial decrease of GABAergic transmission during high-frequency stimulation and in the ensuing recovery phase, but not under resting conditions, which is again consistent with a decrease of the releasable vesicle pool after repetitive synaptic activity. This is in accordance with previous studies, where injection of experimentally generated

anti-amphiphysin antibodies into the lamprey giant synapse led to a greatly reduced presynaptic vesicle pool and to an increased number of clathrin-coated intermediates (Shupliakov *et al.*, 1997; Evergren *et al.*, 2004). Accordingly, in amphiphysin-deficient mice, deficits in synaptic vesicle recycling were unmasked only by stimulation (Di Paolo *et al.*, 2002), indicating a high degree of compensation of the altered amphiphysin function *in vivo*, similar to what we could observe in our passive-transfer animal model. Extrapolating these findings to SPS patients with anti-amphiphysin antibodies, we hypothesize that their GABAergic inhibition may be deficient in a state of high-excitatory activity, such as in stressful situations where finely tuned inhibitory drive is needed. This hypothesis would match the observed worsening of SPS symptoms with sudden noises or frightening emotions. Nevertheless, direct experimental comparison of the effects on excitatory and inhibitory synapses and tonic versus phasic synapses, by antibodies against amphiphysin, should be elucidated in future studies.

In conclusion, the observed phenotype and the electrophysiological alterations in the experimental rats *in vivo* and the *in vitro* findings collectively support our concept that a preferential

disturbance of GABAergic inhibitory synaptic activity may be the crucial pathophysiological basis of SPS.

Acknowledgements

We thank M. Sendtner for helpful suggestions and discussions and for critically reading the article and R.F. Schmidt for helpful advice and discussion of the electrophysiological recordings. We are indebted to P. De Camilli for his continuous support and encouragement, for providing the cDNA clone encoding for amphiphysin protein, the constructs containing its wild-type SH3 domain, amphiphysin KO mice and for helpful suggestions on the interpretation of our findings. L. Biko, S. Hellmig, B. Dekant, H. Bruenner, B. Broll, R. Burger and H. Wetzstein provided expert technical assistance in animal experiments, histology, high-performance liquid chromatography and IgG preparations. The authors declare no competing financial interests.

Funding

Deutsche Forschungsgemeinschaft SFB 581, (TP A7 and HE 2621/4-1); Interdisciplinary Clinical Research Centre (IZKF) of the University of Würzburg School of Medicine; Intramural University Research Funds.

Supplementary material

Supplementary material is available at *Brain* online.

References

Barron DH, Matthews BH. The interpretation of potential changes in the spinal cord. *J Physiol* 1938; 92: 276–321.

Bennett JL, Lam C, Kalluri SR, Saikali P, Bautista K, Dupree C, et al. Intrathecal pathogenic anti-aquaporin-4 antibodies in early neuromyelitis optica. *Ann Neurol* 2009; 66: 617–29.

Bradl M, Misu T, Takahashi T, Watanabe M, Mader S, Reindl M, et al. Neuromyelitis optica: pathogenicity of patient immunoglobulin in vivo. *Ann Neurol* 2009; 66: 630–43.

Buchwald B, Ahangari R, Weishaupt A, Toyka KV. Presynaptic effects of immunoglobulin G from patients with Lambert-Eaton myasthenic syndrome: their neutralization by intravenous immunoglobulins. *Muscle Nerve* 2005; 31: 487–94.

Buchwald B, Toyka KV, Zielasek J, Weishaupt A, Schweiger S, Dudel J. Neuromuscular blockade by IgG antibodies from patients with Guillain-Barre syndrome: a macro-patch-clamp study. *Ann Neurol* 1998a; 44: 913–22.

Buchwald B, Weishaupt A, Toyka KV, Dudel J. Pre- and postsynaptic blockade of neuromuscular transmission by Miller-Fisher syndrome IgG at mouse motor nerve terminals. *Eur J Neurosci* 1998b; 10: 281–90.

Butler MH, Hayashi A, Ohkoshi N, Villmann C, Becker CM, Feng G, et al. Autoimmunity to gephyrin in Stiff-Man syndrome. *Neuron* 2000; 26: 307–12.

Chen XY, Chen L, Chen Y, Wolpaw JR. Operant conditioning of reciprocal inhibition in rat soleus muscle. *J Neurophysiol* 2006; 96: 2144–50.

Coesmans M, Smitt PA, Linden DJ, Shigemoto R, Hirano T, Yamakawa Y, et al. Mechanisms underlying cerebellar motor deficits due to mGluR1-autoantibodies. *Ann Neurol* 2003; 53: 325–36.

Dalakas MC, Fujii M, Li M, McElroy B. The clinical spectrum of anti-GAD antibody-positive patients with stiff-person syndrome. *Neurology* 2000; 55: 1531–5.

Dalmau J, Gleichman AJ, Hughes EG, Rossi JE, Peng X, Lai M, et al. Anti-NMDA-receptor encephalitis: case series and analysis of the effects of antibodies. *Lancet Neurol* 2008; 7: 1091–8.

David C, McPherson PS, Mundigl O, de Camilli P. A role of amphiphysin in synaptic vesicle endocytosis suggested by its binding to dynamin in nerve terminals. *Proc Natl Acad Sci USA* 1996; 93: 331–5.

David C, Solimena M, De Camilli P. Autoimmunity in stiff-Man syndrome with breast cancer is targeted to the C-terminal region of human amphiphysin, a protein similar to the yeast proteins, Rvs167 and Rvs161. *FEBS Lett* 1994; 351: 73–9.

De Koninck Y, Henry JL. Prolonged GABAA-mediated inhibition following single hair afferent input to single spinal dorsal horn neurones in cats. *J Physiol* 1994; 476: 89–100.

Di Paolo G, Sankaranarayanan S, Wenk MR, Daniell L, Perucco E, Caldaroni BJ, et al. Decreased synaptic vesicle recycling efficiency and cognitive deficits in amphiphysin 1 knockout mice. *Neuron* 2002; 33: 789–804.

Eccles JC, Eccles RM, Magni F. Central inhibitory action attributable to presynaptic depolarization produced by muscle afferent volleys. *J Physiol* 1961; 159: 147–66.

Eccles JC, Kostyuk PG, Schmidt RF. Presynaptic inhibition of the central actions of flexor reflex afferents. *J Physiol* 1962a; 161: 258–81.

Eccles JC, Schmidt RF, Willis WD. Presynaptic inhibition of the spinal monosynaptic reflex pathway. *J Physiol* 1962b; 161: 282–97.

Eccles JC, Schmidt R, Willis WD. Pharmacological Studies on Presynaptic Inhibition. *J Physiol* 1963; 168: 500–30.

Evergren E, Marcucci M, Tomilin N, Low P, Slepnev V, Andersson F, et al. Amphiphysin is a component of clathrin coats formed during synaptic vesicle recycling at the lamprey giant synapse. *Traffic* 2004; 5: 514–28.

Ferguson SM, Brasnjo G, Hayashi M, Wolfel M, Collesi C, Giovedi S, et al. A selective activity-dependent requirement for dynamin 1 in synaptic vesicle endocytosis. *Science* 2007; 316: 570–4.

Floeter MK, Valls-Sole J, Toro C, Jacobowitz D, Hallett M. Physiologic studies of spinal inhibitory circuits in patients with stiff-person syndrome. *Neurology* 1998; 51: 85–93.

Folli F, Solimena M, Cofield R, Austoni M, Tallini G, Fassetta G, et al. Autoantibodies to a 128-kd synaptic protein in three women with the stiff-man syndrome and breast cancer. *N Engl J Med* 1993; 328: 546–51.

Fukunaga H, Engel AG, Lang B, Newsom-Davis J, Vincent A. Passive transfer of Lambert-Eaton myasthenic syndrome with IgG from man to mouse depletes the presynaptic membrane active zones. *Proc Natl Acad Sci USA* 1983; 80: 7636–40.

Grabs D, Slepnev VI, Songyang Z, David C, Lynch M, Cantley LC, et al. The SH3 domain of amphiphysin binds the proline-rich domain of dynamin at a single site that defines a new SH3 binding consensus sequence. *J Biol Chem* 1997; 272: 13419–25.

Hayashi M, Raimondi A, O'Toole E, Paradise S, Collesi C, Cremona O, et al. Cell- and stimulus-dependent heterogeneity of synaptic vesicle endocytic recycling mechanisms revealed by studies of dynamin 1-null neurons. *Proc Natl Acad Sci USA* 2008; 105: 2175–80.

Hell SW. Far-field optical nanoscopy. *Science* 2007; 316: 1153–8.

Hultborn H. Spinal reflexes, mechanisms and concepts: from Eccles to Lundberg and beyond. *Prog Neurobiol* 2006; 78: 215–32.

Kissel JT, Elble RJ. Stiff-person syndrome: stiff opposition to a simple explanation. *Neurology* 1998; 51: 11–4.

Kittel RJ, Wichmann C, Rasse TM, Fouquet W, Schmidt M, Schmid A, et al. Bruchpilot promotes active zone assembly, Ca²⁺ channel clustering, and vesicle release. *Science* 2006; 312: 1051–4.

- Klingauf J, Kavalali ET, Tsien RW. Kinetics and regulation of fast endocytosis at hippocampal synapses. *Nature* 1998; 394: 581–5.
- Kraushaar U, Jonas P. Efficacy and stability of quantal GABA release at a hippocampal interneuron-principal neuron synapse. *J Neurosci* 2000; 20: 5594–607.
- Lalli G, Bohnert S, Deinhardt K, Verastegui C, Schiavo G. The journey of tetanus and botulinum neurotoxins in neurons. *Trends Microbiol* 2003; 11: 431–7.
- Lang B, Newsom-Davis J, Prior C, Wray D. Antibodies to motor nerve terminals: an electrophysiological study of a human myasthenic syndrome transferred to mouse. *J Physiol* 1983; 344: 335–45.
- Lee JK, Emch GS, Johnson CS, Wrathall JR. Effect of spinal cord injury severity on alterations of the H-reflex. *Exp Neurol* 2005; 196: 430–40.
- Lennon VA, Kryzer TJ, Pittock SJ, Verkman AS, Hinson SR. IgG marker of optic-spinal multiple sclerosis binds to the aquaporin-4 water channel. *J Exp Med* 2005; 202: 473–7.
- Lev-Tov A, Pinco M. In vitro studies of prolonged synaptic depression in the neonatal rat spinal cord. *J Physiol* 1992; 447: 149–69.
- Levin MC, Lee SM, Kalume F, Morcos Y, Dohan FC, Jr. Hasty KA, et al. Autoimmunity due to molecular mimicry as a cause of neurological disease. *Nat Med* 2002; 8: 509–13.
- Lichte B, Veh RW, Meyer HE, Kilimann MW. Amphiphysin, a novel protein associated with synaptic vesicles. *Embo J* 1992; 11: 2521–30.
- Luthi A, Di Paolo G, Cremona O, Daniell L, De Camilli P, McCormick DA. Synaptojanin 1 contributes to maintaining the stability of GABAergic transmission in primary cultures of cortical neurons. *J Neurosci* 2001; 21: 9101–11.
- Meinck HM, Ricker K, Conrad B. The stiff-man syndrome: new pathophysiological aspects from abnormal exteroceptive reflexes and the response to clomipramine, clonidine, and tizanidine. *J Neurol Neurosurg Psychiatry* 1984; 47: 280–7.
- Meinck HM, Thompson PD. Stiff man syndrome and related conditions. *Mov Disord* 2002; 17: 853–66.
- Murinson BB, Vincent A. Stiff-person syndrome: autoimmunity and the central nervous system. *CNS Spectr* 2001; 6: 427–33.
- Raju R, Rakocevic G, Chen Z, Hoehn G, Semino-Mora C, Shi W, et al. Autoimmunity to GABAA-receptor-associated protein in stiff-person syndrome. *Brain* 2006; 129: 3270–6.
- Roberts M, Willison H, Vincent A, Newsom-Davis J. Serum factor in Miller-Fisher variant of Guillain-Barre syndrome and neurotransmitter release. *Lancet* 1994; 343: 454–5.
- Rogers SW, Andrews PI, Gahring LC, Whisenand T, Cauley K, Crain B, et al. Autoantibodies to glutamate receptor GluR3 in Rasmussen's encephalitis. *Science* 1994; 265: 648–51.
- Saadoun S, Waters P, Anthony Bell B, Vincent A, Verkman AS, Papadopoulos MC. Intra-cerebral injection of neuromyelitis optica immunoglobulin G and human complement produces neuromyelitis optica lesions in mice. *Brain* 2010; 133: 349–61.
- Schmidt RF. Presynaptic inhibition in the vertebrate central nervous system. *Ergeb Physiol* 1971; 63: 20–101.
- Shiang R, Ryan SG, Zhu YZ, Hahn AF, O'Connell P, Wasmuth JJ. Mutations in the alpha 1 subunit of the inhibitory glycine receptor cause the dominant neurologic disorder, hyperekplexia. *Nat Genet* 1993; 5: 351–8.
- Shupliakov O, Low P, Grabs D, Gad H, Chen H, David C, et al. Synaptic vesicle endocytosis impaired by disruption of dynamin-SH3 domain interactions. *Science* 1997; 276: 259–63.
- Sillevis Smitt P, Kinoshita A, De Leeuw B, Moll W, Coesmans M, Jaarsma D, et al. Paraneoplastic cerebellar ataxia due to autoantibodies against a glutamate receptor. *N Engl J Med* 2000; 342: 21–7.
- Smith SM, Renden R, von Gersdorff H. Synaptic vesicle endocytosis: fast and slow modes of membrane retrieval. *Trends Neurosci* 2008; 31: 559–68.
- Solimena M, Folli F, Denis-Donini S, Comi GC, Pozza G, De Camilli P, et al. Autoantibodies to glutamic acid decarboxylase in a patient with stiff-man syndrome, epilepsy, and type I diabetes mellitus. *N Engl J Med* 1988; 318: 1012–20.
- Sommer C, Weishaupt A, Brinkhoff J, Biko L, Wessig C, Gold R, et al. Paraneoplastic stiff-person syndrome: passive transfer to rats by means of IgG antibodies to amphiphysin. *Lancet* 2005; 365: 1406–11.
- Torsney C, MacDermott AB. Disinhibition opens the gate to pathological pain signaling in superficial neurokinin 1 receptor-expressing neurons in rat spinal cord. *J Neurosci* 2006; 26: 1833–43.
- Toyka KV, Drachman DB, Pestronk A, Kao I. Myasthenia gravis: passive transfer from man to mouse. *Science* 1975; 190: 397–9.
- Vasconcelos OM, Dalakas MC. Stiff-person Syndrome. *Curr Treat Options Neurol* 2003; 5: 79–90.
- Vincent A, Roberts M, Willison H, Lang B, Newsom-Davis J. Autoantibodies, neurotoxins and the nervous system. *J Physiol Paris* 1995; 89: 129–36.
- Wessig C, Klein R, Schneider MF, Toyka KV, Naumann M, Sommer C. Neuropathology and binding studies in anti-amphiphysin-associated stiff-person syndrome. *Neurology* 2003; 61: 195–8.
- Wigge P, McMahon HT. The amphiphysin family of proteins and their role in endocytosis at the synapse. *Trends Neurosci* 1998; 21: 339–44.
- Yaksh TL, Rudy TA. Chronic catheterization of the spinal subarachnoid space. *Physiol Behav* 1976; 17: 1031–6.

3.6 Hallermann *et al.*, 2010a, HFSP J, 4:75-84

Seite 78-90

Mechanisms of short-term plasticity at neuromuscular active zones of *Drosophila*

Stefan Hallermann,¹ Manfred Heckmann,^{1,2,3} and Robert J. Kittel^{1,2,3}

¹Carl-Ludwig-Institute of Physiology, Medical Faculty, University of Leipzig, Liebigstrasse 27, 04103 Leipzig, Germany

²Rudolf Virchow Center, DFG Research Center for Experimental Biomedicine, University of Würzburg, Versbacher Strasse 9, 97078 Würzburg, Germany

³Institute of Physiology, University of Würzburg, Röntgenring 9, 97070 Würzburg, Germany

(Received 15 December 2009; accepted 27 January 2010; published online 8 April 2010)

During short bursts of neuronal activity, changes in the efficacy of neurotransmitter release are governed primarily by two counteracting processes: (1) Ca²⁺-dependent elevations of vesicle release probability and (2) depletion of synaptic vesicles. The dynamic interplay of both processes contributes to the expression of activity-dependent synaptic plasticity. Here, we exploited various facets of short-term plasticity at the *Drosophila* neuromuscular junction to dissect these two processes. This enabled us to rigorously analyze different models of synaptic vesicle pools in terms of their size and mobilization properties. Independent of the specific model, we estimate ~300 readily releasable vesicles with an average release probability of ~50% in 1 mM extracellular calcium (~5% in 0.4 mM extracellular calcium) under resting conditions. The models also helped interpreting the altered short-term plasticity of the previously reported mutant of the active zone component Bruchpilot (BRP). Finally, our results were independently confirmed through fluctuation analysis. Our data reveal that the altered short-term plasticity observed in BRP mutants cannot be accounted for by delocalized Ca²⁺ channels alone and thus suggest an additional role of BRP in short-term plasticity. [DOI: 10.2976/1.3338710]

CORRESPONDENCE

Stefan Hallermann:
hallermann@medizin.uni-leipzig.de
Robert J. Kittel:
robert.kittel@uni-wuerzburg.de

Synapses are specialized intercellular contact sites, which serve as the communication link between neurons and their partner cells. At chemical synapses, calcium-ion (Ca²⁺) influx triggers the fusion of transmitter-laden vesicles with the presynaptic membrane at a specific subcellular region termed the active zone. Transmitter substances released by this process then diffuse across the synaptic cleft and are sensed by the postsynaptic reception apparatus to convey signal transduction. The discovery that synaptic transmission is not only highly dynamic but that its strength also crucially depends on the recent history of presynaptic activity, has attracted decades of considerable scientific interest, and has identified synapses as key regulators of complex brain processes. Activity-dependent changes in synaptic function can last from milliseconds to hours or days, and this plasticity enables synapses to filter, modify, or integrate information. In appropriate neural networks, synaptic plasticity

gives rise to processes such as sensory adaptation, rhythm generation, or learning and memory.

During short-term plasticity, the postsynaptic response to brief bursts of presynaptic activity may increase (facilitation) or decrease (depression) over time. Besides postsynaptic changes that contribute to these phenomena, the main presynaptic influences appear to be exerted by two counteracting processes: hand-in-hand with the proposal of the quantal nature of transmitter release, went the suggestion that depression was brought about by a depletion of transmitter “parcels,” whereas facilitation was caused by an elevated probability of their release (del Castillo and Katz, 1954a, 1954b). Derived from this, the postsynaptic response can be expressed as the product of quantal size (q , usually taken as the postsynaptic sensitivity), the number of synaptic vesicles available for release (N , or alternatively: the number of available release sites multiplied by their prob-

ability of occupancy), and the probability of transmitter release from a vesicle (p or p_r).

Regarding p , the calcium hypothesis proposed that the release of neurotransmitter is triggered by elevations of the Ca^{2+} concentration in the presynaptic terminal (Katz and Miledi, 1965). This in turn, led to the suggestion that facilitation of release during closely spaced stimuli was caused by the intracellular build-up of residual Ca^{2+} (Katz and Miledi, 1968).

To address N and to describe the depletion of the store of transmitter during synaptic depression, the concept of functionally distinct vesicle pools, with respect to their release and mobilization properties, was adopted (Liley and North, 1953; Elmqvist and Quastel, 1965). In particular, the idea that a “readily releasable pool” (RRP, Birks and Macintosh, 1961) of synaptic vesicles is supplied by a larger storage pool has been used to explain short-term plasticity phenomena, such as paired-pulse facilitation or depression, in terms of either a change in the size of the RRP or a change in the release probability of the vesicles comprising this pool.

The various expression patterns of short-term plasticity observed at different synapses, in various Ca^{2+} concentrations, and during different frequencies of activity, appear to mainly stem from distinct changes in the influence of p and N on release. And in this respect, we are essentially still faced with the difficulty first formulated by del Castillo and Katz (1954a). To accurately dissect changes in p and N , we need to know “[...] more about the molecular nature of the reaction whose probability we are considering.”

In the present study, we addressed this challenge, by making use of recent advances in our understanding of molecular aspects of presynaptic function. The work was carried out at the larval neuromuscular junction (NMJ) of *Drosophila*. This synaptic system is highly accessible to genetic manipulations, which can be employed to give insight into molecular mechanisms of synaptic communication. Our approach was based on applying different stimulation protocols in several extracellular Ca^{2+} concentrations ($[\text{Ca}^{2+}]_e$) to sample a broad range of synaptic plasticity. We then utilized several previously reported, independent models of activity-dependent facilitation (Tsodyks and Markram, 1997; Trommershäuser *et al.*, 2003). By focusing mainly on a mechanistic description of the relationship between vesicle release probability and Ca^{2+} dynamics (Trommershäuser *et al.*, 2003), information was gained regarding p . This was then used to examine the behavior of various vesicle pool concepts during plasticity and to resolve N . Based on their ability to faithfully reproduce the experimental data, the pool concepts were evaluated and their implications for active zone function at the *Drosophila* NMJ were interpreted. Additionally, the resting parameters determined in this manner were independently supported by nonstationary fluctuation analysis.

Finally, the models were applied to analyze the physiology of synapses lacking the active zone component Bruchpilot (BRP, Kittel *et al.*, 2006b; Wagh *et al.*, 2006). Our

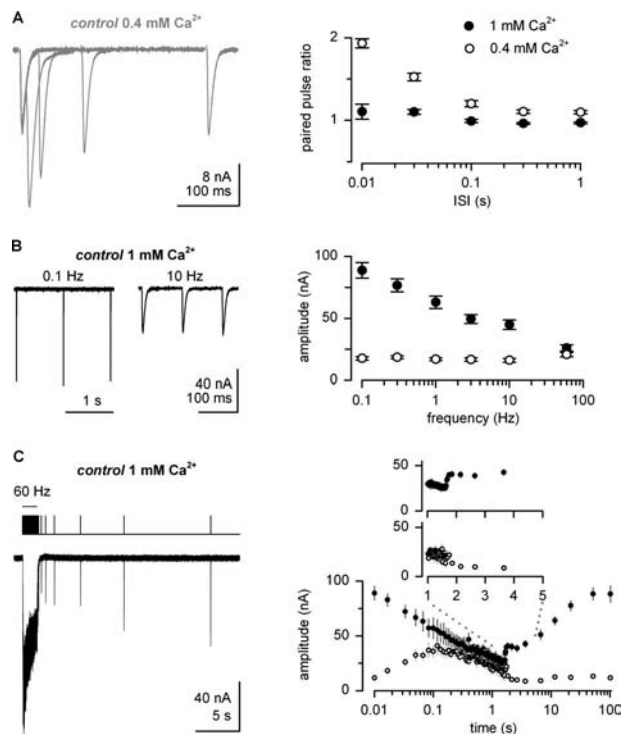


Figure 1. Measurements of short-term plasticity. (A) Superimposed EPSCs recorded in TEVC mode in response to paired-pulse stimulation in 0.4 mM $[\text{Ca}^{2+}]_e$ and average paired-pulse ratios plotted against interstimulus intervals (ISI; filled symbols: 1.0 mM $[\text{Ca}^{2+}]_e$, $n=9$ (Kittel *et al.*, 2006b, open symbols: 0.4 mM $[\text{Ca}^{2+}]_e$, $n=8$). (B) Examples of steady-state EPSCs and summary of average amplitudes versus frequency (1 mM $[\text{Ca}^{2+}]_e$, $n \geq 10$ (Kittel *et al.*, 2006b), 0.4 mM $[\text{Ca}^{2+}]_e$, $n=6$). (C) Example of 100 stimuli applied at 60 Hz followed by stimuli at increasing intervals. The stimulation protocol is illustrated above the current trace (left). The average peak amplitudes are plotted on a logarithmic time scale (1 mM $[\text{Ca}^{2+}]_e$, $n=6$, 0.4 mM $[\text{Ca}^{2+}]_e$, $n=5$). Inset: average EPSC amplitudes plotted on a linear time scale to illustrate the initial phase of recovery. In 1.0 mM $[\text{Ca}^{2+}]_e$, recovery after the train is biphasic whereas in low $[\text{Ca}^{2+}]_e$ EPSC amplitudes decrease during the first 100 ms after the train.

results indicate that BRP mutant active zones are not only affected by a reduced release probability but also by impaired trafficking of synaptic vesicles.

RESULTS

Measurements of short-term plasticity

A broad range of short-term plasticity (STP) was evoked through prototypical stimulation protocols and sampled via the peak amplitude of excitatory postsynaptic currents (EPSCs) in voltage clamped muscles. Under conditions of low release probability (0.4 mM $[\text{Ca}^{2+}]_e$) paired-pulse stimulation [Fig. 1(A)] led to prominent facilitation, which subsided at higher p_r (1.0 mM $[\text{Ca}^{2+}]_e$) due to simultaneously occurring depression. Assuming that facilitation is based on a build-up of residual Ca^{2+} in the nerve terminal, the time course of paired-pulse facilitation (PPF) in low $[\text{Ca}^{2+}]_e$ (i.e., with little contribu-

tion by depletion) should correspond to the decay of the residual Ca^{2+} concentration. A mono-exponential fit to the PPF revealed a time constant of 57 ms, which is in good agreement with the previously recorded decay of residual Ca^{2+} ($\tau=60$ ms, [Macleod et al., 2002](#)). The models of facilitation used in this study therefore assume that residual Ca^{2+} decays with $\tau=60$ ms.

Next, we measured the amplitude maintained under steady-state conditions at different stimulation frequencies [Fig. 1(B)]. In high $[\text{Ca}^{2+}]_e$ depression became dominant at increased frequencies while under conditions of low p_r high-frequency stimulation was capable of increasing the steady-state level (SSL) of EPSC amplitudes via elevated facilitation.

Finally, a complex stimulation protocol was investigated, consisting of a train of 100 pulses at 60 Hz followed by test pulses at increasing intervals [[Wu et al., 2005](#); Fig. 1(C)]. During the 60 Hz, the tetanus residual glutamate likely accumulates in the synaptic cleft, thereby mediating a “tonic” current [see, e.g., [Sakaba \(2006\)](#)]. In this study we concentrated on the “phasic” component and used the peak EPSC amplitude as a measure for synchronous release. We determined time courses for the facilitation and depression during the train and for the recovery thereof. EPSC amplitudes in high and low $[\text{Ca}^{2+}]_e$ were similar after the first ~ 10 pulses [Fig. 1(C)]. Recovery of EPSCs after the train critically depends on $[\text{Ca}^{2+}]_e$. In 1.0 mM $[\text{Ca}^{2+}]_e$, a biphasic recovery process was discernible ([Wu et al., 2005](#)), characterized by a fast initial component during which EPSC amplitudes increased almost two-fold within the first ~ 100 ms and a slow subsequent phase lasting ~ 50 s. In contrast, low $[\text{Ca}^{2+}]_e$ led EPSC amplitudes to decrease during the first 100 ms after the train, which is most likely attributable to the decay of residual Ca^{2+} in the terminal and with that, cessation of facilitation.

Comparing mechanistic models of short-term plasticity

The observed STP results from the complex interplay of facilitation and depression, which in turn are both subject to specific constraints. Thus for example, a model of facilitation must be capable of describing the twofold PPF at short intervals in low $[\text{Ca}^{2+}]_e$ [Fig. 1(A)]. We focused on implementing a mechanistic model for facilitation proposed by Neher and co-workers ([Neher, 1998](#); [Trommershäuser et al., 2003](#)), which is based on detailed investigations of Ca^{2+} fluxes and Ca^{2+} buffer saturation in the vicinity of Ca^{2+} channels. This work provides estimations of Ca^{2+} concentrations by assuming that microdomains arising from individual Ca^{2+} channels add up linearly ([Neher, 1998](#)). While several parameters of this model were experimentally determined at the calyx of Held synapse, here, two (or three) free parameters were implemented to allow faithful descriptions of the experimental data: (1) the parameter α is related to the distance between Ca^{2+} channels and the Ca^{2+} sensor for vesicle fusion and thereby critically determines p_r (a large value for α corresponds to a high p_r). (2) The parameter γ characterizes the saturation of Ca^{2+} buffers and thus sets the

strength of facilitation. (3) If heterogeneity in p_r is assumed, the parameter η defines the difference in p_r between vesicle populations ([Trommershäuser et al., 2003](#)).

The model of facilitation was then combined with several frameworks describing the kinetics of vesicle trafficking to active zone release sites. Six of such “vesicle pool models” are illustrated in Fig. 2(A). The free parameters of these concepts (including the free parameters of the facilitation model) were now systematically varied to simultaneously describe PPF, SSL, and STP during and after the train in both $[\text{Ca}^{2+}]_e$. The predictions of the models are superimposed on the experimentally recorded data in Figs. 2(B)–2(D) and the best-fit parameters are given in [Supplementary Table S1](#) (see [Supplementary Figs. S1 and S3](#) for more details and further models). The deviation of the model predictions is expressed as the difference between the data and the predictions (χ^2) and is plotted in Fig. 2(E) for all sets of stimulation protocols. As illustrated in Fig. 2(F), vesicle pool model 6 (black) delivered the best description of the experimental data using only six free parameters.

Properties of the vesicle pool models

One RR-pool: We started with a model based on the idea that a number of vesicles are readily releasable (RR) and that after release, new RR vesicles are supplied from a reserve pool of vesicles (Fig. 2, model 1, blue; [Liley and North, 1953](#); [Elmqvist and Quastel, 1965](#); [Betz, 1970](#)). The release probability of a vesicle in the RR-pool changes during the train according to the implemented model of facilitation ([Trommershäuser et al., 2003](#)). The best description of the data was obtained with 262 RR vesicles (N_{RR} , see [Supplementary Table S1](#)) with a p_r of 0.41 in 1.0 mM $[\text{Ca}^{2+}]_e$, a recovery time constant of 83 ms (τ_{RR}), and a facilitation parameter, γ , of to $2.74 \mu\text{M}^{-1}$. This resulted in an increase in p_r from 0.41 to 0.97 based on the rise of residual Ca^{2+} from $0.1 \mu\text{M}$ to $\sim 1 \mu\text{M}$ during the train (see [Supplementary Fig. S1 and Table S1](#) for model rates). After the initial pulses of the train, the number of vesicles released per action potential equals the number of vesicles newly supplied in between stimuli. On average 30 RR vesicles exist in this steady-state condition (see [Supplementary Fig. S1A](#)).

One RR-pool+CDR: It has been suggested that the supply of vesicles is accelerated after stimulation ([Worden et al., 1997](#); [Wang and Kaczmarek, 1998](#); [Sakaba and Neher, 2001a](#); [Hosoi et al., 2007](#)). Especially the rate of vesicle mobilization from the reserve pool to the RR-pool was assumed to be accelerated when residual Ca^{2+} is increased ([Weis et al., 1999](#); [Dittman et al., 2000](#); [Zucker and Regehr, 2002](#); [Hosoi et al., 2007](#)). Consistently, introducing such Ca^{2+} dependent recovery (CDR) led to an improved description of the STP found at the *Drosophila* NMJ (Fig. 2, model 2, pink). The best description was obtained with 386 RR vesicles that recover with a time constant of 5.2 s under resting conditions (see [Supplementary Table S1](#)). During the train, residual Ca^{2+} accumulates and the

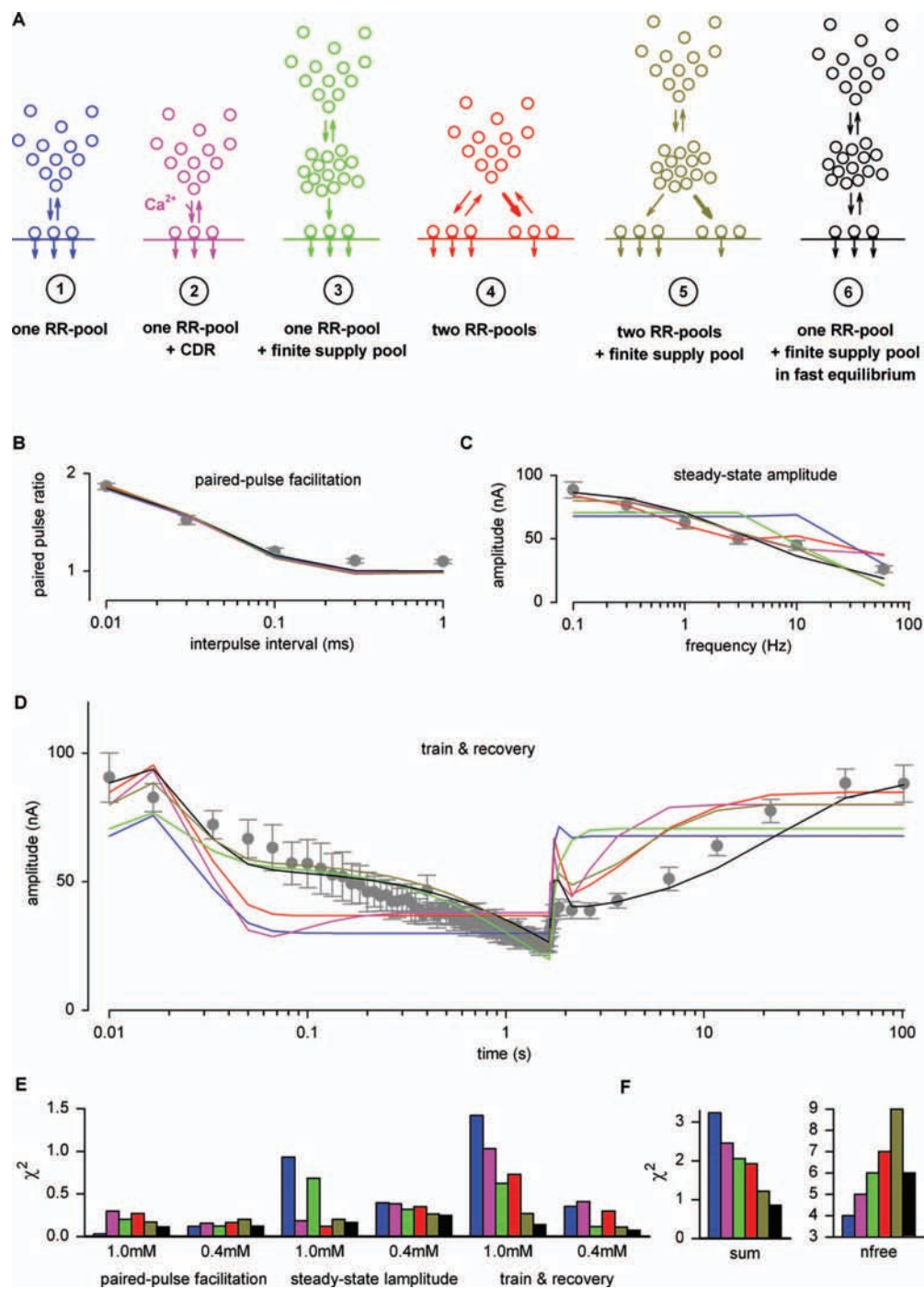


Figure 2. Comparison of mechanistic models of short-term plasticity. To investigate the mechanisms underlying STP, we compared different vesicle pool models. (A) Simple schemes of six models (for more details, see [Supplementary Fig. S1](#)). Note the color code used hereafter. Average values for PPF (B) in 0.4 mM $[Ca^{2+}]_e$, SSL (C), and train plus recovery (D) experiments in 1.0 mM $[Ca^{2+}]_e$ superimposed with model predictions (note that the models also had to fit the corresponding STP experiments in 1 and 0.4 mM $[Ca^{2+}]_e$). The free parameters of each model were optimized to give the best description of the experimental findings (see [Supplementary Table S1](#) for values). (E) The deviation of predictions from the experimental data is plotted as χ^2 for each set of experiments and for each model. (F) Sum of all six χ^2 -values and the number of free parameters used by each model.

mobilization rate increases, elevating the steady-state level. After the train, the mobilization rate drops back to its resting value, resulting in slow refilling of the RR-pool.

One RR-pool+a finite supply pool: The implemented infinite reserve pool is used as an approximation of a large pool of vesicles whose depletion does not limit the supply of vesicles

to the release sites. Abandoning this simplification leads directly to model 3, which incorporates an intermediate supply pool (Fig. 2, green). This model was recently applied to cerebellar mossy fiber bottoms (Saviane and Silver, 2006). At the *Drosophila* NMJ the best description of the data was obtained with 224 RR vesicles, which are supplied with a time constant τ_{RR} of 20 ms by 6941 supply vesicles (N_{suppl}), which in turn, are refilled with a time constant τ_{suppl} of 9 s from the reserve pool. The delayed depression of EPSC amplitudes during the train, which is especially apparent in logarithmic plots, can be interpreted with this model. Since each vesicle in the supply pool is able to refill a depleted RR vesicle, a decreased number of vesicles in the supply pool leads to a proportionally slowed supply of vesicles to the RR-pool. In between stimuli this results in fewer RR vesicles available per action potential. As the intervals between stimuli increase after the end of the train, the RR-pool is refilled quite rapidly from the only partially depleted supply pool. In summary while the depression during the train is captured accurately, the fast monophasic recovery predicted by this model is obviously incorrect.

Two RR-pools: A possible interpretation of the observed biphasic recovery could be that two populations of RR vesicles exist, which recover with different kinetics (Fig. 2, model 4, red). In fact, the calyx of Held synapse appears to harbor one population of vesicles that possess a high p_r but recover slowly and another population that has a low p_r and recovers rapidly (Wu and Borst, 1999; Neher and Sakaba, 2001; Sakaba and Neher, 2001b; Sakaba and Neher, 2001a). At the *Drosophila* NMJ the data are described best by a population of 181 vesicles that recover with a time constant of 44 ms and a population of 163 vesicles that recover with a time constant of 3.7 s. During the train, the slowly recovering vesicles are completely depleted and transmission is sustained by the rapidly recovering pool. However, the delayed depression during the train is not captured by this model and, in contrast to the expectation derived from the findings at the calyx, the data demand similar release probabilities ($p_r = 0.44$ and $p_r = 0.36$) for both populations of vesicles.

Two RR-pools + a finite supply pool: Our aforementioned results indicated that heterogeneous vesicle populations could explain the biphasic recovery after the train and that a finite supply pool of vesicles captured the build-up of depression during the train. We therefore investigated a combination of both mechanisms (Fig. 2, model 5, brown). It turned out that while this model was capable of describing all of the experimental findings (see also Supplementary Fig. S1 and Table S1), some of its properties seemed suspicious. (1) The model predicts a very small population of 82 RR vesicles with a high p_r . Estimates from anatomical investigations suggest that about 500 synapses mediate the EPSCs studied here (Atwood et al., 1993), which implies that only 16% of the synapses would possess a vesicle from this population. (2) The predicted p_r (~ 0.80) of these vesicles is surprisingly high and the remaining vesicles have a p_r of ~ 0.40 , which is similar to the estimated p_r in the

other models (see Supplementary Table S1). According to the results obtained at the calyx of Held, we would expect the high p_r pool to possess a release probability of ~ 0.5 and that these vesicles should dominate the results acquired through fluctuation analysis under resting conditions (Fig. 5). The low p_r pool was expected to have a much lower release probability ($p_r < 0.1$) and to operate preferentially during the train. We therefore addressed whether simpler models might also be able to explain our data appropriately.

One RR-pool in fast equilibrium with a finite supply pool: It emerged that our synaptic recordings could be described by a model consisting of an RR-pool, which is in fast equilibrium with a finite supply pool (Fig. 2, model 6, black, see also Zucker and Regehr, 2002). The most satisfactory fit to the data was obtained with 299 RR vesicles, 11 075 supply vesicles, and an equilibrium time constant of 47 ms. Both the time course of depression during the train, attributable to depletion of the supply pool, and the biphasic recovery thereafter are adequately captured. The initial fast recovery stems from the fast equilibrium between RR vesicles and the supply pool. Since vesicles are able to rapidly leave the RR-pool, its replenishment, in turn, depends on the refilling of the supply pool. Thus, the later phase of recovery follows the slow refilling kinetics of the supply pool.

In summary, the parameters of diverse models were quantified and several of the investigated models were able to reproduce the facets of STP recorded in high and low $[Ca^{2+}]_e$. Notably, several parameters appeared comparably robust despite the substantially different mechanisms assumed by the models (compare, e.g., N_{RR} , N_{suppl} , and p_r of different models in Supplementary Table S1).

Next, we investigated several assumptions underlying the data presented up to this point. First, the implemented model of facilitation, which is based on detailed mechanistic interpretations of calcium dynamics in the terminal (Neher, 1998; Trommershäuser et al., 2003), uses parameters determined at the calyx of Held to describe facilitation at the *Drosophila* NMJ. In addition, we therefore applied an alternative, phenomenological model of facilitation developed at neocortical pyramidal neurons (Tsodyks and Markram, 1997; Markram et al., 1998). Using such an entirely different description of facilitation (see Materials and methods section) to drive vesicle pool models delivered essentially identical results (see Supplementary Table S1B).

Second, we tested how postsynaptic mechanisms of STP would influence our conclusions. To this end, a strong but realistic degree of postsynaptic depression was assumed with kinetic properties based on previous investigations. Again, similar results were obtained (Supplementary Table S1).

Prolonged stimulation

The analysis of STP critically depended on the information gained from the time course of recovery after depression

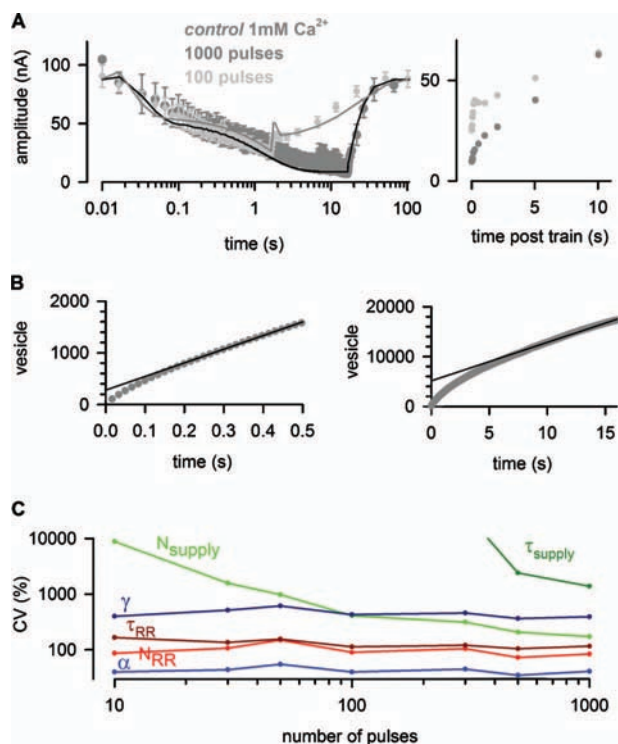


Figure 3. Prolonged stimulation. (A) A train of 1000 stimuli was applied at 60 Hz (EPSC amplitudes in dark gray, superimposed with EPSCs during 100 stimuli in light gray). Consistent with the prediction of model 6 (black line), depression during the train was biphasic while recovery after the train was mono-exponential. The right panel depicts the first 11 s of the recovery phase on a linear time scale. The parameters of the fit to the average 1000 pulses were: $N_{\text{supply}} = 10500$, $\tau_{\text{supply}} = 9.3$ s, $N_{\text{RR}} = 276$, $\tau_{\text{RR}} = 40.0$ ms, $\alpha = 24.9$ μM , and γ was fixed to 2.85 μM^{-1} . (B) The cumulative EPSC amplitude of the 60 Hz train of 1000 stimuli was converted to the number of released vesicles assuming a miniature EPSC amplitude of 0.63 nA (see Materials and methods section). Back-extrapolation of linear fits from 0.3 s to 0.5 s (left) and from 10 s to 16 s (right) resulted in pool estimates of 280 vesicles and 5200 vesicles, respectively. (C) The accuracy of the parameters estimated by model 6 is plotted as the CV versus the number of stimuli within a train. The accuracy of N_{supply} and τ_{supply} critically depends on the number of pulses. Here, only the train and not the time course of recovery is taken into account.

[e.g., Fig. 2(D)]. The different pool models predict very different recovery behavior and only those models with a supply pool (models 3, 5, and 6) would predict an altered recovery after trains with more stimuli. Fig. 3(A) shows the average EPSC amplitudes during and following trains with 1000 stimuli at 60 Hz (dark gray) and, for comparison, the 100 pulse train (light gray). Fitting model 6 to the train of 1000 stimuli including the recovery (black line) gives very similar parameters as estimated using the aforementioned protocols (see legend of Fig. 3 for values). The more rapid recovery of the supply pool may be due to CDR of the supply pool from the reserve pool (Zucker and Regehr, 2002). Notably, model 6 accurately describes the mono-exponential na-

ture of the recovery from 1000 stimuli, whereas model 4, for instance, would predict an unaltered biphasic recovery independent of the train duration.

As an additional approach to gain information about vesicle pools and their mobilization rates, a linear extrapolation of the cumulative EPSC amplitude was performed [Schneggenburger *et al.*, 1999; Fig. 3(B)]. Focus on the first 30 EPSCs of a 60 Hz train suggested ~ 300 RR vesicles. However, when all 1000 EPSCs of a long 60 Hz train were taken into account ~ 5000 vesicles were estimated. Besides indicating that back-extrapolation of cumulative EPSC amplitudes should be interpreted cautiously (as the results depend heavily on the identified SSL), these data also clearly highlight that complex mechanisms (as, e.g., several pools of synaptic vesicles) are involved in the depression during trains of stimuli.

Finally, we addressed how well the parameters of a model were defined depending on the number of stimuli within the train. Focusing on model 6, EPSC amplitudes during 60 Hz trains of 10–1000 stimuli were simulated and subsequently used as data to extract the parameters of the model. The calculated errors of the parameters (square roots of the diagonal elements of the covariance matrix; Colquhoun *et al.*, 2003) were expressed as coefficients of variation (CV) and indicate how well each parameter could be estimated. The values for the supply pool (especially τ_{supply}) could be estimated only poorly from the depression during the train [Fig. 3(C)]. However, when the same calculations were repeated with trains of stimuli including 14 pulses during recovery [as in the experiments lasting ~ 100 s; compare with Fig. 1(C)] all parameters could be determined very reliably and almost independently of the number of stimuli within the train (CV < 100%; data not shown). These results indicate that the parameters of the model can be estimated reliably as long as the information contained in the time course of recovery is included.

The Bruchpilot mutant

Bruchpilot (BRP) is an integral component of the *Drosophila* active zone cytomatrix where it helps clustering pre-synaptic Ca^{2+} channels at vesicle fusion sites to ensure adequate release probability (Kittel *et al.*, 2006a, 2006b; Wagh *et al.*, 2006; Fouquet *et al.*, 2009). The modeling study presented here was partially motivated by findings made at BRP null mutant synapses. In particular, the strongly altered recovery of BRP mutants after a train [Fig. 4(A)] prompted us to develop quantitative models of active zone function that would allow us to interpret the complex observations.

Figures 4(A)–4(C) (right column) shows the PPF, the SSL, and the train plus recovery recorded at BRP mutant neuromuscular synapses in 1.0 mM $[\text{Ca}^{2+}]_e$ (blue). The train experiments were also performed in 2 mM $[\text{Ca}^{2+}]_e$ [light gray, Fig. 4(A)] in order to give roughly the same p_r as experienced by control animals in 1 mM $[\text{Ca}^{2+}]_e$ [compare initial values of trains in Fig. 4(A)]. By applying model 6 to the STP data of BRP mutants and by optimizing all six free parameters, we were

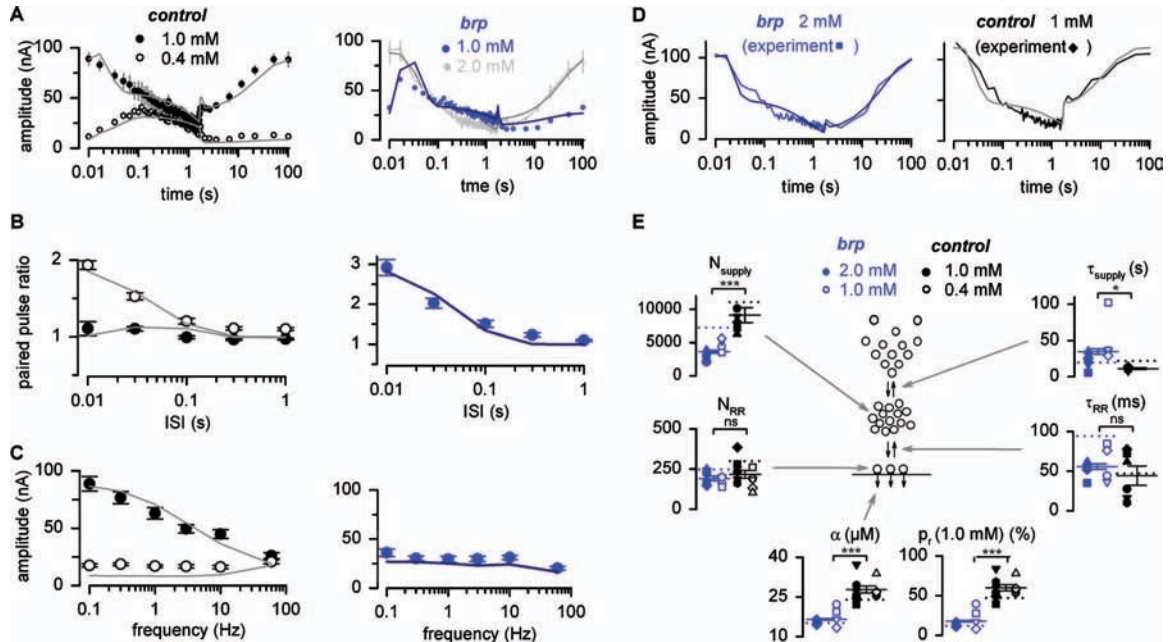


Figure 4. The Bruchpilot mutant. Average EPSCs during trains plus recovery (A), PPF (B), and at SSL (C), in controls (left column) and BRP mutants (right column), overlaid with descriptions of the experimental data by model 6 (solid lines). (D) Examples of single experiments in controls and BRP mutants to confirm the reliability of model parameters (symbols identify single experiments in the summary). (E) Summary of model parameters. Values from single experiments are given by symbols and their averages by solid lines \pm SEM ($n=6$ and 5 for 1 mM and 0.4 mM $[Ca^{2+}]_e$ in controls, $n=5$ and 4 for 2 mM and 1 mM $[Ca^{2+}]_e$ in BRP mutants). The parameters obtained from fitting all STP protocols in both $[Ca^{2+}]_e$ are denoted by dotted lines. According to model 6, BRP mutant active zones have a low p_r [defined by α (Trommershäuser *et al.*, 2003)], less supply vesicles (N_{supply}), and refill the supply pool (τ_{supply}) more slowly than controls.

able to obtain good fits to the experimental observations [dark blue and dark gray lines in Figs. 4(A)–4(C)]. Figure 4(E) summarizes the parameters used by the model to fit both controls (black dotted lines) and mutants (blue dotted lines).

Importantly, the modeling approach captured the previously reported low p_r of BRP mutants (Kittel *et al.*, 2006a). However, while the number of RR vesicles appeared unaltered, BRP mutant active zones were described as possessing a significantly smaller supply pool with slower refilling kinetics [compare with Fig. 4(E)].

To confirm the reliability of the extracted parameters, we fitted single experiments of the train with subsequent recovery and estimated the variability of the parameters from one experiment to the next (Figs. 4(D) and 4(E) and Supplementary Fig. S2). The data were acquired separately under conditions of low and high release probability (0.4 mM and 1 mM $[Ca^{2+}]_e$ for controls; 1 mM and 2 mM $[Ca^{2+}]_e$ for BRP mutants) and model 6 was utilized to fit the results. The available information was now strongly reduced compared to the previous approach of simultaneously fitting the averages of PPF, SSL, and train plus recovery in both Ca^{2+} concentrations. Nevertheless, in 1 mM $[Ca^{2+}]_e$ the single trains sufficed to extract most of the model parameters. The parameter γ critically depends on PPF and was therefore fixed to the value estimated previously ($2.74 \mu M^{-1}$). In addition, vesicle release in 0.4 mM $[Ca^{2+}]_e$ is so moderate that it was not significantly limited by the

size and the kinetics of the supply pool. For single experiments in low $[Ca^{2+}]_e$ the number of supply vesicles and their refilling kinetics were therefore fixed to the previously obtained values (Fig. 4(E), see Supplementary Table S1). The reproducibility of the individual parameters [open and filled symbols in Fig. 4(E)] supports the validity of the investigated model (Colquhoun and Sigworth, 1995).

In addition, we tested model 2 (Wang and Kaczmarek, 1998; Hosoi *et al.*, 2007) and assumed that the miniature amplitude was decreased by 1% per action potential with a recovery time constant of $\tau=1.5$ s, resembling, e.g., postsynaptic receptor saturation, desensitization, or Ca^{2+} -dependent Ca^{2+} channel inactivation (Forsythe *et al.*, 1998; Hennig *et al.*, 2008; see Supplementary Fig. S3). Although this model assumes different mechanisms it also highlighted that the BRP mutant phenotype cannot be accounted for by lower release probability alone (compare the changes in k and $k_{1,b}$ in Supplementary Fig. S3)

Independent verification of the model parameters

Fluctuation analysis can be used to determine the three quantal parameters N , p , and q under resting conditions (Silver *et al.*, 1996; Quastel, 1997; Meyer *et al.*, 2001; Scheuss and Neher, 2001) and independently of the modeling approach. To increase the signal to noise ratio, all EPSCs used for fluctuation analysis were recorded with a focal electrode

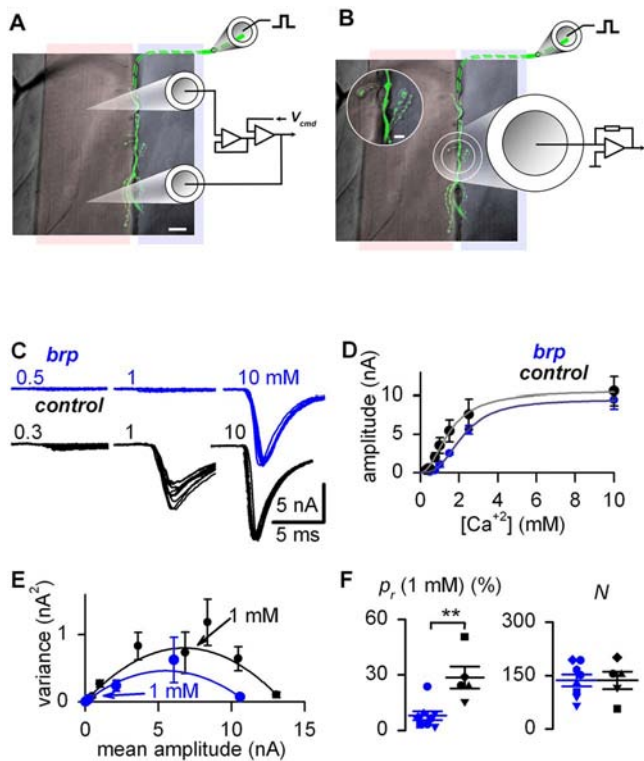


Figure 5. Independent verification of the model parameters. (A, B) Differential-interference contrast image of larval longitudinal muscles 6 (red) and 7 (blue), superimposed with a confocal image of motoneurons expressing GFP. For STP protocols the two-electrode voltage clamp recording configuration was used (A) while data for fluctuation analysis (C-F) were collected with a focal electrode. In both cases a suction electrode triggers action potentials in the innervating nerve. (C) Example EPSCs from BRP mutants (blue) and control animals (black), recorded at the indicated $[Ca^{2+}]_e$ (ten traces superimposed). (D) Peak EPSC amplitude versus $[Ca^{2+}]_e$. The data were fitted with a Hill equation and show a right-shift of BRP mutants in the Ca^{2+} -dependency of release (controls: $n=5$, BRP mutants: $n=7$). (E) Example of a mean-variance relationship of the peak current amplitude [same experiments as in (A)]. (F) From the parabolic fits, the binomial parameters N , the number of release sites, and p_r , the release probability in 1 mM $[Ca^{2+}]_e$, were extracted. Plots show mean \pm SEM (controls: $n=5$, BRP mutants: $n=8$).

[Fig. 5(B)], whereas the two-electrode voltage clamp method had been applied for STP protocols to prevent muscle contractions [Fig. 5(A)]. Elevating $[Ca^{2+}]_e$ increased the peak amplitude of EPSCs such that similar values were reached by BRP mutants and controls in high $[Ca^{2+}]_e$ [Figs. 5(C) and 5(D)]. The variance of EPSC amplitudes rose with increase in $[Ca^{2+}]_e$, reached a maximum at intermediate values, and then decreased again. To obtain the number of RR vesicles (N), the quantal size (q), and the release probability (p_r), mean-variance plots were generated and stationary fluctuation analysis was used [Fig. 5(E)]. Consistent with earlier work (Kittel *et al.*, 2006b) and confirming the modeling results, p_r was reduced to 0.08 ± 0.02 in BRP mutants compared to 0.29 ± 0.06 in controls ($P < 0.01$) while N was unchanged [Fig. 5(F)]. The absolute

value obtained for N is smaller in focal recordings because the two-electrode voltage clamp technique (TEVC), applied for STP protocols samples a larger number of synapses (Fig. 5; see also Materials and methods section). Furthermore, the absolute values obtained for p_r with fluctuation analysis are smaller compared to the values determined through STP experiments because the fluctuation analysis was performed at 18 °C (to prevent muscle contraction in the focal recording configuration) and not at 22 °C as for the TEVC recordings. Assuming a temperature coefficient Q_{10} of 4 (Hille, 2001), a p_r of 0.29 at 18 °C would correspond to a p_r of 0.50 at 22 °C. This is in good agreement with the model estimates based on TEVC recordings (see Supplementary Table S1).

DISCUSSION

To gain insight into the mechanisms underlying short-term plasticity at neuromuscular active zones of *Drosophila*, we compared several mechanistic models and quantified their parameters. Through utilization of these models we were then able to further analyze the function of the active zone protein BRP. Finally, the basic parameters under resting conditions were confirmed independently for both control animals and BRP mutants via fluctuation analysis.

In this study, we focused on the peak EPSC amplitude and related it linearly to the number of vesicles released per action potential. While linear summation of quanta has been demonstrated over a wide range of release probabilities at, e.g., cerebellar mossy fiber synapses (Sargent *et al.*, 2005), a number of mechanisms could corrupt this assumption. For instance, increased asynchronous release may change the time course but not necessarily the peak amplitude of EPSCs (see, e.g., Sakaba 2006). However, deconvolving EPSCs during 60 Hz trains with templates of recorded miniature EPSCs (single quanta) resulted in very similar time courses of vesicle release per stimulus (data not shown). Also, the similar release probabilities estimated for both RR-pools of models 4 and 5 is consistent with recent data, which indicates that asynchronous release contributes little to the peak EPSC amplitude at the calyx of Held (Sakaba, 2006).

Furthermore, Ca^{2+} -dependent Ca^{2+} channel modulation (Forsythe *et al.*, 1998; Hennig *et al.*, 2008; Mochida *et al.*, 2008) and action potential broadening have been reported to influence STP (Geiger and Jonas, 2000). It is thus also conceivable that the increased p_r during the train may be influenced by such mechanisms in addition to buffer saturation (Trommershäuser *et al.*, 2003). Postsynaptic depression is an obvious mechanism that contributes to STP (Scheuss *et al.*, 2002; Zucker and Regehr, 2002; Taschenberger *et al.*, 2005; Scheuss *et al.*, 2007). Therefore, both fluctuation analysis in high $[Ca^{2+}]_e$ (Fig. 5) and investigations of SSLs and trains (Figs. 1–4) could be distorted by, e.g., postsynaptic receptor desensitization or saturation. This would underestimate the number of RR vesicles and thereby overestimate p_r . However, implementing strong postsynaptic depression in our simula-

tions did not affect the presented conclusions (see [Supplementary Table S1C](#), Materials and Methods Section). Since the time course of recovery differs after 100 versus 1000 pulses [Fig. 3(A)] it appears unlikely that postsynaptic mechanisms elicit the biphasic recovery after 100 pulses (as by this time a steady-state situation concerning the glutamate concentration in the cleft and receptor saturation and desensitization should already have been attained ([Adelsberger et al., 1997](#); [Heckmann and Dudel, 1997](#); [Pawlu et al., 2004](#)). Instead, it appears more likely that a steady-state is not reached after 100 stimuli because the depletion of vesicles has not yet been completed.

Previous work has described variations in p_r across active zones formed on the same axon or innervating the same target ([Wojtowicz et al., 1994](#); [Murthy et al., 1997](#); [Marrus and DiAntonio, 2004](#); [Wairkar et al., 2009](#)). Similarly, our estimations of p_r most likely reflect a mean value given by a broad distribution. As the neuromuscular preparation is innervated by two motoneurons differing in their physiological properties ([Kurdyak et al., 1994](#)), it will be interesting to examine whether these contribute heterogeneously to vesicle pool models.

Taking into account how many active zones (AZs) are present in this preparation (~ 500 , as estimated from serial electron-microscopic images of larval longitudinal muscle 6 ([Atwood et al., 1993](#)), our estimated rate of vesicle recruitment during sustained release is $\sim 15/s$ per AZ ($N_{\text{supply}} \times k_{\text{RR}} = 10,000 \times 0.7/s$ per 500 AZs (model 6) and $k_{1,b} + \Delta\text{Ca}^{2+} \times k = 0.2/s + 1 \mu\text{M} \times 15/(\mu\text{M s})$ per AZ [modified model 2 in [Supplementary Fig. S3](#)]). Hence, an AZ requires about 70 ms to recruit a vesicle during sustained release. This is faster than previous calculations at the *Drosophila* NMJ (500 ms, [Delgado et al., 2000](#); [Kidokoro et al., 2004](#)) but within the range of recent estimates at other synapses (12 ms, [Saviane and Silver, 2006](#)), 250 ms ([Hosoi et al., 2007](#)). Our model 6 assumes a fast equilibrium between RR and supply vesicles. Such a mass-action model was previously suggested for the *Drosophila* NMJ in order to account for the delayed depression during the train ([Li and Schwarz, 1999](#)). However, the estimated undocking rate of RR vesicles at central synapses ([Murthy and Stevens, 1999](#)) is lower than the high transition rate of vesicles from the RR to the supply pool described by model 6 (21.1 s^{-1}).

While these differences may be reconciled by distinct functional specializations present at different synapses, the aim of our modeling approach was to generate experimentally testable hypotheses for further analysis. For each investigated model a set of parameters was determined and several of these estimates appeared relatively independent of the underlying vesicle pool model (compare, e.g., N_{RR} , N_{supply} , and p_r of different models in [Supplementary Table S1](#)). Together with additional experimental confirmations, such as through fluctuation analysis, this increases the confidence in the parameter estimates. Finally, both models 6 and 2 identified defective trafficking of vesicles to BRP mutant active zones

(Fig. 4 and [Supplementary Fig. S3](#)). Examining the precise molecular mechanisms underlying this supply defect will be of great interest.

MATERIALS AND METHODS

Genetics

As control animals we used the genotype w^1 and the genotype of Bruchpilot null mutants was $brp^{69}/df(2R)BSC29$ ([Kittel et al., 2006b](#)).

Electrophysiology

TEVC recordings of EPSCs were obtained at room temperature from late third instar male *Drosophila* larvae (ventral longitudinal muscle 6, segments A2 and A3, and Fig. 5), essentially as previously described ([Kittel et al., 2006b](#)). For the TEVC experiments, both mutants and control animals carried a copy of either *elav-GAL4* or *ok6-GAL4* to ensure comparability with a previous study ([Kittel et al., 2006b](#)). The composition of the extracellular hemolymph-like saline (HL-3, [Stewart et al., 1994](#)) was (in mM): NaCl 70, KCl 5, MgCl₂ 20, NaHCO₃ 10, trehalose 5, sucrose 115, HEPES 5, CaCl₂ as indicated, and pH adjusted to 7.4. Recordings were made from cells with an initial V_m between -50 mV and -70 mV (holding potential at -60 mV) using intracellular electrodes with resistances of $10\text{--}32 \text{ M}\Omega$, filled with 3 M KCl. Train stimulation protocols consisted of either 100 or 1,000 pulses applied at 60 Hz. The recovery was assessed by evoking APs at (in ms following the last pulse in the train): 25, 50, 100, 200, 500, 1,000, 2,000, 5,000, 10,000, 20,000, 50,000, and 100,000 ([Wu et al., 2005](#)). EPSCs reflect the compound response to stimulation of both motoneurons innervating muscle 6, and care was therefore taken to ensure their stable recruitment. Infrequently observed recruitment failures were linearly interpolated. Only cells that recovered at least 70% of their initial EPSC amplitude following tetanic stimulation were included in the analysis. The recordings were analyzed with pClamp 9 (now Molecular Devices, Sunnyvale, CA, USA) and the peak amplitude was determined as the difference between the peak value of the EPSC and the baseline value before onset of that EPSC. The amplitude of the second response in 10 ms interpulse recordings was measured from the peak to the point of interception with the extrapolated first response.

EPSCs for fluctuation analysis were recorded with a focal electrode from third instar larvae (Fig. 5), in HL-3 essentially as reported ([Pawlu et al., 2004](#)). For each $[\text{Ca}^{2+}]_e$, more than ~ 20 EPSC were recorded at 0.2 Hz, after a steady-state amplitude was reached. The bath temperature was kept within $18 \text{ }^\circ\text{C} \pm 0.5 \text{ }^\circ\text{C}$ with a Peltier element (27 W, Conrad Electronic, Hirschau, Germany) glued to the bath inflow with heat-conductive paste (Fischer Elektronik, Lüdenscheid, Germany). Focally recorded EPSCs were analyzed with Igor Pro 5.04 (WaveMetrics, Lake Oswego, OR). EPSCs were digitally filtered at 3 kHz (Gaussian filter), baseline subtracted, and the average of all failures was subtracted from the currents. Whether

action potentials had been initiated was assessed by the presence of the current resulting from action potential invasion of the nerve terminal (Dudel, 1981). The peak amplitude of the EPSCs was determined within a 5-ms-window after the presynaptic action potential. The average peak amplitude of the failures was subtracted from the peak amplitude of the EPSCs.

To plot the relationship between EPSC amplitudes and $[Ca^{2+}]_e$, [Fig. 5(D)], the EPSC amplitudes of each experiment were first normalized to the amplitude in 1 mM $[Ca^{2+}]_e$. The normalized values were then averaged across experiments and subsequently the average was rescaled with the average amplitude of all experiments in 1 mM $[Ca^{2+}]_e$. The data were fitted with a Hill equation according to $I([Ca^{2+}]_e) = I_{\max} [1 + (EC_{50}/[Ca^{2+}]_e)^{\text{slope}}]^{-1}$, where $I_{\max} = 10.6$ and 9.5 nA, $EC_{50} = 1.5$ and 2.2 mM, and $\text{slope} = 2.1$ and 2.8 for controls and BRP mutants, respectively.

To calculate the variance (and the variance of the variance) we followed the procedures described by Neher and co-workers (Meyer *et al.*, 2001; Scheuss and Neher, 2001; Scheuss *et al.*, 2002). For a set of N peak amplitudes x_i ($i = 1, \dots, N$) recorded at a certain $[Ca^{2+}]_e$, the sample variance was calculated as the average of the sample variance of overlapping segments of size two. The variance of the variance was calculated as the standard error of the mean (SEM) of all sample variances (Meyer *et al.*, 2001).

Stationary EPSC fluctuation analysis was performed as formerly reported (Meyer *et al.*, 2001; Scheuss and Neher, 2001; Silver, 2003). Based on a binomial model for synaptic transmission, the variance of the EPSC amplitude depends on the quantal size (q), the number of release sites (N), and the probability of release at each site (p_r), resulting in a parabolic dependence of the EPSC variance on the average EPSC amplitude. The variance-mean plots were fitted with $\text{Var}(I) = \frac{q}{N} I - \frac{I^2}{N}$ and weighted with the reciprocals of $\text{Var}(\text{Var})$ and constrained to pass the origin. To correct for the variability in q , we corrected for intrasite variance (CV_{qI}) and intersite variance (CV_{qII}). The apparent \tilde{q} and \tilde{N} estimates are related to the true parameters by (Frerking and Wilson, 1996; Meyer *et al.*, 2001; Scheuss and Neher, 2001; Silver, 2003)

$$q = \tilde{q}(1 + CV_{qI}^2 + CV_{qII}^2)^{-1} \quad (1)$$

$$N = \tilde{N}(1 + CV_{qII}^2) \quad (2)$$

The experimentally determined variance of q at the *Drosophila* NMJ [Pawlu *et al.*, 2004; $CV_Q = 0.30 = (CV_{qI}^2 + CV_{qII}^2)^{0.5}$] in combination with the assumption of $CV_{qI} = CV_{qII}$ (Frerking and Wilson, 1996; Meyer *et al.*, 2001; Scheuss and Neher, 2001; Silver, 2003) results in $q = 0.92\tilde{q}$ and $N = 1.05\tilde{N}$.

Modeling

The simulations were based on a biophysical interpretation of facilitation described in Trommershäuser *et al.* (2003). In brief, a linear build up of residual calcium (ΔCa^{2+}) was as-

sumed, where each AP leads to a constant increase in ΔCa^{2+} by $x_0 = 0.4 \mu\text{M}$ and decays mono-exponentially with $\tau_x = 60$ ms. Instead of 100 ms (Helmchen *et al.*, 1997; Trommershäuser *et al.*, 2003) we used 60 ms since (1) recent data indicate $\tau_x \approx 30$ ms for undialysed Calyces (Müller *et al.*, 2007); (2) measurements at the *Drosophila* NMJ indicated $\tau_x = 60$ ms (Macleod *et al.*, 2002); and (3) a mono-exponential fit of the paired pulse facilitation versus interval duration recorded in 0.4 mM extracellular Ca^{2+} concentration ($[Ca^{2+}]_e$) gave $\tau = 57$ ms.

Two types of readily releasable vesicles can be considered (Trommershäuser *et al.*, 2003): vesicles close to Ca^{2+} channels (pool2) and vesicles further away from Ca^{2+} channels (pool1). The corresponding peak local Ca^{2+} concentration at a release site of pool j , $[Ca^{2+}]_j$, can be expressed as (Trommershäuser *et al.*, 2003):

$$[Ca^{2+}]_j = [Ca^{2+}]_{gl} + J([Ca^{2+}]_e) \alpha [\delta_{j,2} + \eta(1 + \gamma \Delta Ca^{2+})] \quad (3)$$

where $\delta_{j,2}$ is the Kronecker symbol, which has the value 1 for $j=2$ and 0 for $j=1$. The local $[Ca^{2+}]$ at the release site is related to the probability of release according to a fourth power relationship with a half-maximal release at $K_{1/2} = 42.5 \mu\text{M}$ (Trommershäuser *et al.*, 2003). The global Ca^{2+} concentration ($[Ca^{2+}]_{gl}$) is elevated above the resting Ca^{2+} concentration ($[Ca^{2+}]_r$) by the residual Ca^{2+} concentration. The Ca^{2+} influx (J) depends on $[Ca^{2+}]_e$ as described by a Michaelis–Menten saturation equation

$$J([Ca^{2+}]_{\text{out}}) = J_{\max} \frac{[Ca^{2+}]_e}{[Ca^{2+}]_e + EC_{50}} \quad (4)$$

with half-maximal Ca^{2+} -influx at an EC_{50} of 2.61 mM $[Ca^{2+}]_e$ and a dimensionless quantity $J_{\max} = 2.31$ (Schneppenburger *et al.*, 1999; Trommershäuser *et al.*, 2003). In addition, the increase per AP (x_0) was scaled according to

$$x_0([Ca^{2+}]_{\text{out}}) = 0.4 \mu\text{M} \frac{[Ca^{2+}]_e}{[Ca^{2+}]_e + EC_{50}} \quad (5)$$

The parameter α is proportional to the inverse of the distance between Ca^{2+} channels and the vesicles (Trommershäuser *et al.*, 2003) and defines the resting release probability. The parameter η determines the difference in release probability between pool1 and pool2. The parameter γ quantifies facilitation.

The free parameters (α , η , and γ) were used to fit the experimental data of control animals including paired-pulse plasticity, frequency-dependent steady-state levels, and the response to and recovery from a train of 100 pulses at 60 Hz, in 0.4 mM and 1.0 mM $[Ca^{2+}]_e$ (Fig. 2). In models with only one pool of readily releasable vesicles (e.g., model 6), only the vesicles close to Ca^{2+} channels (pool2) were simulated (compare Sakaba, 2006; Hosoi *et al.*, 2007) and η was fixed to the value in Trommershäuser *et al.* (2003). Due to the degree of facilitation required to reproduce the twofold paired pulse facilitation at short intervals in low $[Ca^{2+}]_e$, γ was ($2.74 \mu\text{M}^{-1}$).

When individual experiments (train plus recovery) were fitted [Fig. 4(D) and Supplementary Fig. S2], γ was fixed to $2.85 \mu\text{M}^{-1}$ because the paired-pulse ratio in low Ca^{2+} critically constrained the degree of facilitation. For fitting individual train-experiments in $0.4 \text{ mM } [\text{Ca}^{2+}]_e$, in addition, N_{supply} , τ_{supply} , and τ_{RR} (model 6, Fig. 4(D), and Supplementary Fig. S2) and α , $k_{1,b}$, and k (model 2, see Supplementary Fig. S3D) were fixed to the values obtained from the average data [Fig. 4(E) and Supplementary Fig. S2].

Starting with analytically calculated steady-state values, the number of vesicles in each pool was numerically calculated with a fifth-order Cash–Karp Runge–Kutta method with adaptive stepsize control (Cash and Krarp, 1990). For computational speed, global calcium $[\text{Ca}^{2+}]_g(t)$ was calculated as an array with a temporal resolution of $100 \mu\text{s}$. For steady-state EPSC amplitude, 10, 30, 50, 70, 100 and 150 stimuli were simulated at a frequency of 0.1 Hz, 0.3 Hz, 1 Hz, 3 Hz, 10 Hz, and 60 Hz, comparable to the experiments. The last EPSC of the simulated sweep was taken as the steady-state level at the corresponding frequency. The predicted number of released vesicles was converted to a current assuming a miniature EPSC amplitude of 0.63 nA for controls and 0.87 nA for BRP mutants (based on 0.84 nA for controls and 1.17 nA for BRP mutants recorded at -80 mV holding potential (Kittel *et al.*, 2006b) and scaled to -60 mV , assuming 0 mV reversal potential and a linear current voltage relation).

For parameter optimization, all free parameters were varied with a simplex algorithm as described (Press *et al.*, 2002). The deviations of the model predictions from the experimental data were measured as the sum of squared differences, χ^2 , as follows: first, the number of data points obtained from the train and recovery experiments (100 during the train + 13 from the recovery) was reduced by exponential sampling to 28 values (15 during the train + 13 from the recovery). Second, the six values from the steady-state and the five values from paired-pulse plasticity were weighted fivefold. Finally, the χ^2 values from the steady-state and train plus recovery were scaled by the inverse of the squared average current amplitude under resting conditions. This resulted in six χ^2 values of similar size for the paired-pulse plasticity, the steady-state level, and the train plus recovery at both 0.4 mM and $1.0 \text{ mM } [\text{Ca}^{2+}]_e$ [compare with Fig. 2(E)].

Subsequently, the model predictions and the experimental data were plotted superimposed using MATHEMATICA 5.0 (Wolfram Research, Champaign, IL, USA) for visual inspection. Simulation and plotting lasted only several seconds on a conventional 2.7 GHz dual core computer, which allowed us to gain a better understanding of the reliability and the constraints of the parameters. After the fit was completed, internal estimates of the errors of the best-fit parameters were calculated as the square roots of the diagonals of the covariance matrix [Colquhoun *et al.*, 2003; compare with Fig. 3(C)]. To confirm that the global minimum was reached, the best-fit parameters were shown to be independent of the starting

values within a plausible range. In addition, the reproducibility of the best-fit parameters to individual experiments, as performed in the analysis of single channel recordings (Colquhoun *et al.*, 2003; Hallermann *et al.*, 2005), indicated that the global minimum was reached (Colquhoun and Sigworth, 1995).

Statistical analysis

The nonparametric Mann–Whitney rank sum test was used for statistical analysis. The data are reported as mean \pm SEM, n indicates the sample number and P denotes the significance (* $P < 0.05$, ** $P < 0.01$, and *** $P < 0.001$).

ACKNOWLEDGMENTS

We thank Jens Eilers and Stephan J. Sigrist for scientific exchange. This work was supported by grants from the DFG to M.H. (Contract Nos. HE 2621/4-2 and TP B27/SFB 581) and by *formel.1* grants to S.H. and R.J.K. from the Medical Faculty of the University of Leipzig. R.J.K. is supported by the DFG Emmy–Noether Program.

REFERENCES

- Adelsberger, H, Heckmann, M, and Dudel, J (1997). “The amplitude of quantal currents is reduced during short-term depression at neuromuscular synapses in *Drosophila*.” *Neurosci. Lett.* **225**, 5–8.
- Atwood, HL, Govind, CK, and Wu, CF (1993). “Differential ultrastructure of synaptic terminals on ventral longitudinal abdominal muscles in *Drosophila* larvae.” *J. Neurobiol.* **24**, 1008–1024.
- Betz, WJ (1970). “Depression of transmitter release at the neuromuscular junction of the frog.” *J. Physiol.* **206**, 629–644.
- Birks, RI, and Macintosh, FC (1961). “Acetylcholine metabolism of a sympathetic ganglion.” *Can. J. Biochem. Physiol.* **39**, 787–827.
- Cash, JR, and Krarp, AH (1990). “A variable order Runge-Kutta method for initial value problems with rapidly varying right-hand sides.” *ACM Trans. Math. Softw.* **16**, 201–222.
- Colquhoun, D, Hatton, CJ, and Hawkes, AG (2003). “The quality of maximum likelihood estimates of ion channel rate constants.” *J. Physiol.* **547**, 699–728.
- Colquhoun, D, and Sigworth, FJ (1995). “Fitting and Statistical Analysis of Single-Channel Records.” *Single-Channel Recording*, 2nd Ed., Sakmann, B, and Neher, E (eds.), pp 483–587, Plenum, New York.
- del Castillo, J, and Katz, B (1954a). “Statistical factors involved in neuromuscular facilitation and depression.” *J. Physiol.* **124**, 574–585.
- del Castillo, J, and Katz, B (1954b). “Quantal components of the end-plate potential.” *J. Physiol.* **124**, 560–573.
- Delgado, R, Maureira, C, Oliva, C, Kidokoro, Y, and Labarca, P (2000). “Size of vesicle pools, rates of mobilization, and recycling at neuromuscular synapses of a *Drosophila* mutant, *shibire*.” *Neuron* **28**, 941–953.
- Dittman, JS, Kreitzer, AC, and Regehr, WG (2000). “Interplay between facilitation, depression, and residual calcium at three presynaptic terminals.” *J. Neurosci.* **20**, 1374–1385.
- Dudel, J (1981). “The effect of reduced calcium on quantal unit current and release at the crayfish neuromuscular junction.” *Pflugers Arch. Gesamte Physiol. Menschen Tiere* **391**, 35–40.
- Elmqvist, D, and Quastel, DM (1965). “A quantitative study of end-plate potentials in isolated human muscle.” *J. Physiol.* **178**, 505–529.
- Forsythe, ID, Tsujimoto, T, Barnes-Davies, M, Cuttle, MF, and Takahashi, T (1998). “Inactivation of presynaptic calcium current contributes to synaptic depression at a fast central synapse.” *Neuron* **20**, 797–807.
- Fouquet, W, Oswald, D, Wichmann, C, Mertel, S, Depner, H, Dyba, M, Hallermann, S, Kittel, RJ, Eimer, S, and Sigrist, SJ (2009). “Maturation of active zone assembly by *Drosophila* Bruchpilot.”

- J. Cell Biol.* **186**, 129–145.
- Frerking, M, and Wilson, M (1996). “Effects of variance in mini amplitude on stimulus-evoked release: a comparison of two models.” *Biophys. J.* **70**, 2078–2091.
- Geiger, JRP, and Jonas, P (2000). “Dynamic control of presynaptic Ca^{2+} inflow by fast-inactivating K^+ channels in hippocampal mossy fiber boutons.” *Neuron* **28**, 927–939.
- Hallermann, S, Heckmann, S, Dudel, J, and Heckmann, M (2005). “Short openings in high resolution single channel recordings of mouse nicotinic receptors.” *J. Physiol.* **563**, 645–662.
- Heckmann, M, and Dudel, J (1997). “Desensitization and resensitization kinetics of glutamate receptor channels from *Drosophila* larval muscle.” *Biophys. J.* **72**, 2160–2169.
- Helmchen, F, Borst, JG, and Sakmann, B (1997). “Calcium dynamics associated with a single action potential in a CNS presynaptic terminal.” *Biophys. J.* **72**, 1458–1471.
- Hennig, MH, Postlethwaite, M, Forsythe, ID, Graham, BP (2008). “Interactions between multiple sources of short term plasticity during evoked and spontaneous activity at the rat calyx of Held.” *J. Physiol.* **586**, 3129–3146.
- Hille, B (2001). *Ionic Channels of Excitable Membranes*, 3rd Ed., Sinauer, Sunderland, MA.
- Hosoi, N, Sakaba, T, and Neher, E (2007). “Quantitative analysis of calcium-dependent vesicle recruitment and its functional role at the calyx of Held synapse.” *J. Neurosci.* **27**, 14286–14298.
- Katz, B, and Miledi, R (1965). “The effect of calcium on acetylcholine release from motor nerve terminals.” *Proc. R. Soc. London, Ser. B* **161**, 496–503.
- Katz, B, and Miledi, R (1968). “The role of calcium in neuromuscular facilitation.” *J. Physiol.* **195**, 481–492.
- Kidokoro, Y, Kuromi, H, Delgado, R, Maureira, C, Oliva, C, and Labarca, P (2004). “Synaptic vesicle pools and plasticity of synaptic transmission at the *Drosophila* synapse.” *Brain Res. Rev.* **47**, 18–32.
- Kittel, RJ, Hallermann, S, Thomsen, S, Wichmann, C, Sigrist, SJ, and Heckmann, M (2006a). “Active zone assembly and synaptic release.” *Biochem. Soc. Trans.* **34**, 939–941.
- Kittel, RJ, *et al.* (2006b). “Bruchpilot promotes active zone assembly, Ca^{2+} channel clustering, and vesicle release.” *Science* **312**, 1051–1054.
- Kurdyak, P, Atwood, HL, Stewart, BA, and Wu, CF (1994). “Differential physiology and morphology of motor axons to ventral longitudinal muscles in larval *Drosophila*.” *J. Comp. Neurol.* **350**, 463–472.
- Li, J, and Schwarz, TL (1999). “Genetic evidence for an equilibrium between docked and undocked vesicles.” *Philos. Trans. R. Soc. London, Ser. B* **354**, 299–306.
- Liley, AW, and North, KA (1953). “An electrical investigation of effects of repetitive stimulation on mammalian neuromuscular junction.” *J. Neurophysiol.* **16**, 509–527.
- Macleod, GT, Hegström-Wojtowicz, M, Charlton, MP, and Atwood, HL (2002). “Fast calcium signals in *Drosophila* motor neuron terminals.” *J. Neurophysiol.* **88**, 2659–2663.
- Markram, H, Wang, Y, and Tsodyks, M (1998). “Differential signaling via the same axon of neocortical pyramidal neurons.” *Proc. Natl. Acad. Sci. U.S.A.* **95**, 5323–5328.
- Marrus, SB, and DiAntonio, A (2004). “Preferential localization of glutamate receptors opposite sites of high presynaptic release.” *Curr. Biol.* **14**, 924–931.
- Meyer, AC, Neher, E, and Schneggenburger, R (2001). “Estimation of quantal size and number of functional active zones at the calyx of Held synapse by nonstationary EPSC variance analysis.” *J. Neurosci.* **21**, 7889–7900.
- Mochida, S, Few, AP, Scheuer, T, and Catterall, WA (2008). “Regulation of presynaptic $Ca_v2.1$ channels by Ca^{2+} sensor proteins mediates short-term synaptic plasticity.” *Neuron* **57**, 210–216.
- Müller, M, Felmy, F, Schwaller, B, and Schneggenburger, R (2007). “Parvalbumin is a mobile presynaptic Ca^{2+} buffer in the calyx of Held that accelerates the decay of Ca^{2+} and short-term facilitation.” *J. Neurosci.* **27**, 2261–2271.
- Murthy, VN, Sejnowski, TJ, and Stevens, CF (1997). “Heterogeneous release properties of visualized individual hippocampal synapses.” *Neuron* **18**, 599–612.
- Murthy, VN, and Stevens, CF (1999). “Reversal of synaptic vesicle docking at central synapses.” *Nat. Neurosci.* **2**, 503–507.
- Neher, E (1998). “Usefulness and limitations of linear approximations to the understanding of Ca^{2+} signals.” *Cell Calcium* **24**, 345–357.
- Neher, E, and Sakaba, T (2001). “Combining deconvolution and noise analysis for the estimation of transmitter release rates at the calyx of held.” *J. Neurosci.* **21**, 444–461.
- Pawlu, C, DiAntonio, A, and Heckmann, M (2004). “Postfusional control of quantal current shape.” *Neuron* **42**, 607–618.
- Press, WH, Teukolsky, SA, Vetterling, WT, and Flannery, BP (2002). *Numerical Recipes in C++: The Art of Scientific Computing*, 2nd ed., Cambridge UP, Cambridge, UK.
- Quastel, DM (1997). “The binomial model in fluctuation analysis of quantal neurotransmitter release.” *Biophys. J.* **72**, 728–753.
- Sakaba, T (2006). “Roles of the fast-releasing and the slowly releasing vesicles in synaptic transmission at the calyx of Held.” *J. Neurosci.* **26**, 5863–5871.
- Sakaba, T, and Neher, E (2001a). “Calmodulin mediates rapid recruitment of fast-releasing synaptic vesicles at a calyx-type synapse.” *Neuron* **32**, 1119–1131.
- Sakaba, T, and Neher, E (2001b). “Quantitative relationship between transmitter release and calcium current at the calyx of Held synapse.” *J. Neurosci.* **21**, 462–476.
- Sargent, PB, Saviane, C, Nielsen, TA, DiGregorio, DA, and Silver, RA (2005). “Rapid vesicular release, quantal variability, and spillover contribute to the precision and reliability of transmission at a glomerular synapse.” *J. Neurosci.* **25**, 8173–8187.
- Saviane, C, and Silver, RA (2006). “Fast vesicle reloading and a large pool sustain high bandwidth transmission at a central synapse.” *Nature (London)* **439**, 983–987.
- Scheuss, V, and Neher, E (2001). “Estimating synaptic parameters from mean, variance, and covariance in trains of synaptic responses.” *Biophys. J.* **81**, 1970–1989.
- Scheuss, V, Schneggenburger, R, and Neher, E (2002). “Separation of presynaptic and postsynaptic contributions to depression by covariance analysis of successive EPSCs at the calyx of Held synapse.” *J. Neurosci.* **22**, 728–739.
- Scheuss, V, Taschenberger, H, and Neher, E (2007). “Kinetics of both synchronous and asynchronous quantal release during trains of action potential-evoked EPSCs at the rat calyx of Held.” *J. Physiol.* **585**, 361–381.
- Schneggenburger, R, Meyer, AC, and Neher, E (1999). “Released fraction and total size of a pool of immediately available transmitter quanta at a calyx synapse.” *Neuron* **23**, 399–409.
- See supplementary material at <http://dx.doi.org/10.2976/1.3338710>, for detailed illustration and best-fit parameters of modes 1–6 and additional models.
- Silver, RA (2003). “Estimation of nonuniform quantal parameters with multiple-probability fluctuation analysis: theory, application and limitations.” *J. Neurosci. Methods* **130**, 127–141.
- Silver, RA, Cull-Candy, SG, and Takahashi, T (1996). “Non-NMDA glutamate receptor occupancy and open probability at a rat cerebellar synapse with single and multiple release sites.” *J. Physiol.* **494**(Pt 1), 231–250.
- Stewart, BA, Atwood, HL, Renger, JJ, Wang, J, and Wu, CF (1994). “Improved stability of *Drosophila* larval neuromuscular preparations in haemolymph-like physiological solutions.” *J. Comp. Physiol. [A]* **175**, 179–191.
- Taschenberger, H, Scheuss, V, and Neher, E (2005). “Release kinetics, quantal parameters and their modulation during short-term depression at a developing synapse in the rat CNS.” *J. Physiol.* **568**, 513–537.
- Trommershäuser, J, Schneggenburger, R, Zippelius, A, and Neher, E (2003). “Heterogeneous presynaptic release probabilities: functional relevance for short-term plasticity.” *Biophys. J.* **84**, 1563–1579.
- Tsodyks, MV, and Markram, H (1997). “The neural code between neocortical pyramidal neurons depends on neurotransmitter release probability.” *Proc. Natl. Acad. Sci. U.S.A.* **94**, 719–723.
- Wagh, DA, *et al.* (2006). “Bruchpilot, a protein with homology to ELKS/CAST, is required for structural integrity and function of synaptic active zones in *Drosophila*.” *Neuron* **49**, 833–844.
- Wairkar, YP, Toda, H, Mochizuki, H, Furukubo-Tokunaga, K, Tomoda, T,

- and Diantonio, A (2009). “Unc-51 controls active zone density and protein composition by downregulating ERK signaling.” *J. Neurosci.* **29**, 517–528.
- Wang, LY, and Kaczmarek, LK (1998). “High-frequency firing helps replenish the readily releasable pool of synaptic vesicles.” *Nature (London)* **394**, 384–388.
- Weis, S, Schneggenburger, R, and Neher, E (1999). “Properties of a model of Ca^{++} -dependent vesicle pool dynamics and short term synaptic depression.” *Biophys. J.* **77**, 2418–2429.
- Wojtowicz, JM, Marin, L, and Atwood, HL (1994). “Activity-induced changes in synaptic release sites at the crayfish neuromuscular junction.” *J. Neurosci.* **14**, 3688–3703.
- Worden, MK, Bykhovskaia, M, and Hackett, JT (1997). “Facilitation at the lobster neuromuscular junction: a stimulus-dependent mobilization model.” *J. Neurophysiol.* **78**, 417–428.
- Wu, LG, and Borst, JG (1999). “The reduced release probability of releasable vesicles during recovery from short-term synaptic depression.” *Neuron* **23**, 821–832.
- Wu, Y, Kawasaki, F, and Ordway, RW (2005). “Properties of short-term synaptic depression at larval neuromuscular synapses in wild-type and temperature-sensitive paralytic mutants of *Drosophila*.” *J. Neurophysiol.* **93**, 2396–2405.
- Zucker, RS, and Regehr, WG (2002). “Short-term synaptic plasticity.” *Annu. Rev. Physiol.* **64**, 355–405.

3.7 Hallermann *et al.*, 2010b, J Neurosci, 30: 14340-14345

Seite 92-97

Naked Dense Bodies Provoke Depression

Stefan Hallermann,^{1*} Robert J. Kittel,^{1,2,4*} Carolin Wichmann,^{2,3*} Annika Weyhersmüller,¹ Wernher Fouquet,^{2,6} Sara Mertel,² David Oswald,^{2,3,6} Stefan Eimer,⁵ Harald Depner,^{3,6} Martin Schwärzel,³ Stephan J. Sigrist,^{2,3,6} and Manfred Heckmann^{1,2,4}

¹Carl-Ludwig-Institute of Physiology, Medical Faculty, University of Leipzig, 04103 Leipzig, Germany, ²Rudolf Virchow Center, DFG Research Center for Experimental Biomedicine, University of Würzburg, 97078 Würzburg, Germany, ³Institute for Biology/Genetics, Free University Berlin, 14195 Berlin, Germany, ⁴Institute of Physiology, University of Würzburg, 97070 Würzburg, Germany, ⁵European Neuroscience Institute-Göttingen, Center for Molecular Physiology of the Brain, Medical Faculty, University of Göttingen, 37077 Göttingen, Germany, and ⁶Cluster of Excellence NeuroCure, Charite, 10117 Berlin, Germany

At presynaptic active zones (AZs), the frequently observed tethering of synaptic vesicles to an electron-dense cytomatrix represents a process of largely unknown functional significance. Here, we identified a hypomorphic allele, *brp^{nude}*, lacking merely the last 1% of the C-terminal amino acids (17 of 1740) of the active zone protein Bruchpilot. In *brp^{nude}*, electron-dense bodies were properly shaped, though entirely bare of synaptic vesicles. While basal glutamate release was unchanged, paired-pulse and sustained stimulation provoked depression. Furthermore, rapid recovery following sustained release was slowed. Our results causally link, with intramolecular precision, the tethering of vesicles at the AZ cytomatrix to synaptic depression.

Introduction

The rate at which sensory information can be transmitted across synapses is an important factor that limits rapid and precise information processing in the nervous system. The mechanisms that operate in the presynaptic terminals to release neurotransmitter at AZs at high repetition rates are currently intensely investigated (Atwood and Karunanithi, 2002; Zucker and Regehr, 2002; Kidokoro et al., 2004; Neher and Sakaba, 2008). AZs are decorated with electron-dense material of varying shape and size depending on synapse type and species (Zhai and Bellen, 2004).

Recently, the CAST/ERC-family member Bruchpilot (BRP), a coiled-coil rich protein of nearly 200 kDa, was identified via its localization to *Drosophila* AZs. BRP was shown to be crucial for cytomatrix formation, proper Ca²⁺ channel clustering within AZs, and efficient neurotransmitter release at the *Drosophila* neuromuscular junction (Kittel et al., 2006; Wagh et al., 2006). Furthermore, BRP is a direct component of the electron-dense cytomatrix (T-bar) and adopts an elongated conformation, with its N terminus (N-term) facing Ca²⁺ channels at the membrane and its C-term reaching into the cytoplasm (Fouquet et al., 2009).

Materials and Methods

Genetics. Larvae were raised at 25°C [cacophony (Cac) RNA interference (RNAi) larvae and their controls were raised at 29°C] in bottles or on apple agar plates (for high-pressure freezing), and the following genotypes were used: Bruchpilot studies: *brp^{nude}* or *brp^{1,3}* or *brp^{5,45}/df(2R)BSC29*, *ok6-GAL4* (Fouquet et al., 2009), controls: *+/ok6-GAL4*. Cacophony images: *ok6-GAL4*, *UAS-Cac^{GFP}/+* and *brp^{nude}/df(2R)BSC29*, *ok6-GAL4*; *UAS-Cac^{GFP}/+*. Cacophony RNAi studies: *UAS-Cac RNAi* (Transformant ID 5551) (Dietzl et al., 2007)/+; *elav-GAL4/+*, control: *elav-GAL4/+*.

Stimulated emission depletion microscopy. Stimulated emission depletion (STED) microscopy experiments were performed essentially as described by Kittel et al. (2006), using the commercially available Leica TCS STED microscope (Leica Microsystems). Secondary antibodies were conjugated to the Atto 647N dye (AttoTech). Atto 647N fluorophores were excited at a wavelength of 635 nm and depleted at 750 nm. Images were acquired using APD detectors within a range of 645–715 nm. Image processing was performed using the Inspector software (Max-Planck Innovation) by applying a linear deconvolution at single STED slices.

To assess Ca²⁺ channel clustering, neuromuscular junctions were stained with M- α -GFP (Invitrogen) and G- α -M-Atto647N to visualize Ca²⁺ channels (Cac^{GFP}). Additionally, serving as a reference, postsynaptic glutamate receptors were labeled with primary Rb- α -DGluRIID and secondary Sheep- α -Rb-Cy3 (Invitrogen) antibodies and imaged via conventional confocal microscopy. From such images, AZs were selected that appeared planar to the optical slice (i.e., the AZ membrane is parallel to the focal slice). With Mathematica 5.0 (Wolfram Research), each channel (Cac^{GFP} and GluRIID) of each image of a planar AZ was automatically fitted with a two-dimensional Gaussian function. The peak of these Gaussians was used to align the Cac^{GFP} signal either with itself or with the GluRIID signal for subsequent averaging. The average images were again fitted with two-dimensional Gaussian functions and both horizontal and vertical intensity profiles through the peak of the two-dimensional Gaussian functions were averaged and fitted with one-dimensional Gaussian functions (see Fig. 2B).

Received May 15, 2010; revised Aug. 12, 2010; accepted Aug. 26, 2010.

This work was supported by grants from the Deutsche Forschungsgemeinschaft (DFG) to S.J.S. (Exc 257, S1849/2-1, TP A16/SFB 406, TP B23/SFB 581) and to M.H. (HE 2621/4-2 and TP B27/SFB 581), and by *formel.1* grants to S.H. and R.J.K. from the Medical Faculty of the University of Leipzig. R.J.K. is supported by the DFG Emmy Noether-Program (KI 1460/1-1). We acknowledge the VDRC for the cacophony RNAi line.

*S.H., R.J.K., and C.W. contributed equally to this work.

This article is freely available online through the *JNeurosci* Open Choice option.

Correspondence should be addressed to either of the following: Manfred Heckmann, Physiologisches Institut, Röntgenring 9, 97070 Würzburg, Germany, E-mail: heckmann@uni-wuerzburg.de; or Stephan J. Sigrist, Institute for Biology/Genetics, Free University Berlin, Takustrasse 6, 14195 Berlin, Germany, E-mail: stephan.sigrist@fu-berlin.de.

DOI:10.1523/JNEUROSCI.2495-10.2010

Copyright © 2010 the authors 0270-6474/10/3014340-06\$15.00/0

Electron microscopy. Electron microscopy and conventional embedding was performed as previously described (Fouquet et al., 2009) on late third-instar *Drosophila* larvae. The number of docked vesicles was determined along the whole synapse showing the typical close apposition of electron-dense presynaptic and postsynaptic membrane. We counted only vesicles without any discernible distance between vesicle and AZ membrane.

Electrophysiology. Two-electrode voltage-clamp (TEVC) recordings of EPSCs were obtained at room temperature from late third-instar male *Drosophila* larvae (ventral longitudinal muscle 6, segments A2 and A3), essentially as previously described (Kittel et al., 2006). For the TEVC experiments with *brp^{nude}*, *brp^{1,3}*, and *brp^{5,45}* mutants, both mutants and control animals carried a copy of *ok6-GAL4* to ensure comparability with a previous study (Kittel et al., 2006). The composition of the extracellular hemolymph-like saline (HL-3) was as follows (in mM): NaCl 70, KCl 5, MgCl₂ 20, NaHCO₃ 10, trehalose 5, sucrose 115, HEPES 5, CaCl₂ 1 or as indicated, and pH adjusted to 7.4. Recordings were made from cells with an initial resting membrane potential between -50 and -70 mV (holding potential at -60 mV) using intracellular electrodes with resistances of 10–32 M Ω , filled with 3 M KCl. Train stimulation protocols consisted of 100 pulses applied at 60 Hz. The recovery was assessed by evoking APs at (in ms following the last pulse in the train): 25, 50, 100, 200, 500, 1000, 2000, 5000, 10,000, 20,000, 50,000, and 100,000 (Wu et al., 2005). EPSCs reflect the compound response to stimulation of both motoneurons innervating muscle 6, and care was therefore taken to ensure their stable recruitment. Infrequently observed recruitment failures were linearly interpolated. Only cells that recovered at least 70% of their initial EPSC amplitude following tetanic stimulation were included in the analysis. The recordings were analyzed with pClamp 9 (Molecular Devices), and the peak amplitude was determined as the difference between the peak value of the EPSC and the baseline value before onset of that EPSC. The steady-state EPSC amplitudes (see Fig. 3D) were evaluated for each experiment as the average of the last 25 EPSC amplitudes in the train and normalized to the average steady-state EPSC amplitude of the corresponding control for either *brp* or *Cac* RNAi experiments. The time constants of the fast and slow components of recovery (see Fig. 3E,F) were determined from monoexponential functions fitted to the average fast and slow component of recovery and weighted with the errors of the average data with Igor Pro 6.1 (Wavemetrics). The estimated errors of the fit parameters were taken from Igor Pro (which are based on the square roots of the diagonal elements of the covariance matrix). From the time constants, the SEs, and the number of experiments, statistical comparisons were performed with Student's *t* test, and the error bars of the normalized values were calculated according to Gaussian error propagation.

Statistical analysis. The nonparametric Mann–Whitney rank sum test was used for statistical analysis if not stated otherwise. The data are reported as mean \pm SE, *n* indicates the sample number, and *p* denotes the significance (**p* < 0.05, ***p* < 0.01, and ****p* < 0.001).

Results

Impaired vesicle tethering at AZs of a Bruchpilot mutant (*brp^{nude}*) lacking the last 17 C-terminal amino acids

In a chemical [ethyl methyl sulfonate (EMS)] mutagenesis screen, a novel *brp* allele was identified with a premature STOP codon at amino acid position 1724 (*brp^{5,38}*, hereafter *brp^{nude}*) of 1740 aa. While in the previously published mutants *brp^{5,45}* and *brp^{1,3}* a significant proportion of the C-terminal amino acids are absent (50% and 30%, respectively; STOP codons at position 867 or 1390) (Fouquet et al., 2009), *brp^{nude}* lacks only the last 1% (Fig. 1A,C). Nevertheless, all three mutants showed significantly reduced survival rates and motor abilities as adult flies (Fig. 1B).

At neuromuscular junctions of *brp^{nude}*, the reactivities of antibodies directed against the C-term (BRP^{Nc82}; Wagh et al., 2006) and the N-term (BRP^{N-term}) (Fouquet et al., 2009) of BRP are still present (Fig. 1D), and the number of AZs per junction is normal (quantified as BRP^{Nc82} spots per junction; 553 ± 27 and 518 ± 28

for control and *brp^{nude}*; $n_{\text{junction}} = 6$ and 6 ; $p = 0.24$). Furthermore, high-resolution light microscopic images (STED microscopy) (Hell, 2007) of BRP^{Nc82} acquired simultaneously with confocal images of BRP^{N-term} appeared unchanged compared to controls. Especially, the previously described ring-like distribution of Nc82 reactivity (Kittel et al., 2006) is preserved at *brp^{nude}* synapses (Fig. 1D). The normal distribution of C- and N-terminal signals at *brp^{nude}* AZs indicates that the missing 1% of BRP does not alter the overall structure of the cytomatrix. In fact, an electron microscopic analysis of the ultrastructure of *brp^{nude}* synapses revealed normal amounts of AZ cytomatrix and an ordinary height and platform length of dense bodies (T-bars) (Fig. 1E,F). Furthermore, the diameter of the synaptic vesicles as well as the total number of synaptic vesicles per bouton section were unchanged in *brp^{nude}* (diameter: 36 ± 1.7 and 35 ± 0.3 nm for control and *brp^{nude}*, $n_{\text{vesicles}} = 220$ and 243 (10 larvae each), respectively; $p = 0.9$; number: 114 ± 24 and 131 ± 7 SV/ μm^2 for control and *brp^{nude}*, $n_{\text{bouton-section}} = 6$ and 6 , respectively; $p = 0.2$). Finally, the number of docked vesicles per AZ section was not significantly different between *brp^{nude}* and controls (1.8 ± 0.2 and 1.4 ± 0.3 for control and *brp^{nude}*, $n_{\text{AZ}} = 21$ and 24 , respectively; $p = 0.4$) (see Fig. 1G; for definition of docked vesicles, see Materials and Methods). However, T-bars at *brp^{nude}* AZs were bare of vesicles (Fig. 1E). A quantification of the number of vesicles within three shells of each 50 nm thickness surrounding the AZ revealed a significant reduction in the average number of vesicles near the T-bar at *brp^{nude}* synapses (Fig. 1G). These data indicate that while the basic ultrastructure of the cytomatrix is unaltered at *brp^{nude}* AZs, vesicle tethering is specifically impaired.

Normal Ca²⁺ channel clustering and basal release at *brp^{nude}* synapses

Using STED microscopy, we tested whether Ca²⁺ channel clustering is affected at *brp^{nude}* synapses. STED images of GFP-labeled Ca²⁺ channels (*Cac^{GFP}*) were acquired simultaneously with confocal images of postsynaptic glutamate receptors (GluRIID) to identify the position of AZs (opposite GluRIID patches) independently of Ca²⁺ channel clustering (Fig. 2A). Fitting Gaussian functions to the intensity profiles of average images revealed a normal Ca²⁺ channel distribution at *brp^{nude}* synapses (Fig. 2B). Comparable results were obtained when the *Cac* signals were aligned with themselves. With this method, the delocalization of Ca²⁺ channels in *brp* null mutants (Kittel et al., 2006) could clearly be resolved (supplemental Fig. S1, available at www.jneurosci.org as supplemental material). Thus, we isolated a *brp* allele lacking only the last 1% of C-terminal amino acids, which severely affects vitality but not the clustering of AZ Ca²⁺ channels.

Next, we tested the functional consequences of defective vesicle tethering. EPSCs evoked at 0.2 Hz at *brp^{nude}* synapses did not differ in terms of their peak amplitude, rise time, or decay time constant from those of controls (Fig. 2C). In *brp^{1,3}* and *brp^{5,45}* mutants, with poorly clustered Ca²⁺ channels (Fouquet et al., 2009), the EPSC amplitudes were reduced to $30 \pm 8\%$ ($n = 4$) and $10 \pm 8\%$ ($n = 12$) of control amplitudes, respectively (Fig. 2C). The amplitude of miniature EPSCs was not significantly affected in any of these three mutants (Fig. 2D). These data indicate that basal release (at 0.2 Hz) requires Ca²⁺ channel clustering, but not vesicles tethered to the cytomatrix.

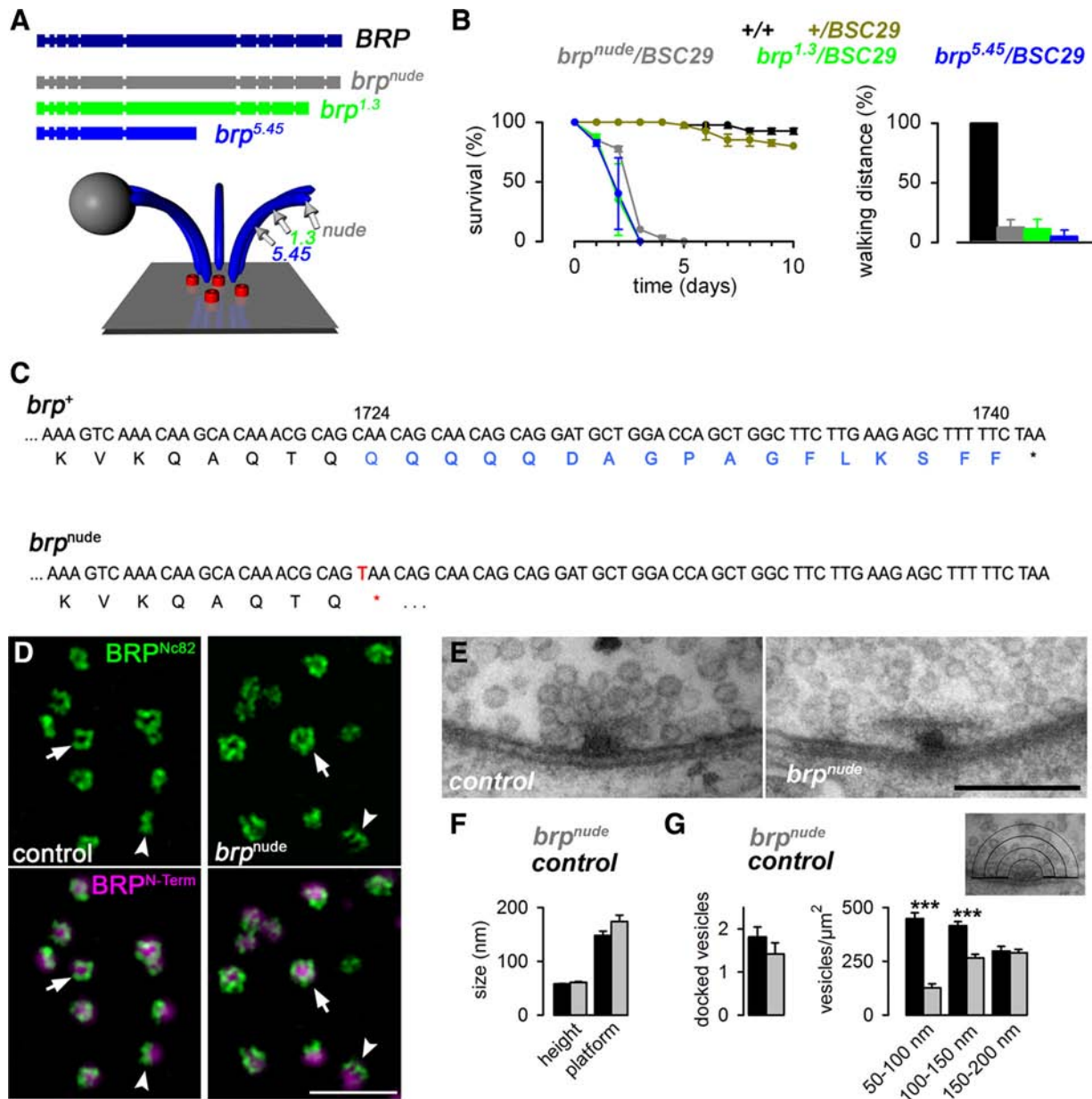


Figure 1. Impaired vesicle tethering at AZs of a *bruchpilot* mutant (*brpnude*) lacking the last 17 C-terminal amino acids. **A**, Chemical induction of premature stop codons resulted in truncated versions of the BRP protein (BRP; dark blue; boxes indicate coiled-coil domains) of ~99% (*brpnude*; gray), of ~70% (*brp^{1.3}*; green), and of ~50% length (*brp^{5.45}*; blue). Below, illustration of the BRP protein (blue) within the AZ (red: Ca²⁺ channels; gray: synaptic vesicle) and the corresponding positions of the truncation (arrows) (Fouquet et al., 2009). **B**, All three BRP mutants (*brpnude*, *brp^{1.3}*, *brp^{5.45}*) showed severely impaired survival rates and walking skills. **C**, In the *brpnude* allele, a single base mutation at the C-terminal position 1724 leads to a premature stop codon and a BRP protein (BRP^{nude}) lacking the last 17 of 1740 aa. **D**, STED images of neuromuscular junctions stained with a C-terminal BRP antibody (green; BRP^{Nc82}) and simultaneous confocal images of an N-terminal BRP antibody (magenta; BRP^{N-term}). The distribution of both antibody signals appears unaltered at *brpnude* synapses (right) compared to controls (left). Arrows and arrowheads indicate planar and vertical AZs, respectively. **E**, Examples of conventionally embedded AZs of control and *brpnude*. Note fewer tethered vesicles in *brpnude*. **F**, Height and length of the platform of the electron-dense cytomatrix (T-bar) for control and *brpnude*. **G**, The number of docked vesicles per AZ section for control and *brpnude* ($n = 22$ and 25 AZs, respectively) and the number of vesicles found within three shells (see inset) each of 50 nm thickness surrounding the AZ ($n = 20$ and 31 AZs, respectively). Scale bars: **D**, 1 μ m; **E**, 200 nm.

Tethering vesicles to the active zone dense body prevents synaptic depression

To investigate the impact of vesicle tethering on short-term plasticity, we analyzed synaptic transmission during paired-pulse stimulation (Fig. 3A). Strikingly, the amplitude of the second EPSC was significantly reduced at short interpulse intervals of 10 and 30 ms (Fig. 3B). This depression decayed with a time constant of 19 ms. Next, synaptic transmission was analyzed during a train of 100 stimuli at 60 Hz (Fig. 3C) (Hallermann et al., 2010). The depression during the train was stronger in *brpnude* as quantified

by a reduction in the steady-state EPSC amplitude at the end of the train to $35 \pm 3\%$ compared to $52 \pm 5\%$ in controls ($n = 21$ and 20 for control and *brpnude* mutants, respectively) (Fig. 3C,D). Consistent with the altered paired-pulse ratio, the amplitude of the second EPSC in the train was already significantly reduced to $80 \pm 10\%$ at *brpnude* synapses ($n = 21$ and 20).

If sustained release is impaired in *brpnude* mutants because fewer vesicles are tethered to the cytomatrix, then sustained release in *brp^{1.3}* and *brp^{5.45}* mutants, both of which show severely impaired cytomatrices (Fouquet et al., 2009), should be im-

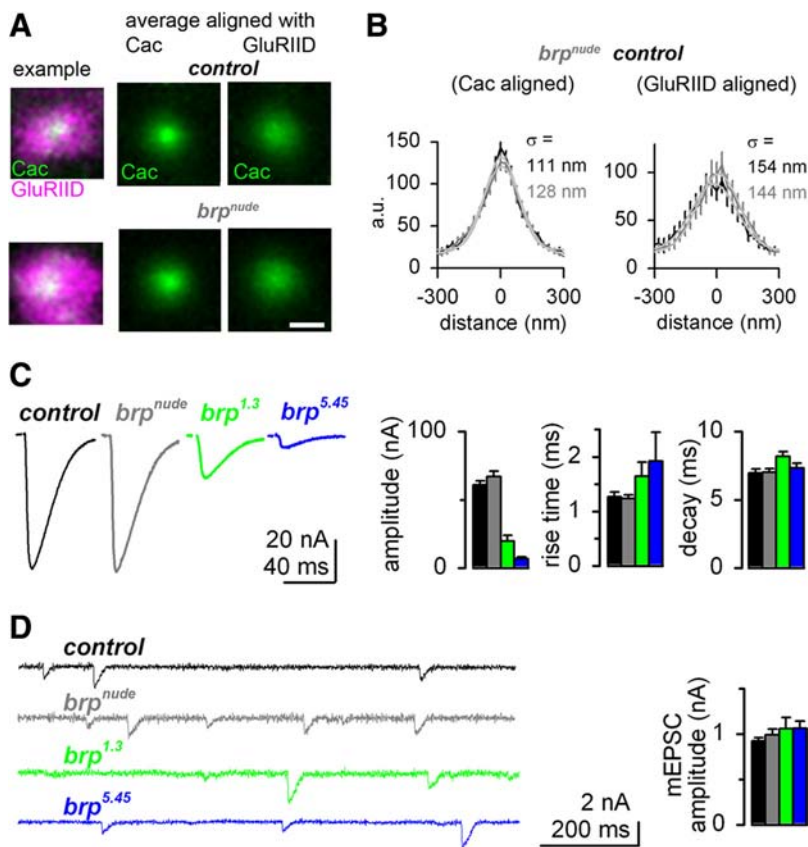


Figure 2. Normal Ca^{2+} channel clustering and basal release at brp^{nude} synapses. **A**, GluRIID labels (magenta, confocal) were used to quantify the Ca^{2+} channel (Cac^{GFP}, green, STED) clusters in control animals (top row) and brp^{nude} mutants (below). The Cac signals at synapses that appeared ideally planar ($n = 16$ each) were averaged after alignment with the postsynaptic GluRIID signal (right panels) or themselves (center panels). While the example images were scaled up individually, all four averages were scaled up with the same factor. **B**, Intensity profiles of the average Cac images in black for controls and in gray for brp^{nude} mutants with SE bars and the corresponding Gaussian fits (standard deviations given by σ) in gray. **C**, Examples of EPSCs elicited at 0.2 Hz in control (black), brp^{nude} (gray), $brp^{1.3}$ (green), and $brp^{5.45}$ mutants (blue; average of 10 each) in 1.0 mM Ca^{2+} . The average peak EPSC amplitudes and rise and decay kinetics were normal in brp^{nude} mutants. In $brp^{1.3}$ and $brp^{5.45}$ mutants EPSC amplitudes were reduced and rise times increased ($n = 22, 18, 4,$ and 12 for control, brp^{nude} , $brp^{1.3}$, and $brp^{5.45}$, respectively). **D**, Example traces of mEPSCs of control (black), brp^{nude} (gray), $brp^{1.3}$ (green), and $brp^{5.45}$ mutants (blue). The average mEPSC amplitudes were normal in brp^{nude} , $brp^{1.3}$, and $brp^{5.45}$ mutants ($n = 6, 6, 4,$ and 6 for control, brp^{nude} , $brp^{1.3}$, and $brp^{5.45}$, respectively). Scale bar in **A**, 250 nm.

paired, too. Indeed, investigations of sustained release in $brp^{1.3}$ and $brp^{5.45}$ mutants revealed stronger synaptic depression than in controls (supplemental Fig. S2A, C, available at www.jneurosci.org as supplemental material). To analyze whether the stronger depression in $brp^{1.3}$ and $brp^{5.45}$ mutants is simply the consequence of impaired Ca^{2+} channel clustering, we sought to compensate (“rescue”) the reduced Ca^{2+} channel density by increasing the extracellular Ca^{2+} concentration. In high Ca^{2+} (2 mM and 2.5 mM for $brp^{1.3}$ and $brp^{5.45}$ mutants, respectively), their EPSC amplitudes were comparable to those of controls in 1 mM Ca^{2+} . However, depression during sustained release was still pronounced (Fig. 3D; supplemental Fig. S2B, D, available at www.jneurosci.org as supplemental material).

Since vesicle recruitment critically depends on the intracellular spatiotemporal Ca^{2+} dynamics (Neher and Sakaba, 2008), we performed control experiments by reducing the density of Ca^{2+} channels genetically and tested whether subsequent elevations of extracellular Ca^{2+} could rescue sustained release. To this end, transgene-mediated RNAi directed against the $\alpha 1$ subunit of the *Drosophila* Ca^{2+} channel (Cac) was performed, resulting in a reduction of EPSC amplitudes by $\sim 50\%$. Extracellular Ca^{2+} was then elevated to 1.5 mM to obtain control EPSC amplitudes. However, in

contrast to $brp^{1.3}$ and $brp^{5.45}$ mutants, sustained release was unaltered by Cac RNAi (Fig. 3D; supplemental Fig. S2E, available at www.jneurosci.org as supplemental material).

Next, we addressed whether the enhanced depression during sustained high-frequency transmission at brp^{nude} synapses is accompanied by alterations in the kinetics of recovery from depression. Therefore, the recovery from synaptic depression after a train was investigated with test stimuli of increasing intervals following the train (Fig. 3E, F) (Wu et al., 2005; Hallermann et al., 2010). A biphasic recovery with time constants of $\tau_1 = 50$ ms and $\tau_2 = 6.1$ s was found in controls. In brp^{nude} mutants, the first component was slower (114 ms), while the second component was unaltered (5.6 s) (Fig. 3E, F). Consistently, the first component of recovery was also slower in $brp^{1.3}$ and $brp^{5.45}$ mutants with Ca^{2+} concentrations that rescued the basal EPSC amplitude. In contrast to the normal second component of recovery at brp^{nude} synapses, the second component of recovery in $brp^{1.3}$ and $brp^{5.45}$ mutants was also significantly slower (Fig. 3E, F; supplemental Fig. S2, available at www.jneurosci.org as supplemental material). Finally, in experiments with Cac RNAi, which serve as a control for the approach of elevating Ca^{2+} , both components were normal (Fig. 3E, F; supplemental Fig. S2, available at www.jneurosci.org as supplemental material). In summary, these data indicate that the basal EPSC amplitude (cf. Fig. 2) as well as the second component of recovery rely on adequate Ca^{2+} channel clustering (impaired in $brp^{1.3}$ and $brp^{5.45}$) and that high-frequency sustained release as well as the

first component of recovery also rely on proper vesicle tethering at the AZ (selectively impaired in brp^{nude}).

Discussion

To our knowledge, the specific impairment of vesicle tethering reported here delivers the first direct demonstration that efficient sustained release relies on the ability of the AZ to tether vesicles. While the overall AZ structure, including the distribution of Ca^{2+} channels, was unaffected, the impairment of vesicle tethering provoked pronounced synaptic depression and a slowed first component of recovery.

The C-terminal half of BRP consists of ~ 1000 aa of essentially contiguous coiled-coil sequence (Wagh et al., 2006), reminiscent of Golgi/ER-resident tethering factors such as, e.g., GM130 (Lupashin and Sztul, 2005). These coiled-coils typically form rod-like structures, where 100 aa residues extend ~ 15 nm when dimerized, and proteins such as Uso1p (Yamakawa et al., 1996) extend over 150 nm (Lupashin and Sztul, 2005). These rod-like proteins are believed to act before SNARE protein assembly by forming contacts between membranes at a distance, thereby increasing the specificity or efficiency of the initial at-

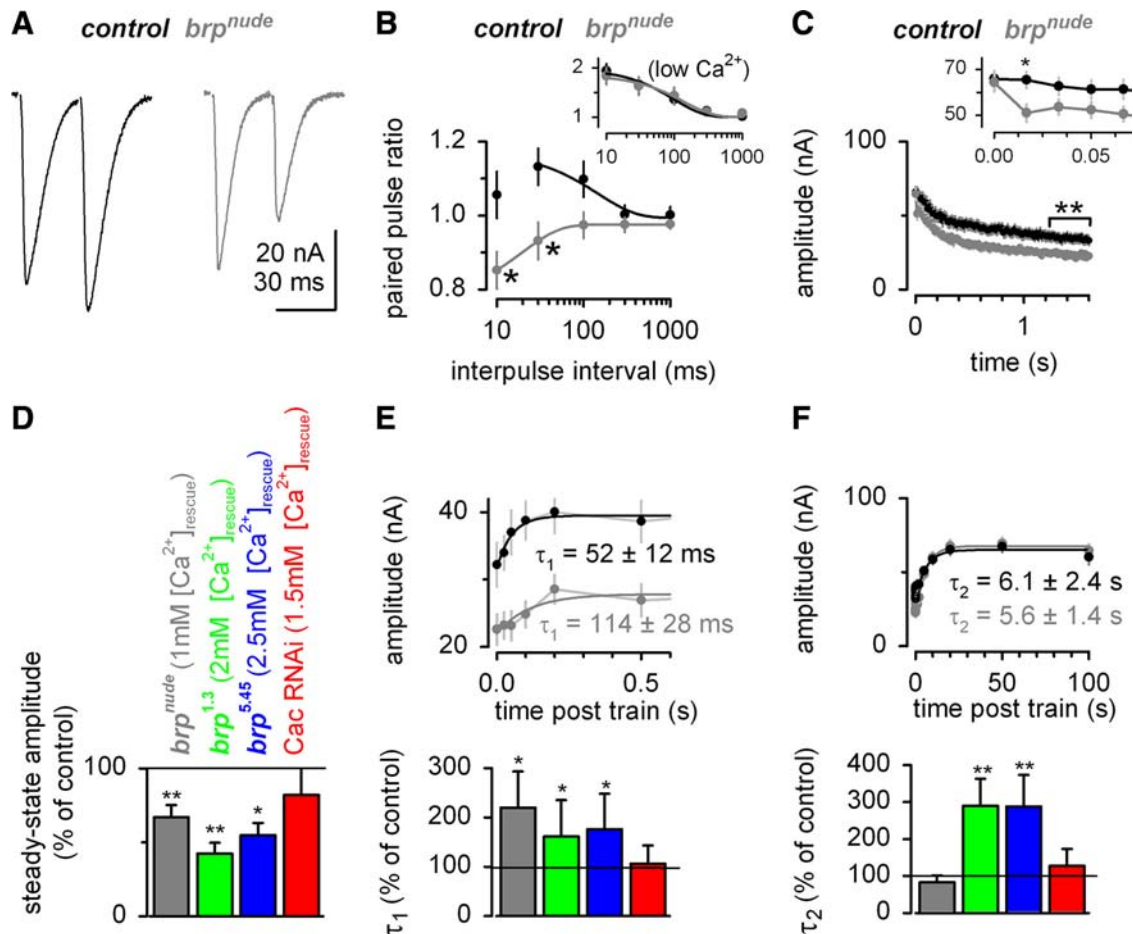


Figure 3. Tethering vesicles to the AZ dense body prevents synaptic depression. **A**, Examples of EPSCs elicited by a paired-pulse protocol with 30 ms interpulse interval in control (black) and *brp^{nude}* (gray). **B**, Average paired-pulse ratios plotted versus interpulse interval in 1.0 mM Ca^{2+} for control (black, $n = 12$) and *brp^{nude}* (gray, $n = 9$; asterisk indicates significant differences) superimposed with exponential fits (time constants are indicated). Inset, 0.6 mM Ca^{2+} . **C**, Average peak EPSC amplitudes during the 60 Hz train for control (black, $n = 21$) and *brp^{nude}* (gray, $n = 20$). Inset, Average amplitudes of the first 5 EPSCs of the train. The steady-state amplitude (average of EPSC amplitudes marked by the bracket) was significantly reduced in *brp^{nude}* mutants compared to controls. **D**, Steady-state amplitudes normalized to the steady-state amplitude of the respective control, for *brp^{nude}* (gray), *brp^{1.3}* (green), *brp^{5.45}* (blue), and Cac RNAi synapses (red) in extracellular Ca^{2+} concentrations that lead to normal ("rescued") basal EPSC amplitudes ($[Ca^{2+}]_{rescue}$) (see supplemental Fig. S2, available at www.jneurosci.org as supplemental material). **E**, Average peak EPSC amplitudes during the first rapid component of recovery after the train (τ_1) for control (black, $n = 21$) and *brp^{nude}* (gray, $n = 20$) fitted exponentially (lines). Time constants with SEs are indicated. Bottom, The time constants of the first component of recovery normalized to the corresponding time constant of the control (color code as in **D**). **F**, Corresponding average peak EPSC amplitudes during the second slower component of recovery after the train (τ_2) with corresponding average data.

tachment of vesicles (tethering) (Guo et al., 2000). We have provided morphological and functional evidence that BRP filaments tether vesicles, and thus further mechanistic comparisons between AZ and Golgi/ER trafficking, e.g., concerning the role of small GTPases, might well be informative.

The C-terminal half of BRP is very highly conserved in insects but not elsewhere (Wagh et al., 2006). Interestingly, the *Drosophila* genome does not appear to encode homologs of the vertebrate AZ components Piccolo and Bassoon (Wagh et al., 2006), which are key regulators of the vertebrate cytomatrix (Khimich et al., 2005). At central vertebrate synapses, CAST and Bassoon immunoreactivities (closer and further from the AZ membrane, respectively) were recently found to be associated with filaments that may connect vesicles to the AZ (Siksoo et al., 2007). It is tempting to speculate that at AZs of central vertebrate synapses, CAST associates with coiled-coil domain proteins, such as bassoon, to perform the dual functions of Ca^{2+} channel clustering and vesicle tethering executed by the N-terminal and the C-terminal domains of BRP, respectively.

How synapses manage to repetitively release transmitter with high precision is intensely investigated. Vesicles tethered to

electron-dense bodies may represent a reservoir of vesicles required for sustained release (Zhai and Bellen, 2004). Consistent with this hypothesis, synaptic stimulation provokes depletion of vesicles tethered at dense bodies (LoGiudice et al., 2008; Jackman et al., 2009). While the supply of vesicles appears rate limiting during the train and the first component of recovery (Saviane and Silver, 2006), the maturation of vesicles closer to Ca^{2+} channels appears rate limiting during the second component of recovery [cf. *brp^{1.3}* and *brp^{5.45}* (Kittel et al., 2006; Fouquet et al., 2009)]. One may argue that the rapid component of depression observed at *brp^{nude}* synapses (Fig. 3A,B) could be partially attributed to fewer docked vesicles (though not significantly; cf. Fig. 1G) with a higher initial release probability. However, a functional estimation of the number of readily releasable vesicles using back-extrapolation from the cumulative EPSC amplitudes in the trains (Schneppenburger et al., 1999) revealed similar numbers of readily releasable vesicles in *brp^{nude}* and controls (supplemental Fig. S3, available at www.jneurosci.org as supplemental material). Finally, we would like to point out that the C-term of BRP could be involved in endocytotic mechanisms, which have been shown to be crucial for sustained release (Koenig et al., 1998;

Kawasaki et al., 2000; Dickman et al., 2005; Hosoi et al., 2009; Yao et al., 2009). Novel techniques have begun to address the spatial organization of local vesicle reuse within active zones (Zhang et al., 2009). It will have to be clarified via which routes vesicles move within active zones and in which direction Bruchpilot steers their translocation.

References

- Atwood HL, Karunanithi S (2002) Diversification of synaptic strength: pre-synaptic elements. *Nat Rev Neurosci* 3:497–516.
- Dickman DK, Horne JA, Meinertzhagen IA, Schwarz TL (2005) A slowed classical pathway rather than kiss-and-run mediates endocytosis at synapses lacking synaptojanin and endophilin. *Cell* 123:521–533.
- Dietzl G, Chen D, Schnorrer F, Su KC, Barinova Y, Fellner M, Gasser B, Kinsey K, Oettel S, Scheiblaue S, Couto A, Marra V, Keleman K, Dickson BJ (2007) A genome-wide transgenic RNAi library for conditional gene inactivation in *Drosophila*. *Nature* 448:151–156.
- Fouquet W, Oswald D, Wichmann C, Mertel S, Depner H, Dyba M, Hallermann S, Kittel RJ, Eimer S, Sigrist SJ (2009) Maturation of active zone assembly by *Drosophila* Bruchpilot. *J Cell Biol* 186:129–145.
- Guo W, Sacher M, Barrowman J, Ferro-Novick S, Novick P (2000) Protein complexes in transport vesicle targeting. *Trends Cell Biol* 10:251–255.
- Hallermann S, Heckmann M, Kittel RJ (2010) Mechanisms of short-term plasticity at neuromuscular active zones of *Drosophila*. *HFSP J* 4:72–84.
- Hell SW (2007) Far-field optical nanoscopy. *Science* 316:1153–1158.
- Hosoi N, Holt M, Sakaba T (2009) Calcium dependence of exo- and endocytotic coupling at a glutamatergic synapse. *Neuron* 63:216–229.
- Jackman SL, Choi SY, Thoreson WB, Rabl K, Bartoletti TM, Kramer RH (2009) Role of the synaptic ribbon in transmitting the cone light response. *Nat Neurosci* 12:303–310.
- Kawasaki F, Hazen M, Ordway RW (2000) Fast synaptic fatigue in shibire mutants reveals a rapid requirement for dynamin in synaptic vesicle membrane trafficking. *Nat Neurosci* 3:859–860.
- Khimich D, Nouvian R, Pujol R, Tom Dieck S, Egner A, Gundelfinger ED, Moser T (2005) Hair cell synaptic ribbons are essential for synchronous auditory signalling. *Nature* 434:889–894.
- Kidokoro Y, Kuromi H, Delgado R, Maureira C, Oliva C, Labarca P (2004) Synaptic vesicle pools and plasticity of synaptic transmission at the *Drosophila* synapse. *Brain Res Brain Res Rev* 47:18–32.
- Kittel RJ, Wichmann C, Rasse TM, Fouquet W, Schmidt M, Schmid A, Wagh DA, Pawlu C, Kellner RR, Willig KI, Hell SW, Buchner E, Heckmann M, Sigrist SJ (2006) Bruchpilot promotes active zone assembly, Ca²⁺ channel clustering, and vesicle release. *Science* 312:1051–1054.
- Koenig JH, Yamaoka K, Ikeda K (1998) Omega images at the active zone may be endocytotic rather than exocytotic: implications for the vesicle hypothesis of transmitter release. *Proc Natl Acad Sci U S A* 95:12677–12682.
- LoGiudice L, Sterling P, Matthews G (2008) Mobility and turnover of vesicles at the synaptic ribbon. *J Neurosci* 28:3150–3158.
- Lupashin V, Sztul E (2005) Golgi tethering factors. *Biochim Biophys Acta* 1744:325–339.
- Neher E, Sakaba T (2008) Multiple roles of calcium ions in the regulation of neurotransmitter release. *Neuron* 59:861–872.
- Saviane C, Silver RA (2006) Fast vesicle reloading and a large pool sustain high bandwidth transmission at a central synapse. *Nature* 439:983–987.
- Schneggenburger R, Meyer AC, Neher E (1999) Released fraction and total size of a pool of immediately available transmitter quanta at a calyx synapse. *Neuron* 23:399–409.
- Siksoo L, Rostaing P, Lechaire JP, Boudier T, Ohtsuka T, Fejtová A, Kao HT, Greengard P, Gundelfinger ED, Triller A, Marty S (2007) Three-dimensional architecture of presynaptic terminal cytomatrix. *J Neurosci* 27:6868–6877.
- Wagh DA, Rasse TM, Asan E, Hofbauer A, Schwenkert I, Dürrbeck H, Buchner S, Dabauvalle MC, Schmidt M, Qin G, Wichmann C, Kittel R, Sigrist SJ, Buchner E (2006) Bruchpilot, a protein with homology to ELKS/CAST, is required for structural integrity and function of synaptic active zones in *Drosophila*. *Neuron* 49:833–844.
- Wu Y, Kawasaki F, Ordway RW (2005) Properties of short-term synaptic depression at larval neuromuscular synapses in wild-type and temperature-sensitive paralytic mutants of *Drosophila*. *J Neurophysiol* 93:2396–2405.
- Yamakawa H, Seog DH, Yoda K, Yamasaki M, Wakabayashi T (1996) Uso1 protein is a dimer with two globular heads and a long coiled-coil tail. *J Struct Biol* 116:356–365.
- Yao CK, Lin YQ, Ly CV, Ohyama T, Haueter CM, Moiseenkova-Bell VY, Wensel TG, Bellen HJ (2009) A synaptic vesicle-associated Ca²⁺ channel promotes endocytosis and couples exocytosis to endocytosis. *Cell* 138:947–960.
- Zhai RG, Bellen HJ (2004) The architecture of the active zone in the presynaptic nerve terminal. *Physiology (Bethesda)* 19:262–270.
- Zhang Q, Li Y, Tsien RW (2009) The dynamic control of kiss-and-run and vesicular reuse probed with single nanoparticles. *Science* 323:1448–1453.
- Zucker RS, Regehr WG (2002) Short-term synaptic plasticity. *Annu Rev Physiol* 64:355–405.

3.8 Hallermann *et al.*, 2010c, Neuron im Druck

Seite 99-112

Bassoon Speeds Vesicle Reloading at a Central Excitatory Synapse

Stefan Hallermann,^{1,*} Anna Fejtova,² Hartmut Schmidt,¹ Annika Weyhersmüller,¹ R. Angus Silver,³ Eckart D. Gundelfinger,² and Jens Eilers¹

¹Carl Ludwig Institute of Physiology, Medical Faculty, University of Leipzig, Liebigstrasse 27, 04103 Leipzig, Germany

²Department of Neurochemistry and Molecular Biology, Leibniz Institute for Neurobiology, 39118 Magdeburg, Germany

³Department of Neuroscience, Physiology and Pharmacology, University College London, Gower Street, London WC1E 6BT, UK

*Correspondence: hallermann@medizin.uni-leipzig.de

DOI 10.1016/j.neuron.2010.10.026

SUMMARY

Sustained rate-coded signals encode many types of sensory modalities. Some sensory synapses possess specialized ribbon structures, which tether vesicles, to enable high-frequency signaling. However, central synapses lack these structures, yet some can maintain signaling over a wide bandwidth. To analyze the underlying molecular mechanisms, we investigated the function of the active zone core component Bassoon in cerebellar mossy fiber to granule cell synapses. We show that short-term synaptic depression is enhanced in Bassoon knockout mice during sustained high-frequency trains but basal synaptic transmission is unaffected. Fluctuation and quantal analysis as well as quantification with constrained short-term plasticity models revealed that the vesicle reloading rate was halved in the absence of Bassoon. Thus, our data show that the cytomatrix protein Bassoon speeds the reloading of vesicles to release sites at a central excitatory synapse.

INTRODUCTION

Many sensory systems, such as the vestibular (Arenz et al., 2008; Bagnall et al., 2008), proprioceptive (van Kan et al., 1993), somatosensory (Jörntell and Ekerot, 2006), auditory (Lorteije et al., 2009), and visual (Azouz et al., 1997) systems, exploit a broad bandwidth of action potential frequencies to represent information as sustained rate codes. Synapses in sensory organs typically employ large, vesicle-tethering, electron-dense cytomatrix structures at their active zones (AZs), the sites where vesicles dock and fuse to release their neurotransmitter content into the synaptic cleft (Südhof, 2004). These electron-dense structures are decorated with vesicles and vary in size and shape in a species- and cell type-specific manner (Zhai and Bellen, 2004). Some extend vertically into the cytoplasm and are referred to as ribbons (Lenzi and von Gersdorff, 2001). These cytomatrix structures are thought to be critical for rapid and sustained vesicle supply at these specialized synapses, which transmit graded signals (Khimich et al., 2005; von Gersdorff et al., 1998). In contrast, central rate-coded synapses have

less prominent cytomatrix structures, but some can nevertheless maintain signaling over a wide bandwidth of action potential frequencies with a relatively small number of conventional release sites (Saviane and Silver, 2006). This is achieved by a large pool of vesicles and rapid vesicle reloading to the AZ (Saviane and Silver, 2006), but the molecular mechanisms underlying this rapid reloading are unknown.

To date, at least five protein families have been characterized whose members are highly enriched at the cytomatrix of the AZs: Munc13s, RIMs, ELKS/CAST proteins, Piccolo and Bassoon, and the liprins- α (Kaeser et al., 2009; Schoch and Gundelfinger, 2006). Bassoon is a very large coiled-coil protein of ~4000 amino acids (~400 kDa) and is one of the core components of the cytomatrix at the AZ of both excitatory and inhibitory synapses (tom Dieck et al., 1998; Wang et al., 2009). Interestingly, whereas other AZ proteins (e.g., RIMs) are present in both vertebrates and invertebrates (e.g., *C. elegans* and *Drosophila*), homologs of Bassoon and Piccolo (also named Aczonin; Wang et al., 2009) appear to be de novo developments of vertebrates (Altrock et al., 2003). At ribbon-type synapses, deletion of Exons 4 and 5 of the Bassoon gene leads to disrupted assembly of the cytomatrix at the AZ (Dick et al., 2003) as well as impaired auditory signaling (Buran et al., 2010; Khimich et al., 2005). At conventional synapses Bassoon is involved in trafficking and synaptic delivery of AZ material (Fejtova et al., 2009) and in partially silencing synapses (Altrock et al., 2003). However, the function of Bassoon in synaptic transmission remains unclear.

We investigated the role of Bassoon by comparing the properties of transmission at cerebellar mossy fiber to granule cell (MF-GC) synaptic connections in control and Bassoon null mutant (*Bsn*^{-/-}) mice. These glutamatergic synapses appear ideally suited to investigate the mechanisms of vesicle reloading because they show rapid vesicle reloading at a limited number of release sites (Saviane and Silver, 2006). In addition, MF-GC synapses are characterized by highly synchronized vesicular release (Sargent et al., 2005), a large pool of releasable vesicles (Saviane and Silver, 2006), and firing frequencies of more than 700 Hz in vivo (Rancz et al., 2007). The excellent voltage clamp afforded by the postsynaptic granule cell leads to excitatory postsynaptic currents (EPSCs) with rise and decay kinetics in the sub-millisecond range with only modest desensitization (DiGregorio et al., 2007), facilitating the analysis of high-frequency signaling.

Here, we show that spontaneous EPSCs and EPSCs evoked at low frequencies are normal at MF-GC synapses in *Bsn*^{-/-} mice

compared to those in control mice. However, the lack of Bassoon caused a pronounced depression during high-frequency transmission that occurred within milliseconds and a delayed recovery from depression. Analysis of the presynaptic and postsynaptic mechanisms of short-term plasticity revealed that the rate of vesicle reloading at AZs of MF-GC terminals was almost halved in *Bsn*^{-/-} mutants compared with controls. Thus, our data demonstrate that the cytomatrix protein Bassoon speeds high-rate vesicle reloading at AZs of a central excitatory synapse, significantly increasing the achievable rate of transmission.

RESULTS

Enhanced Synaptic Depression in Cerebellar MF-GC Synapses in *Bsn*^{-/-} Mice during Sustained Synaptic Signaling

To investigate the role of Bassoon in synaptic signaling, we developed a transgenic mouse line in which the gene encoding Bassoon was deleted (referred to as *Bsn*^{-/-}). Previous studies investigating the function of Bassoon have used a Bassoon mutant (referred to as *Bsn*^{ΔEx4/5}; Altrock et al., 2003; Figures S1–S3 and S6 available online), in which a 180 kDa Bassoon fragment of the Bassoon gene remained expressed. To confirm the absence of Bassoon in *Bsn*^{-/-} animals, we carried out genotyping and immune labeling. Immunohistochemical staining of the cerebellum of *Bsn*^{-/-} and corresponding wild-type littermates revealed normal distribution of the synaptic proteins Piccolo and Synapsin, whereas Bassoon immunoreactivity was reduced to background levels in *Bsn*^{-/-} mutants (Figure 1A). Western blot analysis of the Bassoon expression in homogenates from whole brains showed two major protein bands of 420 and 350 kDa in *Bsn*^{+/+} and *Bsn*^{+/-} representing both major isoforms of Bassoon (tom Dieck et al., 1998). In their *Bsn*^{-/-} littermates, no signal was detectable, confirming that Bassoon expression was abolished in brains of mutant animals (Figure 1B).

To analyze sustained high-frequency signaling over a broad range of frequencies observed in vivo (Jörntell and Ekerot, 2006; van Kan et al., 1993), single mossy fiber inputs to cerebellar granule cells in acute brain slices were identified by the all-or-none appearance of EPSCs in response to local stimulation of graded intensity in the tissue surrounding the granule cell (Figures S1A and S1B; Silver et al., 1996). At individual MF-GC connections in *Bsn*^{-/-} mice and their corresponding control littermates, EPSCs were elicited at frequencies of 20, 100, and 300 Hz with 100, 100, and 20 stimuli, respectively. At an individual connection, each frequency was evaluated at least once and in most cases three times, interleaved by >30 s intervals (Figure 1C). Unless stated otherwise, all experiments were performed on P20–28 mice at 37°C. To evaluate short-term plasticity during the trains, the phasic and tonic component of each EPSC were automatically determined for each EPSC (Figure 1C, lower left; Experimental Procedures; Saviane and Silver, 2006). The average phasic EPSC amplitudes normalized to the first amplitude in the trains were plotted against time for the frequencies investigated (Figure 1D), revealing that the degree of depression was comparable to previously published values estimated for MF-GC connections of rats at physiological temperatures (Saviane and Silver, 2006). However, comparing *Bsn*^{-/-}

with control revealed that the depression of the phasic EPSC amplitude was stronger in *Bsn*^{-/-} (Figure 1D). In order to further quantify this effect, the degree of synaptic depression was determined for the phasic and tonic EPSCs during the steady state (brackets in Figure 1D) for each frequency at each synaptic input. The average across all connections revealed significantly smaller phasic EPSC amplitudes during steady-state while the tonic component was not significantly changed in *Bsn*^{-/-} compared to that of controls (e.g., steady-state phasic EPSC for 300 Hz: 14.9% ± 2.0% and 9.4% ± 1.1%, for control and *Bsn*^{-/-}, n = 13 and 11, respectively, p = 0.03; Figure 1E). Indeed, the synaptic depression of the second and third EPSC amplitude in the 300 Hz train was already significantly different (second EPSC: 55% ± 8% and 32% ± 7% for control and *Bsn*^{-/-}; p < 0.05; Figure 1D). In a previous study investigating the function of Bassoon in the hippocampus of *Bsn*^{ΔEx4/5} mice at 23°C, no alteration in short-term plasticity was observed (Altrock et al., 2003). We therefore repeated the experiments at cerebellar MF-GC connections in *Bsn*^{ΔEx4/5} and control mice at 23°C, but found again significantly enhanced depression in *Bsn*^{ΔEx4/5} (Figures S1C–S1E). These data indicate that the lack of Bassoon enhanced depression within milliseconds at MF-GC connections during sustained high-frequency signaling.

Normal Basal MF-GC Transmission in *Bsn*^{-/-}

To gain insights into the mechanisms of enhanced depression in *Bsn*^{-/-}, basal low-frequency transmission and its quantal components were analyzed. The amplitudes of EPSCs elicited at 1 Hz (85 ± 17 and 85 ± 16 pA, for control and *Bsn*^{-/-}, n = 14 and 12, respectively, p = 0.8), their coefficients of variation (CV: 28% ± 4% and 29% ± 3%, p = 0.7, respectively), and their kinetic parameters (rise time: 192 ± 15 and 195 ± 12 μs, p = 0.7; weighted decay τ: 2.9 ± 0.4 and 2.4 ± 0.2 ms, p = 0.7, respectively) were not significantly different in control and *Bsn*^{-/-} mice (Figures 2A and 2B). Comparable results were obtained at *Bsn*^{ΔEx4/5} mice at 23°C (Figure S2).

The distribution of spontaneous EPSC amplitudes was slightly skewed to larger amplitudes (Figure 2C) as previously described for quantal EPSCs at this synapse (Cathala et al., 2003). A cumulative histogram of the spontaneous EPSC amplitudes from all experiments showed no statistical differences in the amplitude distribution (Figure 2D; Kolmogorov-Smirnov test: p = 0.26). The average spontaneous EPSC amplitude was similar in *Bsn*^{-/-} and controls (16.6 ± 1.4 and 17.0 ± 1.7 pA, for control and *Bsn*^{-/-}, n = 14 and 12, respectively; p = 0.97; Figure 2E). In addition, the amplitude of the spontaneous EPSCs was similar to the amplitude of previously isolated miniature EPSCs (Cathala et al., 2003), consistent with the finding that spontaneous EPSCs exhibit properties of individual quantal events at this synapse (Cathala et al., 2003). Since glutamate receptors are not saturated during a quantal event (DiGregorio et al., 2007) and quanta sum linearly over a wide range of release probabilities (Sargent et al., 2005), the quantal content (i.e., the number of vesicles per EPSC) was estimated by dividing the first evoked EPSC amplitude by the spontaneous EPSC amplitude (Del Castillo and Katz, 1954). To account for jitter in the latency of quantal release and spillover from neighboring release sites, the quantal size (q) was reduced by 14%, corresponding to the previously

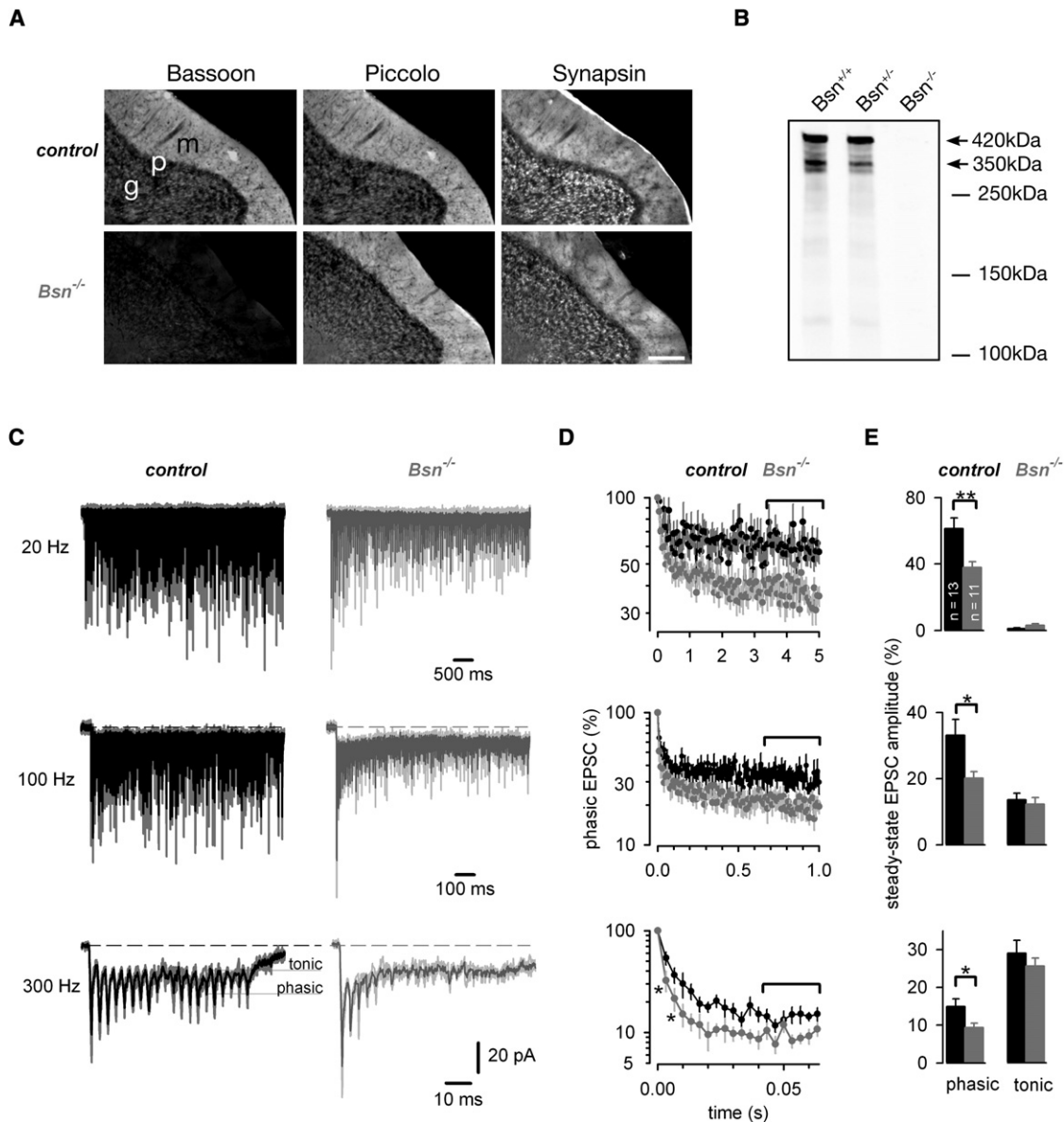


Figure 1. Enhanced Synaptic Depression in Cerebellar MF-GC Synapses in *Bsn*^{-/-} Mice during Sustained Synaptic Signaling

(A) Immunohistochemical stainings of Bassoon, Piccolo, and Synapsin in cerebellar slices of Bassoon knockout mice (*Bsn*^{-/-}, bottom) and their wild-type littermates (control, top). The granular cell (g), purkinje cell (p), and molecular layer (m) are indicated (scale bar: 100 μ m).

(B) Western blot analysis of Bassoon expression in homogenates from whole brains of *Bsn*^{+/+}, *Bsn*^{+/-}, and *Bsn*^{-/-} mice. With anti-Bassoon antibodies, two major protein bands of 420 and 350 kDa were detected in *Bsn*^{+/+} and *Bsn*^{+/-}, but not in *Bsn*^{-/-} mice.

(C) Examples of EPSCs recorded during 20 and 100 Hz (100 stimuli) and 300 Hz (20 stimuli) in one control and one *Bsn*^{-/-} MF-GC connection. For each frequency, three traces (gray) and the corresponding average (control: back; *Bsn*^{-/-}: dark gray) are superimposed. The phasic and tonic components are indicated by horizontal black lines and were automatically determined for each EPSC and each trace (see [Experimental Procedures](#)).

(D) Average phasic EPSC amplitude versus time for a 20, 100, and 300 Hz stimulation for control mice (black; n = 13) and *Bsn*^{-/-} mice (gray; n = 11; mean \pm SEM; normalized to the first EPSC within the train; asterisks indicate significant differences, p < 0.05; note the logarithmic scale).

(E) Average steady-state EPSC amplitude (see brackets in D) of phasic and tonic EPSC amplitudes in control mice (black; n = 13) and *Bsn*^{-/-} mice (gray; n = 11; mean \pm SEM; for data on *Bsn* ^{Δ Ex4/5} see [Figure S1](#)).

determined ratio of the stimulus- and rise-aligned quantal responses ([Sargent et al., 2005](#)). In *Bsn*^{-/-}, the quantal content was similar to controls (5.6 ± 0.8 and 5.5 ± 0.6 , for control and *Bsn*^{-/-}, n = 14 and 12, respectively, p = 0.6; [Figure 2E](#)).

Evoked EPSC Amplitudes Recover More Slowly from Synaptic Depression in *Bsn*^{-/-} Mice Than in Control Mice

Next, we asked whether the enhanced depression during sustained high-frequency transmission in *Bsn*^{-/-} is accompanied

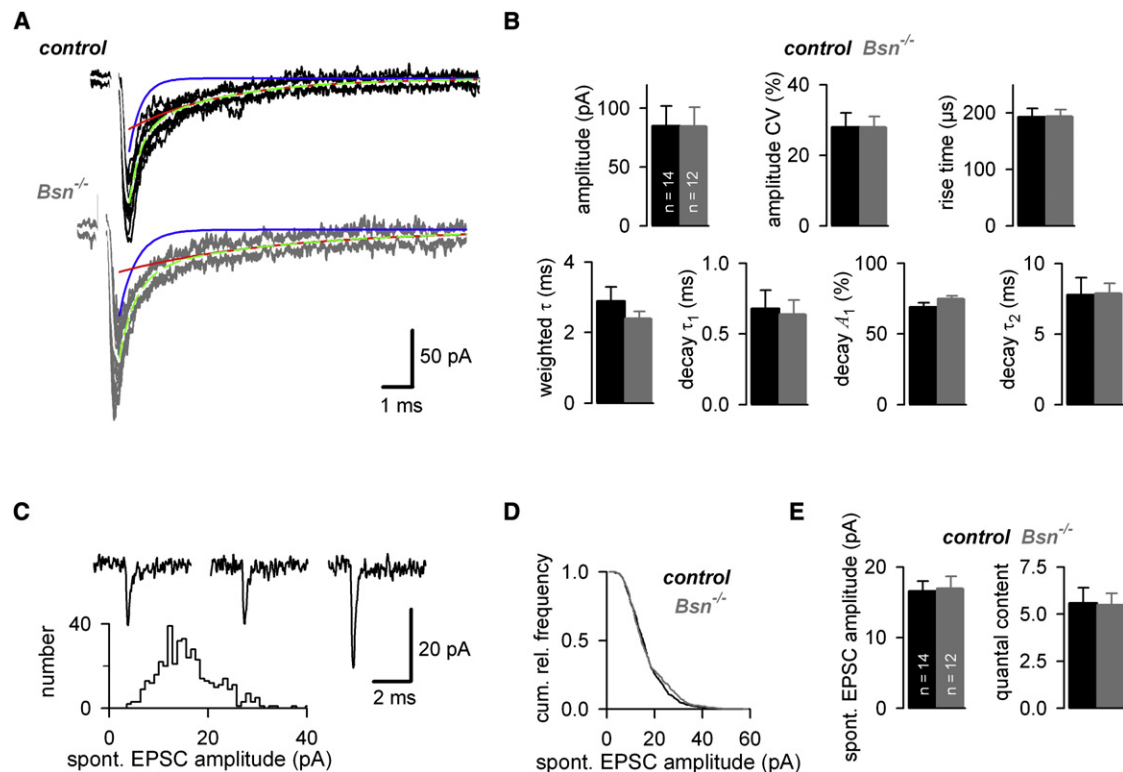


Figure 2. Basal MF-GC Transmission Is Normal in *Bsn*^{-/-}

(A) Fifteen consecutive EPSCs superimposed with the average EPSC (white) for control (top) and *Bsn*^{-/-} (bottom) mice recorded at 37°C (stimulus artifacts removed). Biexponential fits to the current decay are superimposed (single components: red and blue; sum: green dashed).

(B) Average EPSC amplitude, its coefficient of variation (CV), the 20%–80% rise time, the amplitude-weighted decay time constant, the decay time constant of the fast exponential component (τ_1), its relative amplitude (A_1), and the decay time constant of the slower exponential component (τ_2) for control (black, n = 14) and *Bsn*^{-/-} (gray, n = 12) mice.

(C) Three examples of spontaneous EPSCs and the corresponding amplitude histogram of this control experiment.

(D) Cumulative histogram of amplitudes of spontaneous EPSCs from all experiments of control mice (black) and *Bsn*^{-/-} mice (gray, Kolmogorov-Smirnov test: $p = 0.26$).

(E) Average amplitude of spontaneous EPSCs and estimated quantal content for control mice (black, n = 14) and *Bsn*^{-/-} mice (gray, n = 12; for data on *Bsn* ^{Δ Ex4/5} see Figure S2).

by alterations in the kinetics of recovery from depression. To this end, EPSCs were elicited by stimuli with increasing intervals following the 20, 100, and 300 Hz stimulation. In Figure 3A, 20 consecutive current traces (gray) of 300 Hz trains recorded in a control cell followed by stimuli of increasing interval (25 ms – 5 s) are superimposed with the average (black). The initial phase of the recovery after 300 Hz trains (Figure 3B, left) was slower in *Bsn*^{-/-} compared with control ($47\% \pm 4\%$ versus $66\% \pm 7\%$, $p < 0.05$ at 140 ms). Biexponential fits to the recovery revealed time constants of 26 and 36 ms with amplitudes of 62% and 46% for the fast component for control and *Bsn*^{-/-}, respectively, and a slower component with a time constant of ~ 2 s for both control and *Bsn*^{-/-} (see Figure S3E for the analysis of the recovery after 20 and 100 Hz stimulations).

Spontaneous EPSC Amplitudes Recover Rapidly from Depression in Both *Bsn*^{-/-} and Control Mice

To dissect presynaptic and postsynaptic components of the recovery in control and *Bsn*^{-/-}, we analyzed how rapidly the postsynaptic component of the depression, which could be

due to, for example, desensitization of glutamate receptors, recovers in *Bsn*^{-/-} and control mice. Therefore, we analyzed the amplitudes of spontaneous EPSCs during the recovery (Figures 4A and 4B). Exponential fits to data from all cells of the corresponding genotype revealed an initial reduction after 300 Hz trains to $\sim 65\%$, and a subsequent recovery within ~ 100 ms (Figures 4A and 4B). Assuming a constant amount of glutamate per spontaneously fusing vesicle, these data indicate that the q is decreased to $\sim 65\%$ during the train and recovers with a time constant of ~ 100 ms. After the 100 and 20 Hz stimulation, the average quantal size (q_0) was $\sim 73\%$ and $\sim 100\%$, respectively (data not shown). These estimates are comparable to previous estimates with 100 Hz experiments at MF-GC synapses in rats (Saviane and Silver, 2006). Furthermore, the kinetics of recovery in the 100 ms range is consistent with previous estimates of recovery from desensitization of glutamate receptors at MF-GC synapses in rats (DiGregorio et al., 2007; Xu-Friedman and Regehr, 2003). These data indicate that the differences in short-term plasticity between *Bsn*^{-/-} and controls cannot be attributed to postsynaptic mechanisms.

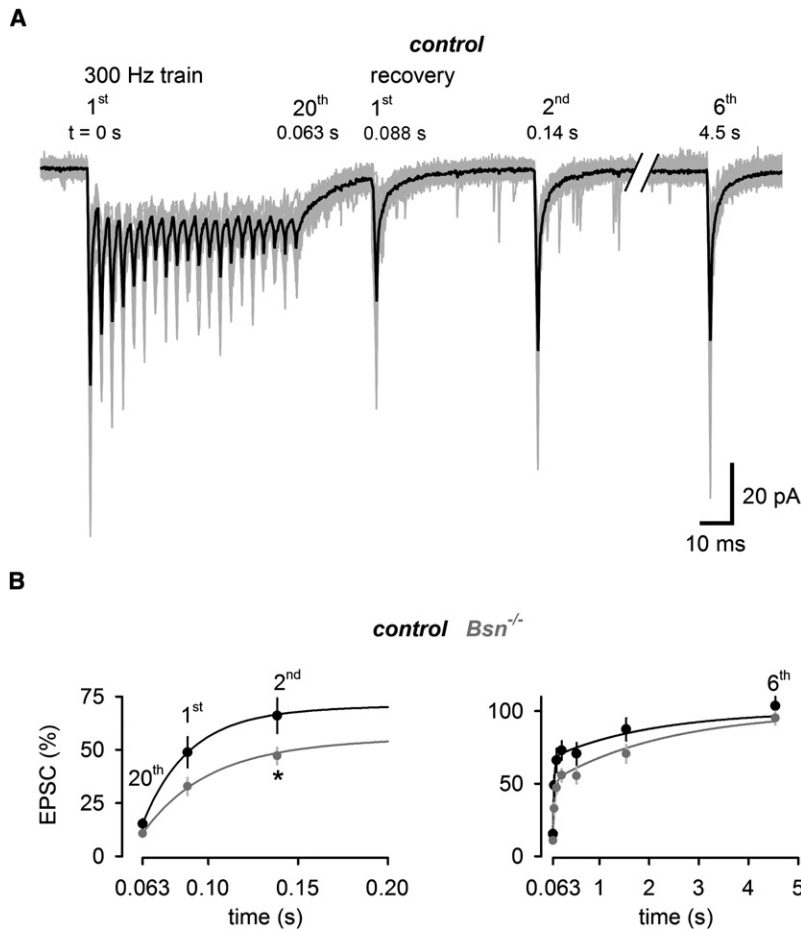


Figure 3. Evoked EPSC Amplitudes Recover More Slowly from Synaptic Depression in *Bsn*^{-/-} Mice Than in Control Mice

(A) Twenty consecutive current traces elicited by a 300 Hz train followed by test stimuli of increasing intervals (the first two and the last EPSC out of six are shown) recorded in a control mouse. The average is superimposed in black. Note the spontaneous EPSCs after the train.

(B) Average phasic amplitudes of the twentieth EPSC at the end of 300 Hz trains followed by the first and second EPSC (left) and all (first–sixth) EPSCs (right) of the recovery for control mice (black; n = 13) and *Bsn*^{-/-} mice (gray; n = 11; asterisks indicates significant differences) superimposed with biexponential fits (for recovery from 20 and 100 Hz trains and for data on *Bsn*^{ΔEx4/5}, see Figure S3).

stable during successive trains (Figure 5B). The variance of the phasic EPSC amplitudes during and after the train was plotted versus the corresponding mean amplitude (Figure 5C). Only the variance of the first and second EPSC during the recovery was significantly lower than predicted by the blue parabolic variance versus mean relationship, which is based on a constant *q* measured independently from spontaneous EPSCs in the same cell (Figure 5C). This supported the finding that the *q* recovered rapidly from depression (cf. Figure 4).

To determine the reduction in *q* during high-frequency stimulations, the *q* at the end of the train was determined from the slope of a straight line through the origin fitted to the last 15 stimuli (red line; Figure 5C) and related to the *q* determined from the spontaneous EPSCs under

From the measured postsynaptic component of short-term plasticity (i.e., the *q*) during and after high-frequency transmission, the presynaptic component of short-term plasticity could be isolated by assuming that the presynaptic and postsynaptic components multiply to give the overall short-term plasticity of the phasic EPSC amplitude (Figure 4C). The presynaptic component showed a small “overshoot” directly after the 300 Hz train, which could be due to elevated intraterminal [Ca²⁺] and thus elevated release probabilities at the end of the train. Subsequently, a slow component of the presynaptic recovery from depression was apparent (green line in Figure 4C). The dissection of presynaptic and postsynaptic mechanisms of short-term plasticity, illustrated here, was mandatory for the further mechanistic analysis.

Analysis of Presynaptic and Postsynaptic Mechanisms Underlying Short-Term Plasticity in *Bsn*^{-/-} and Control Mice

To analyze the mechanisms of the enhanced synaptic depression and slower recovery in *Bsn*^{-/-} compared with control mice, we first used fluctuation analysis of peak EPSC amplitudes, taking account of quantal variance and release jitter (Scheuss et al., 2002; Silver, 2003; Silver et al., 1998). Three-hundred-Hertz trains followed by test stimuli of increasing intervals were repetitively elicited at 30 s intervals (Figure 5A). The EPSC amplitudes were

resting conditions. The resulting reduction in *q* was 64% ± 9% and 66% ± 14% during the 300 Hz trains (n = 5 and 4, for control and *Bsn*^{-/-}, respectively; p > 0.9), consistent with the estimates of desensitization from the spontaneous EPSCs. To estimate the number of functional release sites (*N*; which can also be considered as the maximum number of readily releasable vesicles at the synaptic connection) and the initial probability of vesicular release from each site (*p_r*), the variance of the first EPSC during the train and a fixed *q* determined independently from the amplitude of the spontaneous EPSCs at that MF–GC connection (blue lines; Figure 5C) were used for the variance–mean analysis (see Experimental Procedures). The initial *p_r* was 0.55 ± 0.09 and 0.47 ± 0.04 and *N* was 7.1 ± 1.4 and 8.6 ± 2.7 (n = 5 and 4, for control and *Bsn*^{-/-}, respectively; p > 0.4). These data suggest that neither the *p_r* nor the *N* were significantly different between *Bsn*^{-/-} and control. Furthermore, the enhanced synaptic depression in *Bsn*^{-/-} was not due to enhanced postsynaptic depression in *Bsn*^{-/-}. Our data therefore suggest that the reloading of vesicles at each release site might be impaired in *Bsn*^{-/-} mice.

Estimation of Release Properties and Vesicle Reloading at MF–GC Synapses with Short-Term Plasticity Models

To quantify the kinetic properties of release and vesicular reloading, three deterministic models of short-term plasticity were

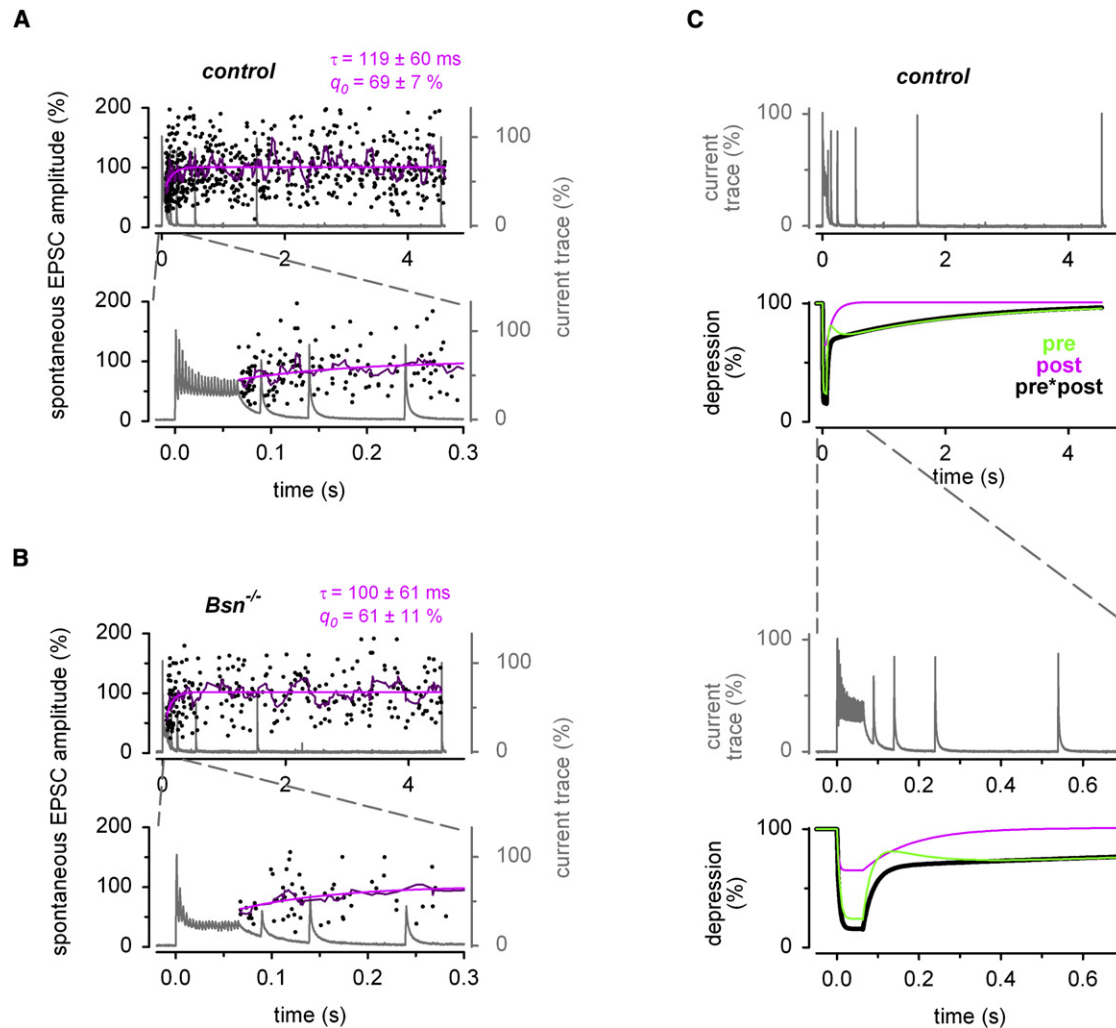


Figure 4. Spontaneous EPSC Amplitudes Recover Rapidly from Depression in Both *Bsn^{-/-}* and Control Mice

(A and B) Normalized amplitudes of spontaneous EPSCs (black) measured after the 300 Hz trains pooled across all control (A) and *Bsn^{-/-}* recordings (B). A corresponding average current trace is shown in gray (note gray scale on the right). A sliding average of 11 consecutive spontaneous EPSCs amplitudes is superimposed in dark magenta. An exponential fit to the spontaneous EPSC amplitudes is superimposed in magenta ($y(t) = 100 - (100 - q_0) \exp[-t/\tau]$). The initial amplitude of the spontaneous EPSC after the trains (q_0) and the time constant of recovery (τ) are indicated. The 624 and 261 spontaneous EPSCs were detected in 132 and 101 300-Hz traces. Note that the average frequency of spontaneous EPSCs per MF-GC connection was not significantly different (0.4 ± 0.1 and 0.6 ± 0.2 s⁻¹ for control and *Bsn^{-/-}*, $n = 13$ and 11, respectively, $p = 0.4$).

(C) Average current trace of a control 300 Hz experiment (gray). Below, the time course of the average depression of the phasic EPSC amplitude during and after the 300 Hz stimulations in control mice is plotted in black (monoexponential fit to the average depression and biexponential fit to the recovery). In addition, the corresponding postsynaptic (“post,” magenta) and presynaptic components of depression (“pre,” green) are shown.

used (Figure 6), taking into account the reduction in q during the train (cf. Figures 4 and 5). Fitting each model simultaneously to the EPSC amplitudes during and after the 300, 100, and 20 Hz data in controls gave estimates of the model parameters (see Supplemental Experimental Procedures and Hallermann et al., 2010). In the simplest possible model, a synaptic connection is characterized by a number of readily releasable vesicles (N) with a release probability (p_r) and a rate of vesicle reloading (k) from an inexhaustible reserve pool (model 1; Figure 6, green). Since model 1 could not reproduce the prominent slow component of the presynaptic recovery (Figures 6B–6D), two more

sophisticated plasticity models were tested that included Ca²⁺-dependent vesicle replenishment (model 2, blue; Dittman and Regehr, 1998; Hosoi et al., 2007) or two pools of readily releasable vesicles with different release probabilities and different kinetics of recovery (model 3, red; Neher, 2006; Sakaba and Neher, 2001). Indeed, such heterogeneous release probabilities would be consistent with the CV of the p_r previously determined at MF-GC synapses (Sargent et al., 2005). Surprisingly, the onset and recovery time courses of the EPSC amplitudes at 20, 100, and 300 Hz were equally well described by the Ca²⁺-dependent model 2 and the Ca²⁺-independent model 3

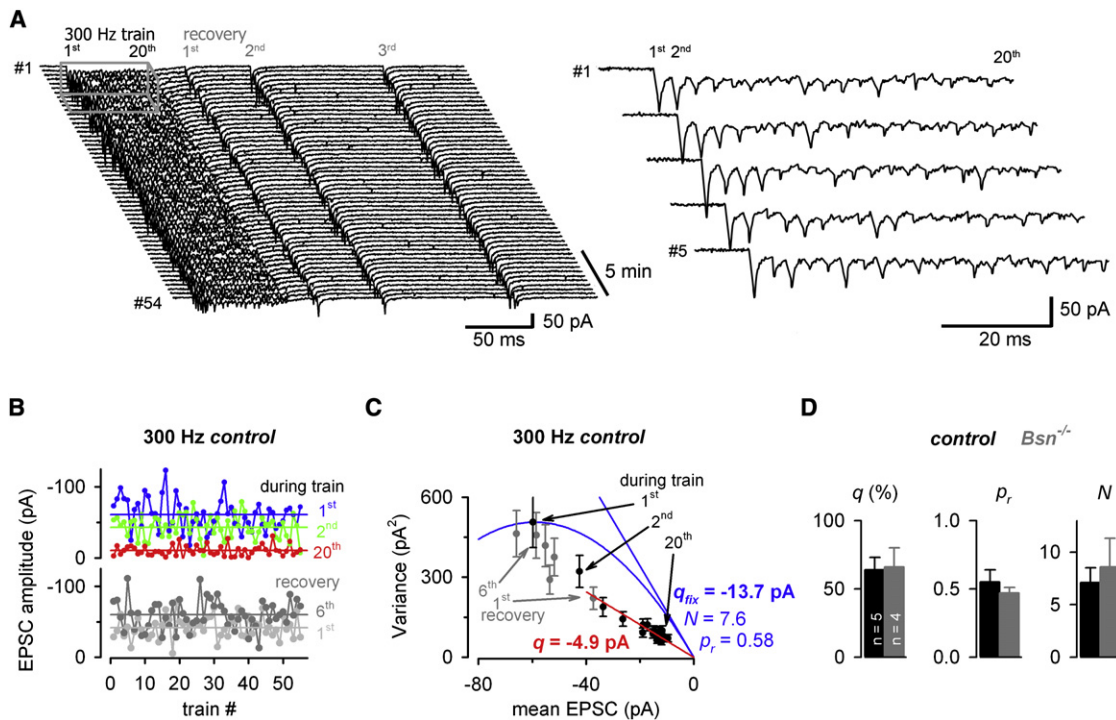


Figure 5. Estimating Quantal Parameters during Short-Term Plasticity with Fluctuation Analysis in *Bsn*^{-/-} and Control Mice

(A) Example of 54 consecutive current traces (30 s intervals) elicited by 300 Hz trains of 20 stimuli followed by test stimuli of increasing intervals (the first three out of six are shown) recorded in a control mouse. On the right, the first five traces are shown in higher resolution (cf. gray boxed area on the left; stimulus artifacts were removed for clarity).

(B) Amplitude of the first (blue), second (green), and twentieth (red) EPSC during, and the first (gray) and sixth (dark gray) EPSC after, the train plotted versus the trace number for control experiment shown in (A). The corresponding mean EPSC amplitude is indicated as a horizontal line in the corresponding color.

(C) Variance of the EPSC amplitudes during the train (black) and during the recovery (gray) plotted versus the corresponding mean for the control experiment shown above, superimposed with a parabolic fit, constrained through the origin, the first EPSC during the train, and by the quantal size (q_{fix}) determined independently from the spontaneous EPSCs measured at this connection (the blue straight line indicates the constrained initial slope q_{fix}). The resulting number of release sites (N) and resting release probability (p_r) are indicated. A linear fit (red) to the last 15 EPSCs during the train constrained through the origin reveals the quantal size during the train (q).

(D) Average data for control and *Bsn*^{-/-} experiments ($n = 5$ and 4 , respectively).

(Figures 6B–6D; see Supplemental Discussion and Figure S4 for a detailed explanation of the models).

To further test the robustness of the models, we examined how well they predicted the onset and recovery of EPSC depression when the extracellular Ca^{2+} concentration ($[Ca^{2+}]_e$) was lowered to 1.25 mM (Figures 6E–6H). For each MF-GC connection, the EPSC amplitudes were normalized to the amplitude measured in 2 mM $[Ca^{2+}]_e$ at the beginning of the experiment. Lowering $[Ca^{2+}]_e$ reduced the amplitudes of the first EPSC in the train to $52\% \pm 6\%$ and $47\% \pm 4\%$ for control and *Bsn*^{-/-} ($n = 6$ and 5 , respectively; Figure 6F), suggesting that the initial p_r was reduced by $\sim 50\%$. Note that under these conditions the depression during 300 Hz trains was not significantly different between *Bsn*^{-/-} and control (steady-state phasic EPSC: $12\% \pm 3\%$ and $9\% \pm 2\%$, for control and *Bsn*^{-/-}, $n = 6$ and 5 , respectively, $p = 0.4$; Figures 6F and 6G). After simply scaling down the initial p_r by a factor of two and with all other fit parameters held constant at the best-fit parameters obtained with 2 mM $[Ca^{2+}]_e$, all three models predicted the time course of the 300 Hz train experiments in 1.25 mM $[Ca^{2+}]_e$ well (Figure 6H).

Thus, without further parameter adjustment, the experiments in low $[Ca^{2+}]_e$ were captured well by the Ca^{2+} -dependent and Ca^{2+} -independent vesicle reloading models.

We then tested the validity of the model parameters by comparing the quantal content estimated from the models to the quantal content estimated directly from the ratio of the evoked EPSC and quantal amplitude (cf. Figure 2E) for each MF-GC connection. Figure 7A shows an example of an individual recording from a control animal. As shown in Figure 7B, there was a close to unitary relationship between the quantal content estimated from model 3 and that measured directly from the same MF-GC connections at both 23°C and 37°C. Furthermore, the predicted CV of an evoked EPSC, with the quantal parameters estimated from the fit of model 3 (which itself is deterministic, see Equation 6 in Supplemental Experimental Procedures), corresponded well to that measured directly from the same MF-GC connections at both 23°C and 37°C (Figure 7B; Del Castillo and Katz, 1954; see Figure S5 for comparable tests of model 1 and 2).

In summary, we used three release models that captured the time course of depression and recovery over a broad range of

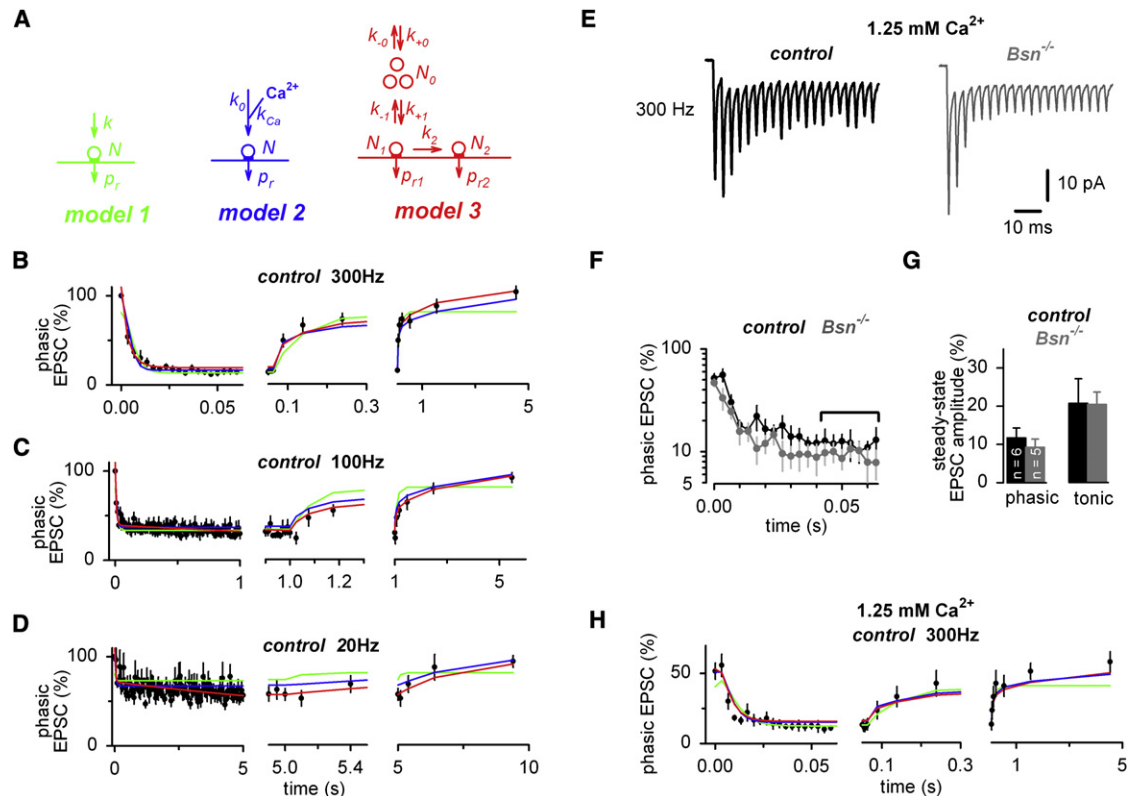


Figure 6. Estimating Quantal Parameters and the Kinetics of Vesicle Reloading at MF-GC Synapses with Three Short-Term Plasticity Models

(A) In model 1, a MF-GC connection is characterized by N release sites with a release probability, p_r , and a rate of vesicle reloading, k . In model 2, the rate of vesicle reloading, k_0 , is nonlinearly accelerated by the residual Ca^{2+} concentration with the maximal rate, k_{Ca} . In model 3, a MF-GC connection is characterized by N_1 and N_2 release sites with low and high release probability, p_{r1} and p_{r2} , respectively. Vesicles in N_1 are in equilibrium with a pool of N_0 releasable vesicles.

(B) Average phasic EPSC amplitudes of 300 Hz control experiments at 37°C superimposed with predictions of model 1, 2, and 3 in green, blue, and red, respectively. Model 1 underestimates the first EPSC amplitude and therefore does not recover to 100%. Note three different partially overlapping timescales (left: during the train, middle: end of train and beginning of recovery, right: complete 5 s lasting recovery).

(C and D) Corresponding graphs for 100 and 20 Hz control trains (see Figure S4 for more details).

(E) Examples of EPSCs recorded during 300 Hz stimulation (20 stimuli) in control and $Bsn^{-/-}$ MF-GC connections with 1.25 mM $[\text{Ca}^{2+}]_e$ (average of ~20 traces each; control: black; $Bsn^{-/-}$: dark gray).

(F) Average phasic EPSC amplitudes of 300 Hz trains at 1.25 mM $[\text{Ca}^{2+}]_e$ normalized to the basal EPSC amplitude recorded at 2 mM $[\text{Ca}^{2+}]_e$ in each connection for control mice (black; $n = 6$) and $Bsn^{-/-}$ mice (gray; $n = 5$; note the logarithmic scale).

(G) Average phasic and tonic steady-state EPSC amplitudes in 300 Hz trains at 1.25 mM $[\text{Ca}^{2+}]_e$ for control mice (black; $n = 6$) and $Bsn^{-/-}$ mice (gray; $n = 5$).

(H) Average phasic EPSC amplitudes of 300 Hz control experiments recorded with 1.25 mM $[\text{Ca}^{2+}]_e$ superimposed with the predictions of model 1, 2, and 3 in green, blue, and red, respectively, in which the release probabilities were scaled down by a factor of 2.

transmission frequencies and release probabilities with varying degrees of accuracy. Despite different degrees of complexity of the models, the estimated quantal parameters predict both the quantal content and the EPSC variability, indicating that they provide a reasonable estimate of the p_r , the N , and the k during and following EPSC trains across a wide range of frequencies.

Comparison of Vesicular Reloading and Release in Control, $Bsn^{-/-}$, and $Bsn^{\Delta Ex4/5}$ mice

To examine the mechanisms underlying the enhanced EPSC depression in $Bsn^{-/-}$ mice, we next used the models to estimate synaptic parameters from train experiments at MF-GC connections in $Bsn^{-/-}$ mice (for $Bsn^{\Delta Ex4/5}$, see below). An example of such an individual experiment is superimposed with the corre-

sponding predictions of model 3 in Figure 7C. As for the control case, the tests of robustness revealed that the synaptic parameters estimated with model 3 and the predicted CV for the $Bsn^{-/-}$ mice matched well to that measured directly from the same MF-GC connections (Figure 7D; see Figure S5 for corresponding tests for model 1 and 2).

Comparison of the presynaptic parameters determined from individual MF-GC connections of $Bsn^{-/-}$ and control mice revealed that the p_r and the N were similar in $Bsn^{-/-}$ and control MF-GC connections, confirming the estimates with fluctuation analysis in a subset of experiments (cf. Figure 5). However, the rate of vesicle reloading at each release site during sustained high-frequency transmission was significantly reduced in $Bsn^{-/-}$ compared with control MF-GC connections, independent of the model of vesicle reloading (Figures 8A and S6). For model 3, the

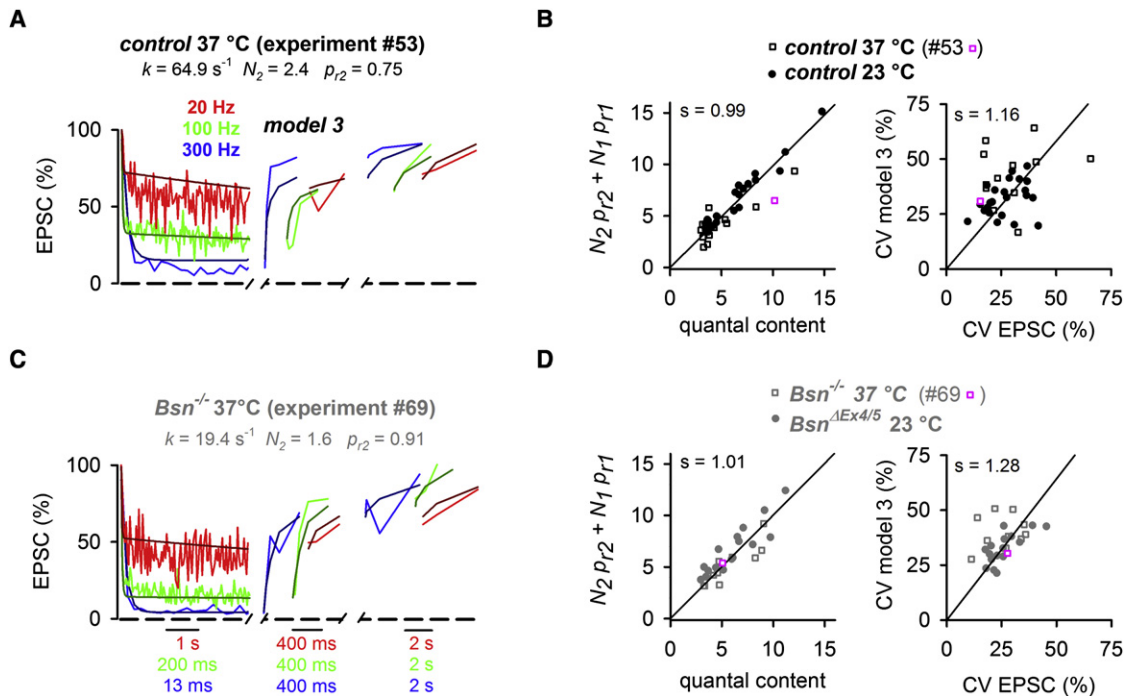


Figure 7. Testing the Robustness of Presynaptic Parameters Estimated with a Short-Term Plasticity Model at Individual MF-GC Connections

(A) Examples of EPSC amplitudes recorded at an individual MF-GC connection in a control mouse at 37°C (20 Hz: red; 100 Hz: green; 300 Hz: blue) superimposed with the corresponding predictions of model 3 (dark colors, best-fit parameters are indicated). The recovery is shown on two different, nonoverlapping timescales and shifted horizontally. Note the color-coded timescales in (C).

(B) Quantal content and coefficient of variation (CV) of EPSC amplitudes at 1 Hz stimulation (cf. Figure 1) correlated to the predictions of the model 3 for each individual control connection at 37°C (open symbols) and 23°C (closed symbols), respectively (examples in A are highlighted in pink). For calculation of CV, see Equation 6 in Supplemental Experimental Procedures. Linear fits (constrained through the origins) had slopes (s) as indicated in the graphs (nonparametric Spearman correlation coefficient, $r = 0.9$ and 0.3 with $p < 0.0001$ and $p = 0.07$, for quantal content and CV, respectively).

(C) Corresponding example as shown in (A) for $Bsn^{-/-}$.

(D) Corresponding data as shown in (B) for $Bsn^{-/-}$ (nonparametric Spearman correlation coefficient, $r = 0.9$ and 0.5 with $p < 0.0001$ and $p = 0.008$, for quantal content and CV, respectively). See Figure S5 for corresponding test of model 1 and 2.

average rate of vesicle reloading across individual MF-GC connections was 70 ± 28 and $29 \pm 4 \text{ s}^{-1}$ in control and $Bsn^{-/-}$ ($p = 0.02$, $n = 13$ and 11 , respectively) (right panel, Figure 8A). Fits to the average data revealed 61 and 27 s^{-1} in control and $Bsn^{-/-}$ mice, respectively (see Figures S6E and S6F). The consistency of the values determined from individual MF-GC connections with those from the average data further supports our approach of analyzing individual MF-GC connections to uncover significant differences and revealed that the rate of vesicle reloading in $Bsn^{-/-}$ MF-GC connections was halved. The number of readily releasable vesicles (N_1 and N_2) and the release probabilities (p_{r1} and p_{r2}) were on average not significantly different ($p > 0.3$ for N_1 and N_2 and $p > 0.6$ for p_{r1} and p_{r2} , Figures S6E and S6F). A significant reduction in vesicle reloading rate in $Bsn^{-/-}$ mice compared to control was also obtained with the two other models (Figure 8A) in which the other parameters were also unchanged (Figures S6A–S6D).

In a previous study investigating the function of Bassoon in $Bsn^{\Delta Ex4/5}$ mutants, in which a 180 kDa Bassoon fragment was still expressed (Altrock et al., 2003), no comparable alterations in short-term plasticity were found in the hippocampus. To analyze possible functions of this fragment, we repeated the

experiments with $Bsn^{\Delta Ex4/5}$ mutant mice at 23°C (the temperature used by Altrock et al., 2003). However, the observed phenotype was very similar to the experiments with $Bsn^{-/-}$ mice at 37°C (see Figures S1–S3). Again, the mechanistic analysis revealed unaltered p_r and N but a reduced k in $Bsn^{\Delta Ex4/5}$ mutant mice at 23°C compared to controls at 23°C (Figures 8A and S6). In controls at 23°C, the p_r and the N were similar to controls at 37°C; however, the k was reduced at 23°C (temperature coefficient $Q_{10} = 1.2$ and 1.3 , for control and $Bsn^{\Delta Ex4/5}$). These results are consistent with the findings obtained at the calyx of Held, where an increase in temperature resulted in a similar p_r and vesicle pool size but accelerated vesicle recruitment (Kushmerick et al., 2006). Thus, in contrast to the finding by Altrock et al. (2003) that the absence of Bassoon partially silences hippocampal synapses, our results at physiological and room temperature indicate that Bassoon is required for efficient vesicle reloading at AZs of cerebellar MF-GC synapses.

DISCUSSION

In this study, electrophysiological analysis of a well-characterized conventional central excitatory synapse allowed us to

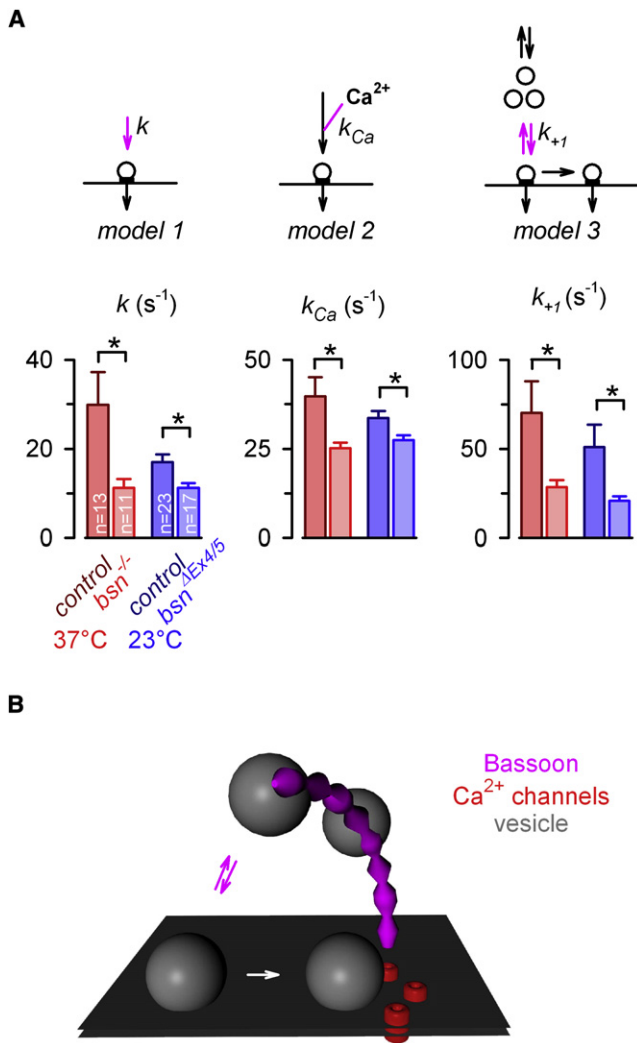


Figure 8. Slower Vesicle Reloading in *Bsn*^{-/-} and *Bsn*^{ΔEx4/5} Mice as Compared with Control Mice

(A) The rates k , k_{Ca} , and k_{+1} , which are highlighted in pink in model 1, 2, and 3, respectively, determine the speed of vesicle reloading during activity. The average reloading rates of the individual MF-GC connections are shown for the indicated temperatures and genotypes. While the remaining free parameters of the models for each MF-GC connection were on average unaltered (see Figure S6), the vesicle reloading rates were significantly reduced in *Bsn*^{-/-} (37°C, red) and *Bsn*^{ΔEx4/5} (23°C, blue) compared with those of corresponding control mice.

(B) Illustration of the hypothesized function of Bassoon at conventional AZs. Our data show that Bassoon speeds the rapid vesicle reloading at AZs during high-frequency transmission (pink arrows). The basal synaptic transmission and the slower component of recovery from depression, which might be limited by the maturation of vesicles closer to the Ca²⁺ channels (white arrows), appeared normal in the absence of Bassoon. Based on the comparison with electron-dense structures at ribbon-type synapses and recent high-resolution anatomical studies at conventional synapses (see Discussion), we hypothesize that the large protein Bassoon builds, anchors, or organizes the proper assembly of “miniribbons,” which speed vesicle reloading at conventional synapses.

isolate a specific function of the large cytomatrix protein Bassoon. The lack of Bassoon enhanced the depression of release within milliseconds during high-frequency transmission at MF-GC synapses; however, basal transmission was normal. Presynaptic and postsynaptic mechanisms of short-term plasticity were analyzed with quantal EPSC analysis, EPSC fluctuation analysis, and short-term plasticity models of vesicle release and reloading during and following high-frequency stimulation. While the p_r , the N , and the postsynaptic component of short-term plasticity were unaltered, the k was halved in Bassoon mutants. Thus, we have identified an AZ protein that speeds vesicle reloading at a conventional synapse.

Slow and Rapid Vesicle Recruitment at MF-GC Synapses

Our main result is that rapid reloading of vesicles at the MF-GC synapse (Saviane and Silver, 2006) depends on the presence of Bassoon, indicating that this cytomatrix protein is responsible for or takes part in rapid vesicle loading. Our analysis of the recovery from high-frequency synaptic transmission also identified a second presynaptic recovery component on a much slower timescale (time constants of ~2 s; Figures 3 and S3). Postsynaptic desensitization could not account for this component, since the amplitude of the spontaneous EPSCs recovered with a much faster time constant (~100 ms time, Figure 4). Our models suggest that the fast and slow components of recovery in release could arise from a steep and nonlinear dependence of vesicle reloading rate on intraterminal Ca²⁺ concentration (model 2; Dittman and Regehr, 1998; Hosoi et al., 2007). However, EPSC depression during trains of different frequencies and the subsequent recovery, together with behavior at low [Ca²⁺]_e, were equally well described by model 3, in which reloading was Ca²⁺ independent. For this model the slow recovery component was mediated by a small subpopulation of vesicles with a high p_r , which recovered slowly (Neher, 2006; Sakaba and Neher, 2001). Such a nonuniform p_r is consistent with the results of multiple probability fluctuation analysis at this synapse (Sargent et al., 2005). The slow recovery component was hardly affected by the lack of Bassoon (Figures 3 and S3), suggesting that Bassoon or a protein network relying on Bassoon supports the rapid reloading of vesicles that are less tightly coupled to Ca²⁺ channels and that a subsequent slower maturation step could produce tighter Ca²⁺ secretion coupling (see Figure 8B).

Rate-Limiting Steps during High-Frequency Transmission

Although rapid release of a large number of synaptic vesicles has been described at several synapses (Hallermann et al., 2003; Hosoi et al., 2007; Saviane and Silver, 2006; von Gersdorff et al., 1998), the underlying molecular mechanisms remain debated. MF-GC synapses can signal over a wide bandwidth, which is ultimately limited by the vesicle reloading speed at a relatively small number of conventional release sites. Vesicle reloading is an integral component of the synaptic vesicle cycle that involves many steps (Neher and Sakaba, 2008; Südhof, 2004), including the clearing of the release site from the previous fusion event and the translocation, docking, and priming of the next transmitter-laden vesicle close to Ca²⁺ channels. Which of these processes are rate limiting during high-frequency

transmission remains unclear (Neher and Sakaba, 2008). In the following, different possible molecular functions of Bassoon will be discussed in the light of our findings.

Potential Molecular Functions of the Cytomatrix Protein Bassoon at AZs

Bassoon could accelerate vesicle reloading by regulating the number of vesicles clustered near the AZ to accommodate a reservoir of primed releasable vesicles, as has been proposed for the prototypical large ribbons at sensory synapses (von Gersdorff et al., 1998; Zhai and Bellen, 2004). Recent evidence obtained at the calyx of Held indicates that clearing of release sites after the fusion of a vesicle is also an important step limiting repetitive release (Hosoi et al., 2009; Kim and von Gersdorff, 2009; Neher and Sakaba, 2008; Young and Neher, 2009). Impairments of the function of the endocytotic protein Dynamin in both vertebrates and invertebrates (Hosoi et al., 2009; Kawasaki et al., 2000) lead to results similar to the ones observed in this study. This would be consistent with a role of Bassoon in Dynamin-related endocytosis. Bassoon could also support the clearance of release sites near Ca^{2+} channels by binding to, for example, RIM1 (Wang et al., 2009), which interacts with the β -subunits of voltage-gated Ca^{2+} channels (Kiyonaka et al., 2007). However, given that Bassoon has a large cytoplasmic component that could interact with intact vesicles, and that our data suggest it speeds the fast reloading and recovering of a population of low-release-probability vesicles, it seems more likely that it is involved in enhancing vesicle supply as outlined in the following.

Filamentous cytomatrix structures that link vesicles to the AZ membrane have been identified with high-resolution techniques at AZs of conventional synapses (Fernández-Busnadiego et al., 2010; Siksou et al., 2007). Furthermore, synaptic vesicles were found to be linked to the AZ by short and long tethers (Fernández-Busnadiego et al., 2010). While short tethers were absent in samples treated with tetanus toxin, indicating that they consist of SNARE proteins, longer tethers were retained after mild synaptic stimulation, suggesting that they are involved in earlier steps of release. These long tethers might be built or anchored by the large cytomatrix protein Bassoon (see Figure 8B, Gundelfinger et al., 2003). Consistently, immunocytochemistry revealed Bassoon immuno-gold labeling at filaments emanating from the plasma membrane at the AZ (Siksou et al., 2007). Furthermore, Bassoon clusters overlapped with synaptic vesicle clusters in 3D confocal analysis of AZs at the calyx of Held (Dondzillo et al., 2010). In addition, Bassoon and Piccolo double knockout mutants showed impaired vesicle clustering at AZs (Mukherjee et al., 2010). Bassoon might directly bind to vesicles via, for example, interaction with PRA1 and Rab3 (Schoch and Gundelfinger, 2006) or anchor cytomatrix structures that bind to vesicles (Dick et al., 2003). Thus, the comparison with electron-dense structures at ribbon-type synapses suggests that the large protein Bassoon could serve as, or organize the proper assembly of, a “mini-ribbon” that tethers vesicles and speeds vesicle reloading at conventional synapses (Figure 8B; Verhage and Toonen, 2007).

Interestingly, the number and the size of Bassoon clusters increases during early postnatal development at the calyx of Held synapse (Dondzillo et al., 2010). Thus, immature calyces

might functionally correspond to $Bsn^{-/-}$ mutants. In fact, detailed analysis (Taschenberger et al., 2002) indicated that mature calyces can maintain a 80%–90% higher sustained release than immature calyces, a fact only partially explained by their increased number of readily releasable vesicles (29%, consistent with 25% more ultrastructurally docked vesicles) but also by accelerated release of “undocked” vesicles (Taschenberger et al., 2002). These data correspond well to our finding of impaired release during sustained stimulation at $Bsn^{-/-}$ MF-GC connections. Thus, together with other filamentous AZ proteins, such as Septin 5, which overlapped with Bassoon only in immature calyces (Yang et al., 2010), the developmentally regulated accumulation of Bassoon at AZs may account for part of the functional maturation of the calyx, or at least correlate with it.

Comparison of the Synaptic Function of Bassoon at Conventional and Ribbon-Type Synapses

The function of Bassoon has been investigated at ribbon-type synapses of cochlear inner hair cells (Buran et al., 2010; Khimich et al., 2005), which can sustain high rates of neurotransmitter release (Pangršić et al., 2010). At inner hair cell synapses of Bassoon mutant mice, synchronous vesicular release was impaired because of a reduction in the number of release sites and an impaired vesicle replenishment (Buran et al., 2010; Khimich et al., 2005; Frank et al., 2010). At MF-GC connections we found no clear indications for a reduction in the number of release sites, which suggests that the mechanisms defining the number of release sites differ in ribbon-type and conventional synapses. At conventional synapses, short-term plasticity during 10 and 50 Hz stimulation was normal at autaptic hippocampal primary cultures of $Bsn^{\Delta Ex4/5}$ mutants (Altrock et al., 2003). Furthermore, in a recent study investigating Piccolo and Bassoon double mutants (Mukherjee et al., 2010), no alterations in short-term plasticity during 10 Hz stimulation were observed at excitatory and inhibitory synapses of cultured neurons. However, a significantly enhanced depression was observed during 14 Hz stimulation at hippocampal Schaffer collateral to CA1 pyramidal cell synapses in acute brain slices of Piccolo knockout mice (Mukherjee et al., 2010). Thus, while at hippocampal synapses and synapses of cultured neurons the Bassoon phenotype of impaired vesicle reloading seems moderate or not apparent at all (Altrock et al., 2003; Mukherjee et al., 2010), a robust effect was observed at MF-GC synapses. These discrepancies may be partially due to the experimental approach (high-frequency transmission at individual synaptic connections in acute brain slices versus 10–50 Hz transmission at [autaptic] cell cultures). However, it is equally likely that the type of synapse investigated explains the discrepancies: impaired vesicle reloading would not be detected at synapses at which vesicle reloading is not rate limiting. The latter explanation is further supported by experiments with reduced $[\text{Ca}^{2+}]_e$. Due to the high p_r of MF-GC synapses, the readily releasable pool is quickly depleted, and vesicle reloading is expected to become quickly rate-limiting during high-frequency transmission. In experiments with lower $[\text{Ca}^{2+}]_e$ and thus lower p_r , the phenotypic differences between $Bsn^{-/-}$ and control appeared smaller and were not significantly different (Figures 6E–6G). In

summary, these data indicate that synapses that possess high demands on sustained release, such as cerebellar MF-GC and ribbon-type synapses, rely on the function of the cytomatrix protein Bassoon for efficient vesicle reloading.

Implications for Information Processing

It has been reported that proprioceptive mossy fibers of the lateral reticular nucleus and the cuneocerebellar tract can fire at up to 1 kHz under appropriate peripheral activation (see references in Jörntell and Ekerot, 2006). Recently, whole-cell recordings from granule cells in vivo also indicated firing frequencies of mossy fibers at 1 kHz (Jörntell and Ekerot, 2006) and whole-cell recordings directly from mossy fibers in vivo revealed frequencies of more than 700 Hz (Rancz et al., 2007). Other cells, such as interneurons in the cat striate cortex, show comparable firing frequencies in vivo (>500 Hz; Azouz et al., 1997). Here we demonstrated that the lack of Bassoon almost halved the rate of vesicle reloading at AZs of MF-GC synapses. Our findings predict that Bassoon increases the bandwidth of rate-coded signaling and thus the fidelity of information transmission at synapses that fire at high rates. Moreover, short-term depression during high-frequency transmission enables neurons to respond to changes in firing rate rather than absolute rate and can enable inhibition-mediated neuronal gain control (Rothman et al., 2009). By reducing frequency-dependent short-term depression, Bassoon will also shift the frequency range for synaptic and neuronal gain modulation, thereby allowing multiplicative scaling of rate-coded inputs at faster timescales. Thus, the de novo development of vertebrates (Altrock et al., 2003), Bassoon, seems to be a critical component for AZs to increase their speed limit.

In summary, the combination of genetic tools and functional characterizations of presynaptic and postsynaptic mechanisms of a specific high-fidelity synapse allowed us to link rapid vesicle reloading at a conventional synapse with the function of the AZ protein Bassoon. Our data indicate that Bassoon speeds vesicle reloading at excitatory synapses of the vertebrate brain.

EXPERIMENTAL PROCEDURES

Mutant Animals

Mutant mice carrying a gene-trapped allele of the *Bassoon* gene were derived from Omnibank ES cell line OST486029 by Lexicon Pharmaceuticals, Inc. (The Woodlands, TX). In this line, the gene trapping of *Bassoon* was achieved by insertion of gene trapping vector VICTR 48 into Introns 1–2. Homozygous Bassoon mutant mice are here referred to as *Bsn*^{-/-} and their wild-type littermates as *Bsn*^{+/+} or controls. Bassoon mutant mice lacking the central part of the protein encoded by Exons 4 and 5 of the Bassoon gene (Altrock et al., 2003) were used for the experiments at 23°C (here referred to as *Bsn*^{ΔEx4/5}). The mice exhibit a mixed genetic background of C57BL/6J and 129/SvEmsJ strains, which is controlled by using sustained C57BL-backcrossed and 129 inbred mice to breed the heterozygous parents. The mice, bred at the Leibniz Institute for Neurobiology in Magdeburg, Germany, were between 20 and 28 days of age at the time of the experiments. Experiments were performed in an interleaved manner with the corresponding controls.

Immunoblotting and Immunohistochemistry

Western blotting and immunohistochemical staining were performed similarly to that described previously (Altrock et al., 2003). Rabbit anti-Bassoon antibody (SAP7f; tom Dieck et al., 1998) was used for immunodetection. For details, see Supplemental Information.

Electrophysiology

Acute cerebellar brain slices were prepared similarly to those described previously (Edwards et al., 1989). The recording temperature was either 23°C ± 1°C in experiments with *Bsn*^{ΔEx4/5} mutants or 37°C ± 0.5°C (temperature controller TC-324B, Warner Instruments Corporations, Hamden, CT) in experiments with *Bsn*^{-/-} mutants. See Supplemental Information for a detailed description of the electrophysiological recording conditions.

During trains of stimuli, the phasic amplitude of each EPSC of each train was detected with procedures written in Igor Pro 6.1 (Wavemetrics, Lake Oswego, OR) as the peak EPSC amplitude within a window of 1–2 ms after the stimulation artifact measured relative to a baseline (tonic component) of 0.1–0.5 ms preceding the pulse (Saviane and Silver, 2006). For each connection, the phasic and tonic steady-state amplitudes were determined as the average of the phasic and tonic amplitude of the last third of the EPSCs during the trains (indicated by the brackets in Figures 1D and 6F). For each genotype, the steady-state amplitude was subsequently averaged across all connections (Figure 1E). The EPSCs recorded here in mice were on average larger than the EPSCs recorded previously in rats (Sargent et al., 2005), but within the range of values previously obtained. Besides the species differences, a selection bias for inputs that did not exhibit failures could explain the differences. Interestingly, the normal basal EPSC amplitudes were slightly though not significantly reduced in *Bsn*^{ΔEx4/5} mutant (Figure S1B) as observed in hippocampal cell cultures (Altrock et al., 2003), which could represent a dominant-negative effect of the 180 kDa Bassoon fragment remaining in *Bsn*^{ΔEx4/5} mutant. Alternatively, a reduction in the basal EPSC amplitude of Bassoon mutants might have been not detected in this study at MF-GC synapses because of the mentioned bias for inputs without failures.

Analysis of Presynaptic and Postsynaptic Mechanisms of Short-Term Plasticity

The spontaneous EPSCs were detected with a template-matching algorithm (Clements and Bekkers, 1997) applied directly after the trains, during the recovery (Figure 4). All amplitudes of spontaneous EPSCs following the corresponding trains were normalized to the spontaneous EPSC amplitude under resting conditions, plotted versus time and fitted monoexponentially. As an alternative approach, we estimated the reduction in *q* during 300 Hz trains with EPSC fluctuation analysis in a similar manner to that formerly reported (Scheuss et al., 2002; Silver, 2003; Silver et al., 1998). See Supplemental Information for a detailed description of the fluctuation analysis and of the short-term plasticity models (Hallermann et al., 2010).

Statistical Analysis

The nonparametric Mann-Whitney-U rank sum test was used for statistical analysis unless otherwise noted. The data are reported either as mean ± SEM or as box plots with the middle line, box boundaries, and whiskers indicating the median, the 25%, 75%, 10%, and 90% quantiles, respectively. Analyses were carried out with Igor Pro 6.1 and SigmaPlot (Systat Software, Erkrath, Germany). *n* indicates the sample number and *p* denotes the significance of a Mann-Whitney-U test (**p* < 0.05, ***p* < 0.01).

SUPPLEMENTAL INFORMATION

Supplemental Information for this article includes six figures, Supplemental Experimental Procedures, and a Supplemental Discussion and can be found with this article online at doi:10.1016/j.neuron.2010.10.026.

ACKNOWLEDGMENTS

We would like to thank Dr. Erwin Neher for helpful discussions and for critically reading the manuscript, and Gudrun Bethge and Bettina Kracht for expert technical assistance. This work was supported by a *formel.1* grant from the Medical Faculty of the University of Leipzig to S.H. and from the DFG to E.D.G. (SFB 779/B9), J.E., and H.S. (EI 342/4-1). R.A.S. is in receipt of a Wellcome Trust Senior Research Fellowship in Basic Biomedical Science. R.A.S. and E.D.G. are supported by the European Commission (Marie Curie Training Network “BrainTrain”).

Accepted: October 11, 2010
Published: November 17, 2010

REFERENCES

- Altrock, W.D., tom Dieck, S., Sokolov, M., Meyer, A.C., Sigler, A., Brakebusch, C., Fässler, R., Richter, K., Boeckers, T.M., Potschka, H., et al. (2003). Functional inactivation of a fraction of excitatory synapses in mice deficient for the active zone protein bassoon. *Neuron* 37, 787–800.
- Arenz, A., Silver, R.A., Schaefer, A.T., and Margrie, T.W. (2008). The contribution of single synapses to sensory representation in vivo. *Science* 321, 977–980.
- Azouz, R., Gray, C.M., Nowak, L.G., and McCormick, D.A. (1997). Physiological properties of inhibitory interneurons in cat striate cortex. *Cereb. Cortex* 7, 534–545.
- Bagnall, M.W., McElvain, L.E., Faulstich, M., and du Lac, S. (2008). Frequency-independent synaptic transmission supports a linear vestibular behavior. *Neuron* 60, 343–352.
- Buran, B.N., Strenzke, N., Neef, A., Gundelfinger, E.D., Moser, T., and Liberman, M.C. (2010). Onset coding is degraded in auditory nerve fibers from mutant mice lacking synaptic ribbons. *J. Neurosci.* 30, 7587–7597.
- Cathala, L., Brickley, S., Cull-Candy, S., and Farrant, M. (2003). Maturation of EPSCs and intrinsic membrane properties enhances precision at a cerebellar synapse. *J. Neurosci.* 23, 6074–6085.
- Clements, J.D., and Bekkers, J.M. (1997). Detection of spontaneous synaptic events with an optimally scaled template. *Biophys. J.* 73, 220–229.
- Del Castillo, J., and Katz, B. (1954). Quantal components of the end-plate potential. *J. Physiol.* 124, 560–573.
- Dick, O., tom Dieck, S., Altrock, W.D., Ammermüller, J., Weiler, R., Garner, C.C., Gundelfinger, E.D., and Brandstätter, J.H. (2003). The presynaptic active zone protein bassoon is essential for photoreceptor ribbon synapse formation in the retina. *Neuron* 37, 775–786.
- DiGregorio, D.A., Rothman, J.S., Nielsen, T.A., and Silver, R.A. (2007). Desensitization properties of AMPA receptors at the cerebellar mossy fiber granule cell synapse. *J. Neurosci.* 27, 8344–8357.
- Dittman, J.S., and Regehr, W.G. (1998). Calcium dependence and recovery kinetics of presynaptic depression at the climbing fiber to Purkinje cell synapse. *J. Neurosci.* 18, 6147–6162.
- Dondzillo, A., Sätzler, K., Horstmann, H., Altrock, W.D., Gundelfinger, E.D., and Kuner, T. (2010). Targeted three-dimensional immunohistochemistry reveals localization of presynaptic proteins Bassoon and Piccolo in the rat calyx of Held before and after the onset of hearing. *J. Comp. Neurol.* 518, 1008–1029.
- Edwards, F.A., Konnerth, A., Sakmann, B., and Takahashi, T. (1989). A thin slice preparation for patch clamp recordings from neurones of the mammalian central nervous system. *Pflugers Arch.* 414, 600–612.
- Fejtova, A., Davydova, D., Bischof, F., Lazarevic, V., Altrock, W.D., Romorini, S., Schöne, C., Zusrattner, W., Kreutz, M.R., Garner, C.C., et al. (2009). Dynein light chain regulates axonal trafficking and synaptic levels of Bassoon. *J. Cell Biol.* 185, 341–355.
- Fernández-Busnadiego, R., Zuber, B., Maurer, U.E., Cyrklaff, M., Baumeister, W., and Lucčić, V. (2010). Quantitative analysis of the native presynaptic cytomatrix by cryoelectron tomography. *J. Cell Biol.* 188, 145–156.
- Frank, T., Rutherford, M.A., Strenzke, N., Neef, A., Pangršič, T., Khimich, D., Fejtova, A., Gundelfinger, E.D., Liberman, M.C., Harke, B., et al. (2010). Bassoon and the Synaptic Ribbon Organize Ca²⁺ Channels and Vesicles to Add Release Sites and Promote Refilling. *Neuron* 68, this issue, ■■■-■■■.
- Gundelfinger, E.D., Kessels, M.M., and Qualmann, B. (2003). Temporal and spatial coordination of exocytosis and endocytosis. *Nat. Rev. Mol. Cell Biol.* 4, 127–139.
- Hallermann, S., Pawlu, C., Jonas, P., and Heckmann, M. (2003). A large pool of releasable vesicles in a cortical glutamatergic synapse. *Proc. Natl. Acad. Sci. USA* 100, 8975–8980.
- Hallermann, S., Heckmann, M., and Kittel, R.J. (2010). Mechanisms of short-term plasticity at neuromuscular active zones of *Drosophila*. *HFSP J* 4, 72–84.
- Hosoi, N., Sakaba, T., and Neher, E. (2007). Quantitative analysis of calcium-dependent vesicle recruitment and its functional role at the calyx of Held synapse. *J. Neurosci.* 27, 14286–14298.
- Hosoi, N., Holt, M., and Sakaba, T. (2009). Calcium dependence of exo- and endocytotic coupling at a glutamatergic synapse. *Neuron* 63, 216–229.
- Jörntell, H., and Ekerot, C.F. (2006). Properties of somatosensory synaptic integration in cerebellar granule cells in vivo. *J. Neurosci.* 26, 11786–11797.
- Kaesler, P.S., Deng, L., Chávez, A.E., Liu, X., Castillo, P.E., and Südhof, T.C. (2009). ELKS2/CAST deletion selectively increases neurotransmitter release at inhibitory synapses. *Neuron* 64, 227–239.
- Kawasaki, F., Hazen, M., and Ordway, R.W. (2000). Fast synaptic fatigue in shi-bire mutants reveals a rapid requirement for dynamin in synaptic vesicle membrane trafficking. *Nat. Neurosci.* 3, 859–860.
- Khimich, D., Nouvian, R., Pujol, R., Tom Dieck, S., Egner, A., Gundelfinger, E.D., and Moser, T. (2005). Hair cell synaptic ribbons are essential for synchronous auditory signalling. *Nature* 434, 889–894.
- Kim, J.H., and von Gersdorff, H. (2009). Traffic jams during vesicle cycling lead to synaptic depression. *Neuron* 63, 143–145.
- Kiyonaka, S., Wakamori, M., Miki, T., Uriu, Y., Nonaka, M., Bito, H., Beedle, A.M., Mori, E., Hara, Y., De Waard, M., et al. (2007). RIM1 confers sustained activity and neurotransmitter vesicle anchoring to presynaptic Ca²⁺ channels. *Nat. Neurosci.* 10, 691–701.
- Kushmerick, C., Renden, R., and von Gersdorff, H. (2006). Physiological temperatures reduce the rate of vesicle pool depletion and short-term depression via an acceleration of vesicle recruitment. *J. Neurosci.* 26, 1366–1377.
- Lenzi, D., and von Gersdorff, H. (2001). Structure suggests function: The case for synaptic ribbons as exocytotic nanomachines. *Bioessays* 23, 831–840.
- Lorteije, J.A., Rusu, S.I., Kushmerick, C., and Borst, J.G. (2009). Reliability and precision of the mouse calyx of Held synapse. *J. Neurosci.* 29, 13770–13784.
- Mukherjee, K., Yang, X., Gerber, S.H., Kwon, H.B., Ho, A., Castillo, P.E., Liu, X., and Südhof, T.C. (2010). Piccolo and bassoon maintain synaptic vesicle clustering without directly participating in vesicle exocytosis. *Proc. Natl. Acad. Sci. USA* 107, 6504–6509.
- Neher, E. (2006). A comparison between exocytotic control mechanisms in adrenal chromaffin cells and a glutamatergic synapse. *Pflugers Arch.* 453, 261–268.
- Neher, E., and Sakaba, T. (2008). Multiple roles of calcium ions in the regulation of neurotransmitter release. *Neuron* 59, 861–872.
- Pangršič, T., Lasarow, L., Reuter, K., Takago, H., Schwander, M., Riedel, D., Frank, T., Tarantino, L.M., Bailey, J.S., Strenzke, N., et al. (2010). Hearing requires otoferlin-dependent efficient replenishment of synaptic vesicles in hair cells. *Nat. Neurosci.* 13, 869–876.
- Rancz, E.A., Ishikawa, T., Duguid, I., Chadderton, P., Mahon, S., and Häusser, M. (2007). High-fidelity transmission of sensory information by single cerebellar mossy fibre boutons. *Nature* 450, 1245–1248.
- Rothman, J.S., Cathala, L., Steuber, V., and Silver, R.A. (2009). Synaptic depression enables neuronal gain control. *Nature* 457, 1015–1018.
- Sakaba, T., and Neher, E. (2001). Calmodulin mediates rapid recruitment of fast-releasing synaptic vesicles at a calyx-type synapse. *Neuron* 32, 1119–1131.
- Sargent, P.B., Saviane, C., Nielsen, T.A., DiGregorio, D.A., and Silver, R.A. (2005). Rapid vesicular release, quantal variability, and spillover contribute to the precision and reliability of transmission at a glomerular synapse. *J. Neurosci.* 25, 8173–8187.
- Saviane, C., and Silver, R.A. (2006). Fast vesicle reloading and a large pool sustain high bandwidth transmission at a central synapse. *Nature* 439, 983–987.

- Scheuss, V., Schneggenburger, R., and Neher, E. (2002). Separation of presynaptic and postsynaptic contributions to depression by covariance analysis of successive EPSCs at the calyx of held synapse. *J. Neurosci.* *22*, 728–739.
- Schoch, S., and Gundelfinger, E.D. (2006). Molecular organization of the presynaptic active zone. *Cell Tissue Res.* *326*, 379–391.
- Siksou, L., Rostaing, P., Lechère, J.P., Boudier, T., Ohtsuka, T., Fejtová, A., Kao, H.T., Greengard, P., Gundelfinger, E.D., Triller, A., and Marty, S. (2007). Three-dimensional architecture of presynaptic terminal cytomatrix. *J. Neurosci.* *27*, 6868–6877.
- Silver, R.A. (2003). Estimation of nonuniform quantal parameters with multiple-probability fluctuation analysis: Theory, application and limitations. *J. Neurosci. Methods* *130*, 127–141.
- Silver, R.A., Cull-Candy, S.G., and Takahashi, T. (1996). Non-NMDA glutamate receptor occupancy and open probability at a rat cerebellar synapse with single and multiple release sites. *J. Physiol.* *494*, 231–250.
- Silver, R.A., Momiyama, A., and Cull-Candy, S.G. (1998). Locus of frequency-dependent depression identified with multiple-probability fluctuation analysis at rat climbing fibre-Purkinje cell synapses. *J. Physiol.* *510*, 881–902.
- Südhof, T.C. (2004). The synaptic vesicle cycle. *Annu. Rev. Neurosci.* *27*, 509–547.
- Taschenberger, H., Leão, R.M., Rowland, K.C., Spirou, G.A., and von Gersdorff, H. (2002). Optimizing synaptic architecture and efficiency for high-frequency transmission. *Neuron* *36*, 1127–1143.
- tom Dieck, S., Sanmartí-Vila, L., Langnaese, K., Richter, K., Kindler, S., Soyke, A., Wex, H., Smalla, K.H., Kämpf, U., Fränzer, J.T., et al. (1998). Bassoon, a novel zinc-finger CAG/glutamine-repeat protein selectively localized at the active zone of presynaptic nerve terminals. *J. Cell Biol.* *142*, 499–509.
- van Kan, P.L., Gibson, A.R., and Houk, J.C. (1993). Movement-related inputs to intermediate cerebellum of the monkey. *J. Neurophysiol.* *69*, 74–94.
- Verhage, M., and Toonen, R.F. (2007). Regulated exocytosis: Merging ideas on fusing membranes. *Curr. Opin. Cell Biol.* *19*, 402–408.
- von Gersdorff, H., Sakaba, T., Berglund, K., and Tachibana, M. (1998). Submillisecond kinetics of glutamate release from a sensory synapse. *Neuron* *21*, 1177–1188.
- Wang, X., Hu, B., Zieba, A., Neumann, N.G., Kasper-Sonnenberg, M., Honsbein, A., Hultqvist, G., Conze, T., Witt, W., Limbach, C., et al. (2009). A protein interaction node at the neurotransmitter release site: Domains of Aczonin/Piccolo, Bassoon, CAST, and rim converge on the N-terminal domain of Munc13-1. *J. Neurosci.* *29*, 12584–12596.
- Xu-Friedman, M.A., and Regehr, W.G. (2003). Ultrastructural contributions to desensitization at cerebellar mossy fiber to granule cell synapses. *J. Neurosci.* *23*, 2182–2192.
- Yang, Y.M., Fedchyshyn, M.J., Grande, G., Aitoubah, J., Tsang, C.W., Xie, H., Ackerley, C.A., Trimble, W.S., and Wang, L.Y. (2010). Septins regulate developmental switching from microdomain to nanodomain coupling of Ca²⁺ influx to neurotransmitter release at a central synapse. *Neuron* *67*, 100–115.
- Young, S.M., Jr., and Neher, E. (2009). Synaptotagmin has an essential function in synaptic vesicle positioning for synchronous release in addition to its role as a calcium sensor. *Neuron* *63*, 482–496.
- Zhai, R.G., and Bellen, H.J. (2004). The architecture of the active zone in the presynaptic nerve terminal. *Physiology (Bethesda)* *19*, 262–270.

4 Diskussion und Ausblick

Im ersten Teil der Diskussion werden die gewonnenen Ergebnisse dargestellt, wobei der Schwerpunkt auf der Funktion der Cytomatrix für die hochfrequente synaptische Übertragung liegt (Kapitel 4.1). In Folgenden wird die Ca^{2+} -Abhängigkeit der Vesikelfusion und der Vesikelnachladung diskutiert, die eine hochfrequente Übertragung ermöglicht (Kapitel 4.2). Schließlich werden erste präsynaptische Ableitungen von cerebellären Mossfasersynapsen vorgestellt, die eine weitere Analyse der Mechanismen der hochfrequenten Übertragung entscheidend erleichtern sollten (Kapitel 4.3).

4.1 Die Bedeutung der Cytomatrix für die hochfrequente Übertragung

Mit der vorliegenden Arbeit konnte gezeigt werden, dass die Cytomatrix eine entscheidende Rolle bei der hochfrequenten synaptischen Übertragung spielt. Trotz intensiver Forschung werden folgende teils kontroverse Funktion der Cytomatrix (insbesondere der *ribbons*) diskutiert: (1) ein aktiver „Fließband“-Transport der Vesikel zur Freisetzungsstelle (*conveyer belt*; Griesinger *et al.*, 2005; Lenzi und von Gersdorff, 2001), (2) eine Immobilisierung der Vesikel, um das Fusionieren der Vesikel untereinander (*compound fusion*) zu erleichtern (*safety belt*; He *et al.*, 2009; Matthews und Sterling, 2008; Parsons und Sterling, 2003), sowie (3) ein Schutzschild, das die Anlagerung der schnell diffundierenden Vesikel an die Freisetzungsstelle und damit deren Fusion verhindert (*timing belt*; Holt *et al.*, 2004; Jackman *et al.*, 2009). Die Ergebnisse dieser Arbeit lassen annehmen, dass die Cytomatrix Vesikel an der Freisetzungsstelle bindet und deren Nachladen beschleunigt (siehe Abb. 3 für eine detaillierte Erklärung). An der *Drosophila* konnten erstmal bei intakter Cytomatrix (und normaler Ca^{2+} -Kanalverteilung) die Bindung der Vesikel spezifisch gestört und die funktionelle Konsequenz untersucht werden (Hallermann *et al.*, 2010b). An konventionellen Synapsen des zentralen Nervensystems von Säugetieren konnte die Funktion des Cytomatrixproteins Bassoon auf die Vesikelnachladung nachgewiesen werden (Hallermann *et al.*, 2010c).

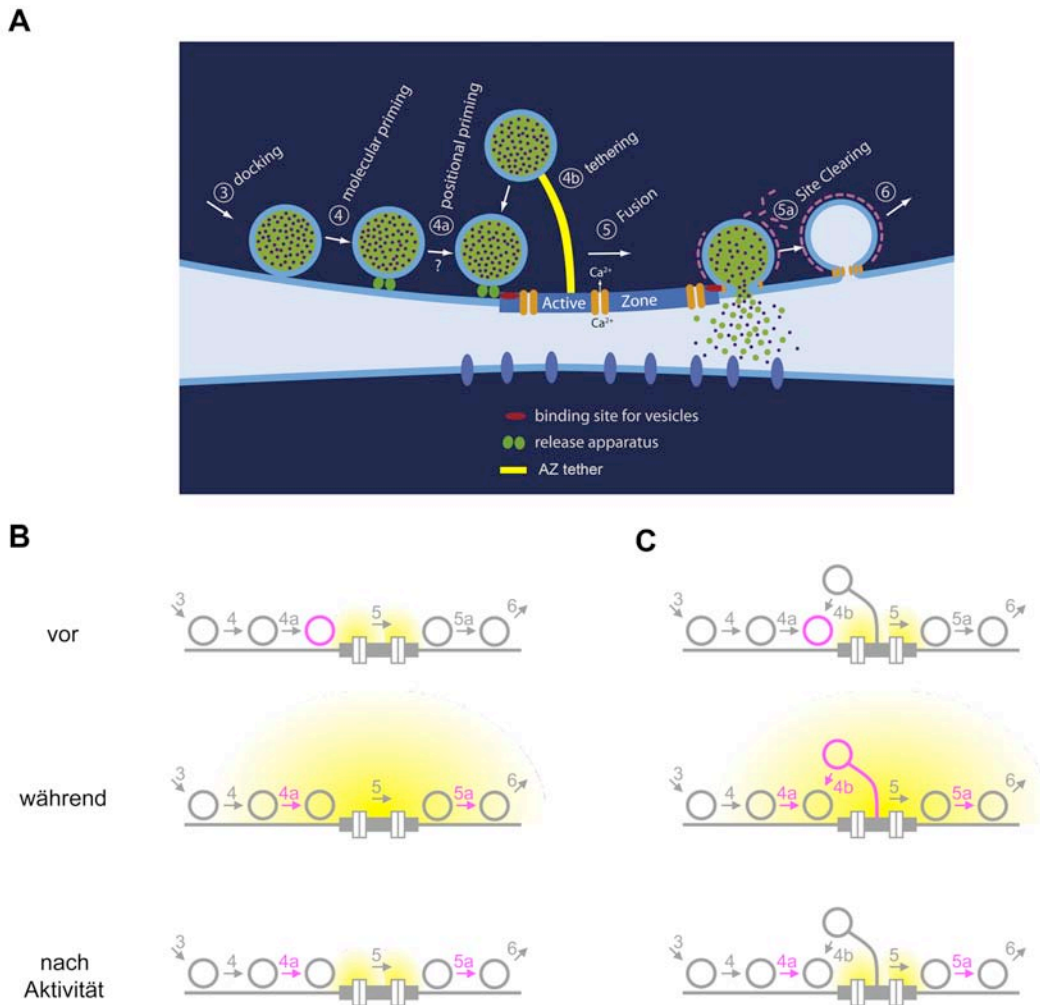


Abb. 3: Mechanismen während hochfrequenter Übertragung

A Teil des synaptischen Vesikelzyklus modifiziert nach Neher und Sakaba (2008). Ein Vesikel ist hinzugefügt, das über ein Filament (gelb) an der Freisetzungsstelle (Active Zone) gebunden ist.

B Illustration des Vesikelzyklus vor, während und nach hochfrequenter Übertragung (Aktivität) nach Südhof (2004) sowie nach Neher und Sakaba (2008). Es wird von folgender Sequenz ausgegangen: Synaptische Vesikel werden mit Transmitter gefüllt (Schritt 1, nicht gezeigt), aus dem Reserve-Pool freigesetzt (Schritt 2, nicht gezeigt), lagern sich der präsynaptischen Membran an (Schritt 3, *docking*), werden fusionsfähig (Schritt 4, *molecular priming*), lagern sich Ca²⁺-Kanälen an (Schritt 4a, *positional priming*), öffnen ihre Fusionspore (Schritt 5), werden von der Freisetzungsstelle entfernt (Schritt 5a, *site clearing*) und werden schließlich endozytiert (Schritt 6). Die Ca²⁺-Verteilung ist in gelb angedeutet. Während und nach Aktivität sind die gleichen Mechanismen Raten-limitierend (z. B. Schritt 4a und Schritt 5a), allerdings werden diese Schritte durch die erhöhte Ca²⁺-Konzentration beschleunigt (Hosoi *et al.*, 2007; Neher und Sakaba, 2008).

C Die in dieser Arbeit gewonnenen Ergebnisse legen nahe, dass die synaptischen Vesikel, die über Filamente gebunden sind, die hochfrequente Übertragung entscheidend unterstützen (Schritt 4b). Die Raten-limitierenden Schritte sind jeweils in magenta dargestellt.

4.2 Ca^{2+} -Abhängigkeit der Vesikelfusion und -nachladung

4.2.1 Ca^{2+} -Abhängigkeit der Vesikelfusion

Im zentralen Nervensystem von Wirbeltieren wurde die Ca^{2+} -Sensitivität der Vesikelfusion nur an einigen wenigen Nervenendigungen bestimmt. Während an Synapsen sensorischer Zellen höhere Ca^{2+} -Konzentrationen für eine schnelle Vesikelfusion notwendig sind (retinale Bipolarzelle: $> 100 \mu\text{M}$; Heidelberger *et al.*, 1994; innere Haarzelle: $50\text{--}100 \mu\text{M}$; Beutner *et al.*, 2001) wird an der Held'schen Calyx eine schnelle Vesikelfusion bereits bei einer Ca^{2+} -Konzentration von $10\text{--}20 \mu\text{M}$ ausgelöst (Bollmann und Sakmann, 2005; Bollmann *et al.*, 2000; Lou *et al.*, 2005; Schneggenburger und Neher, 2000). Kürzlich wurde an einer inhibitorischen Synapse im Cerebellum eine vergleichsweise niedrige Ca^{2+} -Dissoziationsrate und entsprechend eine hohe Ca^{2+} -Affinität gefunden ($\sim 30 \mu\text{M}$; Sakaba, 2008). Die Ca^{2+} -Sensitivität der Vesikelfusion von Synapsen, die hohe Frequenzen über einen längeren Zeitraum übertragen können, wie z.B. cerebelläre Moosfasersynapsen, ist momentan nicht bekannt.

Die erstaunlich synchronen Vesikelfusionen selbst bei lang anhaltenden hohen Stimulationsfrequenzen von cerebellären Moosfasersynapsen (Hallermann, 2010c) legen die Hypothese einer geringen Ca^{2+} -Affinität und einer engen Kopplung der Vesikel mit den Ca^{2+} -Kanälen nahe. Diese Hypothese beruht auch auf dem umgekehrten Befund, dass die Vesikelfusion in Interneuronen des Cerebellums und in der juvenilen Held'schen Calyx weniger synchron als in cerebellären Moosfasersynapsen ist, und dass deren Ca^{2+} -Affinität entsprechend relativ hoch ist (Sakaba, 2008; Schneggenburger und Neher, 2000; Wang *et al.*, 2008). Hierbei liegt die Vorstellung zugrunde, dass eine hohe Affinität (und im Besonderen eine langsame Ca^{2+} -Dissoziationskonstante; Sakaba, 2008) zu einer längeren Bindung von Ca^{2+} am Sensor und damit zu mehr asynchroner Vesikelfusion führt.

4.2.2 Ca^{2+} -Abhängigkeit der Vesikelnachladung

Das Nachladen eines synaptischen Vesikels (*reloading*; Borges *et al.*, 1995) schließt eine Vielzahl von Prozessen ein, die nach der Fusion eines Vesikels an einer Freisetzungsstelle das Fusionieren eines zweiten transmittergefüllten Vesikels erlauben (Abb. 3). Welche dieser Mechanismen während hochfrequenter synaptischer Übertragung frequenzlimitierend sind, ist momentan ungeklärt (Neher, 2010). Selbst über die maximal erreichbare Nachladerate, die all diese Prozesse beinhaltet, herrscht Uneinigkeit. Höchstwahrscheinlich kann die Nachladerate je nach Synapsentyp sehr unterschiedliche Werte erreichen. Während beispielsweise die Geschwindigkeiten der Vesikelnachladung an der retinalen Bipolarzelle (Mennerick und Matthews, 1996) und an der Held'schen Calyx (Wu und Borst, 1999) im Bereich von Sekunden liegt, wurden an cerebellären Moosfaser- und Parallelfasersynapsen im Kleinhirn (Crowley *et al.*, 2007; Saviane und Silver, 2006) Geschwindigkeiten im 10–100 Millisekunden-Bereich bestimmt. Es ist allerdings nicht auszuschließen, dass die verschiedenen Methoden, mit denen die Nachladeraten bestimmt wurden, zu diesen um mehrere Größenordnungen unterschiedlichen Abschätzungen beitragen.

Neben den unterschiedlichen Raten der Vesikelnachladung werden mindestens drei unterschiedliche Mechanismen der Vesikelnachladung mit unterschiedlichen Ca^{2+} -Abhängigkeiten diskutiert:

- (1) An der Held'schen Calyx wurden in Reaktion auf Ca^{2+} -Einstrom *langsam* fusionierende Vesikel gefunden, die *schnell* nachgeladen wurden, während gleichzeitig *schnell* fusionierende Vesikel mit *langsamer* Nachladerate gefunden wurden (Sakaba und Neher, 2001). Die schnell fusionierenden Vesikel scheinen für den Großteil der synchronen synaptischen Übertragung verantwortlich zu sein (Sakaba, 2006), und ihre Nachladegeschwindigkeit zeigte eine starke Abhängigkeit von der intrazellulären Ca^{2+} -Konzentration (Dittman *et al.*, 2000; Hosoi *et al.*, 2007; Neher und Sakaba, 2008). Auch an einer andere Synapse im auditorischen System des Hirnstamms (*end bulb of Held*) wurde eine Ca^{2+} -abhängige Rate der Vesikelnachladung beschrieben (Yang und Xu-Friedman, 2008).
- (2) Im Gegensatz hierzu wurde an cerebellären Moosfasersynapsen eine

Nachladerate gefunden, die sich Ca^{2+} -unabhängig erklären lässt (Saviane und Silver, 2006). Auch Experimente mit Ca^{2+} -Puffern an afferenten Synapsen im Nucleus vestibularis deuteten darauf hin, dass die Nachladerate hier Ca^{2+} -unabhängig ist (Bagnall *et al.*, 2008).

- (3) Schließlich wurde in inhibitorischen Neuronen des Kleinhirns eine Ca^{2+} -Abhängigkeit der Nachladerate bestimmt, die erst durch hohe Ca^{2+} -Konzentration ($> 10\mu\text{M}$) beschleunigt wurde (Sakaba, 2008). Diese Ca^{2+} -konzentrationen werden im Zellinneren nur in der Nähe der Ca^{2+} -Kanälen erreicht, was auf lokale Vesikelnachladung innerhalb der Freisetzungsstelle hindeutet.

Welche dieser Mechanismen zur effektiven Vesikelnachladung von Synapsen genutzt werden, die hohe Frequenzen übertragen können, wie z.B. von cerebellären Moosfasersynapsen, ist bisher nicht geklärt. In Untersuchungen mit axonaler Stimulation lässt sich die Vesikelnachladung entweder Ca^{2+} -unabhängig oder mit einer sehr steilen und erstaunlich sensitiven Ca^{2+} -Abhängigkeit erklären (170 nM; Hallermann *et al.*, 2010c). Es wird zu klären sein, ob bzw. wie die schnelle Vesikelnachladung durch Ca^{2+} gesteuert wird, oder ob eine leere Freisetzungsstelle unabhängig von der Ca^{2+} -Konzentration die schnelle Nachladung bewirkt.

4.3 Ableitungen von cerebellären Moosfaserendigungen

Um zu verstehen, wie Cytomatrixproteine wie z. B. Bassoon die Vesikelnachladungen beschleunigen, erschien es notwendig, präsynaptische Ableitungen mit der *patch-clamp* Technik von cerebellären Moosfaserendigungen durchzuführen. Im Rahmen der begonnenen Etablierung dieser Ableitungen konnte ich eine Thy1-Mauslinie benutzen, bei der einzelne cerebelläre Moosfasern Fluoreszenz-markiert sind (Winter *et al.*, 2007), und die mir von Dr. J. Hirrlinger (Leipzig) zur Verfügung gestellt wurden. Diese Fluoreszenzmarkierung, die ein gezieltes Ansteuern von Moosfaserendigungen mit der Zwei-Photonen-Mikroskopie in Kombination mit gleichzeitiger Infrarot-Differenz-Interferenz-Kontrast (IR-DIC)-Mikroskopie der Transmission des infraroten Laseranregungslichts erlaubte, erhöhte die Erfolgsrate der *patch-clamp*

Ableitungen erheblich (Abb. 4). Cerebelläre Moosfaserendigungen zeigten charakteristische elektrophysiologische Eigenschaften (Rancz *et al.*, 2007; Thomsen, 2010): das Fehlen von spontanen Strömen und Potentialen, eine kleine Kapazität, typische Auswärtsgleichrichtung mit einem zeitabhängigem Potentialverlauf bei Hyperpolarisation (*sag*) sowie die Generierung nur eines Aktionspotentials bei lang andauernder Depolarisation (Abb. 4B).

Im nächsten Schritt wurden Kapazitätsmessungen an cerebellären Moosfasersynapsen etabliert. Hierbei wurde der Depolarisations-induzierte Ca^{2+} -Einstrom pharmakologisch isoliert, und die resultierende Kapazitätserholung bei verschiedenen Dauern der Depolarisation bestimmt (Abb. 5). In ersten Experimenten mit Polarisierungen auf 0 mV und 30 ms Dauer zeigten sich

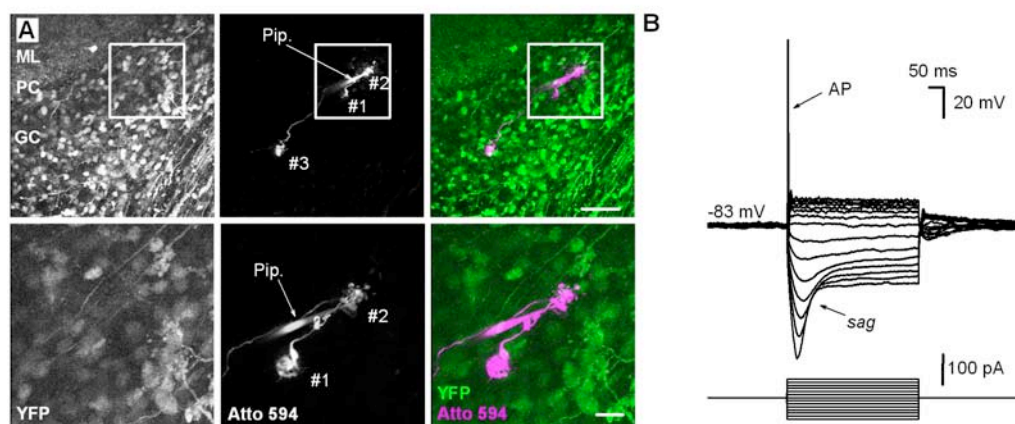


Abb. 4: Whole-cell patch-clamp Ableitung von einer cerebellären Moosfaserendigung im akuten Hirnschnitt einer 23 Tage alten Maus

A Projektion Zwei-Photonen-mikroskopischer Aufnahmen eines ~80 μm dicken Bilderstapels (1 μm Ebenenabstand). Links: Fluoreszenz der YFP-Expression in einem Teil der Moosfasern (Winter *et al.*, 2007). ML: *molecular layer*; PC: *purkinje cell*; GC: *granule cell*. Mitte: Fluoreszenz des Farbstoffs Atto 594, mit dem eine Moosfaserendigung (#2) und zwei benachbarte Moosfaserendigungen (#1 und #3) über die *patch-clamp* Pipette (Pip.) gefüllt wurden [200 μM]. Rechts: Überlagerung des YFP (grün) und des Atto 594 Signals (magenta). Für die Zwei-Photonen-Mikroskopie wurden beide Farbstoffe gleichzeitig mit einer Wellenlänge von 850 nm angeregt (Bestvater *et al.*, 2002; Spiess *et al.*, 2005) und die Emission von YFP und Atto 594 auf 510 - 540 nm und 610-700 nm eingegrenzt. Skalierungsbalken, 50 μm . Unten: Vergrößerung des weiß umrahmten Anteils. Skalierungsbalken, 5 μm .

B Das mit der *patch-clamp* Technik gemessene Membranpotential der in A dargestellten Moosfaserendigung während Injektion von Strompulsen (Kalium-Glukonat-basierte intrazelluläre Lösung). Die Moosfaserendigung zeigte eine Auswärtsgleichrichtung mit typischem Potentialverlauf bei Hyperpolarisation (*sag*) sowie die Generierung nur eines Aktionspotentials (*AP*) bei lang andauernder Depolarisation.

Kapazitätserhöhungen von ca. 150 fF. Nimmt man 70 aF pro Vesikel an, würde diese Kapazitätserhöhung der Fusion von ~2000 Vesikeln entsprechen. Werden außerdem ~300 Freisetzungstellen pro Moosfaserendigung angenommen (Hamori und Somogyi, 1983; Xu-Friedman und Regehr, 2003), ergäben sich ~7 fusionsbereite Vesikel pro Freisetzungstelle. Pro Moosfaser-Körnerzell-Verbindung mit etwa 5 Freisetzungstellen ergäben sich damit ~35 fusionsbereite Vesikel. Diese Abschätzung ist konsistent mit der Abschätzung von 10-15 Fusionen pro Moosfaser-Körnerzell-Verbindung pro Aktionspotential bei einer hohen Fusionswahrscheinlichkeit von ~50% (Hallermann *et al.*, 2010c). Interessanterweise scheinen an einer Freisetzungstelle der hippocampalen Moosfaserendigung ~40 fusionsbereite Vesikel [1400 Vesikel an 37 Freisetzungstellen (Hallermann *et al.*, 2003)] mit einer etwa 10-fach geringeren Fusionswahrscheinlichkeit zu existieren (Jonas *et al.*, 1993; Lawrence *et al.*, 2004; McBain, 2008). Die geringere Anzahl an fusionsbereiten Vesikeln und die geringere Fusionswahrscheinlichkeit ist konsistent mit einer geringen Faszilitierung an cerebellären Moosfasersynapsen (Hallermann *et al.*, 2010c) verglichen mit der äußerst stark ausgeprägten Faszilitierung an hippocampalen Moosfasersynapsen (Salin *et al.*, 1996). An der Held'schen Calyx wurden nur ~3 fusionsbereite Vesikel pro Freisetzungstelle gefunden (Neher und Sakaba, 2008). Durch weitere Experimente müssen methodische Unterschiede ausgeschlossen werden (z. B. unterschiedliche Ca^{2+} -Pufferkapazitäten der verwendeten intrazellulären Lösung), und es sollen quantitative Modelle genutzt werden (Hallermann *et al.*, 2005; Hallermann *et al.*, 2010a,c), um die funktionellen Konsequenzen der unterschiedlichen Anzahl von fusionsbereiten Vesikeln pro Freisetzungstellen zu verstehen.

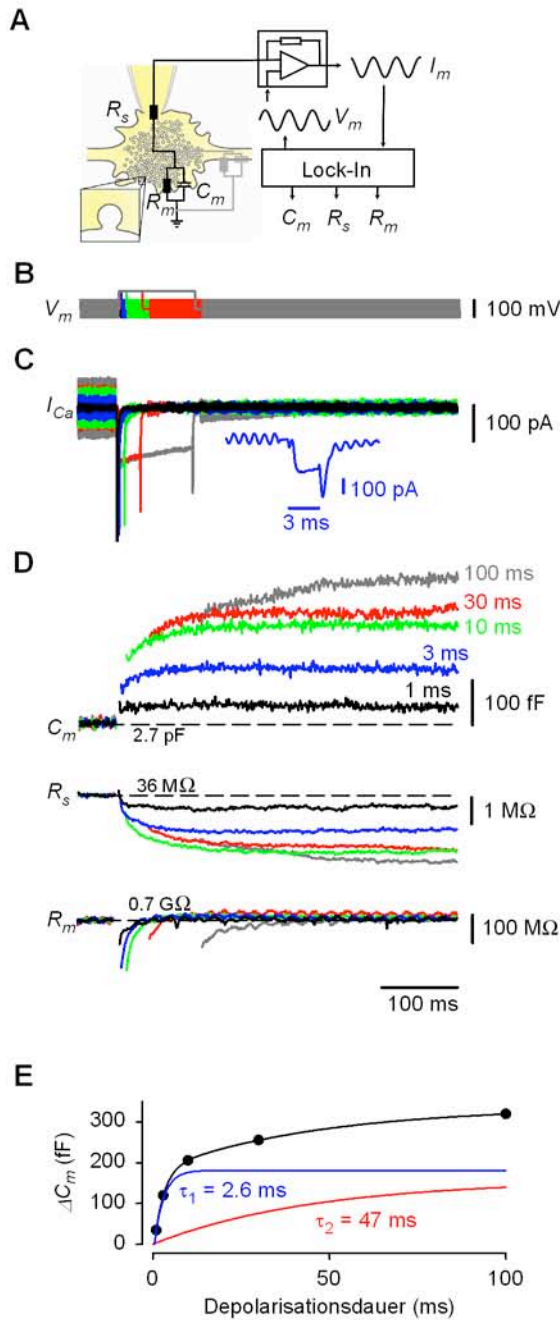


Abb. 5: Präsynaptische whole-cell Kapazitätsmessung einer cerebellären Moosfaserending im akuten Hirnschnitt einer 28 Tage alten Maus

A Mit einem Software-Lock-In-Verstärker (EPC10, HEKA Elektronik, Lambrecht/Pfalz, Deutschland) wurden unter Verwendung der „sine+DC“-Technik (Lindau und Neher, 1988) aus der Phasenverschiebung der angelegten sinusförmigen Kommandospannung (V_m) und dem gemessenen Strom (I_m) die Membrankapazität (C_m), der Zugangswiderstand (R_s) und der Membranwiderstand (R_m) bestimmt.

B Überlagerung der Kommandospannungen des Membranpotentials (V_m) einer Moosfaserending in der whole-cell Spannungsklemme. Bei -100 mV wurde eine Sinusspannung appliziert (1 kHz, ± 50 mV; Hallermann *et al.*, 2003), die durch Depolarisationen auf 0 mV von 1, 3, 10, 30 und 100 ms Dauer unterbrochen ist (dargestellt in schwarz, blau, grün, rot und grau).

C Überlagerung der pharmakologisch isolierten Ca^{2+} -Ströme (I_{Ca}) entsprechend des Farbcodes in A. Es wurde eine CsCl-basierte intrazelluläre Lösung verwendet, und nach Erreichen der whole-cell Konfiguration die Natrium- und Kaliumkanäle durch 1 μ M Tetrodotoxin (TTX), 20 mM Tetraethylammoniumchlorid (TEA) und 5 mM 4-Aminopyridin (4AP) blockiert. Die Kompensation der Leckströme und der kapazitiven Ströme mit sog. P/N-Protokollen führt zu sinusförmigen Artefakten vor den Depolarisation in der Ca^{2+} -Stromspur

(Hallermann *et al.*, 2003). *Inset*: Ca^{2+} -Strom bei 3 ms Depolarisation mit höherer zeitlicher Auflösung.

D Die Änderungen von C_m , R_s und R_m sind nach Depolarisationen unterschiedlicher Dauer entsprechend des obigen Farbcodes ausgehend von $C_m = 2.7$ pF, $R_s = 36$ M Ω und $R_m = 0.7$ G Ω dargestellt. Bei Kapazitätserhöhung zeigte sich eine Reduktion des Zugangswiderstandes, die durch die komplexe Struktur der Nervenendingung erklärt werden kann (siehe graue Illustration des elektrischen Kompartiments des Axons; Hallermann *et al.*, 2003).

E Maximale Kapazitätserhöhung (ΔC_m) dargestellt gegen die Depolarisationsdauer überlagert mit einer bi-exponentiellen Funktion (schwarz) und den entsprechenden Komponenten in blau und rot.

5 Literaturverzeichnis

- Altrock, W.D., tom Dieck, S., Sokolov, M., Meyer, A.C., Sigler, A., Brakebusch, C., Fassler, R., Richter, K., Boeckers, T.M., Potschka, H. *et al.* (2003). Functional inactivation of a fraction of excitatory synapses in mice deficient for the active zone protein bassoon. *Neuron* 37, 787-800.
- Arenz, A., Silver, R.A., Schaefer, A.T. und Margrie, T.W. (2008). The contribution of single synapses to sensory representation in vivo. *Science* 321, 977-980.
- Bagnall, M.W., McElvain, L.E., Faulstich, M. und du Lac, S. (2008). Frequency-independent synaptic transmission supports a linear vestibular behavior. *Neuron* 60, 343-352.
- Bestvater, F., Spiess, E., Stobrawa, G., Hacker, M., Feurer, T., Porwol, T., Berchner-Pfannschmidt, U., Wotzlaw, C. und Acker, H. (2002). Two-photon fluorescence absorption and emission spectra of dyes relevant for cell imaging. *J. Microsc.* 208, 108-115.
- Betz, W.J. und Bewick, G.S. (1992). Optical analysis of synaptic vesicle recycling at the frog neuromuscular junction. *Science* 255, 200-203.
- Beutner, D., Voets, T., Neher, E. und Moser, T. (2001). Calcium dependence of exocytosis and endocytosis at the cochlear inner hair cell afferent synapse. *Neuron* 29, 681-690.
- Bollmann, J.H. und Sakmann, B. (2005). Control of synaptic strength and timing by the release-site Ca^{2+} signal. *Nat. Neurosci.* 8, 426-434.
- Bollmann, J.H., Sakmann, B. und Borst, J.G. (2000). Calcium sensitivity of glutamate release in a calyx-type terminal. *Science* 289, 953-957.
- Borges, S., Gleason, E., Turelli, M. und Wilson, M. (1995). The kinetics of quantal transmitter release from retinal amacrine cells. *Proc. Natl. Acad. Sci. U. S. A.* 92, 6896-6900.
- Crowley, J.J., Carter, A.G. und Regehr, W.G. (2007). Fast vesicle replenishment and rapid recovery from desensitization at a single synaptic release site. *J. Neurosci.* 27, 5448-5460.
- Dick, O., tom Dieck, S., Altrock, W.D., Ammermüller, J., Weiler, R., Garner, C.C., Gundelfinger, E.D. und Brandstätter, J.H. (2003). The presynaptic active zone protein bassoon is essential for photoreceptor ribbon synapse formation in the retina. *Neuron* 37, 775-786.
- Dittman, J.S., Kreitzer, A.C. und Regehr, W.G. (2000). Interplay between facilitation, depression, and residual calcium at three presynaptic terminals. *J. Neurosci.* 20, 1374-1385.
- Fernández-Busnadiego, R., Zuber, B., Maurer, U.E., Cyrklaff, M., Baumeister, W. und Lucic, V. (2010). Quantitative analysis of the native presynaptic cytomatrix by cryoelectron tomography. *The Journal of Cell Biology* 188, 145-156.
- Forsythe, I.D. (1994). Direct patch recording from identified presynaptic terminals mediating glutamatergic EPSCs in the rat CNS, in vitro. *J. Physiol.* 479, 381-387.

- Fouquet, W., Oswald, D., Wichmann, C., Mertel, S., Depner, H., Dyba, M., Hallermann, S., Kittel, R.J., Eimer, S. und Sigrist, S.J. (2009). Maturation of active zone assembly by *Drosophila* Bruchpilot. *J. Cell Biol.* 186, 129-145.
- Frank, T., Rutherford, M.A., Strenzke, N., Neef, A., Pangrsic, T., Khimich, D., Fejtova, A., Gundelfinger, E.D., Liberman, M.C., Harke, B. *et al.* (2010). Bassoon and the synaptic ribbon organize Ca^{2+} channels and vesicles to add release sites and promote refilling. *Neuron im Druck.*
- Geiger, J.R.P. und Jonas, P. (2000). Dynamic control of presynaptic Ca^{2+} inflow by fast-inactivating K^+ channels in hippocampal mossy fiber boutons. *Neuron* 28, 927-939.
- Geis, C., Weishaupt, A., Hallermann, S., Grunewald, B., Wessig, C., Wulsch, T., Reif, A., Byts, N., Beck, M., Jablonka, S. *et al.* (2010). Stiff person syndrome-associated autoantibodies to amphiphysin mediate reduced GABAergic inhibition. *Brain* 133, 3166-3180.
- Griesinger, C.B., Richards, C.D. und Ashmore, J.F. (2005). Fast vesicle replenishment allows indefatigable signalling at the first auditory synapse. *Nature* 435, 212-215.
- Gundelfinger, E.D., Kessels, M.M. und Qualmann, B. (2003). Temporal and spatial coordination of exocytosis and endocytosis. *Nature Reviews Molecular Cell Biology* 4, 127-139.
- Hallermann, S., Fejtova, A., Schmidt, H., Weyhersmüller, A., Silver, R.A., Gundelfinger, E. und Eilers, J. (2010c). Bassoon speeds vesicle reloading at a central excitatory synapse. *Neuron im Druck.*
- Hallermann, S., Heckmann, M. und Kittel, R.J. (2010a). Mechanisms of short-term plasticity at neuromuscular active zones of *Drosophila*. *HFSP Journal* 4, 72-84.
- Hallermann, S., Heckmann, S., Dudel, J. und Heckmann, M. (2005). Short openings in high resolution single channel recordings of mouse nicotinic receptors. *J Physiol (London)* 563, 645-662.
- Hallermann, S., Kittel, R., Wichmann, C., Weyhersmüller, A., Fouquet, W., Mertel, S., Oswald, D., Eimer, S., Depner, H., Schwärzel, M. *et al.* (2010b). Naked dense bodies provoke depression. *J. Neurosci.* 30, 14340-14345.
- Hallermann, S., Pawlu, C., Jonas, P. und Heckmann, M. (2003). A large pool of releasable vesicles in a cortical glutamatergic synapse. *Proc. Natl. Acad. Sci. U. S. A.* 100, 8975-8980.
- Hamori, J. und Somogyi, J. (1983). Differentiation of cerebellar mossy fiber synapses in the rat: a quantitative electron microscope study. *J. Comp. Neurol.* 220, 365-377.
- He, L., Xue, L., Xu, J., McNeil, B.D., Bai, L., Melicoff, E., Adachi, R. und Wu, L.-G. (2009). Compound vesicle fusion increases quantal size and potentiates synaptic transmission. *Nature* 459, 93-97.
- Heidelberger, R., Heinemann, C., Neher, E. und Matthews, G. (1994). Calcium dependence of the rate of exocytosis in a synaptic terminal. *Nature* 371, 513-515.
- Holt, M., Cooke, A., Neef, A. und Lagnado, L. (2004). High mobility of vesicles supports continuous exocytosis at a ribbon synapse. *Curr. Biol.* 14, 173-183.

- Hosoi, N., Sakaba, T. und Neher, E. (2007). Quantitative analysis of calcium-dependent vesicle recruitment and its functional role at the calyx of Held synapse. *J. Neurosci.* 27, 14286-14298.
- Iacoboni, M. (2001). Playing tennis with the cerebellum. *Nat. Neurosci.* 4, 555-556.
- Jackman, S.L., Choi, S.Y., Thoreson, W.B., Rabl, K., Bartoletti, T.M. und Kramer, R.H. (2009). Role of the synaptic ribbon in transmitting the cone light response. *Nat. Neurosci.* 12, 303-310.
- Jonas, P., Major, G. und Sakmann, B. (1993). Quantal components of unitary EPSCs at the mossy fibre synapse on CA3 pyramidal cells of rat hippocampus. *J. Physiol.* 472, 615-663.
- Jörntell, H. und Ekerot, C.F. (2006). Properties of somatosensory synaptic integration in cerebellar granule cells in vivo. *J. Neurosci.* 26, 11786-11797.
- Katz, B. (1969). *The Release of Neural Transmitter Substances* (Liverpool, U.K.: Liverpool Univ. Press).
- Khimich, D., Nouvian, R., Pujol, R., Tom Dieck, S., Egnér, A., Gundelfinger, E.D. und Moser, T. (2005). Hair cell synaptic ribbons are essential for synchronous auditory signalling. *Nature* 434, 889-894.
- Kittel, R.J., Wichmann, C., Rasse, T.M., Fouquet, W., Schmidt, M., Schmid, A., Wagh, D.A., Pawlu, C., Kellner, R.R., Willig, K.I. *et al.* (2006b). Bruchpilot promotes active zone assembly, Ca²⁺ channel clustering, and vesicle release. *Science* 312, 1051-1054.
- Kole, M.H.P., Hallermann, S. und Stuart, G.J. (2006). Single Ih channels in pyramidal neuron dendrites: properties, distribution, and impact on action potential output. *J. Neurosci.* 26, 1677-1687.
- Kumar, A., Rotter, S. und Aertsen, A. (2010). Spiking activity propagation in neuronal networks: reconciling different perspectives on neural coding. *Nat. Rev. Neurosci.* 11, 615-627.
- Kushmerick, C. und von Gersdorff, H. (2003). Exo-endocytosis at mossy fiber terminals: toward capacitance measurements in cells with arbitrary geometry. *Proc Natl Acad Sci U S A* 100, 8618-8620.
- Lawrence, J.J., Grinspan, Z.M. und McBain, C.J. (2004). Quantal transmission at mossy fibre targets in the CA3 region of the rat hippocampus. *J. Physiol. (Lond.)* 554, 175-193.
- Lenzi, D. und von Gersdorff, H. (2001). Structure suggests function: the case for synaptic ribbons as exocytotic nanomachines. *Bioessays* 23, 831-840.
- Lien, C.C. und Jonas, P. (2003). Kv3 potassium conductance is necessary and kinetically optimized for high-frequency action potential generation in hippocampal interneurons. *J. Neurosci.* 23, 2058-2068.
- Lindau, M. und Neher, E. (1988). Patch-clamp techniques for time-resolved capacitance measurements in single cells. *Pflügers Arch.* 411, 137-146.
- Llinás, R.R. (1999). *The Squid Giant Synapse* (New York: Oxford Univ. Press).
- London, M., Roth, A., Beeren, L., Hausser, M. und Latham, P.E. (2010). Sensitivity to perturbations in vivo implies high noise and suggests rate coding in cortex. *Nature* 466, 123-127.

- Lou, X., Scheuss, V. und Schneggenburger, R. (2005). Allosteric modulation of the presynaptic Ca^{2+} sensor for vesicle fusion. *Nature* 435, 497-501.
- Matthews, G. und Sterling, P. (2008). Evidence that vesicles undergo compound fusion on the synaptic ribbon. *J Neurosci* 28, 5403-5411.
- McBain, C.J. (2008). Differential mechanisms of transmission and plasticity at mossy fiber synapses. *Prog. Brain Res.* 169, 225-240.
- Mennerick, S. und Matthews, G. (1996). Ultrafast exocytosis elicited by calcium current in synaptic terminals of retinal bipolar neurons. *Neuron* 17, 1241-1249.
- Mukherjee, K., Yang, X., Gerber, S.H., Kwon, H.B., Ho, A., Castillo, P.E., Liu, X. und Sudhof, T.C. (2010). Piccolo and bassoon maintain synaptic vesicle clustering without directly participating in vesicle exocytosis. *Proc. Natl. Acad. Sci. U. S. A.* 107, 6504-6509.
- Neher, E. (2010). What is rate-limiting during sustained synaptic activity: vesicle supply or the availability of release sites. *Front. Neurosci.* doi: 10.3389/fnsyn.2010.00144.
- Neher, E. und Sakaba, T. (2008). Multiple roles of calcium ions in the regulation of neurotransmitter release. *Neuron* 59, 861-872.
- Parsons, T.D. und Sterling, P. (2003). Synaptic ribbon. Conveyor belt or safety belt? *Neuron* 37, 379-382.
- Rancz, E.A., Ishikawa, T., Duguid, I., Chadderton, P., Mahon, S. und Häusser, M. (2007). High-fidelity transmission of sensory information by single cerebellar mossy fibre boutons. *Nature* 450, 1245-1248.
- Sakaba, T. (2006). Roles of the Fast-Releasing and the Slowly Releasing Vesicles in Synaptic Transmission at the Calyx of Held. *J. Neurosci.* 26, 5863-5871.
- Sakaba, T. (2008). Two Ca^{2+} -dependent steps controlling synaptic vesicle fusion and replenishment at the cerebellar basket cell terminal. *Neuron* 57, 406-419.
- Sakaba, T. und Neher, E. (2001). Calmodulin mediates rapid recruitment of fast-releasing synaptic vesicles at a calyx-type synapse. *Neuron* 32, 1119-1131.
- Salin, P.A., Scanziani, M., Malenka, R.C. und Nicoll, R.A. (1996). Distinct short-term plasticity at two excitatory synapses in the hippocampus. *Proc. Natl. Acad. Sci. U. S. A.* 93, 13304-13309.
- Sargent, P.B., Saviane, C., Nielsen, T.A., DiGregorio, D.A. und Silver, R.A. (2005). Rapid vesicular release, quantal variability, and spillover contribute to the precision and reliability of transmission at a glomerular synapse. *J Neurosci* 25, 8173-8187.
- Saviane, C. und Silver, R.A. (2006). Fast vesicle reloading and a large pool sustain high bandwidth transmission at a central synapse. *Nature* 439, 983-987.
- Schmid, A., Hallermann, S., Kittel, R.J., Khorramshahi, O., Frölich, A.M.J., Quentin, C., Rasse, T.M., Mertel, S., Heckmann, M. und Sigrist, S.J. (2008). Activity-dependent site-specific changes of glutamate receptor composition in vivo. *Nat. Neurosci.* 11, 659-666.
- Schneggenburger, R. und Neher, E. (2000). Intracellular calcium dependence of transmitter release rates at a fast central synapse. *Nature* 406, 889-893.

- Siksou, L., Rostaing, P., Lechaire, J.P., Boudier, T., Ohtsuka, T., Fejtova, A., Kao, H.T., Greengard, P., Gundelfinger, E.D., Triller, A. und Marty, S. (2007). Three-dimensional architecture of presynaptic terminal cytomatrix. *J Neurosci* 27, 6868-6877.
- Silver, R.A., Cull-Candy, S.G. und Takahashi, T. (1996). Non-NMDA glutamate receptor occupancy and open probability at a rat cerebellar synapse with single and multiple release sites. *J. Physiol.* 494, 231-250.
- Spiess, E., Bestvater, F., Heckel-Pompey, A., Toth, K., Hacker, M., Stobrawa, G., Feuerer, T., Wotzlaw, C., Berchner-Pfannschmidt, U., Porwol, T. und Acker, H. (2005). Two-photon excitation and emission spectra of the green fluorescent protein variants ECFP, EGFP and EYFP. *J. Microsc.* 217, 200-204.
- Südhof, T.C. (2004). The synaptic vesicle cycle. *Annu Rev Neurosci* 27, 509-547.
- Thomsen, L.B., Jorntell, H. und Midtgaard, J. (2010). Presynaptic calcium signalling in cerebellar mossy fibres. *Front Neural Circuits* 4, 1-15.
- Todorov, E. (2004). Optimality principles in sensorimotor control. *Nat. Neurosci.* 7, 907-915.
- tom Dieck, S., Sanmarti-Vila, L., Langnaese, K., Richter, K., Kindler, S., Soyke, A., Wex, H., Smalla, K.H., Kampf, U., Franzer, J.T. *et al.* (1998). Bassoon, a novel zinc-finger CAG/glutamine-repeat protein selectively localized at the active zone of presynaptic nerve terminals. *J. Cell Biol.* 142, 499-509.
- von Gersdorff, H. und Matthews, G. (1994). Dynamics of synaptic vesicle fusion and membrane retrieval in synaptic terminals. *Nature* 367, 735-739.
- Wagh, D.A., Rasse, T.M., Asan, E., Hofbauer, A., Schwenkert, I., Durrbeck, H., Buchner, S., Dabauvalle, M.C., Schmidt, M., Qin, G. *et al.* (2006). Bruchpilot, a protein with homology to ELKS/CAST, is required for structural integrity and function of synaptic active zones in *Drosophila*. *Neuron* 49, 833-844.
- Wang, L.Y., Neher, E. und Taschenberger, H. (2008). Synaptic vesicles in mature calyx of Held synapses sense higher nanodomain calcium concentrations during action potential-evoked glutamate release. *J. Neurosci.* 28, 14450-14458.
- Wigge, P. und McMahon, H.T. (1998). The amphiphysin family of proteins and their role in endocytosis at the synapse. *Trends Neurosci.* 21, 339-344.
- Winter, S.M., Hirrlinger, J., Kirchhoff, F. und Hulsman, S. (2007). Transgenic expression of fluorescent proteins in respiratory neurons. *Respir. Physiol. Neurobiol.* 159, 108-114.
- Wu, L.G. und Borst, J.G. (1999). The reduced release probability of releasable vesicles during recovery from short-term synaptic depression. *Neuron* 23, 821-832.
- Xu-Friedman, M.A. und Regehr, W.G. (2003). Ultrastructural contributions to desensitization at cerebellar mossy fiber to granule cell synapses. *J. Neurosci.* 23, 2182-2192.
- Yang, H. und Xu-Friedman, M.A. (2008). Relative roles of different mechanisms of depression at the mouse endbulb of Held. *J. Neurophysiol.* 99, 2510-2521.
- Zhai, R.G. und Bellen, H.J. (2004). The architecture of the active zone in the presynaptic nerve terminal. *Physiology (Bethesda)* 19, 262-270.

6 Erklärung

Unter Anerkennung der für die Medizinische Fakultät der Universität Leipzig geltenden Habilitationsordnung vom 10.12.2008 und der Änderungssatzungen vom 26.06.2009 werden folgende Erklärungen abgegeben:

Diese Habilitationsschrift wurde in dieser oder ähnlicher Form an keiner anderen Stelle zum Zweck eines Graduerungsverfahrens vorgelegt.

Diese Arbeit wurde von mir selbständig verfasst, es wurden keine anderen als die angegebenen Quellen und Hilfsmittel verwendet und wörtlich oder inhaltlich übernommene Stellen wurden als solche kenntlich gemacht.

Die in der Habilitationsschrift enthaltenen Veröffentlichungen, deren Erstautor oder gleichberechtigter Erstautor ich bin, wurden von mir zu einem entscheidenden Teil geschrieben, geplant sowie experimentell durchgeführt. Bei Fouquet *et al.* (2009; Kapitel 3.4) und Geis *et al.* (2010; Kapitel 3.5) war ich entscheidend an der Analyse der Daten und am Verfassen der Arbeit beteiligt.

Leipzig, den 11. November 2010

Dr. Stefan Hallermann

7 Lebenslauf

Dr. med. Dipl. phys. Stefan Jens Hallermann
geboren am 24. Juli 1975 in Würzburg, verheiratet

Studium und Schulbildung

- 1995 Abitur am Theodor-Heuss-Gymnasium, Freiburg i. Br.
- 1995-1998 Studium der Physik, Ludwig-Maximilians-Universität, München
- 1998-2000 Studium der Medizin und der Physik, Ludwig-Maximilians-Universität, München
- 2000 Abschluss Diplom Physik
- 2000-2004 Studium der Medizin, Albert-Ludwigs-Universität, Freiburg i. Br., University of Stellenbosch, Südafrika und University of Sydney, Canberra, Australien
- 2004 Staatsexamen Medizin
- 2005 Approbation als Arzt

Wissenschaftliche Arbeit

- 1998-2000 Wissenschaftlicher Mitarbeiter am Physiologischen Institut der Technischen Universität München (Direktor: Prof. Dr. J. Dudel und Prof. Dr. A. Konnerth)
Studien zur Funktion des nikotinischen Acetylcholin-Rezeptor-Kanals
- 2000 Diplomarbeit: „Die Feinstruktur des kinetischen Verhaltens des nikotinischen Azetylcholin-Rezeptor-Kanals“, Fakultät für Physik, Ludwig-Maximilians-Universität München
- 2000-2005 Wissenschaftlicher Mitarbeiter am Physiologischen Institut der Albert-Ludwigs-Universität Freiburg (Direktor: Prof. Dr. P. Jonas)
Studien zur synaptischen Übertragung im Hippocampus
- 2004 Gastaufenthalt an der John Curtin School, Division of Neuroscience, Canberra, Australia (Direktor: Prof. Dr. G. Stuart)
Studien an dendritischen HCN-Kanälen
- 2005 Dissertation: „Untersuchungen zur Glutamatfreisetzung an einer kortikalen Synapse mit präsynaptischen Kapazitätsmessungen“, Medizinischen Fakultät, Albert-Ludwigs-Universität Freiburg
- 2006-2007 Wissenschaftlicher Mitarbeiter am Institut für Klinische Neurobiologie, Julius-Maximilians-Universität Würzburg (Arbeitsgruppe: Prof. Dr. M. Heckmann, Direktor: Prof. Dr. M. Sendtner)
Studien zur synaptischen Übertragung in *Drosophila melanogaster*
- seit 2008 Wissenschaftlicher Mitarbeiter am Carl-Ludwig Institut für Physiologie der Universität Leipzig (Direktor: Prof. Dr. J. Eilers)
Studien zur synaptischen Übertragung im Kleinhirn

Lehrerfahrung

- 1999-2000 Betreuung des Physiologie-Praktikums für Mediziner an der Technischen Universität München
- 2003+2005 Betreuung des Physiologie-Praktikums für Mediziner an der Albert-Ludwigs-Universität Freiburg

- 2006 Vorlesungen und Seminare der klinischen Neurobiologie an der Julius-Maximilians-Universität Würzburg
 seit 2008 Vorlesungen, Seminare, Betreuung des Physiologie-Praktikums und bestellter Prüfer im ersten Abschnitt der ärztlichen und zahnärztlichen Prüfung (mündliches Physikum) an der Universität Leipzig

Stipendien

- 2001-2003 Promotionsförderung durch die Studienstiftung des deutschen Volkes

Intramurale Förderung

- 2008 Nachwuchsförderung der Medizinischen Fakultät Leipzig (*Formel.1*)

Schriftenverzeichnis**Originalarbeiten**

Hallermann S, Fejtova A, Schmidt H, Weyhersmüller A, Silver RS, Gundelfinger ED, Eilers J. Bassoon speeds vesicle reloading at a central excitatory synapse (2010) **Neuron im Druck**

Hallermann S*, Kittel RJ*, Wichmann C*, Weyhersmüller A, Fouquet W, Mertel S, Oswald D, Eimer S, Depner H, Schwärzel M, Sigris SJ, Heckmann M (2010) Naked dense bodies provoke depression. **J Neurosci** 30: 14340-14345

Geis C, Weishaupt A, Hallermann S, Grünewald B, Wessig C, Wulsch T, Reif A, Byts A, Beck M, Jablonka S, Boettger MK,i, Üçeyler N, Fouquet W, Gerlach M, Meinck HM, Sirén AL, Sigris SJ, Toyka KV, Heckmann M*, Sommer C* (2010) Stiff person syndrome associated autoantibodies to amphiphysin mediate reduced GABAergic inhibition. **Brain** 133: 3166-80

[Kommentar von A. Vincent, Brain 133: 3164–3165]

Hallermann S, Heckmann M, Kittel RJ (2010) Mechanisms of short-term plasticity at neuromuscular active zones of Drosophila. **HFSP J** 4:72-84

Meuth SG, Herrmann AM, Simon OJ, Siffrin V, Melzer N, Bittner S, Meuth P, Langer HF, Hallermann S, Boldakowa N, Herz J, Munsch T, Landgraf P, Aktas O, Heckmann M, Lessmann V, Budde T, Kieseier BC, Zipp F, Wiendl H. (2009) Cytotoxic CD8⁺ T cell-neuron interactions: perforin-dependent electrical silencing precedes but is not causally linked to neuronal cell death. **J Neurosci**. 29:15397-409

Fouquet W, Oswald D, Wichmann C, Mertel S, Depner H, Dyba M, Hallermann S, Kittel RJ, Eimer S, Sigris SJ. (2009) Maturation of active zone assembly by Drosophila Bruchpilot. **J Cell Biol** 186:129-45

Schmid A*, Hallermann S*, Kittel RJ, Khorramshahi O, Frölich AM, Quentin C, Rasse TM, Mertel S, Heckmann M, Sigris SJ (2008) Activity-dependent site-specific changes of glutamate receptor composition *in vivo*. **Nat Neurosci** 11:659-666

* geteilte Erstautorenschaft

[Kommentar in *Neurobiology Select*, Cell 143:5-7]

[Artikel des Monats Juli 2008 der Medizinischen Fakultät Leipzig]

Kole MHP*, Hallermann S*, Stuart G. (2006) Single I_h channels in pyramidal neuron dendrites: properties, distribution and impact on action potential output. **J Neurosci** 26: 1677-1687

Hallermann S, Heckmann S, Dudel J, Heckmann M (2005) Short openings in high resolution single channel recordings of mouse nicotinic receptors. **J Physiol** 563: 645-662

Hallermann S, Pawlu C, Jonas P, Heckmann M (2003) A large pool of releasable vesicles in a cortical glutamatergic synapse. **Proc Natl Acad Sci U S A** 100: 8975-8980

[Kommentar von Kushmerick, C, von Gersdorff, H, Proc Natl Acad Sci U S A 100: 8618-20]

Dudel J, Hallermann S, Heckmann M (2000) Quartz glass pipette puller operating with a regulated oxy-hydrogen burner. **Pflügers Arch.** 441:175-180

Übersichtsartikel

Kittel RJ, Hallermann S, Thomsen S, Wichmann C, Sigrist SJ, Heckmann M (2006) Active zone assembly and synaptic release. **Biochem Soc Trans** 34: 939-941

Buchbeiträge

Heckmann M, Hallermann S (2007) Fast Drug Application. In: *Patch-Clamp Analysis Neuromethods*, 38: 295-307

Arbeiten in Vorbereitung

Saumweber T, Weyhersmüller A, Hallermann S, Michels B, Bucher D, Funk N, Reisch D, Krohne G, Wegener S, Buchner E, Gerber B. Behavioral and synaptic plasticity are impaired upon lack of the synaptic protein SAP47. **J Neurosci in Revision**

Weyhersmüller A, Wagner N, Eilers J, Hallermann S. The number of release-ready vesicles increases rapidly during homeostatic plasticity.

Hallermann S, Kole MHP. Kinetics of Kv1 channels in the axon of layer 5 pyramidal neurons.

Ausgewählte Vorträge bei internationalen Kongressen

Hallermann S, Fejtova A, Schmidt H, Weyhersmüller A, Silver RS, Gundelfinger ED, Eilers J (2010) Bassoon speeds vesicle reloading at a central excitatory synapse. **Gordon Research Conference** on Synaptic Transmission

Hallermann S*, Kittel RJ*, Wichmann C*, Weyhersmüller A, Fouquet W, Mertel S, Oswald D, Eimer S, Sigris SJ, Heckmann M (2009) Tethering vesicles to the active zone cytomatrix promotes their recruitment during sustained synaptic release. Program No. 9.10. Neuroscience. Chicago, IL, USA: **Society for Neuroscience**, 2009